

Thermal Analysis and Fuel Economy Benefits of Cylinder
Deactivation on a 1.0l Spark Ignition Engine



**University of
Nottingham**
UK | CHINA | MALAYSIA

**Thermal Analysis and Fuel Economy Benefits of Cylinder
Deactivation on a 1.0l Spark Ignition Engine**

Alexander Bech (BEng)

Thesis submitted to the University of Nottingham

for the degree of Doctor of Philosophy

October, 2017

Contents

Nomenclature	I
Subscripts	IV
Symbols	V
Abbreviations	VI
Dimensionless Groups	VII
Abstract	VIII
Chapter 1 Introduction.....	1
1.1 Overview.....	1
1.2 Mandate on CO ₂ Emissions Resulting from the Transport Sector in the EU.....	2
1.2.1 An Introduction to Light Duty Automotive Applications of Cylinder Deactivation ...	3
1.3 Other Routes in Achieving the 98 g CO ₂ /km EU Target by 2020.....	5
1.4 CAE Tools – Application for Proto-type Design and Development.....	6
1.5 Aim and Objectives.....	7
1.6 Layout of Thesis	9
1.7 Contribution to Knowledge.....	9
Chapter 2 Literature Review	11
2.1 Introduction.....	11
2.2 Thermal Management	11
2.2.1 The Role of Cooling Circuits in Reducing Fuel Consumption.....	11
2.2.2 The Integrated Exhaust Manifold (IEM) and Downsizing	12
2.2.3 Inter-Bore Cooling Slit Effects on Local Temperatures, Spark Ignition Advance and Knock.....	13
2.3 Cylinder Deactivation	14
2.3.1 Methods for Deactivating Cylinders	14
2.3.2 Valvetrain Mechanisms for Cylinder Deactivation.....	15
2.3.3 Transition from All Firing Cylinders to Deactivated Cylinders	21
2.3.4 In-cylinder Charge Behaviour When Shutting-Off Valves.....	21
2.3.5 Improving Catalyst Light Off Times	23
2.3.6 Cylinder Deactivation Effects on Emissions.....	24
2.3.7 Varying Valve Lift.....	24
2.3.8 Oil Entrapment in Deactivated Cylinders	25
2.3.9 Minimising NVH when Deactivating a Cylinder.....	25
2.3.10 Other Techniques for Cylinder Deactivation	27
2.3.11 Dynamic Skip Fire	27
2.3.12 Future Advances: Koenigsegg Air Compressed and Free Valve Technology	28
2.4 Cylinder Bore Distortion and Piston Ring Behaviour.....	30
2.4.1 Piston Ring Conformity, Collapse and Flutter.....	31
2.4.2 Methods for Minimising Temperature Differences and Cylinder Bore Distortion	31
2.5 Concluding Remarks.....	32
Chapter 3 PROMETS Theory	34
3.1 Introduction.....	34
3.2 PROMETS: Basics and Model Elements.....	34
3.2.1 Model Inputs	35
3.2.2 Lumped Capacity Analysis	38

3.2.3	Accuracy and Stability	38
3.3	Friction Model	40
3.3.1	Original Friction Model Description.....	40
3.4	Original Gas-side Heat Transfer Correlations.....	42
3.5	Exhaust Gas Temperature Prediction.....	44
3.6	Coolant Side Heat Transfer.....	44
3.6.1	Forced Convection and Nucleate Boiling	44
3.6.2	Coolant Circuit Set-Ups	45
3.7	Oil Circuit Model.....	48
3.8	Fuel Consumption Prediction	51
3.9	Discussion	52
Chapter 4	Advancing PROMETS to Represent the 1.0litre Three Cylinder Engine.....	54
4.1	Introduction.....	54
4.2	Engine Details and Architecture	54
4.3	Location of Thermocouples Used for Model Correlation.....	54
4.3.1	Data Used for Model Correlation.....	59
4.4	Feature Revisions and Additions	59
4.4.1	Integrated Exhaust Manifold (IEM).....	59
4.4.2	Engine Component Masses	60
4.5	Friction Model Revision for the TCE	61
4.5.1	Original Friction Model Description.....	62
4.5.2	Engine Friction Validation.....	63
4.6	Oil Circuit Model.....	65
4.7	Revisions to the Gas-side Heat Transfer Expression	65
4.7.1	Methodology for Revision of Heat Transfer Model	66
4.7.2	Comparison between the Original and Revised Model.....	68
4.8	Revised Coolant Passage Heat Transfer	74
4.8.1	Advanced Cooling Circuit Design Representation	74
4.8.2	Modelling Quiescent Coolant in the Block.....	76
4.9	Piston Cooling Jet Heat Transfer	89
4.9.1	Piston Cooling Jet Discharge and Heat Transfer Coefficient	89
4.9.2	Piston Cooling Jet Model Validation	91
4.10	Revised Fuelling and Intake Manifold Pressure Estimation	93
4.10.1	Method for Estimating Turbocharged Intake Manifold Pressure.....	93
4.10.2	Cylinder Volumetric Efficiency Estimation.....	94
4.10.3	Iteration for Intake Manifold Pressure and Fuel Consumption Prediction	97
4.11	Estimating the Work Done on the Gas in a Deactivated Cylinder.....	101
4.11.1	Incentive for Estimating Motoring Work Penalty.....	101
4.11.2	Procedure for Measuring Reduction in Bottom Dead Centre Pressure.....	101
4.11.3	Work Done on the Gas in the Deactivated Cylinder.....	102
4.11.4	Estimated Mass Loss When Trapping an Exhaust Charge	104
4.11.5	Literary Suggestions for Reducing Prolonged Partial Vacuum and Oil Suction .	105
4.12	Discussion and Conclusions	105
Chapter 5	Modelled Changes in Heat Transfer due to Cylinder Deactivation	108
5.1	Introduction.....	108
5.2	Heat Transfer Model Revision to Account for Cylinder Deactivation	108
5.2.1	Combustion Chamber Heat Transfer	108
5.2.2	Exhaust Side Heat Transfer.....	109

5.2.3	Intake Side Heat Transfer	111
5.2.4	Heat Losses due to Friction with a Deactivated Cylinder	112
5.3	Changes in Heat Transfer to Engine Coolant.....	116
5.4	Changes in Component Temperatures	119
5.4.1	Cylinder Walls	119
5.4.2	Temperature Response Times.....	120
5.4.3	Intake and Exhaust Valves.....	122
5.4.4	Piston Temperatures With and Without Cooling Jets	123
5.5	Temperature Differences between Adjoining Metal Components.....	124
5.5.1	Effect of Varying Compression Ratio and Spark Timing on Temperature Differences	127
5.6	Reducing Adverse Thermal Effects on the TCE.....	129
5.7	Exhaust Gas Temperature Changes when Deactivating	131
5.8	Limiting the Adverse Delay in Warm-Up Time When Deactivating	133
5.9	Discussion	134
Chapter 6 Cylinder Deactivation Effects on Engine Performance		137
6.1	Introduction.....	137
6.2	Modelling Performance Changes with Cylinder Deactivation	138
6.2.1	Pumping Losses and Gross Indicated Thermal Efficiency Calculations	138
6.2.2	Discrepancy between Modelled and ‘Real’ Pumping Losses	139
6.3	Fuel Consumption Improvement on the TCE.....	139
6.3.1	Percentage Improvements at Constant Operation	139
6.3.2	Magnitude of Improvement	141
6.4	Fuel Consumption Improvements on Drive Cycles.....	141
6.4.1	Drive Cycle Brake Torque and Engine Speed Inputs	141
6.4.2	Engine Speed Based Operating Envelopes	144
6.5	Real World Driving.....	145
6.5.1	Description of Routes	145
6.5.2	Operating Condition Residence Times and Related Engine Fuel Consumption ..	146
6.5.3	Representation of the 1.4l Engine	151
6.5.4	Fuel Consumption Improvements for a 4 Cylinder and 3 Cylinder Engine.....	152
6.5.5	Factors Influencing Employment of Cylinder Deactivation	153
6.6	Discussion and Conclusions	155
Chapter 7 Closed Loop Control System for Transient Drive Cycle Testing on ECTBs		158
7.1	Introduction.....	158
7.2	Initial PI Control Configuration and Step-Response Characteristics.....	158
7.3	The Effect of Ramping on Engine Speed Stability	161
7.4	Feed-forward Loop and PID Synergy	163
7.5	Addition of an Integrator Wind-Up Nullifier.....	167
7.6	Transferability to All Engine Builds, Repeatability of Results and Robustness of System Performance	169
7.7	Conclusions.....	176
Chapter 8 Discussion, Future Work and Conclusions.....		177
8.1	Discussion	177
8.2	Future Work.....	181
8.3	Conclusions.....	184

References	186
Appendix	199
A) Method for Calculating Exhaust Port Elements.....	199
B) Fuelling and Intake Manifold Pressure Iteration.....	203
C) Correlation between Modelled and Measured IMAP and PMEP	207
D) Experimental Changes in η_i , g and Modelled Fuel Consumption Benefits	209
E) Input Parameters for Modelling of the 4 cylinder 1.4litre TSI Engine	213
F) LabVIEW Block Diagrams for the Transient Drive Cycle Control System	214

Nomenclature

\dot{m}_f	Fuel flow-rate	kg/sec
$A_{cyl,eff}$	Effective Cylinder Surface Area	m^2
A_{pt}	Exhaust Port Surface Area	m^2
C_1, C_2	Constants	-
C_D	Drag Coefficient	-
C_{be}	Friction coefficient for the big end bearing term in the piston assembly	$kPa\ m^3\ (min/rev)$
C_{cs}	Friction coefficient for crankshaft seal term in the crankshaft assembly	$kPa\ min/rev\ m$
$C_{d,u}$	Discharge Coefficient for Fully Turbulent Flow	-
C_d	Discharge Coefficient	-
C_{ff}	Friction coefficient for flat-follower term in the valvetrain assembly	$kPa\ m$
C_{oh}	Friction coefficient for oscillating hydrodynamic term in the crankshaft assembly	$kPa\ (m\ min/rev)^{0.5}$
C_{oh}	Friction coefficient for oscillating hydrodynamic term in the valvetrain assembly	$kPa\ (m\ min/rev)^{0.5}$
C_{om}	Friction coefficient for oscillating mixed term in the valvetrain assembly	kPa
C_{pr}	Friction coefficient for piston ring term in the piston assembly	$kPa\ m^2\ (rev/min)$
C_{ps}	Friction coefficient for piston skirt term in the piston assembly	$kPa\ s$
C_{rf}	Friction coefficient for the roller-follower term in the valvetrain assembly	$kPa\ m$
C_{td}	Friction coefficient for turbulent dissipation term in the crankshaft assembly	$kPa\ (min/rev\ m)^2$
C_{vb}	Friction coefficient for bearing term in the valvetrain assembly	$kPa\ m^3\ (min/rev)$
D_b	Bearing Diameter	m
F_t	Piston ring tension term	-

F_{to}	Piston ring toughness term	-
K_D	Derivative Gain Coefficient	-
K_I	Integral Gain Coefficient	-
K_p	Proportional Gain Coefficient	-
L_b	Bearing Length	m
L_v	Valve length	m
\dot{Q}	Heat transfer rate	W/mK
\dot{Q}	Heat transfer	W
\dot{V}	Volume Flow-rate	m ³ /s
c_p	Specific Heat Capacity	J/kgK
c_v	Specific Heat Capacity at Constant Volume	J/kgK
d_p	Piston Depth	m
\dot{m}	Mass Flow-rate	kg/s
m'	Apparent Mass	kg
n_b	Number of Bearings	-
n_c	Number of Cylinders	-
n_v	Number of Valves	-
t_s	Skirt Thickness	m
Δt	Time interval	s
h	Convective Heat Transfer Coefficient	W/m ² K
A	Perpendicular Surface Area between Two Elements	m ²
B	Cylinder Bore	m
C	Thermal Capacity	J/K
E	Young's Modulus	N/m ²
F	Force	N
H	Cavity Height	m
L	Cavity Width	m

N	Engine Speed	rpm
P	Power	W
R	Thermal Resistance	W/K
S	Engine Stroke	m
S	Suppression Factor	-
T	Temperature	K
T	Torque	Nm
V	Volume	m ³
W	Work	J
X	Midway Distance between Two Adjacent Elements	m
c	Specific Heat Capacity	J/kgK
$c, deac$	Number of Deactivated Cylinders	-
e	Error between Measured and Target Value	-
f	Road Surface Resistance Coefficient	-
g	Constant for Gravitational Acceleration	m/s ²
k	Thermal Conductivity	W/mK
l	Length	m
m	Mass	kg
m	Ratio of diameters	-
p	Pressure	N/m ²
r	Radius	m
v	Velocity	m/s
z	Orifice Height	m

Subscripts

D	Drag
g	Resistance due to Inclination
I	Intake Port Conditions
m	Momentum
R	Rolling Resistance
LHV	Lower Heating Value of Fuel
amb	Ambient
anc	Ancillary subassembly
c	Coolant
c	Combustion
c, natural	Natural
c, fw	Fully Warm Coolant
c1c2	Combustion chamber and exhaust port
conv	Forced convection
crankshaft	Crankshaft subassembly
cyl	Cylinder
ele, x	Element Number
ex, out	Exhaust Port Exit Aperture
ex, gas	Exhaust Gas
ex, man	Exhaust manifold
f	Friction
f	Fuel
fw	Fully warm
g, a	In-cylinder gas
i	Inner
i, g	Indicated Gross Thermal
m	Manifold
n, boiling	Nucleate boiling
o	Reference dynamic viscosity
o	Outer
oc	Oil cooler
piston	Piston subassembly
pt	Exhaust Port
pt, wall	Exhaust Port Wall
ref, T = 90°C	Reference Temperature at 90°C
s	Surface
s	Swept
sat	Saturation
v	Volumetric
v, fw	Fully Warm Volumetric
v, ideal	Ideal Volumetric
valvetrain	Valvetrain subassembly
wu	Warm-up

Symbols

ε	Strain	m
σ	Stress	Pa
ν	Poisson's Number	
α	Thermal expansion coefficient	-
ρ	Density	kg/m ³
ν	Kinematic Viscosity	
θ_1	First Vogel Equation Constant	°C
θ_2	Second Vogel Equation Constant	°C
α	Thermal Diffusivity	m ² /s
δ	Boundary Layer Thickness	m
β	Volume Expansion Coefficient	-
Δ	Increment or change in variable	-
η	Efficiency	-
λ	Ratio of Actual AFR by Stoichiometric AFR	-
ϕ	Equivalence Ratio (Inverse of λ)	-
θ	Spark Advance	°degrees
γ	Adiabatic Index	-
n	Polytropic Index	-
ω	Angular Velocity	rad/s
τ	Time Constant for Controller Measurement	sec
μ	Dynamic Viscosity	kg/s m

Abbreviations

$IMEP_g$	Gross Indicated Mean Effective Pressure
$IMEP_n$	Net Indicated Mean Effective Pressure
ARTEMIS	Assessment and Reliability of Transport Emissions Models and Inventory Systems
DoD	Displacement on Demand
DOHC	Direct Acting Overhead Camshaft
ECTB	Eddy Current Test Bed
ECU	Engine Control Unit
FFL	Feed-forward Loop
FTP-75	Federal Test Procedure – 75
ICE	Internal Combustion Engine
NEDC	New European Drive Cycle
PID	Proportional, Integral and Derivative System
PROMETS	Program for Modelling of Engine Thermal Systems
TCE	Three Cylinder Engine
WLTC	Worldwide Harmonised Light Duty Test Cycle or Procedure
AFR	Air-to-fuel ratio
BDC	Bottom Dead Centre
EGR	Exhaust gas recovery
$FMEP$	Friction Mean Effective Pressure (bar)
$MBTD$	Minimum Advance for Best Torque Delivery
$PMEP$	Pumping Mean Effective Pressure
TDC	Top Dead Centre

Dimensionless Groups

Biot Number

$$Bi = \frac{hV}{kA}$$

Reynolds Number

$$Re = \frac{\rho v D}{\mu}$$

Prandtl Number

$$Pr = \frac{c_p \mu}{k}$$

Nusselt Number

$$Nu = \frac{hL}{k}$$

Raleigh Number

$$Ra = \frac{g\beta \Delta T \delta^3}{\alpha\nu}$$

Grashoff Number

$$Gr = \frac{g\Delta T\beta\delta^3}{\nu^2}$$

Abstract

The deactivation of a cylinder on a 1.0litre three cylinder turbocharged gasoline engine has been investigated providing novel information on thermal and fuel consumption effects associated with the technology. This comes in light of providing solutions to reduce fuel consumption and CO₂ emissions resulting from internal combustion engines. The investigation has been carried out through the PROgram for Modelling of Engine Thermal Systems (PROMETS). A version of PROMETS was extensively developed to characterise a commercially produced TCE not fitted with cylinder deactivation technology. Developments include an improved gas-side heat transfer expression to account for increased heat transfer to coolant due to the addition of an integrated exhaust manifold; addition of an expression to represent natural convection to model heating of quiescent coolant in the block; and a method to estimate the boosted intake manifold pressure past the throttle due to turbocharging on a gasoline engine. The 0-D approach used in this thesis compared to higher resolution computational tools has allowed for thermal and performance predictions to be made within a couple of minutes compared to several hours or days. In effect, PROMETS has been a time and cost effective tool during the development stages of a prototype engine.

The PROMETS model indicated that no adverse changes in engine thermal behaviour arose with cylinder deactivation. The largest temperature change of $< 400^{\circ}\text{C}$ occurs in the exhaust valve lower stem for the deactivated cylinder. Temperature changes in other components throughout the engine are an order of magnitude smaller. Although the largest temperature differences between the deactivated and firing cylinders were found to be in the range of $< 70^{\circ}\text{C}$, these remain within normal engine operating temperatures of $< 100^{\circ}\text{C}$. Also, by on-setting deactivation past an oil temperature of 40°C , warm-up times were marginally extended compared to operation on all cylinders from key-on.

Experimental inputs representing changes in engine gross indicated thermal efficiency and the work loss associated with the motoring of a piston complemented modelling work in predicting fuel consumption changes due to deactivation. Reductions in pumping losses account for the majority of the fuel consumption benefit associated with deactivating a cylinder. The main limitation in the employment of cylinder deactivation stems from the deterioration in the gross indicated thermal efficiency. Modelled results show that fuel consumption improvements are highest on low and part load operation envelopes. As such over the NEDC and FTP-75 benefits are in the range of 3.5%. Applying the technology over dynamically loaded cycles such as the WLTC and ARTEMIS, results in benefits of less than 1.6%.

Further to modelling work on cylinder deactivation, experimental work has been carried out with the aim of allowing any engine size to be tested to cover transient drive cycles for future research.

Future research could be in the aim of investigating technologies to reduce CO₂ and emissions resulting from ICEs. Results show that the control solution implemented has allowed eddy-current dynamometers normally used for constant speed and brake load conditions to operate cycles such as the WLTC or any transient brake torque and engine speed pattern. Benchmark fuel consumption values for two engines of differing swept volume are within a $\pm 4g$ error band equivalent to a 0.36% and 0.67% percentage error band demonstrating the excellence of the control system.

Acknowledgements

I am foremostly indebted to Professor Paul Shayler. His guidance, knowledge, patience and sincerity have been key to the work produced. For this I would like to give you my uttermost gratitude.

Thanks also go to Dr. M.J. McGhee, Dr. L. Cheng and Dr. J.P. Zammit for their help throughout the course of this work. Those late nights and debates will not be forgotten. Thank you for sharing this ever glowing enthusiasm to learn. I am also grateful for the work of the technicians N. Sykes and J. Lane. Without them experimental work would not have been completed so swiftly.

I would like to acknowledge funding for PhD studies from the Advanced Propulsion Centre UK and Ford Motor Company.

Lastly, my most profound thanks go to my family. Anders, Sophie, William and Holger merci pour votre amour et support. Les mots ne suffisent pas.

Chapter 1 Introduction

1.1 Overview

This thesis is primarily concerned with the development of a computational model and its application to a 1.0l three cylinder turbocharged gasoline engine (TCE) with cylinder deactivation. The main areas of interest have been quantifying the severity or otherwise degree of engine thermal changes produced by cylinder deactivation or reactivation, and the changes in fuel economy. The simulation studies have been complemented by test-bed investigations of engine behaviour including the extension of tests using eddy current dynamometers to cover drive cycles.

The motivation for this study stems from the need to reduce the emission and therefore accumulation of carbon dioxide (CO_2) in the Earth's atmosphere resulting from internal combustion engines (ICEs). In 2015, manmade CO_2 emissions in the United Kingdom (UK) accounted for an estimated 404 metric tonnes of CO_2 (Mt CO_2) wherein 24% resulted from the transportation sector [1]. In 2016, 82.8% of the transport sector in the UK comprised of light-duty vehicles (i.e. passenger cars). According to statistics from the department of transport 61% of these vehicles were powered by internal combustion engines tailored to gasoline [1.1].

Cylinder deactivation has been successfully applied on large displacement spark ignition (SI) engines. As in-cylinder load increases, larger amounts of air are required to be drawn into the combustion chamber further opening the position of the throttle valve. As such pumping losses reduce, minimising wasted fuel. With reduced CO_2 values of 6.2% reported on the environmental protection agency (EPA) city cycle for a 3.9l V6 gasoline engine [1.2] and ~9% for a 1.4l i4 gasoline engine on the New European Drive Cycle (NEDC) [1.3], application of cylinder deactivation on a TCE provides incentive for assessment for the purpose of quantifying fuel consumption benefits.

Understanding any adverse thermal consequences of cylinder deactivation on a TCE is important as heat rejection from the deactivated cylinder will reduce imposing a greater load demand from the firing cylinders. These effects are unknown and investigating this will shed new light on the subject. Temperatures and temperature gradients in the metal must be limited to safe values which neither jeopardise nor penalise the performance of the engine. Identifying and mitigating unwanted temperature differences is also needed to reduce the thermal effects deactivation has such that the engine may behave in a manner similar to that with all cylinder operation. Understanding this with the use of computational tools reduces the need to introduce more expensive experimental approaches, providing a time and cost saving incentive. The

PROgram for **Modelling of Engine Thermal Systems (PROMETS)**; a 0-D spatial resolution computational tool (lumped thermal capacity model), has been used throughout this research as it provides rapid and accurate thermal and performance predictions on engine behaviour. Compared to computational tools which have higher order resolutions; PROMETS provides predictions 10 to 1000 times faster than other tools. Therefore for a drive cycle such as the NEDC or WLTC the time-averaged approach used in PROMETS will take two to three minutes to complete predictions whereas higher order predictions will take a couple of hours to a couple of days or weeks to complete. This also depends on the nature of the model, i.e. whether time-averaged or crank-angle based.

Reducing the time spent warming up an engine to its optimum thermal state improves fuel consumption. Less energy is used to overcome frictional losses while a warmer engine structure also improves combustion quality and reduces hazardous emissions, such as carbon monoxide, THCs and formation of soot in oil [1.4].

The latter part of this thesis describes the development process and application of a control system built for engine test beds with an eddy-current dynamometer (ECTBs) to allow engine tests covering transient operating conditions to be carried out. Normally this type of dynamometer is used for test work covering steady speed and brake load conditions. In the context of the current study, the capability to simulate drive cycle conditions on a test bed greatly extends the possibilities of experimental work. Noted here, however, the reported work did not reach the point of evaluating the dynamics of the cylinder deactivation system on the test bed. A further interest in applying a control system to ECTBs for transient testing is in reducing the cost associated with engine testing providing research and automotive manufacturers an effective manner to test engines and engine technologies.

1.2 Mandate on CO₂ Emissions Resulting from the Transport Sector in the EU

Since the early 1960s, climate simulations run by national space agencies; e.g. National Aeronautical and Space Association (NASA) and the Intergovernmental Panel on Climate Change (IPCC) have shown that greenhouse gases (GHGs) and particulate matter (PM) emitted into the atmosphere have increased the rate at which the Earth warms-ups [1.5] [1.6]. In response to the increased release in greenhouse and carcinogenic gases, legislative bodies have tightened and imposed emission thresholds in all sectors due to human activity in the aim of providing a sustainable and eco-friendly future for forthcoming generations. These thresholds are based on ‘tail-pipe’ measurements. In the UK, the 2008 Climate Change Act has mandated that CO₂

emissions reduce by 80% by 2050 with reference to a 1990 baseline. The 20% reduction baseline is to be reviewed in 2020 [1].

In 1998 members of the European Automobile Manufacturers Association (ACEA) voluntarily agreed to incur in a fleet average CO₂ emissions threshold. The test or drive cycle used to homologate emissions was titled the NEDC. This consists of four repeated segments representative of a city-route, known as the ECE-15, followed by a short highway passage, named EUDC. The target was to achieve an average 140 g CO₂/km by 2008 for newly sold cars in the EU. Joined by commitments from the Japanese (JAMA) and Korean Automobile Manufacturers Associations (KAMA), automobile manufacturers failed in achieving to reach the target. In light of this the Economic Commission for Europe (ECE), today known as the United Nations Economic Commission for Europe (UNECE), legally imposed a 130 g CO₂/km limit (known as the ‘limit-value curve’) to be achieved by 2012 by the entire automobile fleet (i.e. cars, trucks, etc.) through improvement of internal combustion engine technologies. This limit was postponed and successfully met in 2015. The average emission of a new car sold in 2016 was of 118.1 g CO₂/km, proportional to a 16% reduction compared to 2010 values [1.7].

From the end of the third quarter of 2017 new legislative tests for the purpose of homologating fuel consumption and emissions will bring an end to the NEDC. These tests will fall under the label of Euro6c. Newly sold vehicles will be tested for CO₂ emissions on a more dynamic and aggressive drive cycle known as the WLTC. By fitting vehicles with an on-board emissions kit a Real-world Driving Emissions (RDE) test will also be implemented for the monitoring of CO₂ and other emissions. The onset of these tests coupled with the fleet 98 g CO₂/km limit to be set in 2020, for newly sold vehicles, are pushing automobile manufacturers to drastically improve engine efficiency and seek other solutions for reduction of CO₂ emissions. More detailed figures concerning emission thresholds on the Euro6c, for gasoline engines, may be read [1.7].

1.2.1 An Introduction to Light Duty Automotive Applications of Cylinder Deactivation

Early applications of cylinder deactivation were mainly made to improve the part load efficiencies of large capacity and higher cylinder count spark ignition engines. The *Cadillac* L62 V8-6-4 engine fitted with cylinder deactivation for the *1980 Cadillac DeVille* and *Seville* models (i.e. luxury vehicles) is an early example [1.8][1.9]. GM claimed a 30% reduction in fuel consumption during low – load and highway cruising conditions. Production stopped within the year of the application due to a series of unresolved failures [1.10]. In 1999, DaimlerChrysler

adopted the same technology in the European luxury/sports car market on the 5.0-litre V8 and 5.8-litre V12 engines through Mercedes on the *CL600*, *S600* and *CL500* vehicles. The system was claimed to improve fuel economy in city driving conditions by 7% and 20% for steady-state cruising [1.10]. Production of these engines terminated in 2005 and 2002, respectively.

In 2004, DaimlerChrysler introduced deactivation under the term Multi-Displacement System™ (MDS), to 5.7 (HEMI engine) and 6.4 litre V8 [1.11]. These were applied to the *Chrysler 300C*, *Dodge Magnum*, *Dodge Charger*, *Jeep Grand Cherokee*, *Dodge Durango*, *Dodge Ram* and *Jeep Commander* vehicle models. A 10-20% reduction in fuel consumption was claimed under this engine category, however with no reference to a drive cycle. Similarly in 2004, GM re-released deactivation under the term *Displacement on Demand* (DoD), on the *Envoy* and *TrailBlazer* model SUVs. The engine fitted with the technology was the *Vortec* 5.3 litre V8, where deactivation was only deployed during fully-warm engine operation and lightly loaded conditions for engine speeds above idling. Claimed fuel economy benefits were around 5-25%. In the subsequent year, 2005, Honda introduced deactivation coining the variability in displacement as *Variable Cylinder Management* (VCM). This was applied to a bank of cylinders on the V6 3.5litre *Odyssey* and 3.0litre *Accord Hybrid*. A 10% improvement in fuel economy was validated using the US EPA Highway Fuel consumption test, compared to the same engine exempt of the technology. In 2007, GM again coined Active Fuel Management™ (AFM), synonymous to cylinder deactivation, for the 3.9 litre V6 engine which improved fuel consumption at part load by 6.2% with reference to the US EPA City Cycle and 7% on the US EPA Highway cycle [1]. In 2008, the EPA claimed that through cylinder deactivation fuel consumption could be reduced in the range of 6 to 8% [1.12].

With this, cylinder deactivation was first applied to Vee engines due to the relative simplicity in deactivating a whole bank of cylinders through disablement of an entire camshaft. However at the expense of a control strategy such that the catalyst for the specific bank of deactivated cylinders light off without significant delay. In 2011, the Bentley *Mulsanne*, powered by a 6.75l V8 engine, was redesigned to meet LEV2/EU5 emissions legislation requirements by deactivating four of eight cylinders during low load conditions [1.13]. A 15% reduction in fuel consumption was attributed to cylinder deactivation along with the coupling of an 8-speed automatic transmission. In 2012, *Daimler* included deactivation on a 5.5litre V8 engine SLK 55 Mercedes-AMG model. The modal characteristic of the NEDC allowed for the engine to employ deactivation over 60% of the cycle providing a 10% fuel consumption improvement [1.14]. 2012 marked the year where cylinder deactivation was commercially applied to an inline and sub 2.0l

engine. The 1.4l TSI engine fitted to the VW *Polo GT* promises a 0.4 l/100km (~9% reduction) over the NEDC by deactivating the two central cylinders of the inline four [1.3]. Reverting back to large swept volume engines, at the 2015 Geneva Motor Show, Bentley announced the deactivation of either of the W12 6.0l cylinder banks to improve fuel economy and reduce emissions [1.15]. Part of the VW group, this engine is fitted to the Bentley *Continental Flying Spur*, *Continental GT* and *GTC*, VW *Phaeton* and Audi *A8* where calibration and thus rated power, and engine volumetric capacity are dependent on the target vehicle model [1.16].

1.3 Other Routes in Achieving the 98 g CO₂/km EU Target by 2020

Further technology streams for reducing fuel consumption and CO₂ are shown on Figure 1. In areas such as thermal management, weight reduction, start-stop, heat recovery, controlled combustion, down-sizing and lowered rolling resistance have already led to ~30% reduction in CO₂ emissions. Hybridisation of ICE powered vehicles show the largest potential in reducing fuel consumption, i.e. ~22% reduction, given that the ideal gas engine may theoretically achieve a minimum CO₂ emission of 110g/km [1.17]. Programs such as the Zero Emissions Vehicle (ZEV) instigated by the EPA as of 2018 [1.18] are directing ICE powered automobile manufacturers to the trend of hybridisation [1.19].

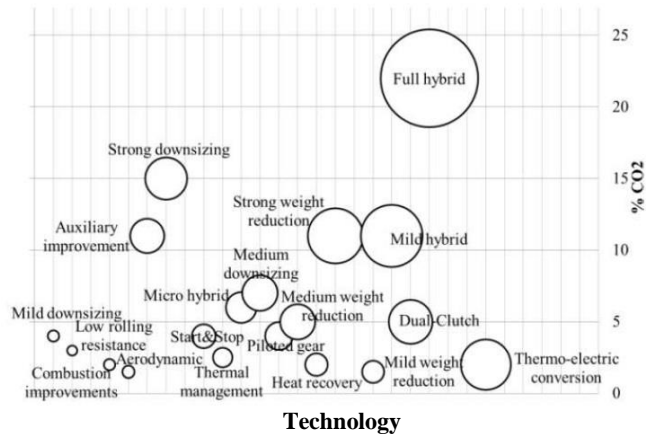


Figure 1: Estimated CO₂ percentage reduction potential for proposed technology areas where the ball size represents a cost of implementation [1.20].

The ZEV program legally instigates that auto-manufacturers in the state of California, Connecticut, Maine, Maryland, Massachusetts, New Jersey, New York, Oregon, Rhode Island and Vermont produce a fixed percentage of hybrid, plug-in hybrid, battery or fuel cell electric vehicles relative to the total number of conventional ICE vehicles sold. This number is projected to exponentially increase over time as the cost of batteries will reduce over time.

Fully electric powered vehicles are desirable from a socio-economic prospect if electricity is produced from renewable technological means (i.e. wind, solar or wave) or natural gas. The trend to fully renewable dependent production of electricity is taking place in countries such as Denmark where 42% of the annual electricity production stems from wind power [1.21]. The global trend in this direction is gaining momentum. However, gasoline hybrid, diesel and CNG engines are still favourable compared to electric powered vehicles where fuel sources still stem from coal fired plants. CO₂ emissions would almost quintuple if the entire transport fleet would convert to electric vehicles [1.22]. As such within the automotive industry, a large proportion of resources are still deployed to improve conventional ICE designs. Such an optimisation is the application of cylinder deactivation to commercially sold vehicles outside the bounds of the luxury car market.

1.4 CAE Tools – Application for Proto-type Design and Development

Computational modelling tools are widely used to facilitate the proto-type design process and in assessing the feasibility of optimisations made to the design of an ICE design and/or technology. The mass availability of computational tools in carrier format such as laptops, touchpads and other portable devices makes simulation work incredibly easy to access and perform.

The aim of this research is to determine the effects of cylinder deactivation on the thermal behaviour and performance of the TCE. The importance and availability of such models are widely discussed in literature [1.23] [1.24] [1.25] with the choice of the computational resolution (i.e. number of dimensions) chosen being dependent on the time frame of the project and resources invested in obtaining set results.

Computer aided design (CAD) tools such as Creo Parametric and AutoCAD are used to create assemblies from which 2D drawings are then used for manufacturing. Computational fluid dynamics (CFD) is used to describe fluid flow and the interaction between molecules in liquid and vapour phases. In application with internal combustion engines these are prevalent in understanding injection and ignition transients in the combustion process while also aiding in the aerodynamic optimisation of gas flow in the aim of reducing pressure losses in piping [1.26] [1.27]. Contrarily, referring to materials remaining in the solid phase, Finite Element Analysis (FEA); applicable from one-dimensional to three-dimensional resolutions, allows for the study of stress analysis of engine components subjected to shearing, tensile, compressive and/or thermal loads. Such simulation tools when solved in three dimensions require large computational time

and user experience (i.e. extremely detailed knowledge) however yielding high fidelity results. For the purpose of modelling ICEs enormous computational efforts are required; in the order of several days, due to the crank-angle based approach.

Compared to 3D design and simulation tools, physics and chemistry based zero dimensional approaches such as lumped element models are most useful for early stage, concept or multi-system studies using limited detail and expense. The **PRO**gram for **Modelling of Engine Thermal Systems** (PROMETS) runs on Matlab™ SIMULINK built at the University of Nottingham, simulates hours of holistic engine operation in several minutes of real-time. This allows for rapid simulation results to be passed on in the aim of improving thermal management during the product development stage while also providing predictive and informative results on engine thermal behaviour and performance.

1.5 Aim and Objectives

The aims of this research cover two areas. The first area relates to the subject of cylinder deactivation. The work reported in this stream has been aimed at providing a detailed investigation on the macroscopic, and in certain cases, component specific effects that cylinder deactivation has on the thermal behaviour of a TCE. For this purpose the computational software PROMETS was used. The development and evaluation of the model was supported by data collected from a 1.0l engine which did not have a cylinder deactivation system. This was supplemented by experimental data made available by independent sources, acknowledged when used. The potential of applying cylinder deactivation in the aim of reducing fuel consumption over drive cycles of various natures was assessed. These aims were pursued through the following objectives:

- Characterise an engine design as a collection of sub-systems to provide a prediction of engine performance and thermal behaviour; which models are available or must be modified or developed to represent each sub-system and assess their individual fit, formulation and function for the intended application.
- Select sub-systems from a mix of physics-based and empirical modelling approaches to achieve a balance between these approaches.
- Utilise this collection of sub-systems to predict the thermal effects of deactivating one of a total of three cylinders for an engine with a swept volume of 1.0 litre.

- Provide an understanding of which components undergo the largest temperature change and between which adjoining components the maximum temperature gradient arises. Also, identify thermal implications of deactivating a cylinder on engine performance and warm-up characteristics.
- Suggest, through modelling, method(s) of minimising temperature changes/differences which may arise due to cylinder deactivation.
- Provide a theoretical solution for estimating the work loss due to the motoring of a cylinder for time-averaged models.
- Predict fuel consumption benefits due to the reduction in pumping work assuming constant combustion and gross indicated thermal efficiencies for drive cycles/routes of varying nature (i.e. modal and transient). Identify and quantify the increased fuel consumption improvement due to changes in gross indicated thermal efficiency.

The second area pertains to devising a control system for the purpose of testing engines on test-beds for fuel consumption evaluation purposes. With the upcoming WLTC drive cycle test, the ability to test engines in laboratory conditions gives auto-manufacturers the liberty to rapidly switch-over engines (i.e. at a cheaper cost compared to chassis based tests), engine components or added technologies for the purpose of evaluating the effects these modifications have on fuel consumption and thus CO₂. Power absorbing engine test beds have not been previously used for this purpose and this would therefore provide a cost and time saving incentive if achieved. This work was carried out requiring that the following objectives be met:

- Understand the limitations of using default engine speed and engine brake torque control modes on dynamometer controllers for the running of transient drive cycle tests on power absorbing eddy-current test beds.
- Seek an automated closed-loop control system which allows for easy implementation of the drive cycle requiring a minimum number of user inputs as well as time and cost efforts.
- Devise, test and validate an experimental method for running transient drive cycles on eddy-current test beds such that fuel consumption may be gauged to a higher standard of accuracy. Accurate and repeatable control of engine speed and brake torque is required regardless of operating temperature.
- Transfer this work to engines of differing sizes and explain the necessary changes required in the transferral process.

1.6 Layout of Thesis

Following this introduction a literature review of the current and future research findings concerning the application of cylinder deactivation are reviewed in Chapter 2.

A description of the state of PROMETS prior to the work carried out in this thesis is set in Chapter 3. Expressions for heat transfer from the gas-side and friction to coolant and oil are described providing information on the major sub-models of PROMETS.

In Chapter 4 a description of the modifications made to the sub-systems of PROMETS specifically pertaining to the mass, heat transfer, friction, coolant and fuelling sub-systems required to characterise the 1.0litre TCE are overviewed. The set-up of thermocouples instrumented on to the TCE is referred to. Validation of each of these subsystems with experimental data is also presented. The method for analytically representing the work loss for the motoring of a piston in a non-hermetically sealed cylinder is also described in this section.

Chapter 5 is composed of predictions of the thermal behaviour of a TCE when cylinder deactivation is enabled. This encompasses quantification of the temperature changes for various components, temperature differences between adjoining components and effects on warm-up time along with suggestions for minimising these occurrences.

In Chapter 6 predictions of the effects that cylinder deactivation has on fuel consumption are assessed over various drive cycles and real-world routes. The effect of driving style on the potential for cylinder deactivation to reduce fuel consumption is discussed.

The process of devising an engine generic closed loop control system for throttle control on eddy-current dynamometers and a finalised control system for the benchmarking of fuel consumption on transient drive cycles is detailed in Chapter 7.

In Chapter 8 conclusions of this work are shown with appraisal of the modified multi-cylinder model of PROMETS for predictive purposes highlighting key findings related to thermal and performance effects of cylinder deactivation. Finally further work and a summary of research findings, significant conclusions and achievements are listed.

1.7 Contribution to Knowledge

New knowledge has been brought forth through modelling with the effects of cylinder deactivation on the thermal behaviour and performance on a 1.0litre three cylinder gasoline engine. Thermally information on the absolute changes in temperature of engine components, e.g. the cylinder wall, valves and piston; for various constant operating conditions have been

quantified. Fuel economy benefits associated with cylinder deactivation for constant operating conditions, drive cycles and routes under real world driving have also been brought to light. The potential fuel economy benefits when deactivating a cylinder have been assessed with respect to operating condition characteristics.

Modelling of the three cylinder engine required additions and modifications to the existing multi-cylinder model in MATLAB SIMULINK such that phenomena specific to the engine be captured. The transition from naturally aspirated to downsized turbocharged gasoline engines required a method for estimating cycle averaged inlet boost pressure past the throttle. Heat transfer through natural convection for coolant in a vertical enclosure of aspect ratio greater than 10 was also added to represent the advanced cooling circuit defined in the three cylinder engine. Further to describing the occurrences associated with cylinder deactivation the penalty associated with the motoring of a piston and the net mass loss of the trapped charge for stabilised conditions have been defined and investigated. Part of the findings for the simulation work described above have been published in the SAE (2016-10-2106) International Journal of Engines V125-3 and V126-3 editions. Further work investigating the effect of driving style and route on a 1.4l four cylinder turbocharged gasoline engine have been published in the FISITA conference paper F2016-ESYA-01. Some of the experimental work concerning: the mass loss of the trapped charge in the deactivated cylinder and temperature changes throughout the engine system, are due for publication in the Proceedings of the Institution of Mechanical Engineers, Part D: Journal of Automobile Engineering.

The final section of this thesis comprises work done on devising a control system allowing for the testing of transient drive cycles on eddy current dynamometers. New knowledge has been brought forth in this area by developing a control system dependent on the symbiosis of a PID controller, integrator windup and feedforward system allowing any engine size to run a given engine brake torque and speed profile. This has allowed for testing and benchmarking of any size engine on fuel consumption and emissions on any brake torque and engine speed profile, whether from a drive cycle or extracted from real-world driving. The result of the work carried out is due for publication in the Control Engineering Practice – Journal (Elsevier) although discussion for a patent has also been proposed.

Chapter 2 Literature Review

2.1 Introduction

This chapter provides information into past and current advances mainly on areas that explain the phenomenon, technologies and effects due to cylinder deactivation. Since this thesis is focused on the simulated effects of cylinder deactivation on engine thermal behaviour and performance the majority of the content in this literature review identifies simulated results on the application of cylinder deactivation. This ranges from mechanisms used to deactivate cylinders, modelled and experimental results describing thermal and performance effects of deactivation to current proto-type technologies that facilitate the application of cylinder deactivation. Apart from the information detailed in this chapter, where applicable literary information also accompanies the working chapters of this thesis supporting explanation of concepts or findings drawn through this work.

2.2 Thermal Management

Compared to previous engines modelled through PROMETS the TCE has the addition of an advanced cooling system, integrated exhaust manifold (IEM) and inter-bore cooling slits. A split cooling system is first described to highlight the benefit of segregating flow in the block and head passages found through the literature. Next the addition of the IEM and inter-bore cooling slits on head temperature and the temperature difference between cylinders, respectively, are described with findings drawn from the literature.

2.2.1 The Role of Cooling Circuits in Reducing Fuel Consumption

One aspect of vehicle thermal management relevant to this work is in examining methods of improving engine warm-up rates in the aim of reducing fuel wasted due to cold starting conditions. Below the optimal engine thermal state fuel is generally wasted due to: cold lubricating oil temperature, inhomogeneous lubricant film and lowered combustion efficiency due to 'cold' cylinder walls that quench available heat [2.1]. As the engine reaches a fully warm state coolant liquid should ideally keep the head cool in order to avoid knock, spontaneous ignition and/or mechanical failure/warping of the head. The bulk of the metal structure contained in the upper and lower block segments should be warmed up rapidly to reduce friction torque.

Three types of cooling circuits are commonly used in internal combustion engines. These are series, parallel and cross-flow circuits. These designs involve a fixed mass of coolant flowing through the block eventually exiting the engine structure through head passages. The thermal inertia of the coolant in these systems is large due to the total engine coolant volume passing

through the engine structure from warm-up [2.2]. Recently the use of split cooling systems has been applied to internal combustion engines. This design segregates coolant volumes to specific parts of the engine reducing coolant thermal inertia, improving warm-up times. Studies conducted by *Cipollone et al* [2.1] on a 1-D lumped thermal capacity model have shown that segregating coolant flow to the intake side of the head, exhaust side of the head and block compared to conventional series type coolant systems improves engine warm-up rates over the NEDC by 100seconds on a 800second warm-up period. However, accurate splitting of the flow is required due to the low thermal inertia the coolant bears with the addition of by-pass passages. *Cipollone et al* had shown that if coolant flow-rates were too low large temperature gradients could arise between the inlet and outlet parts of the engine. However if too much flow was allowed in the head the system behaved like a conventional system.

2.2.2 The Integrated Exhaust Manifold (IEM) and Downsizing

Exhaust gas enthalpy flow accounts for 30 to 37% of the heat energy released as a by-product of combustion [2.3]. To harness a larger proportion of heat energy from exhaust gases auto-manufacturers have integrated the exhaust manifold into the engine head [2.4]. Removing the exterior exhaust manifold and providing longer exhaust ports enveloped by coolant a larger proportion of heat energy is thus transferred to coolant. The difference in engine design is shown in Figure 2. This system is incorporated in the engine design of the TCE reported in this thesis.

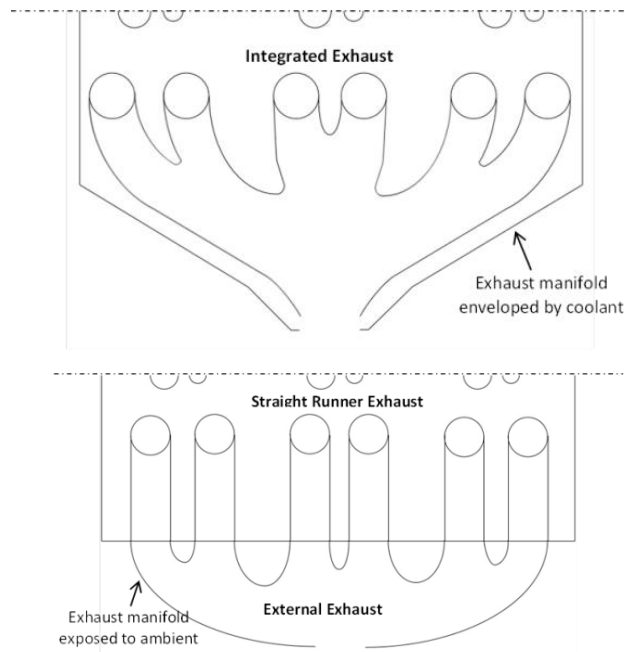


Figure 2: Simplified line drawing differentiating between the external and integrated exhaust manifold with CAD extracted surface areas for the individual ports.

For a 1.6l 4 cylinder gasoline engine the addition of an IEM compared to a conventional external exhaust manifold reduces the build cost of an engine by 5%, catalyst light off time by 20% (approximately 5 seconds with a 30% reduction in surface area leading up to the turbocharger), as well as improved powertrain mass by up to 5kg with improved engine durability. By removing the external exhaust manifold the number of parts required to manufacture the engine reduces significantly saving costs throughout the development cycle and supply chain, from inventory and assembly to aftermarket supply. The exhaust port surface area exposed to coolant for coolant passages whose design remains unchanged increases by roughly 20% [2.5] if optimised to extract as much heat from exhaust gases this has the potential to significantly increase. As a result of this due to increased heat transfer from exhaust gases to coolant, warm-up rates have been shown to increase. As example, fuel consumption has been shown to improve by 1 to 2% over cold-starting tests on the NEDC [2.6]. With this the engine reaches optimum operating efficiency a faster rate allowing for windscreen demist and passenger warm-up periods to reduce too.

With respect to downsizing, providing a thermally balanced head and upper block structure reduces the eventuality for knock. Furthermore, thermo-mechanical loads and effective component fatigue life (i.e. residual and thermal stresses and assembly loads also reduce) allow for turbocharging as combustion pressures increase, increasing thermal loads. As a result of lowered operating loads plastic and creep strain amplitudes reduce improving low and high cycle fatigue safety factors [2.5].

2.2.3 Inter-Bore Cooling Slit Effects on Local Temperatures, Spark Ignition Advance and Knock

As engine power output per unit capacity has increased, manufacturers have added inter-bore cooling slits to improve cooling between cylinders and reduce inter-bore temperatures [2.7]. Experimental studies by *Nishino et al* have shown that the size of the slit is of importance in reducing the inter-bore temperature. The research findings are visually summarised in Figure 3. For speeds ranging from 1000-6000 rpm *Nishino et al* three cylinder blocks designed without slits, with small slits and with large slits experienced increases in temperature of 420-470K, 395-420K and 395-400K, respectively. With reference to Figure 3 (b), as the slit is enlarged, a smaller temperature variance is encountered across the inter-bore with respect to increasing engine speed at WOT. Furthermore, significant reductions in wall thickness between exhaust valves, intake and exhaust valves, valve sheet ring back boss and base thickness were also made by increasing coolant passage size. An average reduction of 3mm was achieved for each of the above

mentioned components allowing for faster warm-up time, reduction in knock and 1° advance in spark-ignition timing. This was feasible due to a 20°C reduction in maximum cylinder wall temperature alongside an approximate 5°C reduction in gas temperature during the compression stroke.

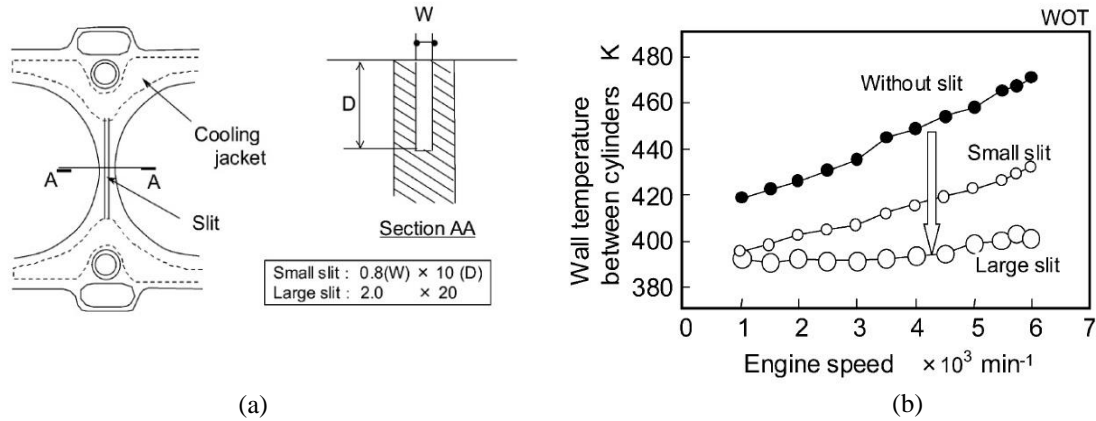


Figure 3: (a) From Nishino et al – 3 cylinder block; inter-bore slit topology defining large and small slit geometry in mm. (b) Comparison of large, small and no slit engine designs effect on inter-bore temperature for varying engine speeds [2.5].

With respect to cylinder deactivation the work of *Nishino et al* shows that the addition of inter-bore cooling slits minimises the thermal effects of neighbouring cylinders. For the TCE medium sized slits; [i.e. 1.2mm (W) x 16mm (D)] are fitted on to the engine.

2.3 Cylinder Deactivation

2.3.1 Methods for Deactivating Cylinders

Three forms of cylinder deactivation process have been found in the literature. The simplest form of deactivation consists of cutting off fuel injection while allowing the valves to operate as they would normally [2.8]. The second also disables intake and exhaust valves, trapping the cylinder charge [2.8]. The third, in addition arrests the reciprocation motion of the piston [2.9]. Each method presents benefits and penalties relative to the other. When solely cutting-off fuel injection pumping losses are not significantly minimised since the motored cylinder still undergoes filling and emptying processes. The intake manifold pressure must therefore compensate for the filling of the motored cylinder. *Leone and Pozar* [2.8] report that when disabling the opening and closing motion of the intake and exhaust valves, pumping losses significantly reduce. When combining this with an inert piston, a further benefit is had by reducing friction rubbing losses at the piston level. Although a reduction is foreseen, proto-type

developments tested by *Doller et al* [2.9] have shown that the added complexity in design allowing pistons to transiently arrest and resume reciprocation causes uncertainty in the net fuel consumption improvement. This means that when the cylinders are disengaged overall engine FMEP increases by

When trapping charge in the motored cylinder, by closing the valves, the BDC pressure rapidly stabilises to conditions below atmospheric. The magnitude of the pressure observed at BDC varies depending on the source conferred due to blowby. *Leone and Pozar* show through a pressure volume trace that the bottom dead centre pressure reaches approximately 0.2barA [2.8]. Contrarily *Ma* [2.10] shows a value close to 0.65barA while *Zammit et al* [2.11] have reported on a value of 1barA. Nonetheless, the reported penalty associated with deactivation has been noted to be negligibly small. *Leone and Pozar* quantified the value for a 6.8l V8 to be in the range of 0.01 - 0.02bar gIMEP [2.8]. There is uncertainty in the actual BDC pressure value giving room for further research.

Depending on the order of closure of intake and exhaust valves, fresh air or hot exhaust gases may be trapped in the deactivated cylinders. Trapping of fresh air would encompass omitting the injection period, spark sequence and exhaust valve opening. *Ihlemann et al* [2.12] explain that when trapping an exhaust charge, fresh air is vented into the cylinder followed by a customary injection and ignition period omitting the exhaust valve opening period. Both methods result in different in-cylinder pressure conditions. *Ihlemann et al* show that trapping fresh air results in low cyclic in-cylinder pressure variations and a rapid decline in the maximum and minimum pressure experienced. *Ihlemann et al* show that when trapping exhaust gases in-cylinder pressures are significantly larger requiring more time to reduce to stabilised conditions. Although changes in the motored pressure traces are described by *Ihlemann et al* [2.12] and *Souflas et al* [2.13] the number of cycles from the onset of deactivation to a repeated stabilised pressure profile has not been investigated. Nonetheless, both investigations explain that when trapping exhaust gases unwanted NVH effects may arise through a load imbalance during the exhaust stroke. Thermally, however, *Ihlemann et al* observes that when trapping exhaust gases, cylinder walls are kept warmer in effect reducing possible thermal gradients between adjoining inter-cylinder metal components. However, pejorative effects of trapping an exhaust charge on oil quality and/or contaminative effects remain unknown.

2.3.2 Valvetrain Mechanisms for Cylinder Deactivation

Four mechanical valvetrain technologies have been commercially developed that allow for valve motion shut down. Two types of design exist; the first consists of modifications between

the cam-lobe and tappet and the second at the camshaft level. *Hoffmann et al* [2.14], *Radulescu et al* [2.15] and *Fujiwara et al* [2.16] describe three designs that exist between the interface of the cam-lobe and tappet based on different valve architectures. These have been undertaken for an end-pivot rocker arm, a centre pivot SRFF and a pushrod rocker arm design, respectively. The above authors all show that disablement of valve movement is achieved through a hydraulic lash adjuster (HLA). Pressurised oil disengages movement from the cam-lobe and camshaft by pushing back a spring within the HLA or in the spring system resulting in lost motion. Commercial applications of these mechanisms with reference to manufacturer are shown below in Figure 4.

Manufacturer	Type of engine	Valve concept	Status
GM	6.0-liter V8-6-4 engine	Pushrod actuation, switchable rocker arm pivot point	SOP/EOP 1980
	3.9-liter V6 engine	Switchable roller tappet	EOP 2008
	5.3-liter V8 engine	Switchable roller tappet	Volume production
	4.3-liter V6 engine	Switchable roller tappet	Volume production
	6.0-liter V8 engine	Switchable roller tappet	Volume production
Daimler	5.0-liter V8 engine	Switchable rocker arm; MB	EOP 2005
	5.8-liter V12 engine	Switchable rocker arm; MB	EOP 2002
Chrysler	5.7-liter V8 engine	Switchable roller tappet	Volume production
	6.4-liter V8 engine	Switchable roller tappet	Volume production
Honda	3.5-liter V6 engine	Switchable rocker arm	Volume production
AMG	5.5-liter V8 engine	Switchable pivot element	Volume production
VW Group	1.4-liter inline 4-cylinder engine	Cam shifting system, VW/Audi	Volume production
	4.0-liter V8 engine	Cam shifting system, Audi	Volume production
	6 3/4-liter V8 engine	Switchable roller tappet	Volume production
	6 3/4-liter V8 engine	Switchable roller tappet	Volume production
	6.5-liter V12 engine	Only the fuel injection supply is cut	Volume production

Figure 4: Valvetrain concepts for the enablement of cylinder deactivation on volume production vehicles [2.12].

End-Pivot Rocker Arm Design

An end-pivot rocker arm design, with an overhead camshaft (OHC), consists of a cam lobe centred above the roller element while the valve is situated on the end of the pivot opposite a hydraulic lash adjuster. An illustration of the mechanism is shown in Figure 5. When deactivation ensues the hydraulic lash adjuster pushes pressurised oil into the roller assembly pushing aside a latch spring, such that the roller element translates vertically without applying force onto the valve pad and thus the valve spring [2.14] [2.15].

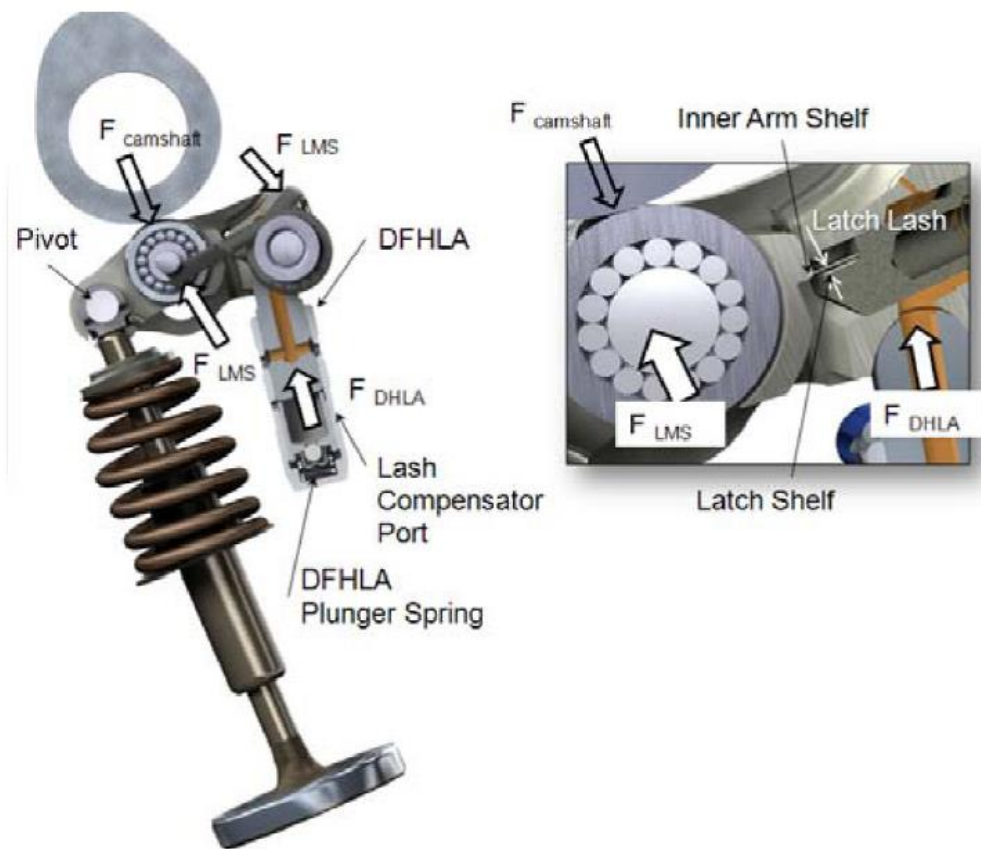


Figure 5: Deactivation mechanism for an end pivot valve architecture [2.15].

Centre Pivot Switchable Roller Finger-Follower

A centre pivot SRFF on the other hand has part of the rocker arm resting on the cam lobe via a bearing element where on the opposite side the rocker arm pushes the valve is pushed down. Disablement of the translational motion of the valve is affected by disengagement of a pin fitted and connecting to adjacent valves via the centre pivot hub. The mechanism for this valve design is shown on Figure 6. Again, hydraulic pressure is used to move the latch between the parallel rocker arms (i.e. for four valve cylinder) disengaging the latch pin which disconnects the rocker arm in contact with the valve thus abstaining valve movement [2.16].

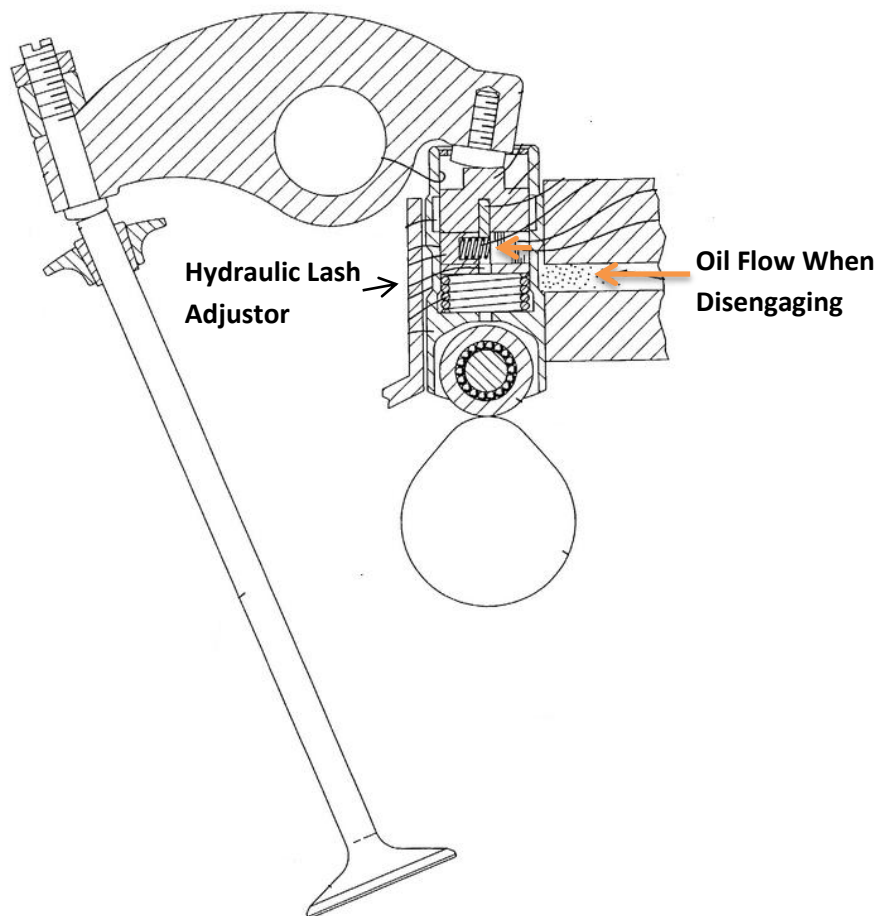


Figure 6: Deactivation mechanism for centre-pivot valve architecture [2.17].

Pushrod Rocker Arm Design

A pushrod rocker-arm design has the cam-lobe fitted in the block acting as the pushrod lifter [2.16]. As shown on Figure 7 for this mechanism, a roller lifter is situated between the contact point between the lobe and the pushrod such that when deactivation of the valves is required the lifter does not exert force onto the rocker arm. An oil control valve is required for each cylinder in this case.

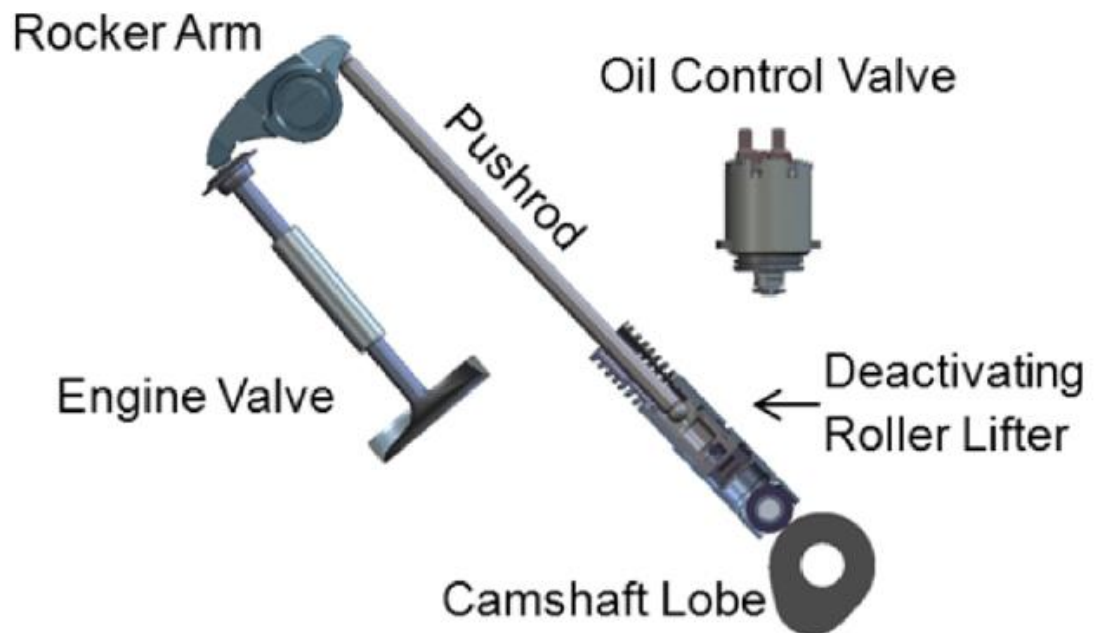


Figure 7: Deactivation mechanism for a pushrod rocker arm valve architecture [2.13].

Cam-Shifting Technology

Cam-shifting technology used in the 1.4l VW TSi stems from the Audi Valvelift System used on four, six and eight cylinder engines. The technology is applied to an OHC roller follower configuration. The system is electronically actuated by merging a grooved shaft with a barrel with involute gearing to ensure that the shafts do not have an unsynchronised angular velocity. Of the four cams the two centre cams are prone to deactivation. Grooved guide paths are machined onto the camshaft below the actuators to allow for the transversal switching of the camshafts. When the actuators are enabled a cylinder pin, 4.0mm in diameter, is fired by inertial switching of coils and pushed against the grooved path sliding the camshaft. The switchover is completed within half a camshaft revolution. Actuation times are dependent on engine speed and range from 72ms at 1400rpm to 28ms at 4000rpm, where at the end of a deactivation event the shaft is locked into place by spring loaded balls. Compared to valvetrain assembly modifications, the cam-shifting technology design adds two kilograms to the total mass of the camshafts [2.19].

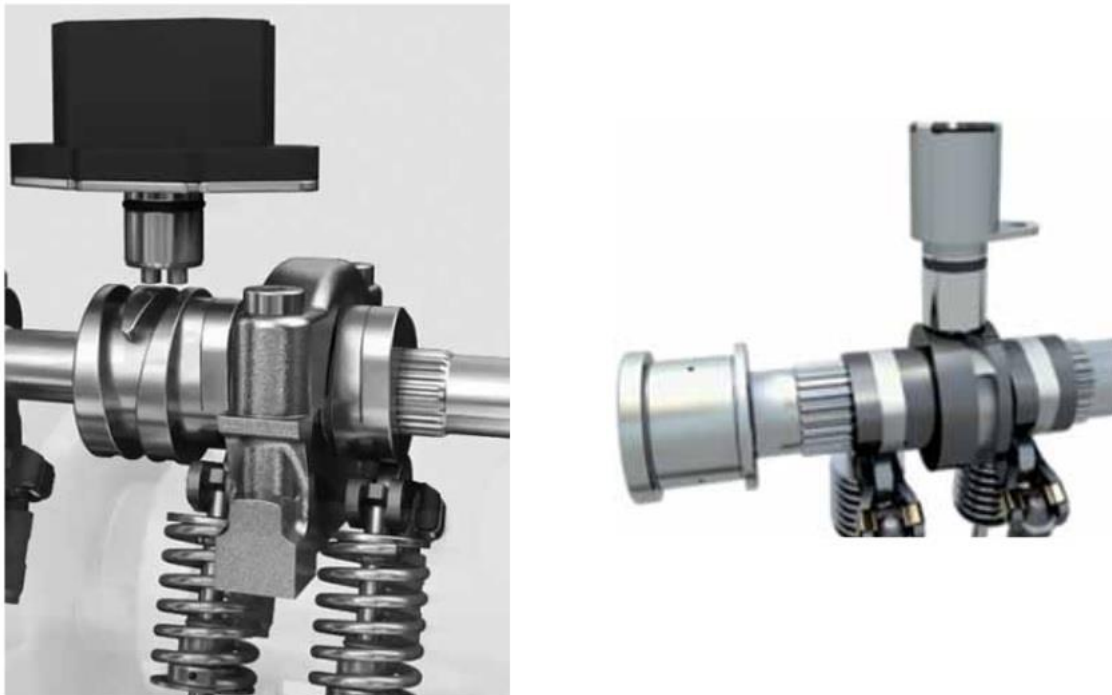


Figure 7.1: Two-stage (left) and three-stage (right) cam-shifting systems, i.e. acting on a single cylinder and acting on two cylinders.

2.3.3 Transition from All Firing Cylinders to Deactivated Cylinders

Studies by *Ilhlemann* [2.12] have shown that when deactivating a cylinder or cylinders fluctuations in engine brake torque occur if mechanisms allowing for deactivation are not well calibrated. Calibration work carried out by *Souflas et al* [2.13] shows that when transitioning from operation on all cylinders to operation on selected cylinders a succession of events occur within a 0.25 second interval. *Kortwittenborg et al* [2.20] show that the charge flowing past the throttle valve is first increased followed by a delay in ignition timing so as not to exceed the demanded engine brake torque. When the desired charge for deactivation is achieved the valve-train ensues by shutting off the designated deactivated cylinder(s) [2.13]. This is followed by a rapid re-configuration, advancement of the injection and ignition timing to deliver the same target brake torque or a brake torque demand within the scope of the deactivation envelope. The change in throttle position, spark-timing and valve overlap during a transition event is illustrated in Figure 8.

2.3.4 In-cylinder Charge Behaviour When Shutting-Off Valves

Information on the in-cylinder charge behaviour of the firing cylinders for an engine subject to cylinder deactivation is limited. The increased air charge flowing past the valves of the firing cylinders when deactivating a cylinder are analogous to studies observing the change in air charge behaviour for cylinders with deactivated valves. Mention of this is also made in this literature review such that the effect of varying the valve lift for firing cylinders remains common knowledge giving way to theories for increased gross indicated thermal efficiency when implementing cylinder deactivation. *Moore et al* [2.21] conducted tests on a 2.0l gasoline turbocharged direct injection engine (GTDi) with dual independent cam phasing (DICP) subject to deactivation of a single intake valve per cylinder. Tests were performed for engine speeds of 1000 to 3000rpm and brake loads of 1 to 8 bar BMEP. All cylinders were kept firing and the effect of deactivating a valve while compensating by delaying the adjacent intake valve closure time (LIVC) showed increased charge motion, doubling the tumble and providing higher swirl ratios. For engine speeds of 1000 to 2000rpm and brake loads of 1 to 2 bar BMEP, early intake valve closure (EIVC) with a deactivated valve, showed improvements in combustion stability and mixing. Contrarily, LIVC demonstrated an increase in particulate emissions, while compensation by further retardation in injection resulted in increased soot and hydrocarbon levels due to a lower burn temperature. This was mitigated by deactivating a valve. For an engine speed of 2000rpm, operating with a singular functional valve and implementing EIVC up to 6.25bar BMEP provided the largest benefits in

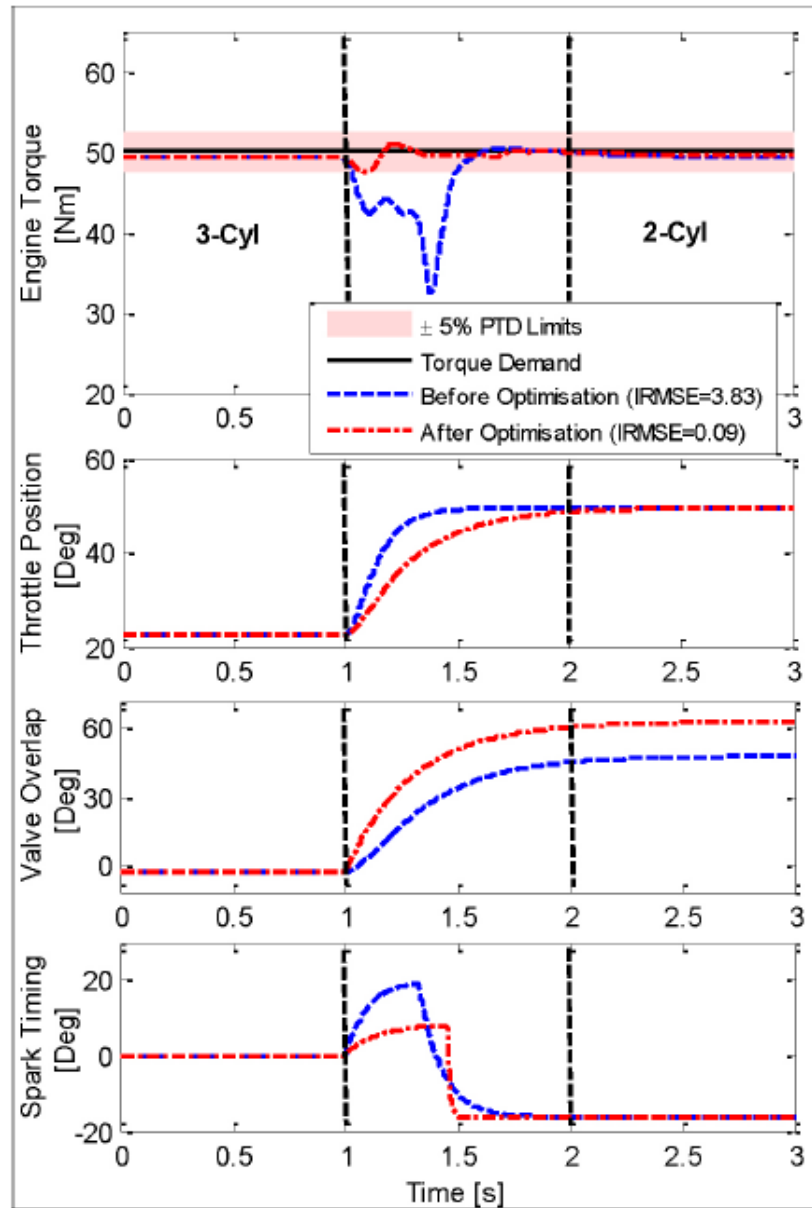


Figure 8: Example of a transitioning event for an un-optimised and optimised deactivation calibration showing the change in throttle position, valve overlap and spark timing for $T_b = 50\text{Nm}$, $N = 3000\text{rpm}$ [2.13].

fuel consumption, where switching to LIVC between 6.25 to 8bar BMEP showed relatively higher improvements compared to a baseline engine with two functioning valves. At high loads, between 10 and 12bar BMEP, using gasoline and low ethanol blends i.e. E0 to E10, resulted in knock leading to power loss. Coupling images from optical tools in the 2.0l engine with a commercial CFD tool, i.e. CONVERGE, improved combustion was observed to be affected by increased in-cylinder charge motion which in turn improved fuel vaporisation, while promoting mixing and increasing the bulk motion leading up to and during combustion.

2.3.5 Improving Catalyst Light Off Times

Cylinder deactivation has proved to a method of improving catalyst light off times. Other methods of improving catalyst light off times exist. As such, *Laing* [2.22], *Socha et al* [2.23] and *Burch et al* [2.24] have shown that catalyst light off times can be reduced by coupling electric heaters to catalysts. However the drawback of electrically coupling heaters to the engine requires that large electrical currents be drawn from the engine driven alternator leading to deterioration in fuel consumption and being more expensive to implement compared to cylinder deactivation.

Apart from cylinder deactivation several other in engine technologies have been investigated aimed at improving catalyst light off times. In light of this, it is interesting to compare other solutions to keep in mind the effectiveness of cylinder deactivation as a technology providing a means other than that of reducing fuel consumption. Simulation work carried out on GT-power by *Bharath et al* [2.25] on a four cylinder diesel engine was used to investigate which in-engine technologies provided the quickest catalyst light off time at low loads. Four factors were investigated specific to a 1bar BMEP and 1500rpm running condition where the required catalyst light of temperature was of 457K. First, varying *combustion phasing* for different gasoline/diesel fuel ratios showed little effect on catalyst light-off temperature. Secondly, adding a *fuel injection* event during the expansion stroke resulted in an undesired 1.34% increase in fuel economy. Based on the work of *Bohac et al* [2.24], *Parvate et al* [2.26] and *Roberts et al* [2.27] *early exhaust valve opening* (EEVO) strategies were also attempted although at the peril of deteriorating fuel consumption due to increased back pressure. *Bharath et al* [2.25] confirmed deterioration in fuel economy with EEVO strategies by observing an increase in specific fuel consumption, i.e. from 553 g/kWh to 1,053 g/kWh. The best strategy for faster catalyst light off times was found by *deactivating* three of the four cylinders predominantly due to significantly reduced fuel consumption, i.e. from 553 g/kWh to 351 g/kWh. Increased in-cylinder combustion efficiency and reduced pumping losses were attributed to be the leading cause in the reduction in fuel economy.

2.3.6 Cylinder Deactivation Effects on Emissions

By increasing in-cylinder loads with cylinder deactivation *Far et al* [2.29] and *Kuruppu et al* [2.30] have shown that for a constant engine brake torque tailpipe emission of CO, CO₂ and HC reduces with an increase in NO_x emissions. The exact proportion of the reduction in emissions varies throughout literature showing dependence on engine size, calibration and catalyst design. The cause of these changes in emissions is attributed to higher burn temperatures. This promotes oxidation of heavy elements through higher thermal efficiency.

2.3.7 Varying Valve Lift

Said et al [2.31] have shown that optimisation of intake and exhaust valve lift (i.e. for normal engine operation) is a proposed method of enhancing fuel economy benefits for the firing cylinders on an engine with cylinder deactivation. Calibrating the valve lift profile such that the optimum lift duration is had reduces pumping losses. *Said et al* have shown through simulation studies on GT-Power for a four cylinder engine operating at a condition of 2500rpm and 3 bar BMEP that the exhaust and intake valve lift could be reduced by 4mm and 2.5mm respectively.

Through a more detailed study *Flierl et al* [2.32] showed that deactivating from four to three cylinders significantly reduced the scavenging of residual gases. The effect of closing the exhaust valve over an 80° CA span showed that internal EGR for the four cylinder engine amounted to 2% at 220° linearly increasing up to 19% at 280°. Contrarily, when running on three cylinders exhaust valve opening overlaps were reduced. In effect, internal EGR was kept below 2% for the same crank angle interval increasing volumetric efficiency due to reduced exhaust valve overlap. Solely having full variable control over the intake valve when deactivating a cylinder provided a 7.5% (2 bar BMEP), 6% (3 bar BMEP), 4% (4 bar BMEP), 1% (6 bar BMEP) and 4% (10 bar BMEP) improvements in fuel consumption. On the other hand with fully variable exhaust valve lift fuel economy improved by 9.25% (2 bar BMEP), 11% (3 bar BMEP), 8% (4 bar BMEP), 4.5% (6 bar BMEP) and no effect was observed at 10bar BMEP. Having passed the simulation stage, a prototype engine was built starting from *key-on* on three cylinders, capable of running on two cylinders, and switching to four cylinders when the rated power was required. Little difference in ISFC improvement when running on either two or three cylinders for an operating point of 2 and 3 bar BMEP was shown. Running the prototype engine on the NEDC, demonstrated no need to run on four cylinders. Furthermore, larger exhaust mass pulsations on the three cylinder engine increased turbocharger angular velocities compared to running on four cylinders improving low-end torque delivery.

Another study published by *Flierl et al* [2.33] showed that the largest fuel consumption benefit to be had with cylinder deactivation arises from removing the throttle plate and optimum calibration of valve lift. Fuel economy benefits for a prototype 1.6l 4 cylinder direct injection gasoline turbocharged engine fitted with an inlet cam-phaser were made against an engine fitted with a double cam-phaser; double cam-phaser and along with deactivation of two cylinders; and finally a double cam-phaser, cylinder deactivation and fully variable exhaust valve lift system. Tests conducted at 2bar and 3bar BMEP load at 2000rpm showed that the additional removal of the throttle plate along with an optimally tuned double cam-phaser reduced fuel consumption by 8.6% and 7.1% respectively. Adding cylinder deactivation resulted in a combined fuel economy benefit of 16.4% and 12.8% respectively. Finally, with complete freedom over the exhaust valve lifts a total of 18.5% and 15% improvement were recorded respectively.

2.3.8 Oil Entrapment in Deactivated Cylinders

Simulation studies by *Ma* [2.10] show that cylinder deactivation promotes oil suction from the crankcase. For a firing cylinder, the top piston ring conforms to the cylinder bore during compression strokes compared to intake strokes due to the pressure difference in both strokes. For a deactivated cylinder, the pressure difference between intake and compression strokes is negligible in comparison to the firing case and consequently the top ring does not conform well to cylinder distortion. As shown in Figure 9, the amount of oil accumulated due to the top ring up-scraping movement is in effect much less however *Ma* has shown that this is depending on the duration of deactivation. Contrary to the firing cylinder, *Tian et al* [2.34] explain that the amount of oil blown-up into the combustion chamber through the top ring end gap increases. *Ma* explains that the reverse blow by time for the cylinder is longer but the force of the gas is shorter and weaker hence less oil is removed towards the crankcase. In effect, more oil is drawn onto the piston lands and therefore compared the firing case; where the trapped oil is either combusted with the fuel where either soot is formed or remains in its liquid form, the amount of oil burnt during combustion is significantly larger when the deactivated cylinder re-activates. The amount of oil accumulated is however dependent on the engine speed and the duration of deactivation and must be well monitored and rings must be well designed in order to reduce unwanted exhaust gases upon reactivation. If not accounted for the heavy land oil accumulation for the deactivated cylinder could reduce the maximum deactivation engine speed threshold limit.

Reduction in land oil accumulation was suggested through improved designs such as reducing piston ring grooves, clearances, gap sizes, cylinder bore distortion, designing of piston

landings to help promote downward oil flow and design of drain-hole structure characteristics of the oil flow onto the piston landing change.

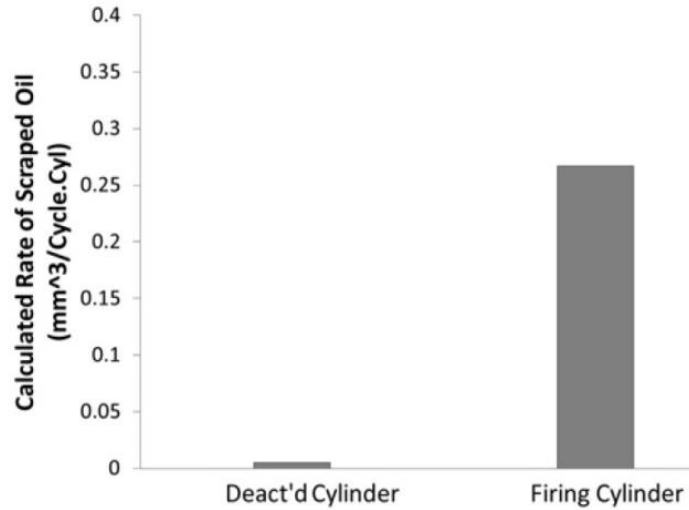


Figure 9: Theoretical rate of oil scrapped onto the top land for deactivated (LHS) and firing (RHS) cylinder scenarios. Although the oil scrapped for the deactivated cylinder case is considerably smaller, the accumulated value tends to be much larger compared to the firing case [2.10]. As example if a cylinder were to be deactivated for 60 cycles the calculated rate of scarped oil would cumulatively be approximately two times more compared to that of the firing cylinder.

2.3.9 Minimising NVH when Deactivating a Cylinder

NVH is a limiting factor for the application of cylinder deactivation on any vehicle build which requires extensive testing. *Senapati et al* [2.35] have shown through work on a *Bentley Muslanne V8 engine* that ‘felt’ vibrations are reduced by iteratively positioning, connecting and disconnecting mounts between the chassis and powertrain and engine and chassis. Torsional dampeners are also installed to reduce torsional vibrations induced from the driveline. For the luxury car market, the low hum produced by a V8 engine is a primordial aspect of enhancing driver feel. Unlike the work done by *Senapati et al*, *Binder et al* [2.7] have suggested that NVH felt by the driver can be significantly reduced by separating the torque paths in torque converters through a static spring set and a path directly connected to the planetary gear carrier. Commonly absorbers in torque converters are tuned to the engine running on all cylinders or highest operating point such that when deactivation takes place the torque converter outputs unwanted NVH characteristics. When disabling cylinders standard torsional dampers, turbine torsional

dampers¹ and twin torsional dampers² are not adaptive enough to dampen changing vibrating modes. However, while the vibrations travel through the spring set they are phased out by 180° such that when they meet a destructive interference is produced reducing the excitation. Work by *Orlamuender et al* [2.37] however states that the planetary carrier must be very rigid to prevent amplitude shifts. Effects of oil entrapment on super knock are referred to in Chapter 8 subsection 8.2.

2.3.10 Other Techniques for Cylinder Deactivation

For designs which arrest piston reciprocation, proposed designs have only reached the prototype and research development stage. One design, coined the *Scalzo Engine* [2.38], consists of an adjustable four bar mechanism comprising of an oscillating member positioned opposite the cylinder relative to the crankshaft connecting to the crankshaft via the main con-rod, disabling piston movement. Simulations performed for a V8 4.6l naturally aspirated and V8 4.0l diesel engine show that potential improvements of 30 and 20% are had at low constant operating conditions. Furthermore a 50% reduction in friction work is achieved. Lateral piston thrust forces are also reduced with the extended crankshaft design thus reducing friction on a crank-angle basis. Additional mass and cost due to added components are claimed to be around 5-8% of the overall engine cost. Although such large benefits are to be had the complexity of the system reduces the attractiveness of implementing the *Scalzo* design.

Doller et al [2.9] disabled reciprocation of two pistons through a split crank assembly [2.9]. Relative to a conventional engine, the split crank system showed friction deterioration (i.e. increase) at all engine speeds with all four cylinders reciprocating. The increase in friction at an oil temperature of 90°C was of 1Nm at 1000rpm up to 9Nm at 5000rpm. For the same oil temperature and when having two inert pistons, friction improved by 2Nm at 1000rpm and 4Nm at 5000rpm. Given the increase in friction due to the assembly of the split crankshaft and the reduction due to having inert pistons compared to a baseline modular crankshaft, it is difficult to estimate the frictional benefits from novel split crank systems. As discussed by *Scalzo et al* the largest contribution to improving fuel economy results from reduced heat loss to the cylinder walls and improved combustion efficiency.

2.3.11 Dynamic Skip Fire

Compared to conventional cylinder deactivation, *Tula Technologies* [2.40] claims increased fuel economy benefits can be achieved through dynamic skip-fire. This changes the cylinder or

¹ Where the torque converter turbine is directly linked to the damper near the drive shaft or stator.

² The torque converter turbine is linked to two separate torque dampers.

cylinders which are deactivated in a repeating pattern. Simulations showing the effectiveness of this technology were run on a 1-D SIMULINK based air flow models using GT-POWER for skip firing events on a GM 6.2l V8. Firing densities, or air charges, were altered between 33% and 50%, on an engine cyclic basis with three and four cylinders firing, respectively. A numeric illustration of cylinder skip firing for a firing order of 1-8-7-2-6-5-4-3 repeating every three cycles on a 33% charge density would be: 1-s-s-2-s-s-4-s (cycle 1), s-8-s-s-6-s-s-3 (cycle 2) and s-s-7-s-s-5-s-s (cycle 3) where s indicates a skip. With this technology, the net indicated specific fuel consumption improved by ~140 g/kWhr at 1bar IMEPn, ~60 g/kWhr at 2bar IMEPn and ~10 g/kWhr at 4bar IMEPn equalising with normal engine operation ISFCn for an engine speed of 1500rpm. As illustrated on Figure 10, a higher fuel consumption improvement is had through skip-fire compared to conventional deactivation by trapping vacuum (note: negative indicates a reduction in fuel consumption and positive a penalty).

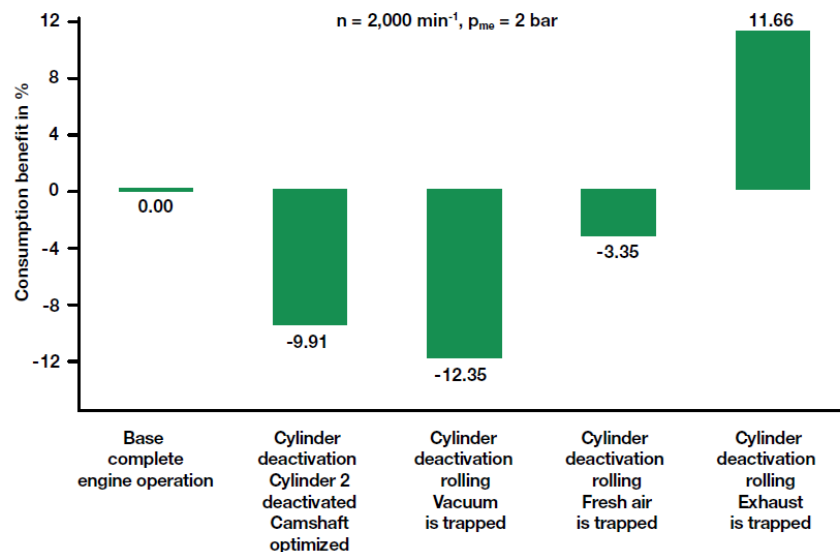


Figure 10: Effect of varying deactivation methods for a three cylinder gasoline engine where $P_{man} = 2\text{bar}$ and $N = 2000\text{rpm}$ [2.12].

2.3.12 Future Advances: Koenigsegg Air Compressed and Free Valve Technology

In 2011, *Koenigsegg's* sister company *FreeValve AB*TM [2.41] patented seven designs describing an assembly pneumatically controlling valves for ICEs. Developed by *Urban Carlson* the system shown in Figure 11 renders the conventional camshaft, valve assembly and throttle body obsolete allowing free and independent control of the valves. In order to constantly supply pressurised air to the valve actuators the engine comprises of one compressor cylinder which delivers compressed air to a storage tank. The cylinder is powered through the same crankshaft

which connects to the working cylinders. Compressed air is directed into the chamber situated above the valve pushing against a piston kept in place by a spring similar to conventional spring systems for mechanically actuated valves. The air compressor, like all other cylinders, may be deactivated by shutting off intake valves such that compressed air is delivered to the air tank upon demand remaining filled at all times. Compressed air is relieved from the air compressor through an escape valve providing the optimised amount of pressurised air. A similar design has also been described by *Venkatesh et al* [2.42] although only reaching proto-type stage on a fixed rig.

It is claimed that a fuel economy improvement of 4 to 5% may be had solely by removing the throttle plate. The removal of the camshaft assembly is claimed to provide a 20kg reduction for a 4 cylinder 1.6litre diesel engine while increasing the rated power by 50% from 160bhp to 240bhp. Furthermore, exhaust ports were also designed such that designated ports lead directly to the catalyst, bypassing the turbocharger, allowing for even faster pre-catalyst and catalyst warm-up times compared to conventional ports. In effect, the need for a waste-gate is rendered obsolete due to complete control over the exhaust valve opening times and lift, allowing for optimised opening profiles given a demanded back pressure. At the time of writing this thesis, Freevalve AB has signed a partnership with the Chinese car company Qoros [2.43] applying a pneumatic valve system to a 4 cylinder 1.6l engine due to be sold in 2018. The performance benefits from applying this technology are still to be reported.

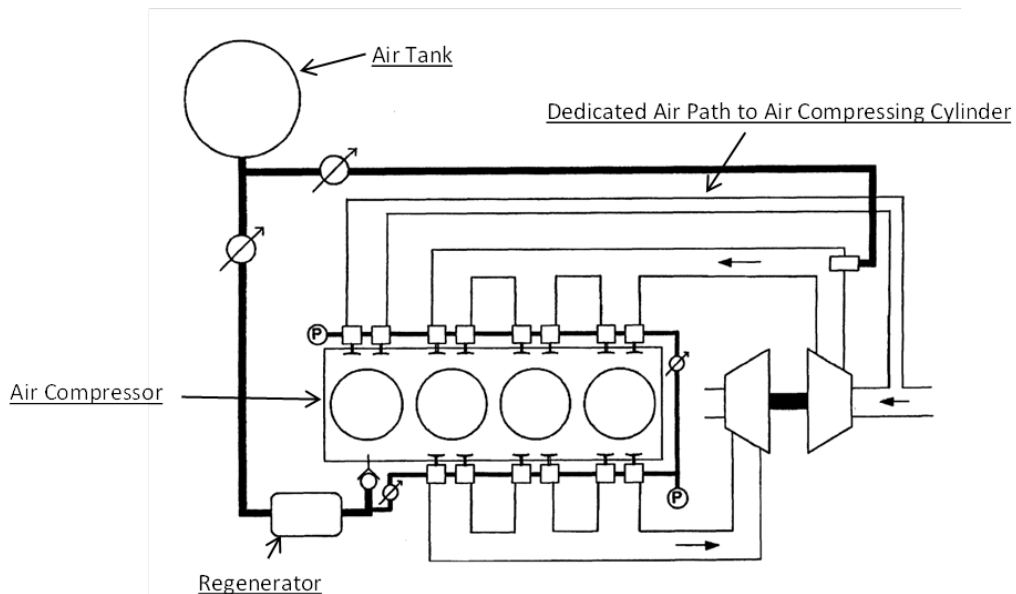


Figure 11: One of the seven Freevalve AB patented air path schematics for an un-throttled turbocharged engine fitted with a cam-less pneumatic and electronic valve actuating mechanism [2.41].

2.4 Cylinder Bore Distortion and Piston Ring Behaviour

Cylinder bore distortion occurs in all internal combustion engines and is difficult to mitigate. Understanding the phenomenon and causes of bore distortion for conventional engine operation is important in regard to this study due to the thermal effects of cylinder deactivation giving rise to increased temperature between cylinders and across the height of the cylinder wall.

Distortions arise from four sources: 1) errors and tolerances in the manufacturing of engines; 2) loading resulting from engine assembly; 3) thermal loading during engine operation; and 4) impulses due to in-cylinder pressures [2.44]. The three dimensional strain resulting from mechanical and thermal loads is expressed through the stress-strain relationship described by Hooke's Law. The strain in the x-plane is described through the following expression:

$$\varepsilon_x = \frac{\sigma_x - \nu(\sigma_y + \sigma_z)}{E} + \alpha(T_2 - T_1)$$

According to *Heywood* [2.5] a three dimensional representation of engine geometry requires a detailed heat flow solution to acquire temperature distributions across the engine while requiring compatibility for each element. Finite element analysis (FEA) tools such as ANSYS or Abaqus are generally used to describe these complex phenomena however these remain outside the scope of this study. In light of this, the effects of cylinder bore distortion on engine performance are explained due to accentuated adverse thermal effects from cylinder deactivation. Furthermore, nominal temperature differences at the inter-bores during normal engine operation are reviewed in *subsection 3.4.2* as a basis for comparison for predicted results for cylinder deactivation shown in *Chapter 5 subsection 5.4*.

As a result of bore distortion the *cylindricity* and *roundness* of the cylinder vary. In turn this affects the straightness, parallelism and true inner diameter of the cylinder. A Fourier series approach is used throughout literature to analytically describe these orders, described below. Zero and first order distortions are generally associated with machine tolerances. Higher order distortions arise due to factors such as: uneven distribution of compressive load applied to head bolts; variations in the coolant heat transfer coefficient along the length of the liner giving rise to differences in thermal expansion; and thin cylinder walls [2.45].

As a result of distortion engine performance is affected in an adverse manner. At the level of the piston ring, a non-circular bore reduces the conformity between the piston ring and liner. With poor *ring conformity* an imperfect seal results, allowing for much higher traversal of gas and liquid from the combustion chamber to the crankcase (and vice-versa) compared to normal engine

operation. This leads to increased oil leakage and thus oil consumption along with excessive engine blow-by [2.46]. As a result of blow-by engine fuel-conversion efficiency reduces due to the loss of in-cylinder pressure during intake and power strokes [2.47].

2.4.1 Piston Ring Conformity, Collapse and Flutter

The basis for the analysis of piston ring conformability was set by *Prescot* [2.48], *Timoshenko* [2.49] and *Englisch* [2.50] through a first principles derivation on elasticity of rings. Piston ring conformability and distortion for automotive application was pioneered by *Gintsburg* [2.51] with reference to a distorted cylinder bore profile [2.52]. *Gintsburg* describes bore and ring distortion through a Fourier series. The Fourier series represents the phenomenon known as radial ring collapse. This occurs when the piston ring is pushed inwards contracting the piston ring. A discontinuity is created between the ring and liner contact interface allowing for gas flow in this gap such that blow-by and oil transport are affected. Along with this, piston rings may lose their stability and flutter inside the piston ring groove. When fluttering gas leaks through the groove at a much higher flow-rate than from the ring gap. Gas flow routes are profoundly affected by this leading to changes in blow-by characteristics, oil transport and consumption [2.53]. The occurrence of these two phenomenon are dependent on the piston ring and groove design whilst the dynamic movement of the ring during an engine cycle is mainly driven by changes in pressure difference between the combustion chamber and crankcase. A complete physical analysis of piston ring behaviour is described in work conducted by *Tian* [2.53].

2.4.2 Methods for Minimising Temperature Differences and Cylinder Bore Distortion

Bore distortion and ring conformability, for third or higher order distortions, are in part due to temperature differences across the cylinder wall and along the height of bore. *Rajput* [2.54] observes that mean temperature differences across the bore wall for SI engines are generally near 100 degrees Celsius. *Rajput* has shown that water cooled cylinder walls compared to air cooled walls (i.e. designed with cooling fins) reduce the mean temperature difference across the wall by the 10 to 20 degrees Celsius. Contrarily, temperature differences along the height of the cylinder wall are generally in the range of 30 to 70 degrees Celsius. Temperature differences across the height of the bore increase as in-cylinder load increases. With nominal temperature differences bore distortions are generally in the range of dozens of micro-meters [2.44]. Although distortion affects engine performance the effect is crank-angle specific requiring large computational tools outside the scope of the study of the 0D simulation tool used in this study.

Although the elastic limit of the materials used in producing cylinder bores defines the maximum permissible strain, or component failure, several methods are suggested in minimising the occurrence of cylinder bore distortion. High order distortions are reduced through optimisation of the block design through improved coolant flow characteristics. As example, by biasing coolant flow on the top part of the bore the heat transfer coefficient is increased at the top of the liner where bore temperatures are highest and distortions most prominent. *Loenne et al* [2.55] showed that this is easily achieved using an open deck design along with positioning the block coolant aperture closer to top of the liner. Furthermore, *Rahnejat* [2.56] accentuates that bore distortion worsens for engines designed without inter-bore cooling slits along with the use of light alloy materials. As described in subsection 2.2.3, *Nishino et al* [2.7] show that inter-bore slits reduce large temperatures experienced at the top of the cylinder wall. In effect these combined designs reduce temperature differences between the top and bottom of the liner/wall to a more uniform temperature, nearing the coolant temperature. For lower order distortions, increased section moduli and reduced bolt loads not only help reduce distortion but engine friction in general. A more radical approach described by *Flores* [2.57] consists of honing bore distortion such that operation by manufacturing a default non-cylindrical bore shape. This requires knowledge of the distortions present during operation through extensive computational effort.

2.5 Concluding Remarks

Engine thermal management for light duty passenger vehicles is primarily aimed at promoting rapid coolant and oil warm-up rates for optimum engine operation. Minimising time spent in ‘cold’ engine operation primarily reduces engine friction through heating of the contained liquids. Oxidation of the injected fuel and engine thermal efficiency is also improved by reducing heat losses to the engine structure. Careful optimisation of the coolant flow-rates and coolant passage geometries is also required to ensure that the engine does not overheat. This could lead to auto-ignition of fuel and catastrophic engine failure. Segregation of the coolant volumes, in the form of a split cooling circuit, reduces coolant thermal inertias improving engine warm-up rates. Compared to conventional cooling circuits where coolant flowing in the block flows through the rest of the engine split circuit flow-rates are favourable. Furthermore, [2.1] has shown that a 1-D lumped thermal capacity model is a particularly useful in quantifying interactions between metal, coolant and oil in a time effective approach.

Generally cylinder deactivation for an engine fitted with a camshaft can be achieved using three different techniques. A review of these three methods has suggested that the form of

cylinder deactivation resulting in the best fuel economy involves fuel cut-off and intake/exhaust valve closure. All three methods provide increased exhaust gas temperatures promoting faster catalyst light off times. However, closing intake and exhaust valves provides a considerable pumping loss reduction compared to solely cutting fuel off. Disabling piston motion on the other hand requires complex engine modifications with negative effect of added weight (i.e. thermal inertia). Net fuel consumption benefits due to friction reduction are thus difficult to quantify [2.39]. Although more innovate solutions of deactivating cylinders are proposed [2.40] [2.41] these require more detailed approaches and accurate characterisation of engine behaviour for modelling purposes. The simple form of cylinder deactivation achieved through cutting off fuel injection and shutting off valves, paves the approach for predicting fuel consumption benefits associated with deactivation. However, the penalty associated with repeatedly compressing and expanding a trapped charge is an area which requires further explanation.

Chapter 3 PROMETS Theory

3.1 Introduction

In this chapter the theories in PROMETS for the modelling of heat transfer and friction in an ICE are described. An overview of heat transfer between gas-side, friction, coolant and oil is touched upon to provide the reader with knowledge of the state of the model prior to work presented in Chapter 4, 5 and 6. This is approached by describing historical work carried out leading to the onset of PROMETS on a SIMULINK user interface. This is then followed by a description of the stability criteria used for lumped capacity analysis, the layout of the elements representing the engine and required model inputs for simulation. Governing equations comprising of the major subsections of the model are also described with modes of heat transfer to the coolant and oil heat sinks. This chapter is concluded with a discussion stating where model advances and modifications are required to represent the TCE for operation on all cylinders.

3.2 PROMETS: Basics and Model Elements

PROMETS provides cycle averaged results on friction and engine heat transfer in a lumped capacity element model. Contact areas, volumes and masses of elements necessary to account for heat transfer throughout the structure of an ICE are defined through a pre-processor named PROGEN (**PRO**gram for **GEN**eric **ENG**ine **REP**resentation). These parameters are determined by inputting selected engine dimensions which are preferably extracted from an existing engine CAD model. Element sizes are diverse and dependent on the magnitude of heat flux passing through a specific area of the engine. Areas exposed to high thermal flux have a higher spatial resolution whereas those with lower flux are represented with larger elements. The accuracy of predictions made by PROGEN may be refined with scaling factors. These help improve volumes and masses of engine components when compared with experimental mass measurements. Apart from the density of different components, input of properties such as thermal conductivity and specific heat capacities are also required to appropriately characterise the thermal behaviour of elements. Once dimensions, material properties and masses are defined, a single cylinder is constructed with a total of 41 elements. The position and size of the elements is illustrated in Figure 12.

Following 2-D thermal analysis studies carried out by *Mason* [3]. The earliest version of PROMETS was developed by *Christian* [3.1]. *Christian* [3.1] investigated an FE approach to computing engine thermal behaviour. To reduce the time spent computing engine thermal behaviour, metal temperatures along the liner, cylinder wall and intake/exhaust ports of a one-

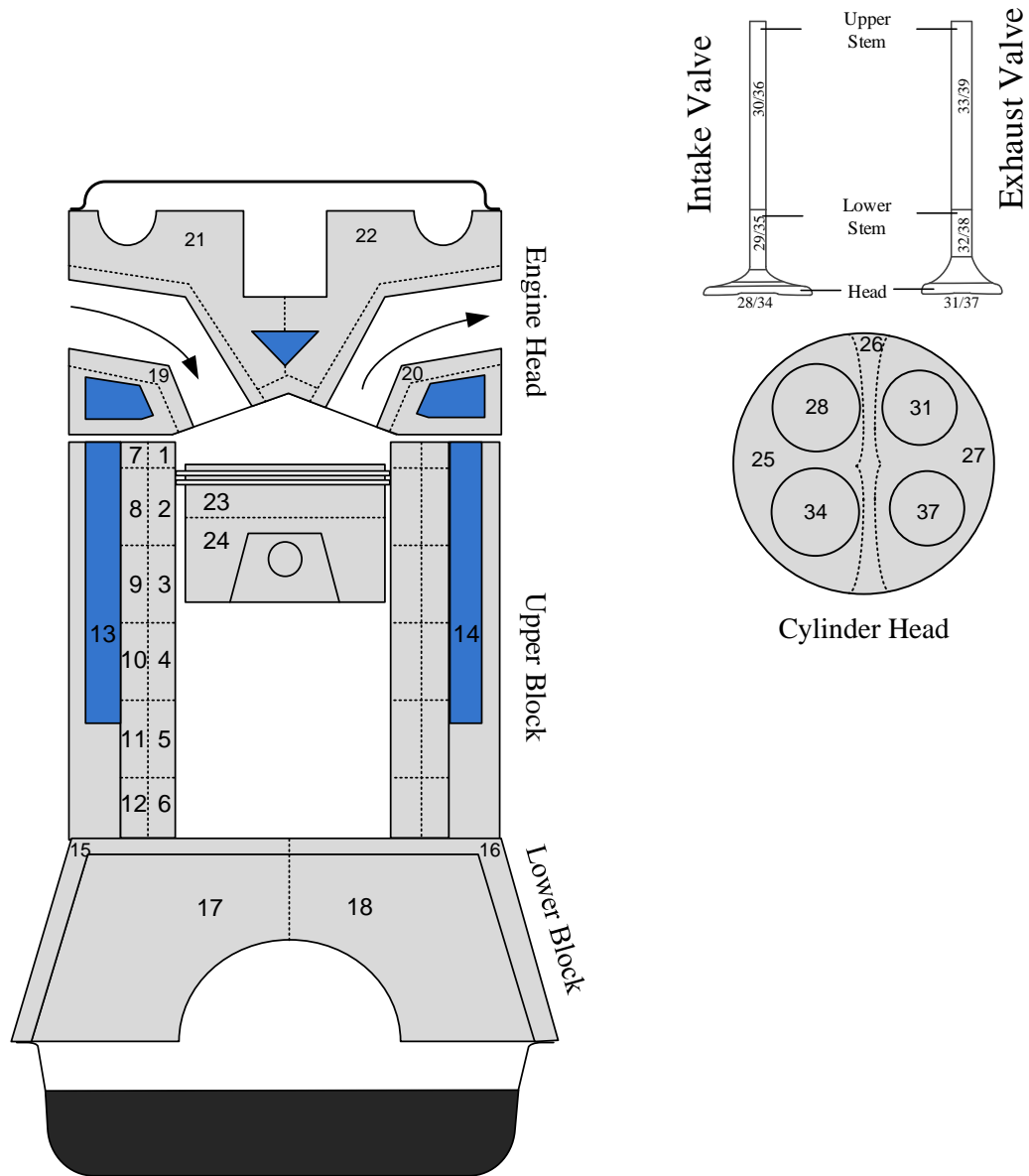
quarter FE cylinder model (with a resolution of several thousand nodes) were compared with the centre metal temperatures of a lumped element model. *Christian* showed good agreement between the two models and thus shaped the sizes of elements in PROMETS such that this agreement remained robust over several operating conditions. The model was subsequently extended upon through several studies numerically representing cycle-averaged phenomenon through empirical and physics based correlations. Engine heat transfer from the gas-side to coolant is described in work done by *Shayler and Yuen* [3.2], *Chick* [3.3] and *Baylis* [3.4]. These account for effects of retarding or advancing spark timing, altering AFR, varying coolant composition and turbocharging specific to a diesel engine. Heat transfer emanating from rubbing friction, for a fully warm engine state, has been based on work done at MIT by *Patton, Nitschke* and *Heywood* [3.5]. Friction viscosity dependence for components undergoing mixed and hydrodynamic lubrication under warm-up conditions is based on work conducted by *Shayler and Leong* [3.6].

Based on the high-level interactions described above and elaborated further in this chapter, two variants of PROMETS exist for either diesel or gasoline engines. The first describes heat transfer in a single cylinder and the second describes heat transfer for all cylinders in the engine. These exist for either inline or V-type engine types. The single cylinder and multi-cylinder models are differentiated by their boundary conditions. For the multi-cylinder model consisting of four cylinders the inboard cylinders are described to be adiabatically connected on both sides. Outboard cylinders have outer surfaces that are connected to ambient. On the coolant side equations describing conservation of mass are used to appropriate coolant flow-rate throughout the engine while traversing the block and head.

The construct of the multi-cylinder model on MATLAB Simulink elaborated upon in the following subsections has been developed by *Morgan* [3.7] and is the basis for revisions described in Chapter 4.

3.2.1 Model Inputs

The lumped mass engine representation is defined by input of key engine geometries. Given the geometries, to run the model on MATLAB Simulink the user must define eleven variables such that the model may commence calculations. The eleven variables consist of time, engine speed, engine brake torque, AFR, fuel flow-rate, coolant flow-rate, heater matrix coolant flow-rate, heater matrix air flow-rate, exhaust gas temperature, spark advance or retard relative to MBTD and % EGR. Of the eleven inputs only the first three have been used in this modelling instance, i.e. engine speed, engine brake torque and AFR, while the rest have been computed



Element 40 - represents thermal inertia of miscellaneous components which are in intimate contact with the coolant flow prior to thermostat opening. These are components not account for by any of the main core elements above. These include the thermostat and thermostat housing, coolant pump, degas bottle, hoses and fittings.

Element 41 - represents the thermal inertia of miscellaneous components which are in intimate contact with the oil flow. These are components which are not accounted for by any of the main core elements stated above. The components included are the oil pump, filter, oil pan and other such components. **Note:** The thermal inertia of miscellaneous components are calculated using actual volume measurements.

Figure 12: Element numbers representing the engine head, upper and lower block for a cylinder.

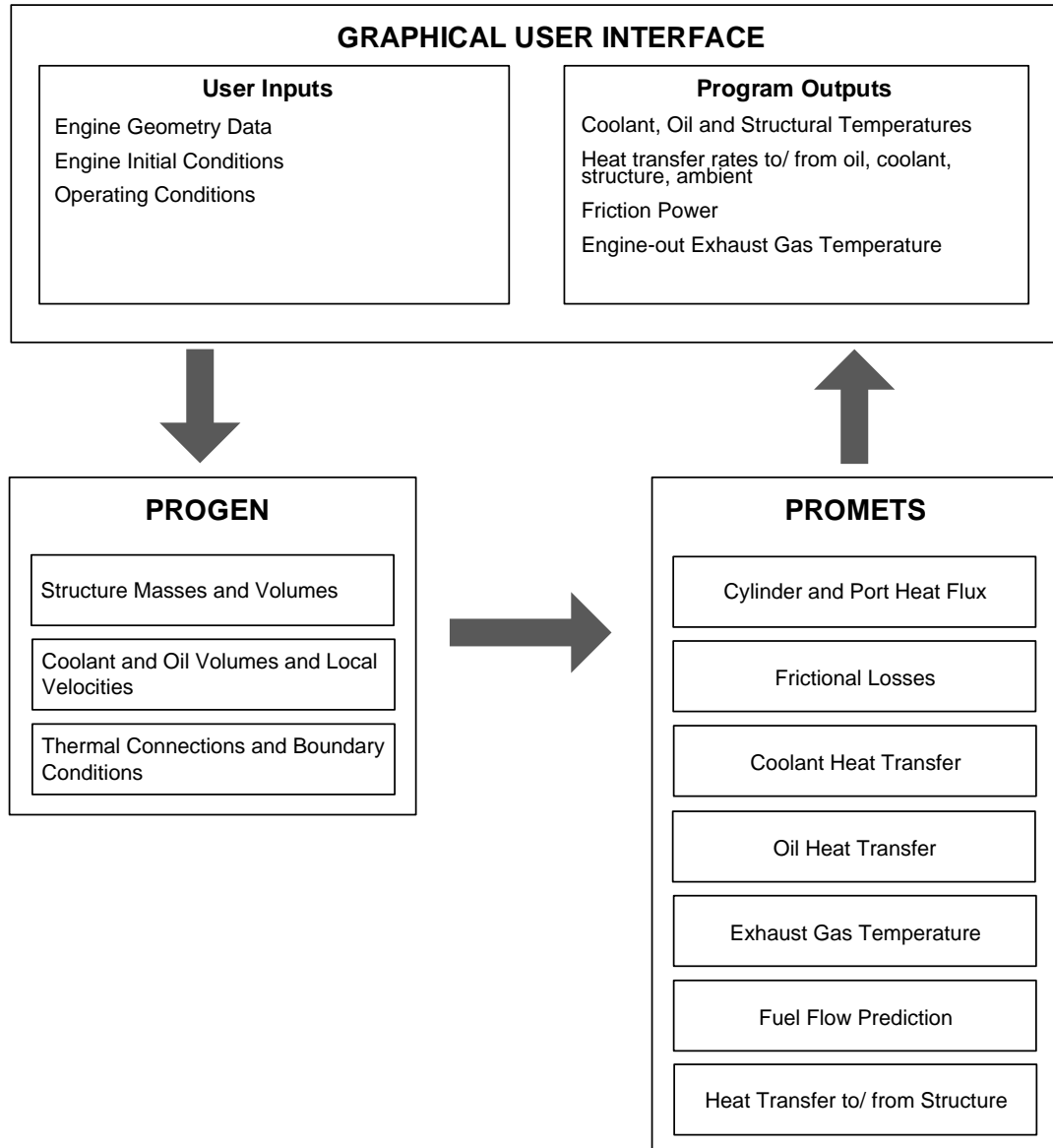


Figure 13: Schematic representation of calculation routine for PROGEN and PROMETS [3.8].

through PROMETS. These three inputs are sufficient to describe a drive cycle. Cylinder deactivation has been defined through a trigger mechanism inputted through a ‘.m’ script on MATLAB. Further to this, the initial thermal state of the engine is also defined by the user. This is done by assigning values to the oil, coolant and metal temperatures. The interaction between user inputs, PROGEN, PROMETS and model outputs is shown in Figure 13.

3.2.2 Lumped Capacity Analysis

Each lumped mass element is represented having a uniform temperature. An energy balance for an element ‘i’ in contact with element ‘j’ is described using the following expression [3.1].

$$\dot{Q}_i + \sum_j \frac{T_j^t - T_i^t}{R_{ij}} = C_i \left(\frac{T_i^{t+1} - T_i^t}{\Delta t} \right) \quad \text{Equation 1}$$

Where \dot{Q}_i is the change in the elements internal energy; R_{ij} the thermal resistance between elements; and Δt is the time-step between successive explicit forward time-marching calculations. C_i represents the extensive form of the specific heat capacity of the element, which is expressed by:

$$C_i = \rho_i c_i \Delta V_i \quad \text{Equation 2}$$

where ρ_i is the element density, c_i the specific heat capacity of the element and ΔV_i is the element volume. Re-arranging the heat balance solution to equate to the temperature of the next time-step, $t + 1$, the following is used to calculate element temperatures,

$$T_i^{t+1} = \frac{\Delta t}{C_i} \left[\dot{Q}_i + \sum_j \frac{T_j^t - T_i^t}{R_{ij}} \right] + T_i^t \quad \text{Equation 3}$$

3.2.3 Accuracy and Stability

To represent a uniform element temperature two criteria are met; this is specific to elements which are solid in nature. These criteria are: 1) the temperature difference between the two elements must be kept to a minimum and 2) elements should contribute equally to the thermal resistance of the interface. In order to keep the temperature difference between elements to a minimum, the size of the element and therefore number of elements is optimised for this purpose. FE simulations run by *Christian* [3.1] found the basis for the element numbers and sizes shown below. Element resolution is increased along areas where heat fluxes are high and thus where significant thermal gradients arise. As example, the cylinder liner and exhaust valves have an increased number of elements. With this, the thermal resistance between two elements, elements 1 and 2 is expressed according to the following,

$$R_{1,2} = \frac{1}{A_{12}} \left(\frac{\Delta X_{1,2}}{k_1} + \frac{\Delta X_{2,1}}{k_2} \right) \quad \text{Equation 4}$$

Where k is the thermal conductivity of the element; A the perpendicular surface area connecting both elements; and ΔX the midway distance from the surface area. An illustration is shown in the figure below.

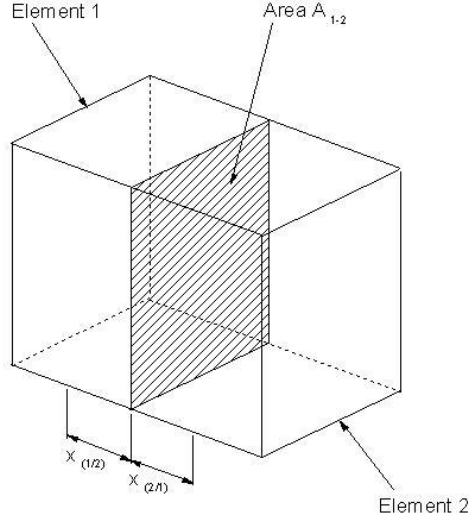


Figure 14: Illustration of the geometries used to define the conductive resistance between elements.

Lumped thermal capacity elements with a solid-liquid interface adhere to a small enough Biot number such that a uniform wall temperature is maintained during thermal transients. The Biot number is expressed as the ratio of convective and conductive heat transfer coefficients.

$$Bi = \frac{hV}{kA} \quad \text{Equation 5}$$

With a Biot number, $Bi \leq 0.1$, the error in the lumped capacity assumption is less than 5% [3.1].

Stability in the numerical estimation of the temperature is ascertained by the size of the time step allocated to calculate heat transfer in the model. This done by considering a case when the internal energy of the element is set to zero such that the following inequality is satisfied,

$$\left[1 - \frac{\Delta t}{c_i} \sum_j \frac{1}{R_{ij}} \right] \geq 0 \quad \text{Equation 6}$$

The criterion ensures that heat transfer obeys Fourier's Law of conduction. As example if R_{ij} is taken as $R_{1,2}$ where element 1 is at a higher temperature than element 2, the inequality will be

satisfied. The time step used in PROMETS is taken as 0.1 seconds although the largest time step value of 0.3 seconds has been used by *Morgan* [3.7].

3.3 Friction Model

3.3.1 Original Friction Model Description

Historically, an engine viscosity correcting factor has been applied to a fully warm friction value to represent increased friction when warming up from low oil temperatures. Although the reference oil temperature is set to 90°C variations in local oil temperature may exist across the engine [3.1]. The effect the variations in oil temperature have on viscosity when the engine is fully warm are however small compared to cold starting conditions of 20°C.

$$FMEP_{wu} = \left(\frac{\mu_{oil}}{\mu_{ref,T=90^{\circ}C}} \right)^n FMEP_{fw} \quad \text{Equation 7}$$

Where fully warm friction, $FMEP_{fw}$, is described through a force based analysis originating from the work of *Patton et al* [3.5]. The expressions for the sub-assemblies in an ICE are shown below. The index $n = 0.19$ is based on findings by *Bayliss* [3.4] for a gasoline engine. The calculation of dynamic viscosity shown in Equation 8 is based on Vogel's formulation shown below.

$$\mu_{oil} = k_v e^{\left(\frac{\theta_1}{T+\theta_2} \right)} \quad \text{Equation 8}$$

Prior to the onset of this work the oil viscosity grade described in PROMETS has been defaulted to a 5W-40 formulation [3.7].

Improvements in the friction model originally conceived by *Patton et al* [3.5] were conducted by *Shayler et al* [3.9]. The improvements consisted of scaling hydrodynamic and mixed lubrication friction terms with a viscosity correction. The correction is in the form of a ratio of the oil viscosity at the current oil temperature by a reference viscosity for an oil temperature of 90°C. Although the work has been focused on studies for diesel engines, components categorised undergoing boundary, mixed and hydrodynamic lubrication remain the same in gasoline engines. Further work by *Addison* [3.10] has focused on determining indices for specific components undergoing hydrodynamic lubrication. In light of this, the index for gasoline engines described by *Bayliss* [3.4], $n = 0.19$, has also proved to result in robustly capturing friction changes throughout warm-up conditions. A description of the friction terms used in this analysis is shown below with equations specific to the crankshaft, valvetrain, and piston assemblies and ancillary devices.

Crankshaft Assembly

Friction at the crankshaft is described by three terms one of which is dependent on the viscosity of oil. The first term describes friction of the main bearing seals assumed to operate under boundary lubrication. The seal lip load is assumed constant. Main bearing hydrodynamic friction is described in the second term and is dependent on oil viscosity. The third term describes windage losses due to the need to pump oil through flow restrictions; it is coupled with losses at the crankshaft for the purpose of grouping terms resulting from specific assemblies in the engine.

$$FMEP_{crankshaft} = C_{cs} \left(\frac{D_b}{B^2 S n_c} \right) + C_{oh} \left(\frac{N D_b^3 L_b n_b}{B^2 S n_c} \right) \sqrt{\frac{\mu}{\mu_o}} + C_{td} \left(\frac{D_b^2 N^2 n_b}{n_c} \right) \quad \text{Equation 9}$$

Valvetrain Assembly

The largest proportion of friction heat generated in the valvetrain assembly is present between the tappet and bore. The first term is an empirical constant adjusted to account for friction at the camshaft bearing seals. The terms with the coefficients C_{ff} and C_{rf} predict friction between the cam-lobe and cam follower for a flat-follower and roller-follower element respectively. Oscillating hydrodynamic friction between valvetrain components such as the valve lifter in the lifter bore or valve guide are represented by the fifth term. Lastly oscillating mixed lubrication friction present in the valve guide or bore is accounted for in the sixth term.

$$FMEP_{valvetrain} = 4.53 + C_{vb} \sqrt{\frac{\mu}{\mu_o}} \left(\frac{N n_b}{B^2 S n_c} \right) + (C_{ff}) \left(1 + \frac{500}{N} \right) \left(\frac{n_v}{S n_c} \right) + C_{rf} \left(\frac{N n_v}{S n_c} \right) + C_{oh} \left(\frac{N^{0.5} n_v L_v^{1.5}}{S n_c B^2} \right) \sqrt{\frac{\mu}{\mu_o}} + C_{om} \left(1 + \frac{500}{N} \right) \frac{n_v L_v}{S n_c} \quad \text{Equation 10}$$

Piston Assembly

Friction for the piston assembly is dominated by boundary lubrication occurring at the piston rings. The first term describes piston friction due to the hydrodynamic sliding motion of the piston skirt against the cylinder wall simply based on a stroke averaged reciprocation velocity with a strong dependence on piston bore size. The second term accounts for rubbing friction emanating from the contact of the piston rings against the cylinder liner occurring under the mixed lubrication regime. If the ratio of the piston ring tension and roughness of the rings is known values may be substituted; in this modelling instance this factor was equated to unity. The third term is representative of hydrodynamic friction present at the connecting rod bearings.

$$FMEP_{piston} = C_{ps} \left(\frac{S_p}{B} \right) \sqrt{\frac{\mu}{\mu_o}} + C_{pr} \left(\frac{F_t}{F_{to}} C_r \right) \left(1 + \frac{500}{N} \right) \left(\frac{1}{B^2} \right) + C_{be} \left(\frac{ND_b^3 L_b n_b}{B^2 S n_c} \right) \sqrt{\frac{\mu}{\mu_o}}$$

Equation 11

Ancillaries

Ancillary loads are dependent on engine size and are specific to targeted performance. An engine with a rated speed of 10,000rpm will require high performance oil pumps such that components remain well lubricated under high frictional loads. Engines designed for light duty passenger vehicles, such as the TCE, generally have a smaller proportion of fuel energy spent powering ancillary devices. As in the original PNH model a second-order polynomial function based on engine speed describes friction losses due to the water, oil and fuel pumps.

$$FMEP_{anc} = \alpha + (\beta N - \gamma N^2) \left(\frac{\mu}{\mu_o} \right)^n$$

Equation 12

The default coefficients for the friction terms in each sub-assembly discussed above are shown in the following chapter for comparative purposes with those of the TCE. These are shown in Table 4.

3.4 Original Gas-side Heat Transfer Correlations

Combustion results in high temperature gases directing heat from the gas-side to lower temperature coolant. In the four stroke engine cycle this is dominant during the power and exhaust strokes. Contrarily, during intake and compression strokes heat is directed from the metal to the intake charge until ignition occurs. This is however magnitudes smaller compared to when combustion occurs. The onset of heat transfer is specific to engine calibration and thus crank-angle. A simplified time-averaged approach describing heat transfer from the gas-side to coolant is used in PROMETS. The formulation is based on the work of Taylor and Toong [3.11] derived on data emanating from 19 engines. An empirical formulation, \dot{Q}_T , represents cycle-averaged heat transfer from the gas-side to coolant, specific to a cylinder.

$$\dot{Q}_T = 10.4 \left(\frac{\pi B^2}{4} \right) \frac{k_g}{B} (T_{g,a} - T_c) Re_g^{0.75}$$

Equation 13

The expression solely requires the cylinder bore to characterise an engine. The magnitude of heat transfer in the combustion chamber and exhaust ports is strongly dependent on changes in the Reynolds number, Re_g .

$$Re_g = \frac{4 \dot{m}_f \left(1 + \frac{AFR}{(1-EGR)} \right)}{\pi \mu_g B}$$

Equation 14

In-cylinder gas temperature changes are weakly dependent on the mass of fuel injected. Instead the cycle averaged in-cylinder gas temperature has a strong dependency on the air-to-fuel ratio relative to stoichiometric, i.e. equivalence ratio (ϕ). Taylor [3.11] thus formulated a simple expression correlating mass averaged gas temperature with the equivalence ratio in the following form:

$$T_{g,a} = \frac{1}{(a-b\phi+c\phi^2-d\phi^3)} + T_{amb} \quad \text{Equation 15}$$

To account for turbocharging the following correction is applied [3.16]:

$$T_{g,a} = \dot{T}_{g,a} + 0.35 (T_{amb} - 300) \quad \text{Equation 16}$$

In-cylinder dynamic viscosity, μ_g , and conductivity, k_g , are also dependent on equivalence ratio:

$$\mu_g = 3.579 \cdot 10^{-8} \cdot (T_g) + 8.573 \cdot 10^{-6} \quad \text{Equation 17}$$

$$k_g = 6.368 \cdot 10^{-5} \cdot (T_g) + 8.227 \cdot 10^{-3} \quad \text{Equation 18}$$

Although predictions based on the work of Taylor and Toong are accurate in describing heat losses to coolant, *Shayler et al* [3.12] identified weaknesses in solely having one term describe the heat released to coolant. Compared to the original expression shown in Equation 13 the revised formulation is shown below.

$$\dot{Q}_{c1c2} + \dot{Q}_{ex,man} + \dot{Q}_f = \dot{Q}_c + \dot{Q}_{amb} + \dot{Q}_{oc} \quad \text{Equation 19}$$

Where \dot{Q}_{c1c2} is the heat transfer from the combustion chamber and exhaust ports to coolant, $\dot{Q}_{ex,man}$ is the heat transfer from the external exhaust manifold to ambient, \dot{Q}_{amb} are ambient heat losses and \dot{Q}_{oc} heat losses from the oil to the OFCA. The original gas-side expression, \dot{Q}_T , was improved to incorporate the effective surface area of the cylinder and the exhaust port surface area while retaining the dimension of the cylinder bore. The revision takes the form:

$$\dot{Q}_{c1c2} = C_1(A_{cyl,eff} + C_2A_{pt}) \frac{k_g}{B} (T_{g,a} - T_c) Re_g^{0.7} \quad \text{Equation 20}$$

Where heat transfer in the combustion chamber and exhaust ports is expressed as follows:

$$\dot{Q}_{cyl} = C_1 A_{cyl,eff} \frac{k_g}{B} (T_{g,a} - T_{cool}) Re_g^{0.7} \quad \text{Equation 21}$$

$$\dot{Q}_{pt} = C_1 C_2 A_{pt} \frac{k_g}{B} (T_{g,a} - T_{cool}) Re_g^{0.7} \quad \text{Equation 22}$$

Constants C_1 and C_2 , characterised for SI engines fitted with an external exhaust manifold, are 1.8 and 1.5 respectively. The Reynolds number index, 0.7, is based on an exhaust port heat transfer

Nusselt-Reynolds expression stemming from data on six engines. Other Nusselt-Reynolds expressions are provided in literature describing time-averaged heat transfer in the exhaust ports are described in the following subsection The relationship used in PROMETS prior to the onset of this study had been derived by *Shayler et al* [3.12].

3.5 Exhaust Gas Temperature Prediction

The exhaust gas temperature is predicted through an energy balance. Equating the enthalpy of the exhaust gas with the source of heat produced due to combustion subtracted by the heat sinks allows determining the exhaust gas temperature. Heat sinks in an internal combustion engine are comprised of: 1) the useful work converted into brake power, 2) heat lost to the coolant through the metal structure and 3) miscellaneous sinks which balances the energy equation. The expression is shown below:

$$T_{ex} = \frac{Q_{LHV} - P_b - Q_{c1c2} - P_f - Q_{amb} + H_a + H_f}{(m_a + m_f) \cdot c_{p,ex}} + T_{amb} \quad \text{Equation 23}$$

3.6 Coolant Side Heat Transfer

3.6.1 Forced Convection and Nucleate Boiling

When both metal and coolant are below the saturation temperature, forced convection is the sole heat transfer mechanism. Heat transfer coefficients are mainly dependent on the velocity of coolant flow and temperature differences between the metal and liquid. Upon reaching the saturation temperature, vapour bubbles form at the interface between the metal and coolant. As the pressure of the vapour bubble increases a threshold is met where the bubble has sufficient kinetic energy to detach from the solid-liquid interface. Subsequently these bubbles are carried away by the flow of coolant. Further disorder due to the presence of these bubbles increases the heat transfer coefficient. As the heat flux rises to the point that flowing coolant is restricted from making contact with the hot metal a ‘critical heat flux’ is reached. At this point large pools of vapour are formed at the surface of the metal forming thin film boiling [3.12]. This in turn reduces the heat transfer coefficient as the metal is abstained from contact with coolant in effect significantly increasing the component metal temperature. Nucleate and pool boiling is most likely to occur in regions with very high heat fluxes such as the valve-bridge area or the top of the cylinder wall.

The total heat transfer coefficient when forced convection and/or nucleate boiling are present are added, as shown in the following expression:

$$h = h_{conv} + h_{n,boiling} \left[\frac{T_s - T_{sat}}{T_s - T_{cool}} \right] \quad \text{Equation 24}$$

The Dittus-Boetler correlation for turbulent fluid flow in smooth pipes is used to describe the heat transfer coefficient for forced convection, h_{conv} [3.13]:

$$h_{conv} = 0.23 Re^{0.8} Pr^{0.4} \frac{k}{D} \quad \text{Equation 25}$$

Where D is the diameter of the pipe, Re is the Reynolds number, Pr is the Prandtl number and k is the thermal conductivity of the fluid. The nucleate boiling term, $h_{nucl,boiling}$, is obtained from the work of Forster and Zuber [3.14], originally sought for pool boiling and is described as follows:

$$h_{n,boiling} = 0.00122 \Delta T_{sat}^{0.24} \Delta p_{sat}^{0.75} S \left[\frac{k_l^{0.79} c_{p,l}^{0.45} \rho_l^{0.49}}{\sigma_l^{0.5} \mu_l^{0.29} (\Delta h_{l,g} \rho_{l,g})^{0.24}} \right] \quad \text{Equation 26}$$

Nucleate boiling is described by the addition of a suppression factor, S , defined by Chen [3.15], which decreases asymptotically with increasing Reynolds number

$$S = \frac{1}{1 + 2.53 \times 10^{-6} Re_l F^{1.25}} \quad \text{Equation 27}$$

For low Reynolds numbers S approaches unity indicating that pool boiling occurs. *Finally et al.* [3.16] have shown that although the expression has been derived for vertical axial flow inside a circular tube, it is applicable for coolant side heat transfer as done in PROMETS.

3.6.2 Coolant Circuit Set-Ups

Three default coolant circuits have previously been used in the multi-cylinder model of PROMETS. The circuits, shown in Figure 15, depict a (A) a cross-flow parallel cooling circuit; (B) series flow cooling circuit; and (C) parallel cross-flow cooling circuit. These circuits, specific to an inline four cylinder engine, have been set-up by *Morgan* [3.7] and the benefits of applying different type circuits are elaborated upon.

Parallel cooling circuits, also known as dual cooling circuits, consist of separate circuits employed for the head and block of the engine. *Morgan* [3.7] states that such circuits are useful during cold and part load operation. Benefits of applying such circuits include reduced fuel consumption, improved knock limits and higher compression ratios for SI engines while improving rated power. These effects have been reported by observing the ratio of heat transferred through forced convection and nucleate boiling.

Flow-rate through the coolant passages is assumed constant and is dependent on the coolant pump speed. This is modelled in PROMETS using the following expression:

$$\dot{V} = a \pi B^2 S N \quad \text{Equation 28}$$

Where a is a scaling factor, B the cylinder bore, S engine stroke and N engine speed. In PROMETS, the split in the mass flow-rate for circuits with cross-flow (i.e. flow directed from the block to the head through bleed holes in the gasket) is modelled using the continuity expression for mass. As example, for a given total flow entering the block passage next to the first cylinder if α is the percentage of flow-rate branched into the cylinder head the total remaining flow in the block is:

$$\dot{V}_2 = \dot{V}_1(1 - \alpha) \quad \text{Equation 29}$$

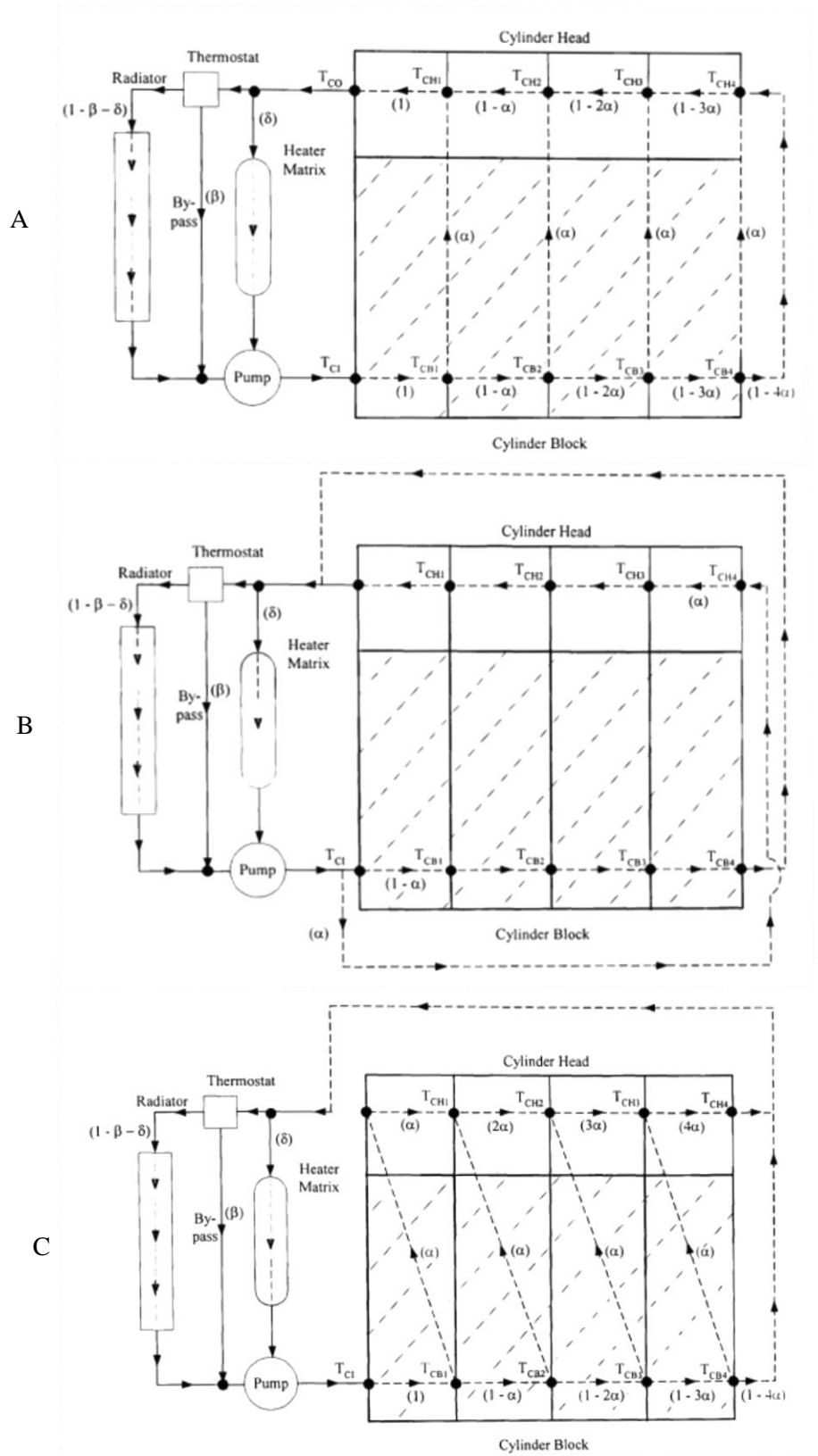


Figure 15: (A) Cross-flow parallel cooling circuit; (B) series flow cooling circuit; and (C) parallel cross-flow cooling circuit previously used in PROMETS.

3.7 Oil Circuit Model

The Reynolds number describes the flow regime in the oil galleries in block and head, this being laminar, transitioning or turbulent. For flow in an oil pipe the characteristic length is taken as the diameter of the pipe and is characterised by the engine. The smaller the pipe diameter the more turbulent the flow becomes with development of eddies or vortices while a larger pipe allows for bulk flow to easily move through the centre of the gallery.

Transition from laminar to turbulent flow occurs for Reynolds numbers ranging from 2000 to 4000. The model describes flow through oil pipes undergoing a laminar regime,

$$Re = \frac{4\dot{m}_{oil}}{\pi d_{main} \nu \rho} = \frac{4\dot{m}_{oil}}{\pi d_{main} \mu} \quad \text{Equation 30}$$

The Nusselt number describes the difference between the advective and diffusive heat transfer mechanisms compared to conductive heat transfer across the boundary. In PROMETS this is expressed as a function of the Reynolds and Prandtl numbers for laminar flow in a pipe [3.10].

$$Nu = 3.66 + \frac{0.0668 \cdot \left(\frac{d_{main}}{l_{main}}\right) \cdot Re \cdot Pr}{\left\{1 + 0.04 \cdot \left[\left(\frac{d_{main}}{l_{main}}\right) \cdot Re \cdot Pr\right]^{0.6667}\right\}} \quad \text{Equation 31}$$

The heat transfer coefficient is then calculated based on re-arranging the Nusselt number expression and substituting values calculated in the above expression:

$$h_{c,oil} = \frac{Nu \cdot k}{d_{main}} \quad \text{Equation 32}$$

Oil flow rate for varying operating conditions are calculated by means of a lookup table which is a function of the engine speed and oil temperature. Viscosity, density and conductivity are calculated as a function of temperature by utilising empirical expressions. Lookup table data is attributed to a positive displacement, gear type pump of fixed capacity equipped with a pressure relief valve.

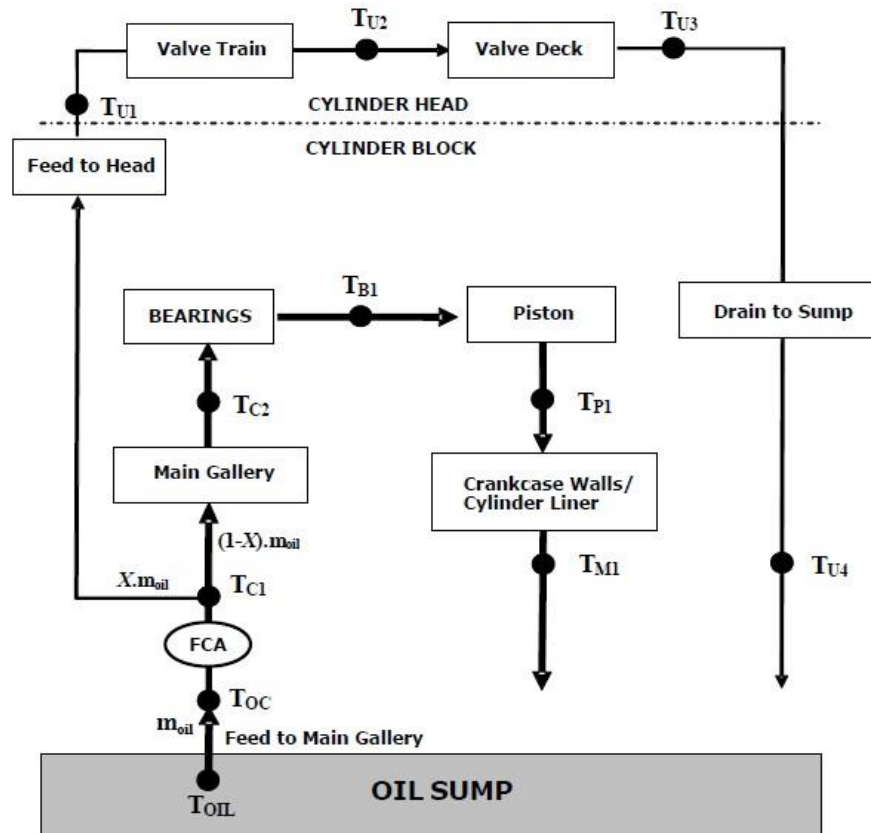


Figure 16: This diagram illustrates the calculation path PROMETS executes in order to estimate heat transfer and node temperatures of the oil at different points throughout the engine.

Eighteen triggers are used to activate calculation of heat transfer and temperatures and different points throughout the oil circuit in the engine as shown in Table 1, below. Heat resulting from friction in the bearings and piston heats the oil being flung around the crankcase. The interaction between the oil mist and metal structure components within the crankcase (i.e. bearings, piston underside, liner, connecting rod and walls) and valve deck is modelled by assigning a convective heat transfer coefficient of $50 \text{ W/m}^2\text{K}$.

In PROMETS the sump model does not account for stratification of the oil during the warm-up phase. It is assumed that the oil temperature is spatially uniform. Heat losses from the sump to the ambient air are assumed to be negligible for steel or iron as the thermal resistance differs by several orders of magnitude.

Function Name	Functionality
Trig 1	Heat Transfer from Metal Structure to Oil in Main Gallery 1
Trig 2	Heat Transfer from Metal Structure to Oil in Main Gallery 2
Trig 3	Temperature of Oil at Crankshaft Main Bearings
Trig 4	Temperature of Oil at Piston
Trig 5	Heat Transfer from Oil to Galleries and Bearing Elements
Trig 6	Heat Transfer to Oil from Block Casing
Trig 7	Temperature of Oil at the Valvetrain
Trig 8	Heat Transfer from Valve Deck to Oil
Trig 9	Temperature Calculation of Oil Prior to Entering Head
Trig 10	Heat Transfer from Block Metal to Oil Prior to Entering Head
Trig 11	Energy Calculation of Block Outer Walls due to Friction
Trig 12	Heat Transfer from Auxiliary Components to Oil
Trig 13	Heat Transfer to Mist within Crankcase due to Oil
Trig 14	Temperature of Oil Mist
Trig 15	Total Heat Lost from Oil to the Structure, Mist and Sump
Trig 16	Temperature of Oil Entering Oil Cooler
Trig 17	Heat transfer from Oil to Oil Cooler
Trig 18	New Temperature of Oil Leaving the Oil Cooler

Table 1: The table below shows the eighteen steps involved in calculating the heat transfer throughout the oil circuit.

3.8 Fuel Consumption Prediction

Fuel flow-rate is the influencing factor on in-cylinder and exhaust port heat transfer. An iterative calculation based on residual convergence is used through a c-script in PROMETS to estimate the required fuel flow-rate given friction power, pumping power, power required to drive the ancillaries and brake power. The summation of the powers for motive and parasitic losses is termed as the gross indicated power and is equated to fuel flow-rate using the following expression.

$$\dot{m}_f = ISFC_{i,g} P_{i,g}$$

Where the gross indicated power, $P_{i,g}$, is defined in relation to the volume swept, engine speed and gross indicated mean effective pressure.

$$P_{g,i} = IMEP_{i,g} \frac{V_s N}{120}$$

Where the gross indicated mean effective pressure, $IMEP_{i,g}$, is split into brake, pumping, friction and ancillary mean effective pressures:

$$IMEP_{i,g} = BMEP + PMEP + FMEP + AMEP$$

Pumping mean effective pressure is determined by subtracting the exhaust manifold pressure by the intake pressure in an iterative process based on a residual convergence scheme. Estimates of friction power throughout a warm-up are defined in *subsection 3.3*.

$$PMEP = (p_{ex} - p_i)$$

To estimate the percentage of total fuel combusted to deliver useful work the combustion and gross indicated efficiencies are defined. These efficiencies describe how well the engine contains heat resulting from combustion and combusts the total amount of fuel injected. For gasoline engines operating at lean or stoichiometric burn combust efficiencies are generally around 98%. Gross indicated thermal efficiency values vary depending on operating condition however previous values used in PROMETS by Addison [3.10] were around 35%.

$$ISFC_{i,g} = \frac{1}{Q_{LHV} \eta_c \eta_{i,g}}$$

Based on the lower heating value of the fuel for gasoline, $Q_{LHV} = 44\text{MJ/kg}$, and the required gross indicated power, the mass of fuel is defined.

$$\dot{m}_f = \frac{IMEP_{i,g} V_s N}{Q_{LHV} \eta_c \eta_{i,g} 120}$$

3.9 Discussion

An overview of the current state of the PROMETS model has been given. Previous models have represented inline and V type engines. For these type engines, equations describing heat transfer stemming from rubbing friction and the gas-side to the metal structure, coolant and oil have been outlined. Although the current state of PROMETS is comprehensive for modelling engine thermal behaviour, several modifications in most areas of the model have been required to represent operation of the 1.0litre TCE. All the changes suggested below are described in Chapter 4.

Firstly PROGEN lacks in representing some design features specific to the TCE. Although PROGEN is suited to represent straight runner exhaust ports, the addition of the integrated exhaust manifold and optimised crankshaft and connecting rod designs has required changes to the PROGEN code. Therefore mass predictions of the TCE resulting from PROGEN require validation in order to appropriately model engine thermal inertia.

Furthermore, the \dot{Q}_{c1c2} correlation described by *Shayler et al* [3.12] has been validated for engines with straight runner exhaust ports. As the TCE is designed with an integrated exhaust manifold, the effect this has on heat transfer in the head remains to be ascertained. Current values for the C_1 and C_2 constants and the exponent for the gas Reynolds numbers also remain to be confirmed.

Also, coefficients for the friction model for all assemblies in PROMETS are currently suited to an inline 2.0l 4 cylinder gasoline engine design reported by *Addison* [3.10]. In order to characterise rubbing friction for the TCE, coefficients have to be adjusted for fully warm operation. Further to this, a SAE 5W-20 oil grade is used for the TCE. Vogel constants for this formulation have not been reported or validated in PROMETS. These are essential to accurately model fuel consumption over engine warm-up. This therefore provides incentive to modify the friction model set-up.

The default coolant circuit layouts reported by *Morgan* [3.7] do not segregate flow in the head. The TCE, as shown in the next chapter, has bespoke passages in the intake and exhaust sides of the head with the addition of a block thermostat. This renders coolant in the block to initially warm-up in a quiescent state while forced convection dominates heat transfer in the exhaust side of the head. In addition to having to modify the coolant circuit the heating of quiescent coolant in the block requires the addition of an expression for natural convection.

Pertaining to the air paths, previous gasoline versions of PROMETS have been modelled to represent naturally aspirated engines. Although an empirical expression has been used by *Addison* [3.10] to estimate the boosted intake pressure past the throttle, the approach provides sub-optimal

predictions over the NEDC and cannot be transferred to the version of PROMETS for the TCE. A robust method for predicting the boost pressure past the throttle for the TCE over various drive cycles is required to. This is important in light of characterising pumping losses specific to the TCE over highly dynamic drive cycles such as the FTP-75 and WLTC. This in turn, affects fuel consumption predictions made through the model. Therefore, an adequate expression calculating the boost pressure has to be found in literature or derived.

Finally, the penalty associated with motoring a piston also remains to be quantified. This is important in trying to weigh the fuel consumption benefits and penalties associated with cylinder deactivation.

In light of the above, the following chapter looks at modifications made to the model requiring correlation with experimental data. These modifications are firstly essential to characterise the operation and thermal behaviour of the TCE from idling to rated power. Secondly, robustly characterising the TCE sets confidence in using PROMETS as a tool for predicting effects of cylinder deactivation on engine thermal behaviour and performance. This is elaborated upon in Chapter 5 and 6.

Chapter 4 Advancing PROMETS to Represent the 1.0litre Three Cylinder Engine

4.1 Introduction

This chapter covers revisions and additions made to the multi-cylinder model of PROMETS in order to characterise the three cylinder engine. The modifications are presented through subsections by firstly giving background knowledge and incentive for modifications; processes undertaken to apply the modifications to the model; and lastly validation of the model if experimental data was present for correlation. Subjects looked at are widespread referring to: engine features, the friction model, coolant side heat transfer and coolant circuit modifications, gas-side heat transfer revisions, piston cooling jets, a simple method for predicting turbocharged engine performance and lastly a motoring loss representation when deactivating a cylinder for robust performance estimations.

4.2 Engine Details and Architecture

The PROMETS model described in the following is developed as a representation of a 1.0l three cylinder engine[4.1]. Specifications of the engine are shown in Table 2. The engine cooling circuit is described using the nomenclature shown in Figure 17. Figure 18 shows coolant flow in the engine prior to the opening of the block thermostat. During this period coolant in the block remains quiescent with flow solely in the exhaust side of head. After the block thermostat opens coolant flows as illustrated in Figures 18, 19 and 20.

4.3 Location of Thermocouples Used for Model Correlation

The TCE was instrumented with chromel-alumel™ K-type thermocouples, to monitor temperatures both in solid (i.e. metal) and liquid mediums (i.e. coolant and oil). Composed mostly of nickel, this is $\geq 90\%$ by volume, these thermocouples are suited for thermodynamic environments outside of the combustion chamber³. Thermocouples were instrumented along the block coolant cavity with the aim of capturing changes in coolant temperature before and after the block thermostat opened. Thermocouples were also instrumented vertically alongside the coolant block to monitor temperature differences between the bottom and top of the coolant cavity. To ensure that heat transferred from the combustion chamber and exhaust ports to the entire engine was appropriately modelled; thermocouples were installed along the vertical axis of the first and second firing cylinders. With this incentive, thermocouples were also installed into

³K-type thermocouples are suited to endure temperatures in the range of -200°C to +1350°C.

Attribute	TCE
Engine Type	Gasoline Turbocharged Direct Injection, Four Stroke (120°)
General Description	Cast aluminium alloy cylinder head with integrated exhaust manifold (IEM), pent-roof cross-flow combustion chambers, grey cast iron cylinder block, aluminium alloy sump pan, aluminium pistons
Engine Layout	Inline 3
Capacity	999cc
Compression Ratio	10:1
Bore / Stroke	71.9mm/82mm
Cam System	DOHC – flat follower
Valvetrain	Double Overhead Camshaft, Wet Belt Drive, Direct Acting Flat-Follower, 2 intake/2 exhaust valves
Fuel	Pump Grade 95 Octane
Main/Connecting Rod Bearings	4 (44mm diameter bearings)/ 40mm connecting rod bearing
Valve Sizes	Inlet Head Dia. 27.1mm Exhaust Head Dia. 23.1mm
Max. Valve Lift	Inlet, 8.26mm Exhaust, 8.26mm
Rated Power	74kW
Idling Speed	850rpm
Injection System	Bosch Management System
Cooling System	50% Water / 50% Ethylene-Glycol, Split cooling System
Coolant Passages	Block Coolant Jacket: 6.5mm thick/ 80mm tall Exhaust Port Coolant Sleeves: variable thickness above and below
Turbocharger	Radial
EGR System	Internal
Variable Displacement Capability	None

Table 2: Technical details of engines installed on the ECTB.

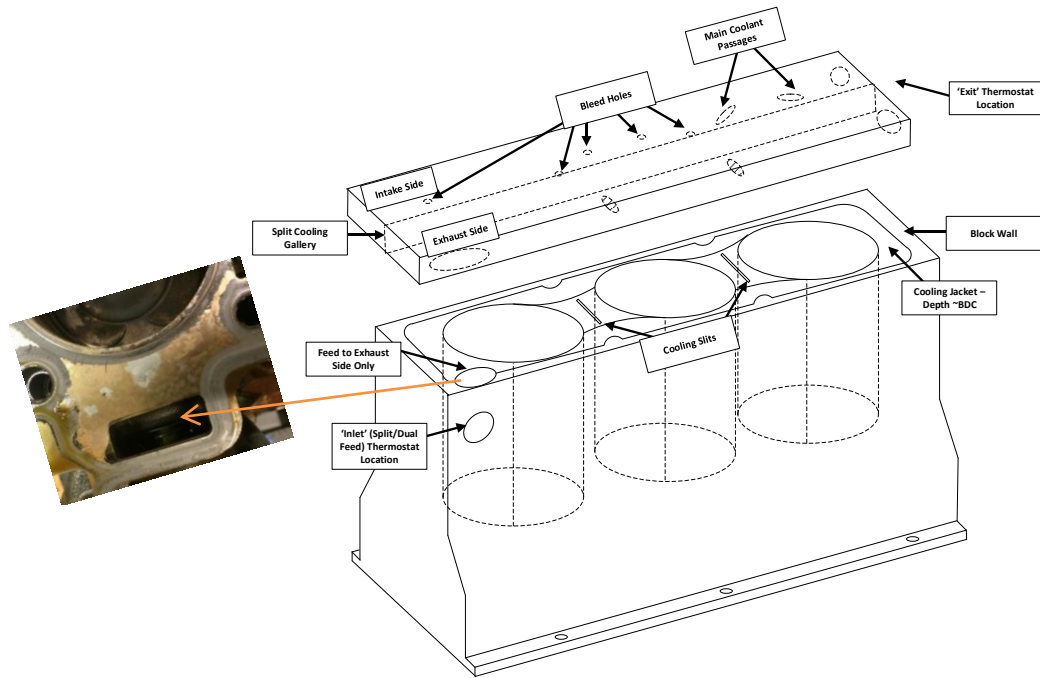


Figure 17: Nomenclature for split cooling system of the engine.

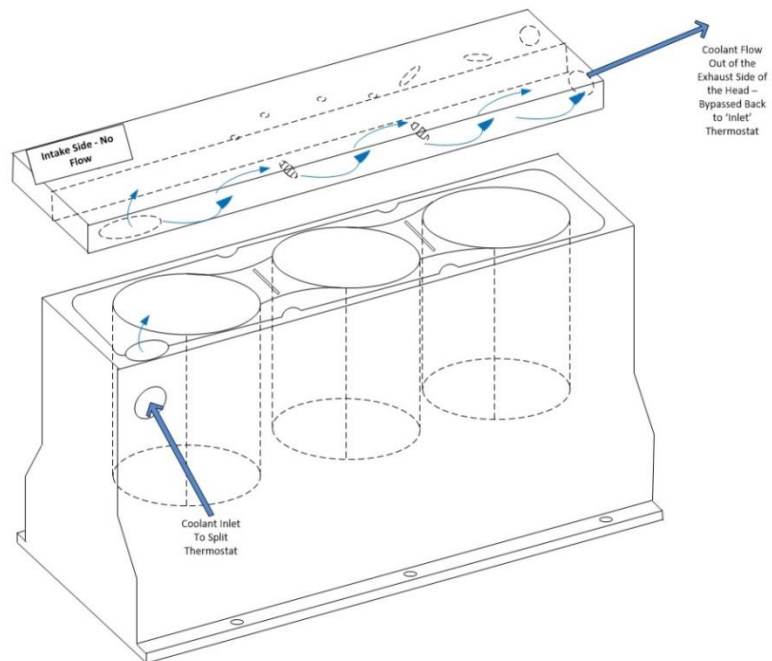


Figure 18: Illustration of coolant flow in the exhaust side of the head while the block thermostat remains closed.

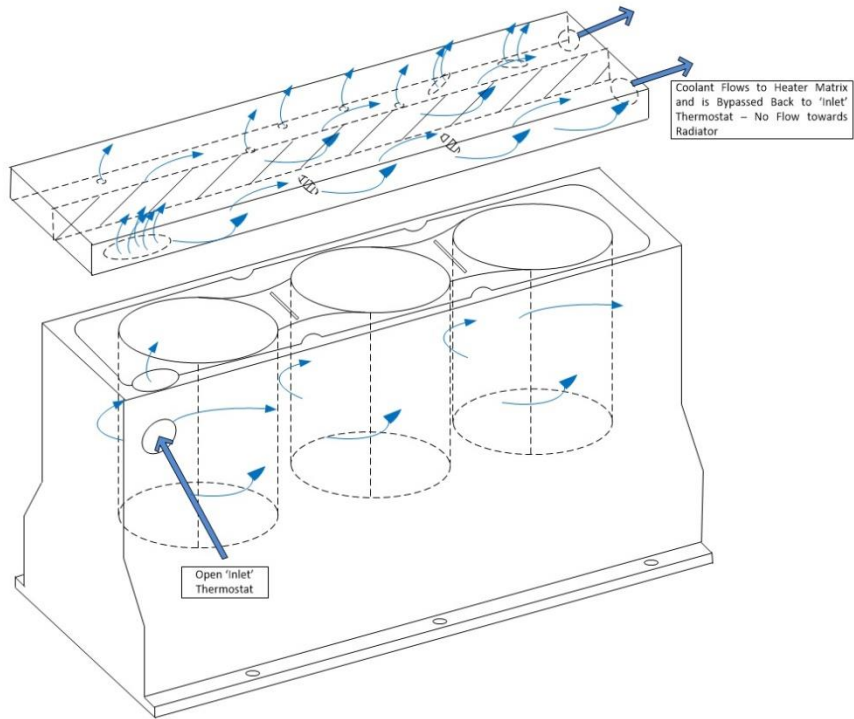


Figure 19: Illustration of coolant flow in the block exiting through the intake side of the head and flow in the exhaust side of the head when the block thermostat is open.

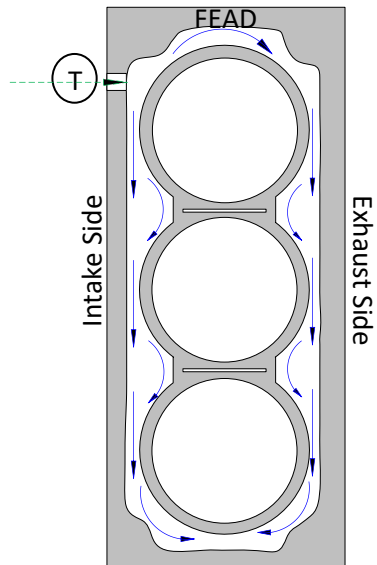


Figure 20: Top-view of the coolant flow paths around the block when the block thermostat is open.

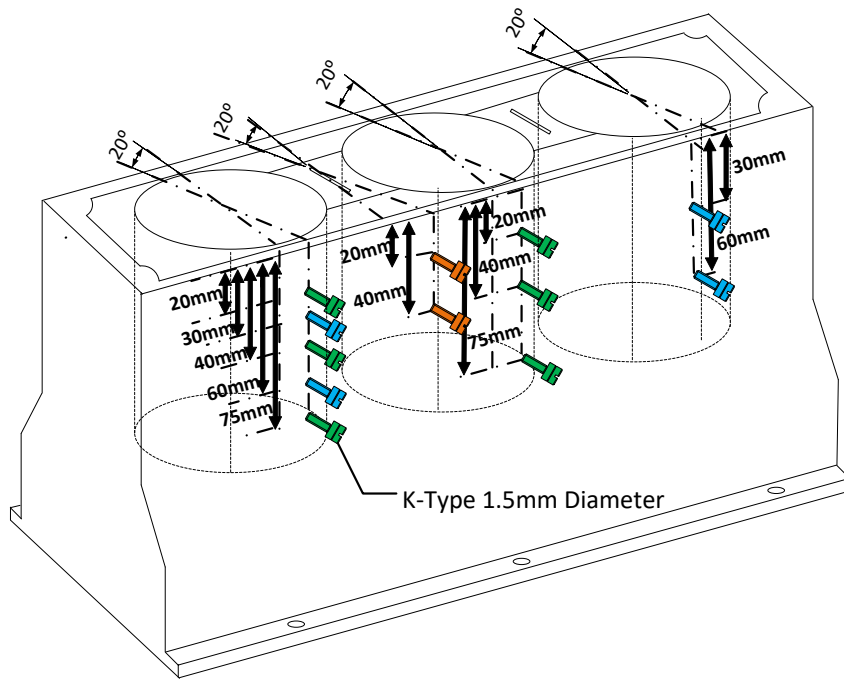
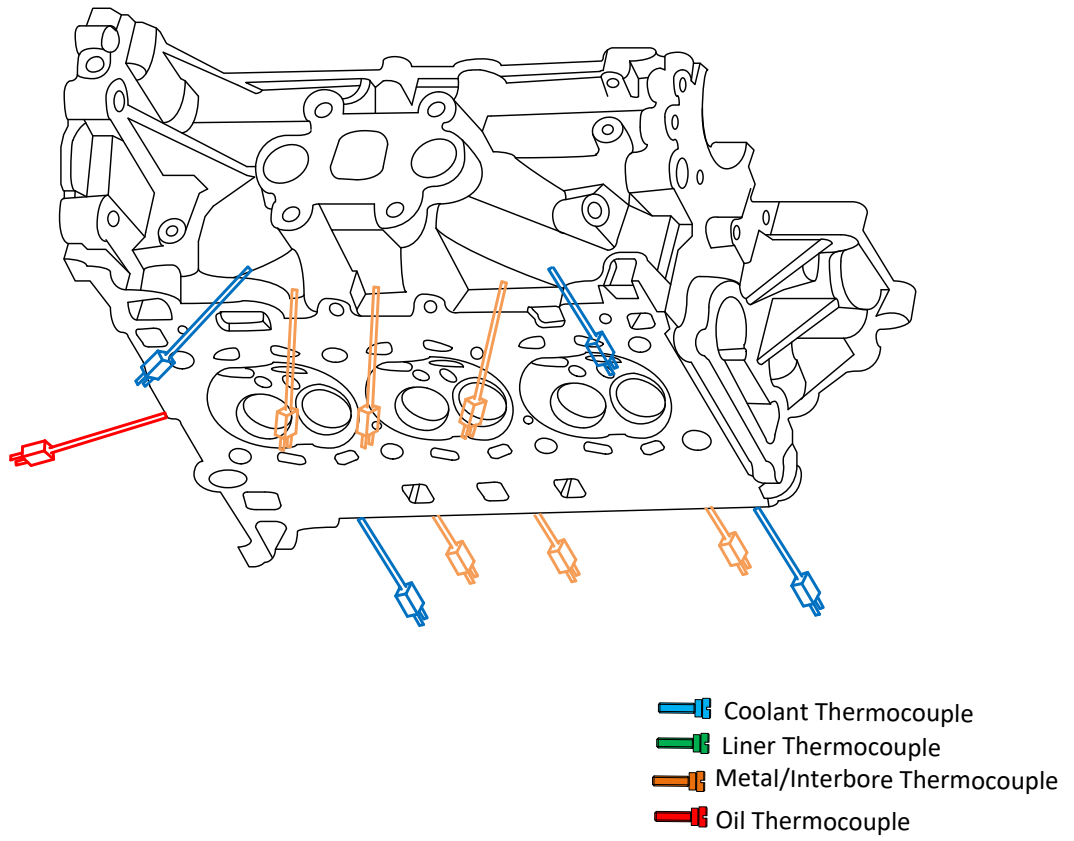


Figure 21: Detailed line drawing of the thermocouple positions in the block and head.

several locations in the engine head. Diagrams of the general location of thermocouples in the engine head and block are shown in Figure 21. Thermocouples in the metal block structure were placed at 20 degrees from the perpendicular of the cylinder due to packaging constraints on the intake side of the engine. In addition thermocouples were drilled half-way through the thickness of structural walls to ensure that cracking due cyclic thermal or stress fatigue did not affect readings. This being said, the thermocouple on the first cylinder at the top of the liner failed after commissioning. With this, thermocouples were used for metal and coolant temperature measurements which then elaborated upon heat flux and enthalpy calculations.

4.3.1 Data Used for Model Correlation

Test-bed data presented in this thesis originates from 1) an eddy-current dynamometer rig (ECTB) [4.2] located at the University of Nottingham and 2) a driving dynamometer test-bed situated on an engine test bed situated at the British Petroleum (BP) Pangbourne Technology Centre. Comparisons between experimental and model outputs using temperature information resulting from cylinder wall and coolant thermocouple data are shown in *subsection 4.7.2*. Drive cycle data emanating from BP for the purpose of comparing coolant and oil temperatures and fuel consumption over the NEDC and FTP-75 are shown in *Chapter 4 subsection 4.8.2.3* and *4.10.3*.

4.4 Feature Revisions and Additions

4.4.1 Integrated Exhaust Manifold (IEM)

For lumped capacity thermal modelling purposes an appropriate estimate of the volume surrounding the IEM was necessary to model inertial effects during warm-up, deactivation and re-activation periods. For this purpose, a singular element was sufficient to define cylinder specific exhaust ports. In this case, three elements have been used in the multi-cylinder instance of PROMETS.

4.4.1.1 Dimensions Used for Mass and Volume Estimation

Two methods of extracting the geometries from an IEM to make a generic estimate of the volume of a lumped element model are suitable for the lumped thermal approach used in this instance. The first is by topographically representing the structure given a physical engine to refer to. Otherwise and if available, CAD drawings provided by the engine manufacturer may be used to extract such information. The latter was chosen for purposes of accuracy and time constraints.

As shown in Appendix A the exhaust port volume metal element in PROGEN is simply calculated by subtracting the volume of the hollow part of the exhaust port by the thickness of the metal surrounding the exhaust port.

$$v_{exhaust,port,element} = v_{exhaust,port2} - v_{exhaust,port1}$$

On the left-hand side of the expression, the total exhaust port element volume solely accounts for the wall thickness. The expression for $v_{exhaust,port1}$ represents the inner volume of the port while $v_{exhaust,port2}$ adds thickness to the inner volume. Each volume is split into three sections described generically in Appendix A.

4.4.1.2 Surface Areas for Heat Transfer to Coolant

The surface areas of the exhaust port metal exposed to coolant were extracted from a CAD model of the engine head. The dimensions of the surface areas assigned and transferred to PROMETS are shown in Figure 22.

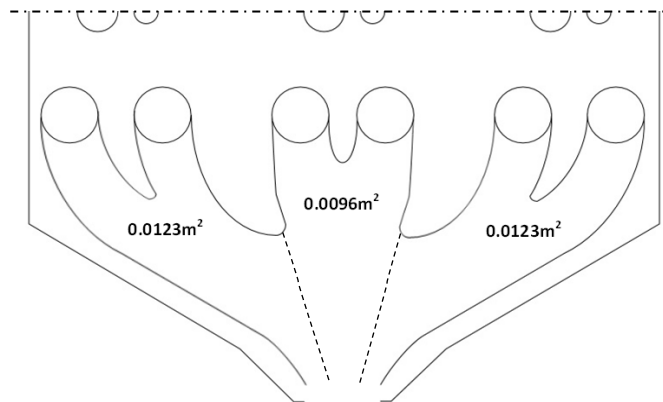


Figure 22: Modelled surface areas exposed to coolant flow in the IEM for specific cylinders.

4.4.2 Engine Component Masses

4.4.2.1 Revisions for Optimised Crankshaft and Connecting Rod Designs

Component masses have been previously described in PROGEN through empirical formulations based on work done by *Chick* [4.3]. Since the inception of these expressions, introduction of weight reducing features on modern engines has required that these formulations be revised. For the crankshaft, mass reduction has been sought through improved web-design, counterweights and hollow crankpin journals [4.4]. Optimisation via CAE has also led engine designers to reduce the mass of connecting rods specifically around the I-beam and small end and

big end bearings [4.5]. Given this knowledge it was found that the original expressions for the mass of the crankshaft and connecting-rod did not give appropriate estimates. To correct for this constants were modified in the source code for PROGEN such that masses compared well with experimental measurements.

4.4.2.2 Comparisons between Modelled and Measured Engine Masses

With the above modifications made to PROGEN the total engine mass (i.e. excluding the fly-wheel) was estimated within a 10% error band. Figure 23 shows a breakdown of the comparison between modelled and measured data for component masses. To allow for such a comparison the engine manufacturer supplied a detailed document with the masses of different components.

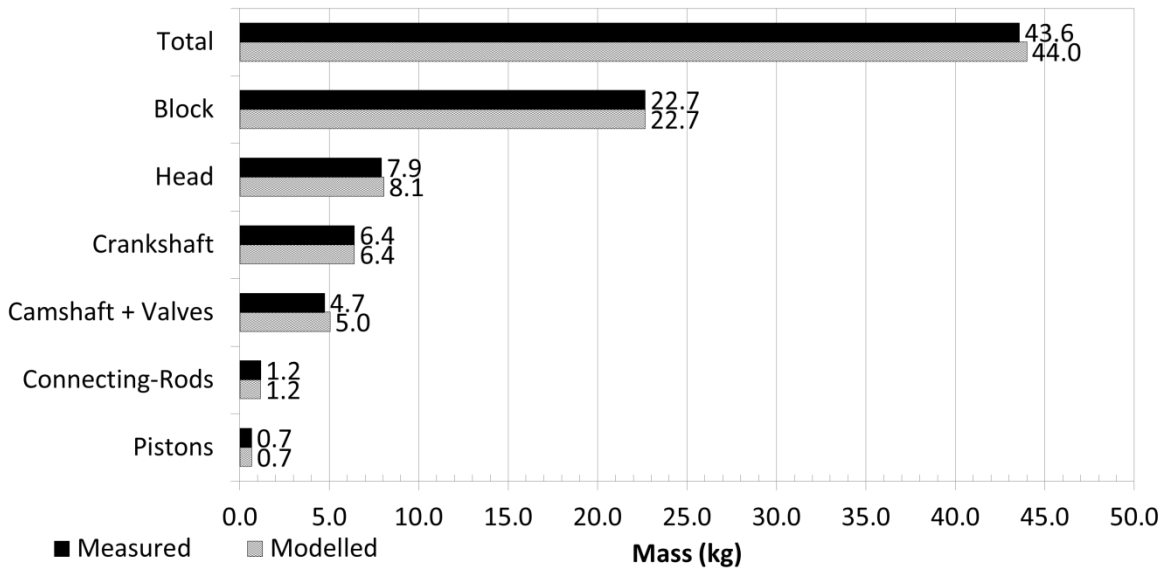


Figure 23: Differences between measured and modelled component masses.

4.5 Friction Model Revision for the TCE

The thermal-friction interactions at rubbing surfaces are difficult to model using an explicit time marching scheme due to strong coupling between oil temperature, friction dissipation and viscosity. For the purpose of modelling cycle averaged friction a mean value model formulated by *Patton et al* [4.6], modified and corrected by *Shayler et al* [4.7] is used in PROMETS. As described in the previous chapter in *subsection 3.3* the original friction model stems from a force analysis coupled with lubrication theory to account for the effect of changes in the viscosity of oil.

4.5.1 Original Friction Model Description

Although in the past other formulations have been added to PROMETS, Vogel constants specific to a 5W-20 oil grade (i.e. present in the TCE) were not previously investigated and were therefore added. Values for the thicker (5W-40) and thinner (5W-20) solutions are shown in Table 3 below.

Oil Grade/ Vogel Constants	5W-20 [4.8]	5W-40 [4.6]
k_v (Pa s)	$4.576 \cdot 10^{-5}$	$1.1220 \cdot 10^{-4}$
θ_1 (°C)	1224	1018
θ_2 (°C)	134.1	125.9

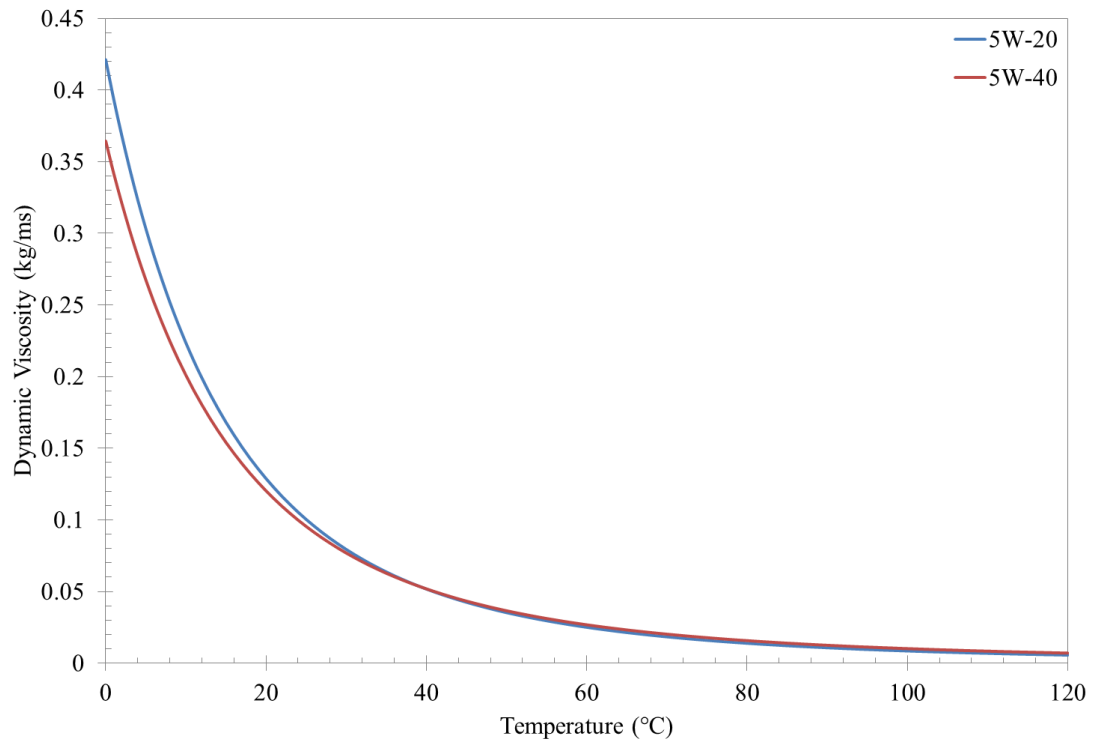


Table 3: Oil viscosity constants for SAE 5W-20 compared to SAE 5W-40.

4.5.2 Engine Friction Validation

The total engine friction for the TCE due to combined rubbing friction and ancillary loads (i.e. vacuum pump, oil pump, coolant pump and fuel pump) while operating on all cylinders were determined experimentally. This was calculated by subtracting the calculated BMEP (based on a measured brake torque value) from the net IMEP (calculated by integrating a pressure-volume trace for one engine cycle) over a range of engine operating conditions emanating from the rig at the University of Nottingham.

The corresponding friction prediction was increased exactly by 10% to match experimentally measured values, at various speeds, with each component contribution scaled by the same factor. The change in the coefficients from the previous PROMETS model for Equations 9 to 12 (shown in *subsection 3.3*) are shown in Table 4. The agreement between the measured and adjusted prediction of the total and the distribution between contributing sources are shown in Figure 24. For the ancillaries, the three pumps (i.e. fuel, coolant and oil pumps) have been coupled together for this application and it is assumed that there are no changes in pump performance when cylinder deactivation is enabled. A comparison between modelled and component specific FMEP from engine teardown tests (conducted in Germany) were supplied by the automotive manufacturer. Perfect agreement lay between measured and modelled FMEP values, however for confidentiality purposes these are not plotted. Furthermore, FMEP points plotted in Figure 24 are limited to four engine speeds (i.e. 1500, 2000, 2500 and 3000rpm); over 20, 40 and 60Nm brake torque points, to ensure that excessive engine speeds would not wear the engine down considering the number of tests required for thermal validation of the model.

	Coefficients	Units	Original	3 Cylinder 1.0l Gasoline Engine (TCE)
Crankshaft Assembly	C_{CS} <i>main bearing seals</i>	kPa min/rev m	$1.10 \cdot 10^{-1}$	$1.21 \cdot 10^{-1}$
	C_{Oh} <i>oscillating hydrodynamic</i>	kPa (m min/rev) ^{0.5}	$2.10 \cdot 10^{-1}$	$2.31 \cdot 10^{-1}$
	C_{td} <i>turbulent dissipation</i>	kPa (min/rev m) ²	$1.20 \cdot 10^{-4}$	$1.33 \cdot 10^{-4}$
Valvetrain Assembly	C_{vb} <i>valvetrain bearing</i>	kPa m ³ (min/rev)	$1.03 \cdot 10^{-8}$	$1.33 \cdot 10^{-8}$
	C_{ff} <i>flat follower</i>	kPa m	$5.03 \cdot 10^{-2}$	$5.59 \cdot 10^{-2}$
	C_{rf} <i>roller follower</i>	kPa m	$2.05 \cdot 10^{-2}$	$2.27 \cdot 10^{-2}$
	C_{Oh} <i>oscillating hydrodynamic</i>	kPa (m min/rev) ^{0.5}	$2.10 \cdot 10^{-1}$	$2.31 \cdot 10^{-1}$
	C_{om} <i>oscillating mixed</i>	kPa	4.49	4.95
Piston Assembly	C_{ps} <i>piston skirt</i>	kPa s	$2.94 \cdot 10^{-1}$	$3.23 \cdot 10^{-1}$
	C_{pr} <i>piston ring</i>	kPa m ² (rev/min)	$4.06 \cdot 10^{-1}$	$4.53 \cdot 10^{-1}$
	C_{be} <i>big end bearings</i>	kPa m ³ (min/rev)	$3.03 \cdot 10^{-1}$	$3.33 \cdot 10^{-1}$
Ancillaries	α	kPa	6.17	6.85
	β	kPa min/rev	$5.17 \cdot 10^{-3}$	$5.74 \cdot 10^{-3}$
	γ	kPa min ² /rev ²	$1.78 \cdot 10^{-7}$	$1.97 \cdot 10^{-7}$

Table 4: Coefficients for engine friction sub-assemblies.

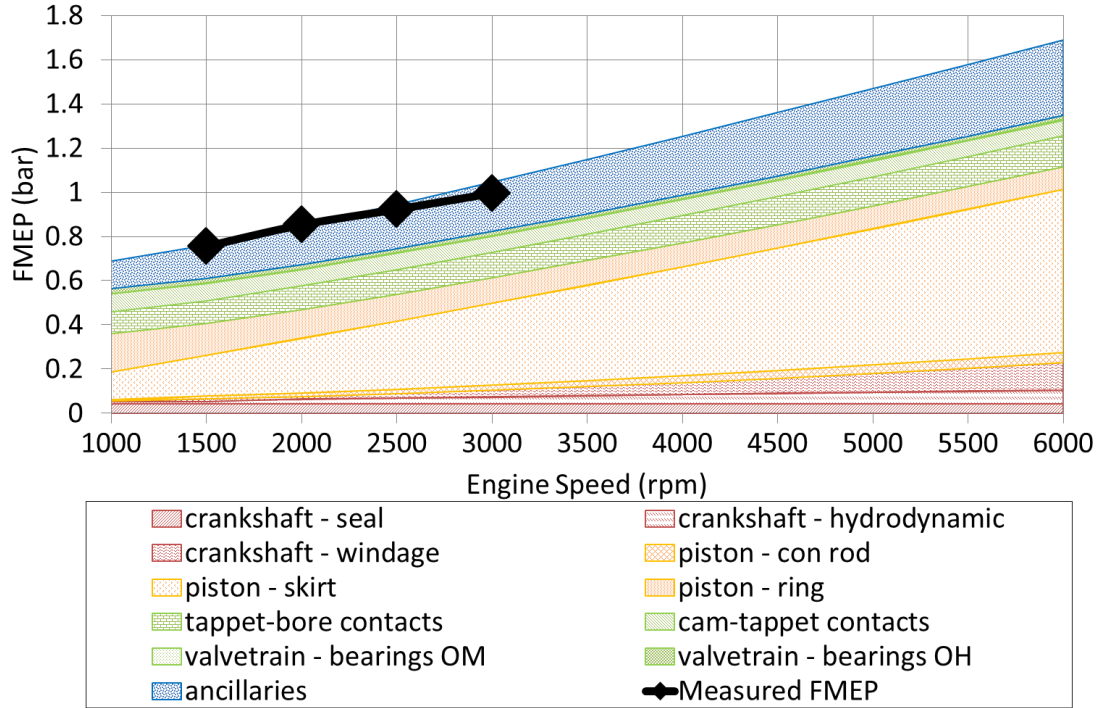


Figure 24: Modelled and measured FMEP values for fully warm conditions, i.e. $T_{oil} = 90^{\circ}\text{C}$ for a flat-follower configuration.

4.6 Oil Circuit Model

For the TCE engine oil is pumped from the sump into two main galleries 9mm in diameter and 286.2mm in length. The head gallery is 7.5mm in diameter traversing a length of 286.2mm. A total of 4.9 litres of oil is contained within the engine. Only dimensional modifications specific to the TCE were made to model the heat transfer across the oil circuit. Therefore the oil circuit is kept the same as that shown in *subsection 3.7*.

4.7 Revisions to the Gas-side Heat Transfer Expression

Ensuring appropriate heat transfer changes are predicted when deactivating a cylinder, the heat transfer expression from the gas-side to coolant was revised to account for the addition of the IEM and direct injection. An accurate prediction of temperature differences and changes for components throughout the modelled engine was required. Importance in verifying this also translates to appropriately estimating warm-up rates for both coolant and oil mediums. This section describes revisions made to account for increased heat transfer from the exhaust ports to coolant and validation of the revision by comparing heat transfer and metal temperatures.

The constants C_1 and C_2 optimised for SI engines by *Shayler et al* are specific to engines with an external exhaust manifold. Addition of an integrated exhaust manifold required that the energy balance between heat sources and sinks be revisited. Also due to the increase in the exhaust port diameter the Nusselt-Reynolds expression was verified with respect to experimental data. The methodology for this modification for the application to the TCE is explained in the next subsection.

4.7.1 Methodology for Revision of Heat Transfer Model

The procedure used in revising the gas-side to coolant heat transfer follows the methodology described by *Shayler et al* [4.9]. Integrating the exhaust manifold into the engine head eliminates heat transfer across the manifold face and raises exhaust gas heat transfer within the head. As the IEM is enveloped by coolant passages the heat transferred from the exhaust ports to the coolant is increased. Thus the energy balance is re-written omitting heat losses through the external exhaust manifold:

$$\dot{Q}_{cyl} + \dot{Q}_{pt} + \dot{Q}_{friction} = \dot{Q}_{cool} + \dot{Q}_{amb} + \dot{Q}_{oc} \quad \text{Equation 33}$$

Where \dot{Q}_{pt} is representative of heat transferred from the IEM. Measuring a value of the heat transferred from the IEM to the coolant is facilitated by the design of the split cooling system. Coolant passages in the exhaust side of the head are segregated from the rest of the engine. Therefore, given the coolant mass flow-rate and the rise in coolant temperature the enthalpy of the coolant flow-rate is directly calibrated in the following manner:

$$\dot{Q}_{pt} = dh = \dot{m}_{cool,pt} c_p dT \quad \text{Equation 34}$$

Where dT is the difference in coolant temperature entering and exiting the passage and \dot{m}_{cool} , the mass flow-rate. The heat transfer from the port required the existing model to be calibrated, specifically to the 1.0l TCE. The Reynolds number index, 0.7 , is based on an exhaust port heat transfer Nusselt-Reynolds expression stemming from data on six engines previously studied at Nottingham. Other Nusselt-Reynolds expressions are provided in literature describing time-averaged heat transfer in the exhaust ports and are shown in Table 5 below [4.9] [4.10] [4.11] [4.12] [4.13] [4.14]. The relationship previously used in PROMETS derived by *Shayler et al* [4.9] lies between the relations found by *Catton and Heywood* [4.13] and *Meisner and Sorenson* [4.14] as shown on Figure 25.

For the TCE an increase in coolant enthalpy was noted due to coupling of coolant flowing from the turbocharger bearing to the exhaust side of the head. The mass flow-rate, at varying engine speeds, accounted for approximately 10% of the total flow from the exhaust side of the head and was thus subtracted from the measured outlet temperature. Changes in measured heat transfer from the IEM to coolant compared to the predicted heat transfer from straight runner ports are compared in Figure 26 C.

Nusselt-Reynolds Relation	Authors
$Nu = 0.023 Re^{0.8} Pr^{0.3}$	Dittus-Boetler [4.10]
$Nu = 0.258 Re^{0.8}$	Hires and Pochmara [4.11]
$Nu = 0.0483 Re^{0.783}$	Malchow, Sorenson and Buckius [4.12]
$Nu = 0.45 Re^{0.6}$	Caton and Heywood [4.13]
$Nu = 0.0774 Re^{0.769}$	Meisner and Sorenson [4.14]
$Nu = 0.18 Re^{0.7}$	Shayler and Chick [4.9]

Table 5: Various Nusselt-Reynolds expressions describing heat transfer at the exhaust ports.

To calculate a Nusselt number for the exhaust port an effective exhaust port diameter was required. An attribute of the IEM is that the exhaust port diameter is not uniform. The diameter was measured with reference to a CAD model of the engine head. Near the exhaust valve the diameter measured 19.8mm, doubling as the ports merge, contracting to a unified exit width of 25mm. An average port diameter of 25mm was calculated using CAD tools. With this, the following Nusselt number expression characterised heat flow to the coolant:

$$Nu_{pt} = \frac{\dot{Q}_{pt} D_{pt}}{A_{pt} k_g (T_{ex,gas} - T_{pt,wall})} \quad \text{Equation 35}$$

A_{pt} is calculated based on the average exhaust port diameter using an average length, $l \sim 0.1m$, for all three cylinders. The conductivity of the exhaust gas was taken to have the same dependency on equivalence ratio as the in-cylinder exhaust gas, i.e. as shown above. To appropriately evaluate the Nusselt number an estimate of the exhaust gas temperature across the exhaust port, $T_{ex,gas}$, and an average port wall temperature, $T_{pt,wall}$, were required. The open flow expression used to estimate the exhaust gas temperature is shown below:

$$T_{ex,gas} = \frac{\dot{Q}_{pt}}{\left(\frac{\dot{m}_f(1+AFR)}{n_{cyl}}\right)\left(\frac{\gamma}{\gamma-1}\right)R} + T_{ex,out} \quad \text{Equation 36}$$

Based on *Heywood's* [4.15] observation an index of 1.3 is a robust estimate for the polytropic of exhaust gas exiting the exhaust ports. The port wall temperature was calculated based on the thermal resistance of the port wall and coolant given the heat transfer through the port to the coolant and coolant temperature. The expression is shown below:

$$T_{pt,wall} = Q_{pt} \left(\frac{\ln \frac{r_i}{r_o}}{2\pi l k_{pt,wall}} + \frac{1}{2\pi r_o l h_{coolant}} \right) + T_{coolant} \quad \text{Equation 37}$$

Experimental values were taken during constant operating conditions such that exhaust gas and coolant temperatures settled. The ratio $\frac{r_i}{r_o}$ was taken uniformly through the extent of the port length, equating to 0.826. $h_{coolant}$ was calculated based on model predicted values using the Dittus-Boetler expression. Variations in the calculated inlet exhaust gas temperature existed due to small oscillations in measured exit temperatures. Knowing this, inlet exhaust gas temperatures were generally 200 – 400°C higher compared to exit exhaust gas temperatures mainly dependent on mass flow-rate. Estimated exhaust port metal temperatures were generally 200 - 400°C hotter compared to the coolant, ranging between 260 - 530°C. Calculation errors primarily stem from uncertainty in estimating the exhaust gas temperature. These errors are difficult to quantify and are dependent on calibration.

To characterise the heat transfer in the exhaust port in a Nusselt-Reynolds power law expression the exhaust port Reynolds number was also calculated. This was done using the following expression:

$$Re_{pt} = \frac{4 \dot{m}_f (1+AFR)}{\pi D_{pt} \mu_g} \quad \text{Equation 38}$$

Where the dynamic viscosity of the exhaust gas, μ_g , has the same dependence on equivalence ratio as the in-cylinder gas.

4.7.2 Comparison between the Original and Revised Model

The Nusselt and Reynolds numbers resulting from the above expressions were then plotted on a log-log scale against exhaust port heat transfer descriptions listed in Table 5. Data in Figure 25 shows Nusselt Reynolds estimate for engine speeds between 1250 and 3000rpm and brake loads

between 20 (i.e. 11% WOT) and 150Nm (i.e. 86% WOT). A mean fit through the data was plotted giving the following Nusselt-Reynolds correlation:

$$Nu_{pt} \approx 0.29 Re_{pt}^{0.723} \quad \text{Equation 39}$$

Figure 25 shows that the IEM increases the Nusselt number above the *Caton and Heywood* [4.13] correlation and those previously described by *Shayler and Chick* [4.9]. This is primarily attributed to an increase in exhaust port diameter. The increase in coolant surface area in contact with the metal is also attributed to this. The Nusselt numbers remain below those observed by Hires and Pochmara representative of heat transfer in the curved port wall section next to the exhaust valves. This is indicative of the Nusselt number not being overestimated.

Using the index inferred from the Nusselt-Reynolds plot, i.e. 0.723, the constants C_1 and C_2 were calculated using the following expression:

$$C_1 C_2 = \frac{\dot{Q}_{pt}}{A_{pt} \frac{k_g}{B} (T_{g,a} - T_c) Re_g^{0.723}} \quad \text{Equation 40}$$

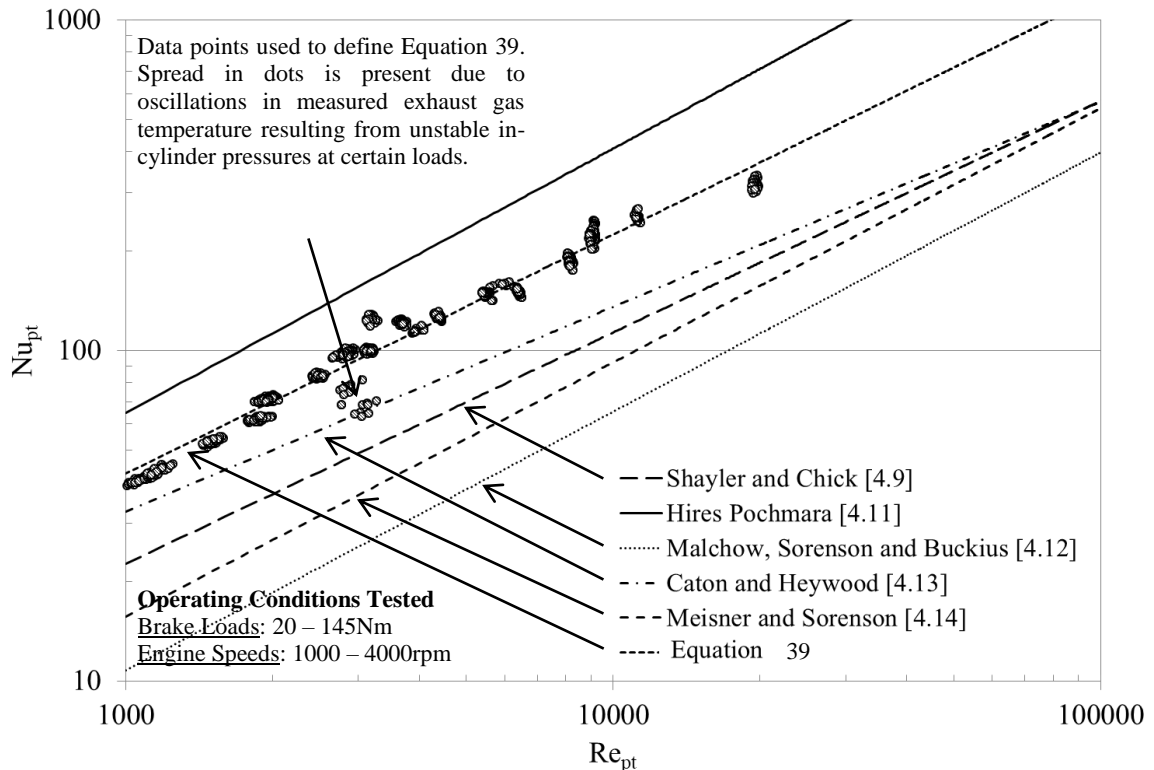


Figure 25: Predicted exhaust port heat rejection compared with published correlations from sets of data for the 1.0l engine designed with an integrated exhaust manifold.

These were evaluated through a simple optimisation process and cross-referenced against the coefficients in Equation 40, giving new constants $C_1 = 1.3$ and $C_2 = 2$ compared to the previous constants $C_1 = 1.8$ and $C_2 = 1.5$.

$$Nu_{pt} = \left[C_1 C_2 \left(\frac{B}{D_{pt}} \right)^{1.7} \frac{T_{ex,gas} - T_{pt,wall}}{T_{g,a} - T_c} \right] Re_{pt}^{0.723} \quad \text{Equation 41}$$

To determine the validity of these new constants modelled and measured heat rejection rates from the gas side to coolant for the engine, cylinder wall and exhaust ports are shown on Figure 26. These are also compared against predicted heat rejection rates using the original expression derived by *Taylor and Toong* [4.16] and *Shayler and Chick* [4.9]. The new constants result in a more accurate description of the heat rejection to coolant as compared on Figure 26 (A). As seen on Figure 26 (B) the influence of changing the coefficients and index on the cylinder based heat transfer to coolant is retained and slightly improved. Figure 26 (C) illustrates the increase in heat transfer from the exhaust port significantly improving the predictions.

To further verify that the appropriate amount of heat is exposed to the metal components comparisons were made between measured and modelled cylinder wall temperatures. Cylinder number one and two were used for this purpose as is illustrated in Figure 27 and Figure 28. For the first cylinder a 5°C difference is present between modelled and measured data. Experimental wall temperatures are generally lower due to the block aperture being located adjacent to the thermocouples. The cylinder wall is locally cooled remaining outside the resolution of a 0-D lumped thermal capacity model where the annular elements consist of single temperature. Thermocouple tips for cylinders one and two were situated mid-way through the cylinder wall thickness such that these matched with the representation of the model elements. Readings at 20mm from the flame-deck are also missing due to thermocouple failure after commissioning of the engine. Modelled wall temperatures for cylinder number two agree well with measured data, remaining within a 3°C difference. Generally the difference increases with brake load and reduces as engine speed increases. The crested temperature profile is generally very well captured indicating that heat paths to the cylinder head and lower crankcase are appropriately modelled.

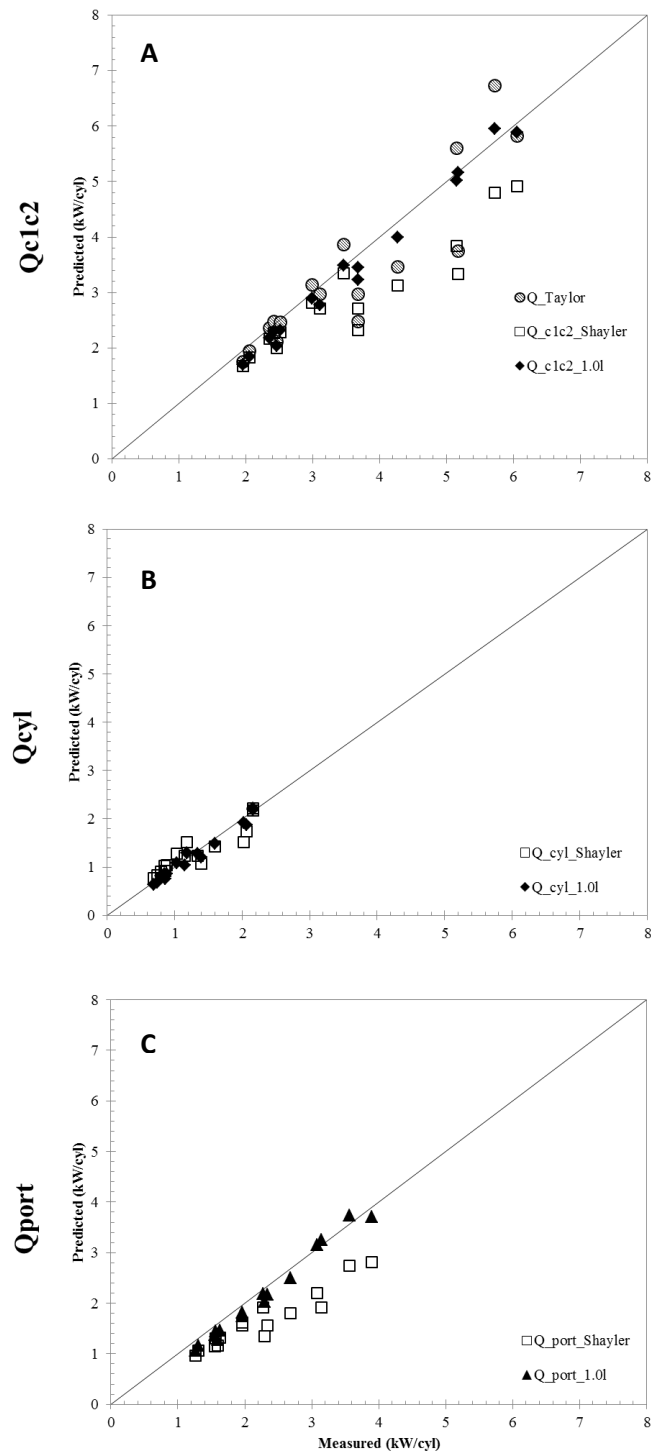


Figure 26: Predicted heat rejected to coolant on (A) a total per cylinder basis, (B) specific to the cylinder walls and (C) specific to the exhaust ports from sets of data for the 1.0l engine designed with an integrated exhaust manifold. Heat released to engine coolant was calculated using an open flow enthalpy equation for coolant passages in the exhaust side of the head and block given a mass flow-rate, temperature difference and empirically based specific heat capacity for coolant.

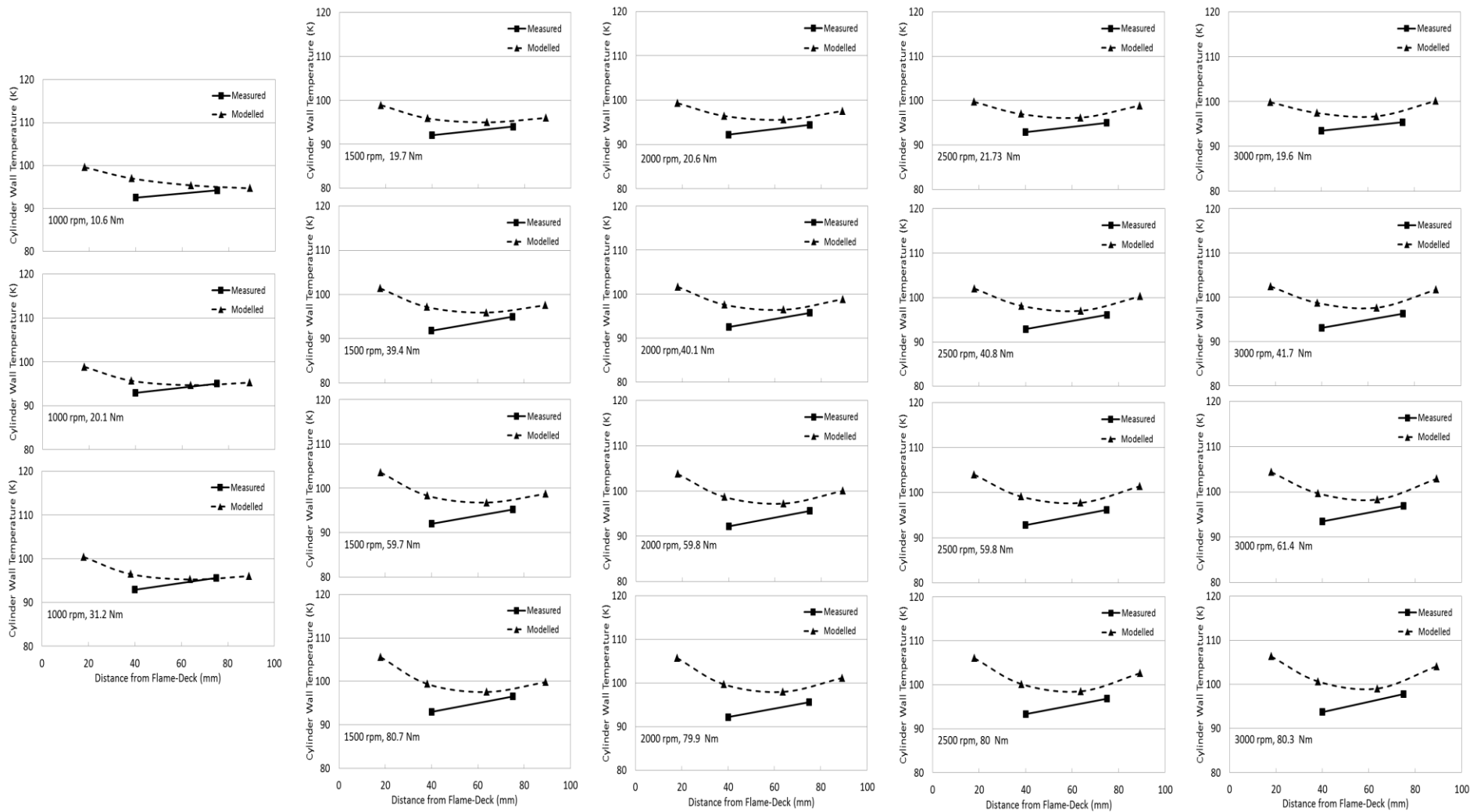


Figure 27: Comparison of modelled and measured cylinder 1 wall temperature for various engine brake loads and speeds.

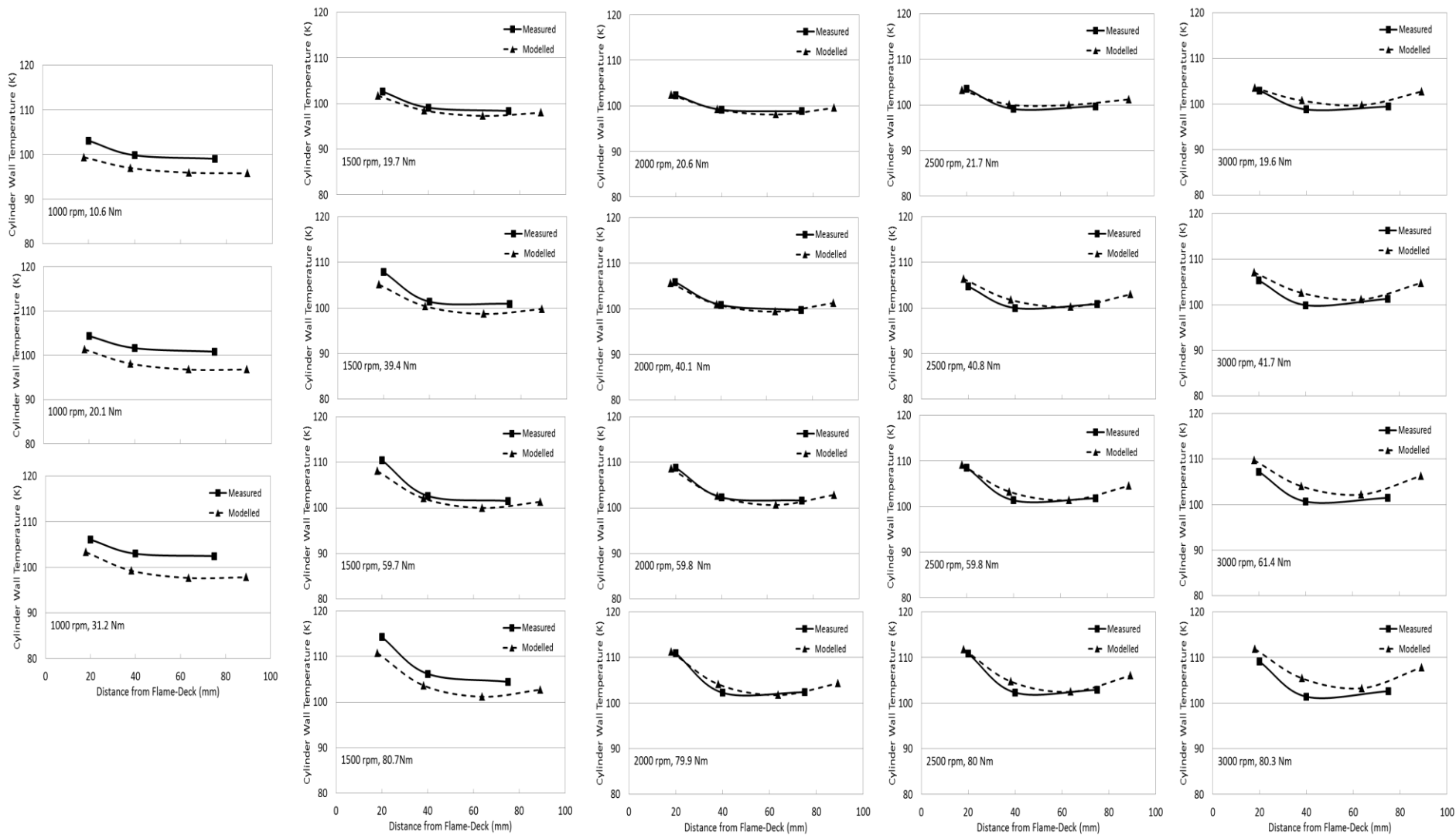


Figure 28: Comparison of modelled and measured cylinder 2 wall temperature for various engine brake loads and speeds.

4.8 Revised Coolant Passage Heat Transfer

Prior to this study modelled heat transfer in coolant passages has been represented through forced convection and nucleate boiling. These have been described in *subsection 3.6.2*. For the TCE, these are still the dominant forms of heat transfer however the addition of a thermostat controlling coolant flow in the block has required the addition of a term describing heat transfer through natural convection. Expressions made available in literature used to describe natural convection have been assessed based on their applicability to the topography of the block coolant passage of the TCE. As a result of expressions in literature not being suited to represent natural convection in the TCE an empirical Nusselt-Rayleigh expression has been used to satisfy this void.

4.8.1 Advanced Cooling Circuit Design Representation

Unlike conventional cooling systems, a split cooling circuit involves the segregation of coolant volumes to specific parts of the engine reducing coolant thermal inertia while promoting engine warm-up rate. The TCE has a single coolant delivery which is split during the warm-up process and re-routed as a parallel cooling system through the use of two thermostats; one situated at the block and a conventional radiator thermostat. This characterises the cooling system for the TCE as an advanced cooling system.

Initially flow passing through the block leads in parallel with the intake side of the head and is segregated from flow in the exhaust side of the head. A schematic of the model representation for the segregated flow is shown on Figure 29 at different stages of the warm-up. As shown in Figure 29 (A) prior to the block thermostat opening, forced convection is only present across the exhaust side of the head. During this stage, coolant in the block is warmed-up by heat transfer in the form of natural convection. When coolant in the block situated adjacent to the block thermostat reaches 75°C forced convection takes place throughout the engine structure, as is shown in Figure 29 (B). Bleed-holes located between the block and the intake coolant passages direct coolant entering the block up through to the intake side coolant gallery. As coolant is directed to the back of the engine, flow from the intake side of the head and exhaust side of the head mix prior to leaving the engine structure. Figure 29 (C) depicts the coolant circuit when the radiator thermostat opens.

When forced convection is present throughout all coolant passages in the engine, during fully warm operation, the physical attributes of flow mixing and bifurcation are accounted for by assigning percentage reductions to the volume flow-rate at designated locations within the model. The total coolant flow-rate at the pump bifurcates into a 25% and 75% split directed to the block and exhaust side of the head respectively (refer to Figure 29 B). With reference to data emanating from CFD models [4.18], as coolant flow in the block traverses each cylinder (i.e. three cylinders) a 33% reduction in volume flow-

rate is directed into the coolant passage in the intake side of the head. Thus as flow merges prior to exiting the head the percentage split between flow sourcing from the exhaust side of the head and intake side of the head are attributed a 25% and 75% split respectively. Flow-rates were extracted from idling to rated power operation from manufacturer supplied data and CFD simulations. The percentage split translates to the temperature balance and mass flow-rate calculation made for merging flow in the model.

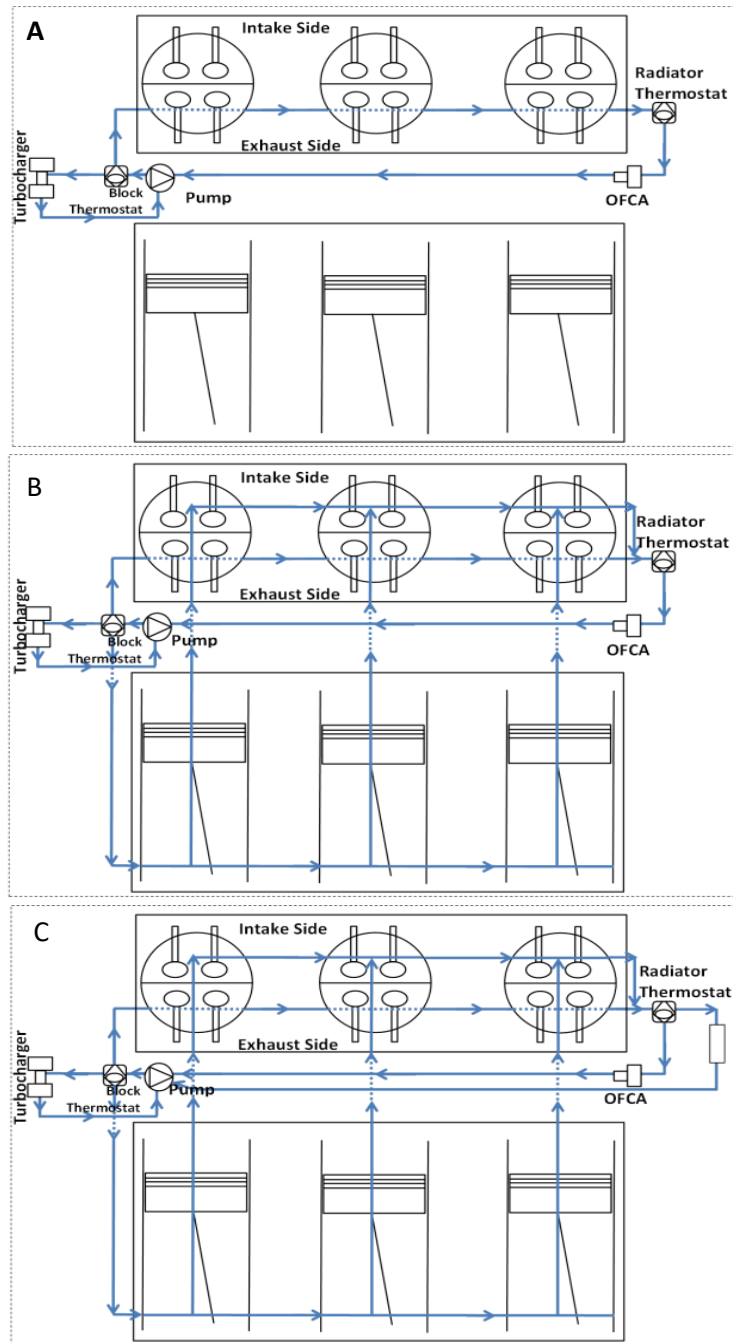


Figure 29: Coolant schematic for the modelled three cylinder engine [A] prior to the block thermostat opening, [B] after the block thermostat opens and [C] when the radiator thermostat opens.

4.8.2 Modelling Quiescent Coolant in the Block

The presence of natural convection in the block required the addition of a correlation for quiescent liquid undergoing heat transfer in an enclosure being heated from a side-wall transferring heat to a cooler side-wall. The phenomenon is first described followed by a description of the available expressions found in literature.

4.8.2.1 Natural Convection in a Rectangular Enclosure

The coolant passage in the block is best described by vertical rectangular enclosure. The fluid is assumed to be Newtonian. At $t \sim 0$ seconds the sidewall is coated with a conduction layer which increases with respect to time as shown [4.19]:

$$\frac{\Delta T}{t} \sim \alpha \frac{\Delta T}{\delta_T^2} \rightarrow \delta_T \sim (\alpha t)^{1/2}$$

Where:

- δ_T is the boundary layer thickness
- $\alpha = \frac{k}{\rho c_p}$ (thermal diffusivity)
- t ; time (sec)

While the fluid does not undergo heating three forces balance out such that the fluid remains quiescent: the inertia, friction (viscous diffusion) and buoyancy forces. Inertia forces are dependent on the momentum diffusivity while the buoyant forces are dependent on the thermal diffusivity. Initially, the Prandtl number $Pr = \frac{\nu}{\alpha} = \frac{\mu/\rho}{k/c_p\rho} = \frac{c_p\mu}{k}$ is small such that the thermal diffusivity is close to the momentum diffusivity. As the fluid heats up, due to conduction through the cylinder wall, the convective effect increases in turn increasing the importance of the buoyancy force compared to the friction forces, $Ra_H > 1$. At this instance, the Prandtl number increases such that the momentum diffusivity dominates the thermal diffusivity such that $Pr > 1$. As the temperature of the cylinder wall increases through the warm-up process there exists a point in time, t_f , when the energy balances between conductive and convective forms such that the enthalpy is carried away vertically by the buoyant forces [4,19]. Beyond that time the layer thickness is:

$$\delta_{T,f} \sim (\alpha t_f)^{1/2} \sim HRa_H^{-1/4}$$

Where the Raleigh number according to Bejan is based on the enclosure height:

$$Ra_H = \frac{g\beta \Delta T L_c^3}{\alpha\nu}$$

Unlike, other sources [4.19] Bejan states that the choice of incorporating the characteristic length as the width of the enclosure, L , instead of the height, H , for the Raleigh number ‘is without foundation from a theoretical scaling viewpoint’. That is, the relation between the property Ra_H is not strongly bounded by the characteristic dimension L . Knowing this, Bejan gives the condition such that ‘if the final thermal boundary layer thickness $\delta_{T,f}$ is smaller than the transversal extent of the enclosure (L), the thermal layers will be distinct’ such that the following criterion is satisfied:

$$\frac{H}{L} < Ra_H^{1/4} \text{ or } \frac{L}{\delta_{T,f}} > 1$$

The enthalpy flow from the hot vertical end to the cold vertical end is expressed in the following manner:

$$q'_{convection_{left \rightarrow right}} \sim (\rho v \delta_T) c_p \Delta T$$

Which simplifies to:

$$q'_{convection_{left \rightarrow right}} \sim k \Delta T Ra_H^{1/4}$$

Heat diffuses vertically from the warm upper branch of the counter-flow to the lower branch at a rate

$$q'_{conduction_{top \rightarrow bottom}} \sim kL \frac{\Delta T}{H}$$

The enthalpy carried by the stream, horizontally reaches the opposite end intact when the vertical diffusion is negligible such that,

$$\frac{H}{L} > Ra_H^{-1/4}$$

When the above condition is met, *Bejan* states that the horizontal streams along the adiabatic walls retain their temperature identity. Four regimes may be used to describe the convective heat transfer dependent on the aspect ratio, $\frac{H}{L}$, of the cavity containing the fluid and the Ra_H number, as shown in Figure 30 [4.19].

- 1) The *first* regime accounts for heat transfer through conduction (where $Ra_H < 1$) and the temperature varies linearly across the cavity, wherein the heat transfer rate across the cold wall is insignificant. There are no distinct layers or striations in this regime.
- 2) The *second* regime is specific to tall enclosures, where the temperature difference across the cavity is linear like that of the *first* regime, with distinct layers close to the top and bottom walls.
- 3) The *third* regime is suited for high Raleigh number cases with thermal boundary layers forming next to the vertical and differentially heated sidewalls. The heat transfer rate obeys a convective

form with a non-linear temperature profile presenting itself between the hot and cold walls. The horizontal walls are adiabatic where within the cavity the fluid is relatively stagnant and thermally stratified (i.e. $\frac{L}{\delta_{T,f}} > 1$) with distinct streamlines providing a rotational flow pattern.

- 4) The *fourth* regime is pertinent to a shallow enclosure, where the rotational flow pattern is obscured by turbulence due to the streamlines being very close to one another, therefore creating an insulating heat barrier. The boundary layer becomes significantly more turbulent compared to regime three.

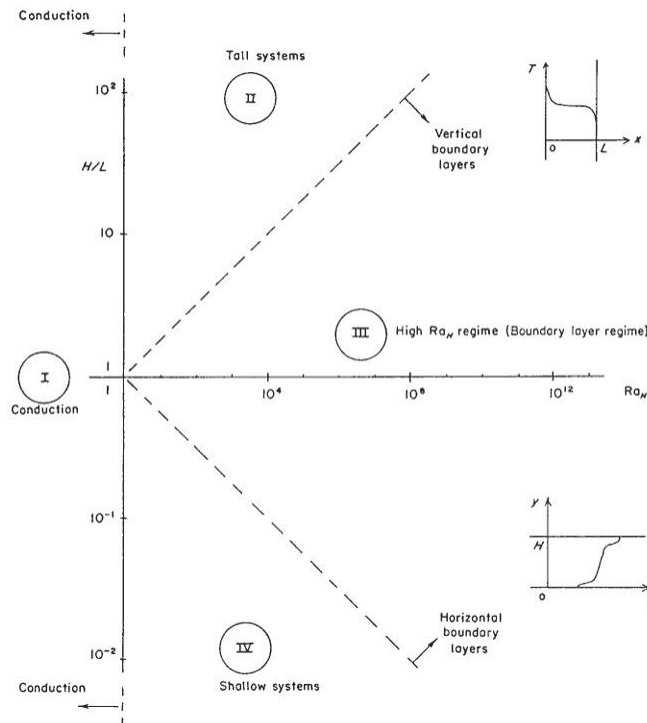


Figure 30: Heat transfer regimes for internal natural convection for an enclosure heated from the side [4.19].

Mention of the four regimes is made such that future studies can refer to the Rayleigh number depending on the coolant passage topology. Such designs could include sectioning of the block passage (i.e. with respect to the fourth regime) or creating long slender passages (i.e. the second regime) such that the effect on coolant warm-up rates may be observed and further studied.

4.8.2.2 Nusselt-Reynolds Empirical Expression for Natural Convection

Several expressions are available describing natural convection in a *vertical enclosure*. These are specific to the aspect ratio of the enclosure and applicable to experimentally observed Prandtl and Rayleigh numbers. These are provided by [4.19] [4.20] and are shown in Table 6.

Author	Equation Number	Expression	Conditions	Dimensional Length for Ra
Cengel	Equation 42	$Nu = 0.042 \cdot \left(\frac{h}{l}\right)^{-0.3} \cdot Pr^{0.012} \cdot Ra_L^{0.25}$	$10 < \frac{H}{L} < 40$ $1 < Pr < 20000$ $10^4 < Ra_L < 10^7$	L
	Equation 43	$Nu = 0.46 \cdot Ra_L^{\frac{1}{3}}$	$1 < \frac{H}{L} < 40$ $1 < Pr < 20$ $10^6 < Ra_L < 10^9$	L
Bejan	Equation 44	$Nu = 0.364 \cdot \left(\frac{L}{H}\right) \cdot Ra_H^{0.25}$	$Pr > 1$ $\frac{H}{L} > 1$ $Ra_H > 10^3$	H

Table 6: Natural convection expressions for fluid trapped in a vertical enclosure heated from a side wall with uniform heat flux [4.19] [4.20].

To appropriately select the Nusselt number expression utilised for 0-D modelling purposes, experimentally occurring Prandtl and Raleigh numbers were first verified against the inequalities shown above. The aspect ratio for the coolant cavity in the block measured $H/L \sim 12.5$. Coolant properties and dimensionless numbers were evaluated for a warm-up encompassing the following engine operating conditions: $N = 1000 - 2000\text{rpm}$ and $T_b = 1 - 44\text{Nm}$. The starting temperature of the coolant, oil and global engine structural temperature measured 19°C . Figure 31 shows the locations of the thermocouples used to capture the temperature profiles of the quiescent coolant shown on Figure 32. Subsequently these temperatures were used to calculate coolant properties.

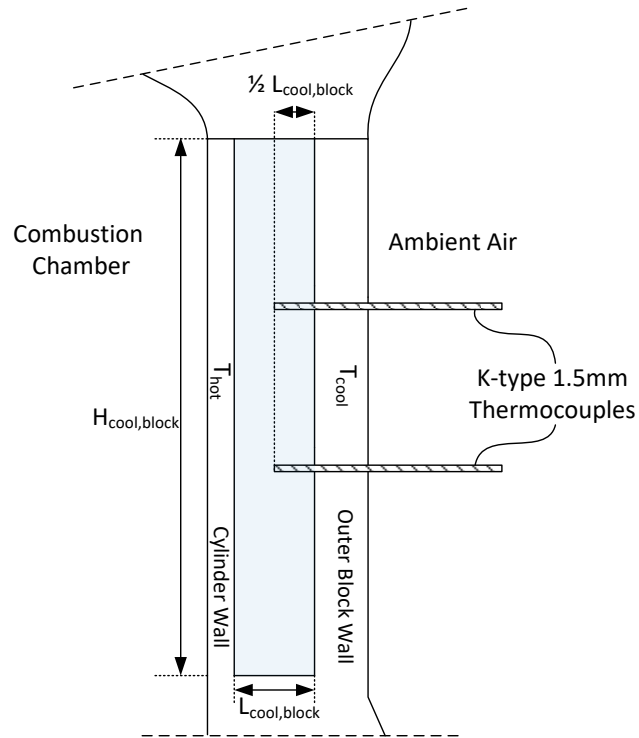


Figure 31: Characteristic dimensions used for the block coolant cavity and location of thermocouples utilised to monitor liquid temperatures.

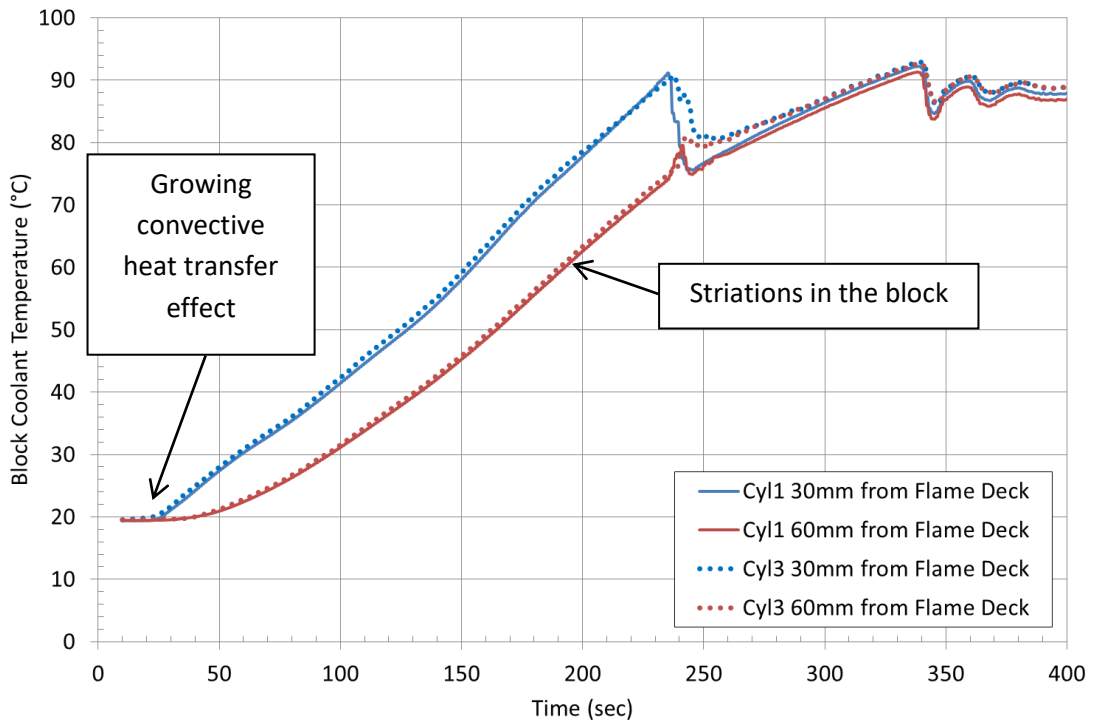


Figure 32: Measured block coolant temperatures opposite cylinder 1 and 3 during a warm-up phase for $N = 1000 - 2500\text{rpm}$, $T_b = 1 - 44\text{Nm}$.

Coolant conductivity (Equation 45), specific heat capacity (Equation 46), viscosity (Equation 47) and density (Equation 48) were determined utilising empirical expressions for a coolant composed of 50% ethylene-glycol and 50% water [4.21].

$$k_{\text{coolant}} = \sqrt{\frac{1.39 \cdot 10^{-1} + (1.26 \cdot 10^{-3}) \cdot T_{\text{cool}} + (1.89 \cdot 10^{-5}) \cdot T_{\text{cool}}^2}{1 + (5.58 \cdot 10^{-3}) \cdot T_{\text{cool}} + (1.15 \cdot 10^{-4}) \cdot T_{\text{cool}}^2}} \quad \text{Equation 45}$$

$$c_{p,\text{coolant}} = \sqrt{\frac{96.9 \cdot 10^4 + (88.4 \cdot 10^{-3}) \cdot T_{\text{cool}}}{1 + (3.96 \cdot 10^{-4}) \cdot T_{\text{cool}} + (5.89 \cdot 10^{-7}) \cdot T_{\text{cool}}^2}} \quad \text{Equation 46}$$

$$\mu_{\text{coolant}} = \frac{(7.52 \cdot 10^{-3}) - (5.31 \cdot 10^{-6}) \cdot T_{\text{cool}}}{1 + (3.11 \cdot 10^{-2}) \cdot T_{\text{cool}} + (5.33 \cdot 10^{-4}) \cdot T_{\text{cool}}^2} \quad \text{Equation 47}$$

$$\rho_{\text{coolant}} = \frac{1075 - (1.65 \cdot 10^{-2}) \cdot T_{\text{cool}}}{1 + (4.04 \cdot 10^{-4}) \cdot T_{\text{cool}} + (1.91 \cdot 10^{-6}) \cdot T_{\text{cool}}^2} \quad \text{Equation 48}$$

These expressions are designed for an absolute pressure of 2.5bar, for forced convection cases however the results are independent of pressure over the range of pressures used in engine coolant systems. Property values were then substituted to calculate the Prandtl number:

$$\text{Pr} = \frac{c_p \cdot \mu}{k} \quad \text{Equation 49}$$

The Raleigh number [$\text{Ra} = \phi(\text{Pr}, \text{Gr})$] was then determined utilising the following expression:

$$\text{Ra} = \text{Pr Gr} = \frac{\mu c_p}{k} \frac{g \Delta T \beta \delta^3}{v^2} = \frac{g \rho^2 c_p \Delta T \beta \delta^3}{\mu k} \quad \text{Equation 50}$$

Where the volume expansion coefficient for a liquid, β , was determined by:

$$\beta = \frac{\rho_{\infty} - \rho}{\rho(T - T_{\infty})} \quad \text{Equation 51}$$

Given that the temperature of the inner block wall was not monitored a simplification was made by equating the upper-outer block wall temperature to the coolant temperature at the centre of the cavity. The effect of this assumption on the estimation of the Grashof number is unknown. This is can however be inferred as marginal as there is no direct contact between the combustion gases and the outer block wall. Following Cengel's approach [4.20], the characteristic length used for the Raleigh number was chosen as the width of the coolant cavity, L . The density of the coolant at the interface between the coolant and

metal structure is evaluated utilising the cylinder wall metal temperature such that $T = T_s$. ρ_∞ is evaluated using coolant temperature, T_∞ , measured mid-way through the block cavity.

Experimentally occurring Prandtl and Raleigh numbers were then compared against the inequalities presented for the three expressions found in literature. Observed Prandtl numbers, shown through the blue line on Figure 34 (D), fall outside the bounds of the inequality for Equation 42. The expression is only pertinent for coolant temperature greater than 40 degrees Celsius, equivalent to a $Pr > 20$. The expression was found unsuitable for modelling purposes as ambient world temperatures range between -89.2°C and 56.7°C [4.22]. Applying thermocouple measurements to Equation 43 resulted in over-estimating the Raleigh number by an order of magnitude also leading to uncertainty. Equation 44 presented in Table 6 proves to satisfy observed dimensionless numbers and the measured cavity aspect ratio, however this was achieved when using the cavity width as the characteristic dimension instead of the suggested cavity height. Given that turbulence in a vertical boundary layer commences when $Gr > 50 \cdot 10^3$ [4.23], applying the cavity height as a characteristic dimension over-estimates the buoyance (i.e. gravitational effect) effect due to heating. This is specifically observed during the early stages of warm-up. Given the lack of certainty in using the equations provided in literature, a simple power law relationship, $Nu \propto aRa^b$ was empirically derived. The process for this is described in the following subsection.

4.8.2.2.1 Method for Empirically Deriving an Expression for Natural Convection

PROMETS utilises a single temperature node to describe cylinder-specific block coolant temperature. Thus the total number of coolant nodes for the TCE is three. A weighted wall temperature is, in effect, used to determine the overall heat transfer coefficient across the cylinder wall. Therefore, a singular metal and adjacent coolant temperature profile has been used to extrapolate a Nusselt-Raleigh relationship.

Heat transfer rates were calculated utilising thermocouple readings for metal situated 40mm from the flame-deck (FFD). Due to the absence of a thermocouple opposite the metal, the coolant temperature at the centre and situated opposite the metal thermocouple was linearly extrapolated from thermocouple data from measurements taken at 30 and 60mm FFD. Measured and extrapolated metal and coolant temperatures were then used as characteristic temperatures to determine the properties and dimensionless numbers described on Table 6. A quasi-static approach was used to solve for the change in internal energy of the fluid.

$$Q_{c,natural} = -mc_v \frac{\partial T}{\partial t} \quad \text{Equation 52}$$

The total mass, m , of fluid contained around each cylinder was approximated by dividing the total volume of liquid in the block by the number of cylinders. Where $\frac{\partial T}{\partial t}$ was monitored over one second intervals. The heat transfer coefficient was resolved next by re-arranging the expression for Newton's Law of Cooling:

$$h_{c,natural} = \frac{Q_{c,natural}}{A_{local} \cdot \Delta T} \quad \text{Equation 53}$$

Where ΔT is the temperature difference between the cylinder wall and the coolant temperature; A_{local} is the total surface area around the cylinder wall assuming a uniform temperature. Heat losses from the coolant to the outer block wall to ambient air significantly less. As such with a heat transfer coefficient a magnitude or two lower through the cooler wall compared to that of the hotter wall the heat transfer could be considered negligible. With this, the expression for the lateral surface area of a cylinder with height 0.085m and width 0.077m was used to calculate the surface area of the cylinder wall. An experimental Nusselt number was calculated based on this dimension using the expression shown below:

$$Nu = \frac{h_{c,natural} \cdot L_{cavity}}{k_{coolant}} \quad \text{Equation 54}$$

Figure 33 shows the log-log plot of the experimental Nusselt-Rayleigh resulting in the following relation:

$$Nu \approx 0.54 Ra_L^{0.17} \quad \text{Equation 55}$$

Expressions with an exponent of $\frac{1}{4}$ are indicative of laminar flow while turbulence is described by an exponent closer to $\frac{1}{3}$ [4.19]. The empirically derived exponent of 0.1738 indicates that laminar flow is present near the centre of the cavity although turbulence may exist between the metal and coolant interface.

The influence of each modelled element temperature was weighted by comparing the individual surface area exposed to the coolant against the total surface. For this particular engine, five cylinder-wall elements of varying temperature were in contact with coolant situated in the block. Thus the uniform wall temperature used to calculate the heat transfer coefficient is described by:

$$T_{avg,cyl} = aT_{ele,7} + bT_{ele,8} + cT_{ele,9} + dT_{ele,10} + eT_{ele,11} \quad \text{Equation 56}$$

Where $a = 6.235\%$, $b, c, d = 29.97\%$ and $e = 3.835\%$. The influence of the modelled cylinder wall temperature on the heat transfer coefficient is centrally biased $\sim 42.5\text{mm}$ FFD. Good agreement exists between empirical and modelled block coolant properties, dimensionless numbers and heat transfer, shown in Figure 34 (A-J).

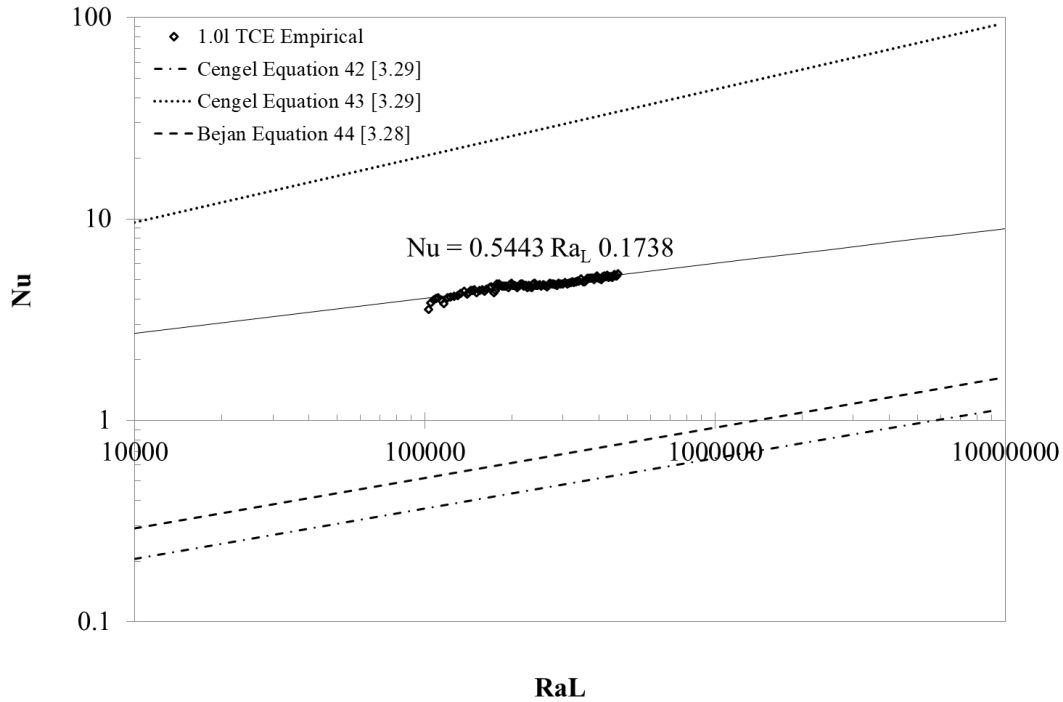


Figure 33: Log-log plot of measured Nusselt and Raleigh numbers used to derive a power law relation for the heat transfer coefficient for internal natural convection for $N = 1000 - 2500\text{rpm}$, $T_b = 1 - 44\text{Nm}$.

4.8.2.3 Validation over Steady-State and Drive Cycle Applications

Second-by-second comparisons of the quiescent coolant temperature resulting from expressions provided in literature and that shown in Equation 55 for a warm-up are shown in Figure 35. Applying the analytically derived expression, Equation 55, correlates well with the rate of change in temperature while changes in gradient due to oscillations in torque are also very well mimicked. This is analogous to changes in the heat transfer coefficient. Using equation 42 and 43 in PROMETS underestimates and overestimates the heat transfer coefficient respectively. Instead of applying the characteristic dimension, H (i.e. cavity height), for Equation 44 as suggested by [4.8], good agreement with experimental data is instead observed when using L (i.e. the cavity width) as the characteristic dimension. Due to uncertainty in applying the cavity width as the characteristic length Equation 55 was used for modelling purposes.

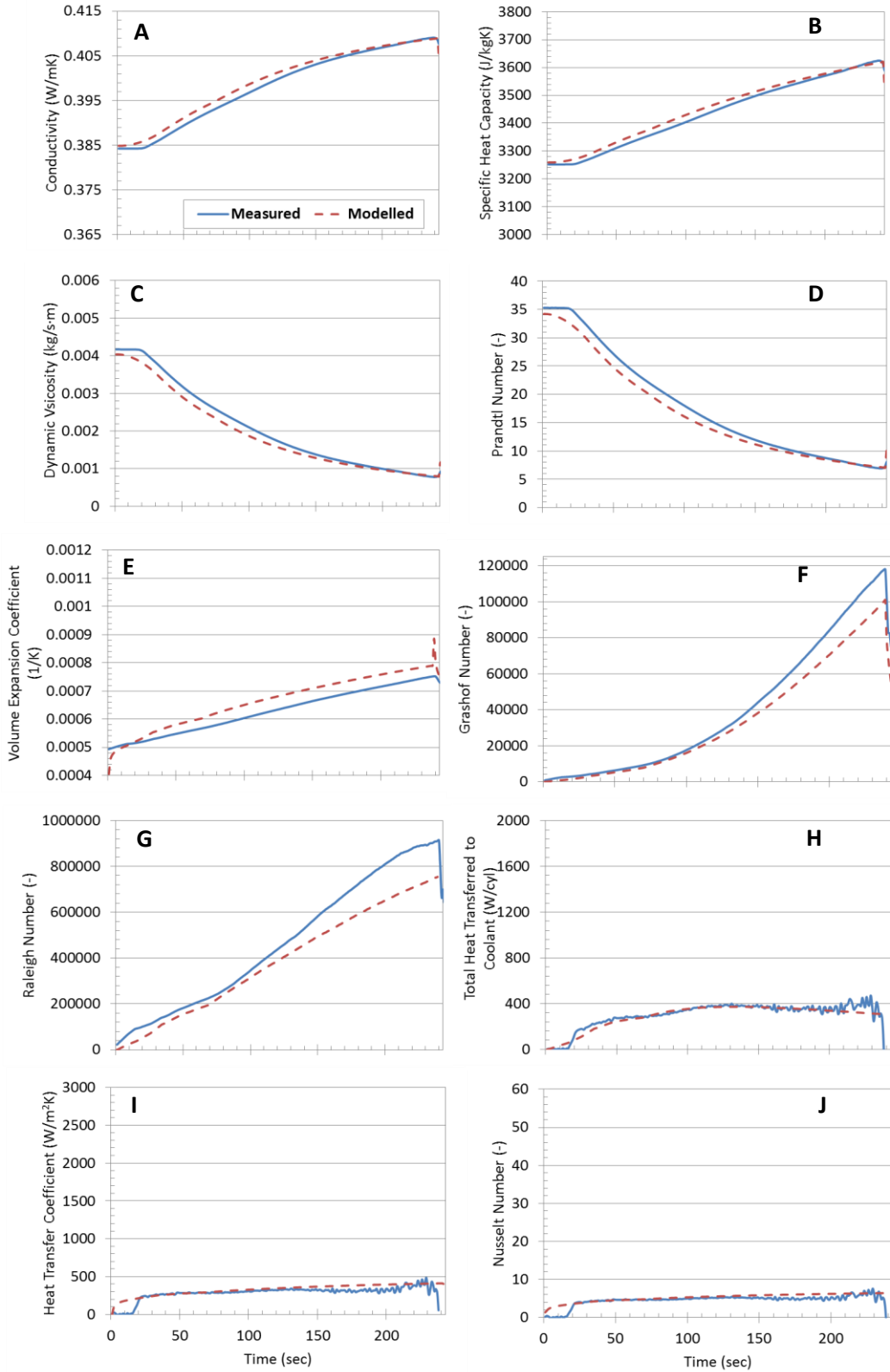


Figure 34: Modelled and measured coolant properties and dimensionless numbers for a warm-up at $N = 1000 - 2500\text{rpm}$, $T_b = 1 - 44\text{Nm}$. Block thermostat opens at $t = 236$ seconds.

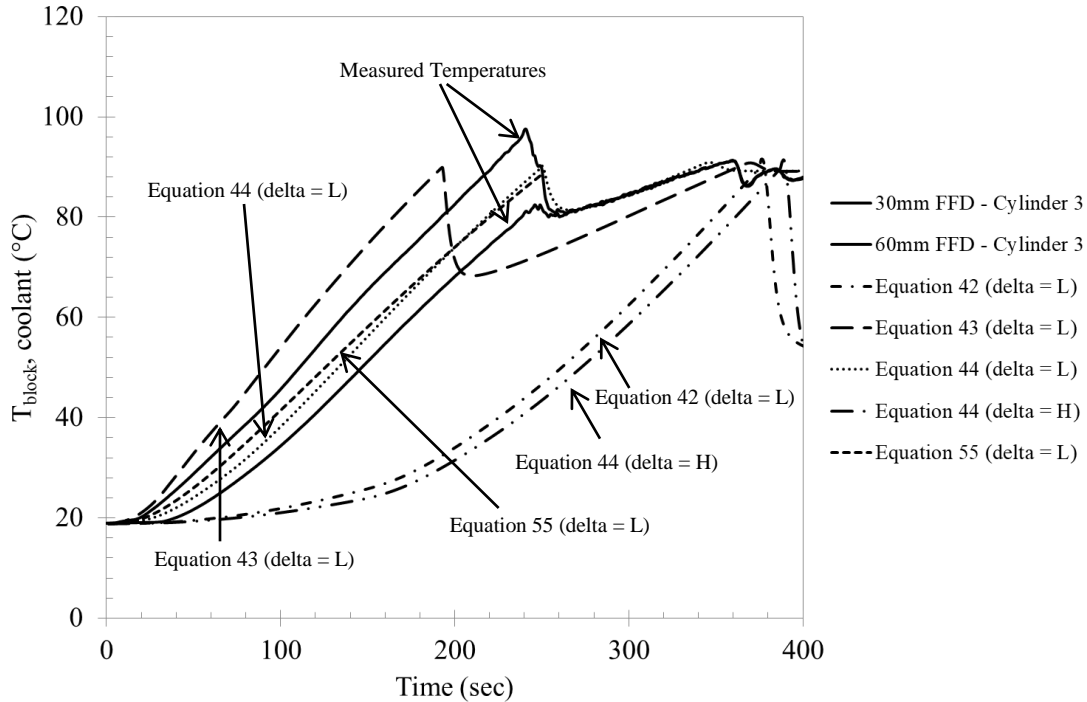


Figure 35: Second-by-second comparison of measured (30mm and 60mm FFD) and modelled coolant temperatures using literary and the analytical $Nu \propto 0.54 Ra_1^{0.17}$ relations for $N = 1000 - 2500\text{rpm}$, $T_b = 1 - 44\text{Nm}$.

Measured coolant volumes were represented and adjusted for modelling purposes. In-engine coolant volumes were acquired through manufacturer supplied CAD models. The percentage split of coolant volume between segregated intake and exhaust sides of the head were determined by filling and draining processes prior to installing the engine on the test-bed at the University of Nottingham. A comparison of the modelled and measured coolant volumes before, Figure 36 (A), and after the block thermostat is opened, Figure 36 (B), are illustrated for steady-state and transient set-ups.

The modelled volume passing through the exhaust side of the head, i.e. 1.3 litres, is in perfect agreement with the measured volume. A larger discrepancy exists during the quiescent phase where the block volume is nearly doubled, ~95% increase, for steady-state operation. This is further increased to ~150% for transient operation when correlating with rig data originating from BP. The large discrepancy is primarily due to the 0D lumped capacity nature used to model the block volume. This is a weakness in the modelling approach employed. However, for the envisaged purpose of observing warm-up rate changes due to cylinder deactivation, increasing the dimensionality of the model was not required. Comparisons of predicted and experimental variations in oil and coolant temperatures over the NEDC are given in Figure 37 (A), (B) and (C).

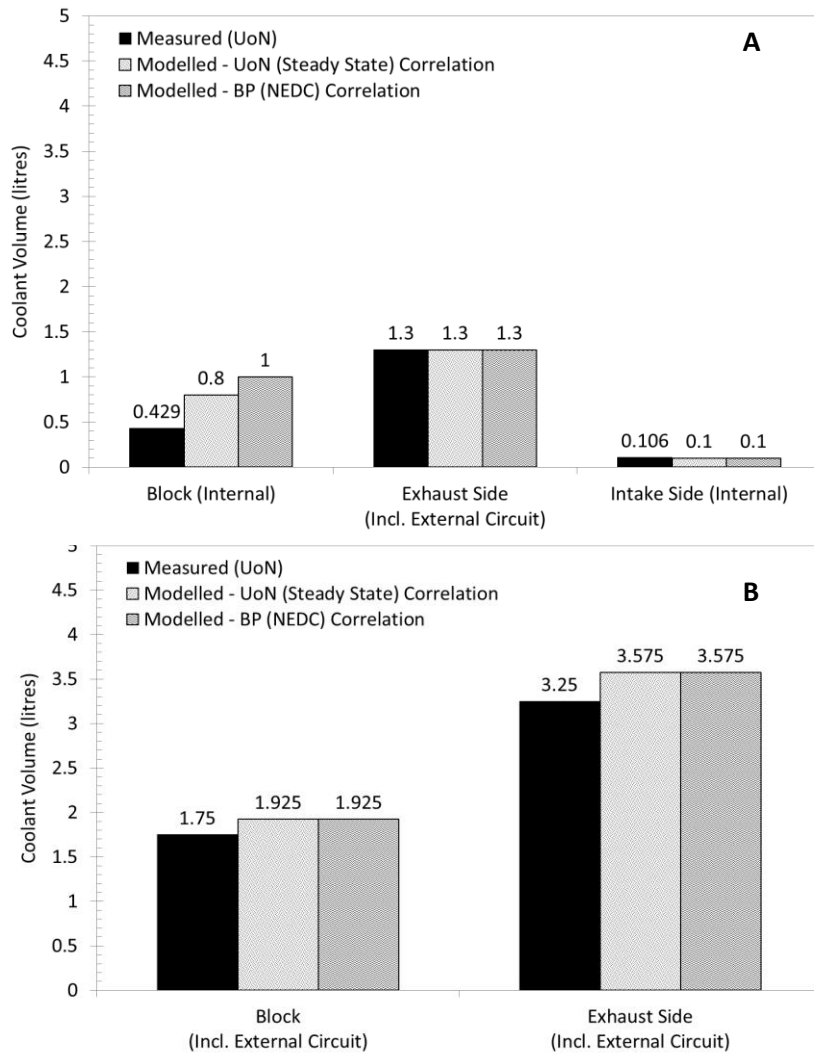


Figure 36: Comparison between measured and modelled in-engine and external coolant volumes (A) before and (B) after the block thermostat opens based on the in-house test-bed.

Figure 37 (A) shows the variation of oil temperature in the engine main oil gallery, (B) shows the coolant temperature in the block bypass to the pump inlet and (C) the coolant temperature in the block. The agreement between predicted and experimental data is good, including the times at which the first and second thermostats open. The opening points at ~200s and ~900s, respectively, are marked by the changes in the rate of coolant temperature change which can be seen in Figure 37 (C).

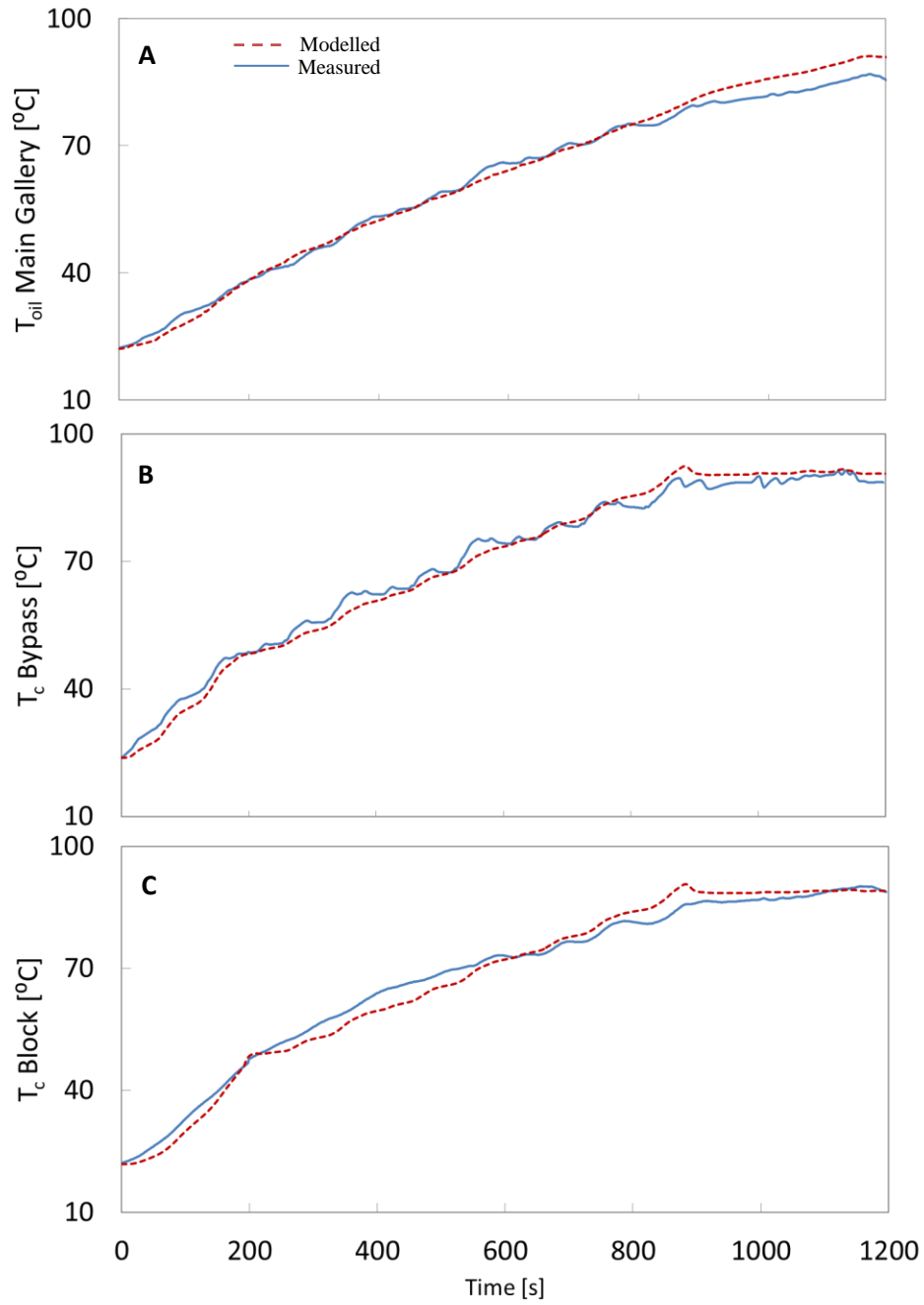


Figure 37: Modelled and experimental (A) oil main gallery, (B) bypass coolant and (C) block coolant passage warm-up rates for the NEDC (supplied by BP).

4.9 Piston Cooling Jet Heat Transfer

In PROMETS pistons are represented using two elements segregating the piston crown and skirt. The respective element numbers are 23 and 24 as seen on Figure 12. As combustion ensues, heat propagates from the piston crown to two components, the connecting rod and cylinder wall. Heat directed towards the connecting rod passes through the piston skirt, connecting rod pin and down to the connecting rod. The cylinder wall on the other hand receives heat from the piston crown through physical contact with the piston rings. In the TCE the presence of an oil jet impinging on the lower surface of the piston crown and the interior of the piston skirt reduces heat transfer to the cylinder liner and connecting rod. Instead heat is stored in the oil splashing down past the crankshaft assembly down to the sump. A brief explanation of the theory behind the piston cooling jets (PCJs) is described in this subsection based on more thorough studies conducted by *Law* [4.24] and *Easter et al* [4.25]. With this a comparison of the modelled and experimentally obtained heat transfer coefficients are compared for model validation purposes. Validation is ensued in light of assuring that robust predictions of the piston temperatures are obtained when enabling piston cooling jets with cylinder deactivation.

4.9.1 Piston Cooling Jet Discharge and Heat Transfer Coefficient

Describing heat transfer from the piston to the oil cooling jet is a complex task [4.24] outside the scope of this study. A cycle averaged solution as described in the work of *Law* [4.24] and *Easter et al* [4.25] has been used for this instance of PROMETS, as has been done in previous versions. Although this is a simplification of the actual phenomenon it is important to capture the volume flow-rate of oil passing through the jet such that the Reynolds number used to calculate the heat transfer coefficient is estimated.

As oil travels from the main oil gallery into the L-shaped nozzle directing a jet of oil towards the piston underside a discharge coefficient is used to characterise the amount of actual oil flow through the orifice. Based on *Mian's* [4.26] observation for Reynolds numbers below 20,000 this may be expressed as a function of the ratio of the length and diameter of the orifice,

$$\frac{1}{C_d} = \frac{1}{C_{d,u}} + \left(\frac{20}{Re_h}\right) \left(1 + 2.25 \left(\frac{l_{orifice}}{d_{orifice}}\right)\right) - \frac{0.005 \left(\frac{l_{orifice}}{d_{orifice}}\right)}{1 + 7.5 \log(0.00015 Re_h)^2} \quad \text{Equation 57}$$

Where C_{du} is the discharge coefficient for fully turbulent flow with Reynolds numbers above 20,000.

$$C_{du} = 0.827 - 0.0085 \left(\frac{l_{orifice}}{d_{orifice}}\right)^{0.5} \quad \text{Equation 58}$$

Mian [4.26] and *Lichtarowicz et al* [4.27] suggest calculating the discharge coefficient without substituting for the Reynolds number with knowledge of the area of the jet at the nozzle exit given the pressure drop across the orifice, Δp ,

$$C_d = \frac{\dot{V}}{A_o \sqrt{2\Delta p / \rho}} \sqrt{1 - m^2} \quad \text{Equation 59}$$

Where m , is the ratio of diameters of the orifice supply pipe and the jet orifice $\frac{d^2}{D^2}$ and A_o is the surface area of the cooling jet nozzle. For most commercial vehicles, Reynolds numbers are within the 2000 region and therefore the discharge coefficient for cases below the 20,000 Reynolds numbers is most commonly used.

$$Re_h = \frac{d_{orifice}}{v_{oil}} \sqrt{\frac{2\Delta p}{\rho}} \quad \text{Equation 60}$$

Thus given the discharge coefficient and hydraulic Reynolds number, the volume flow-rate of the oil passing through the jet orifice is expressed by,

$$\dot{V} = \frac{C_{du} A_o}{\sqrt{1 - m^2}} \sqrt{\frac{2\Delta p}{\rho}} \quad \text{Equation 61}$$

The Reynolds number of the oil stream between the outlet of the piston cooling jet is described as the orifice Reynolds number. This is used to characterise the Nusselt number of the impinging jet for heat transfer coefficient evaluation:

$$Re_o = \frac{4\dot{V}}{\pi d_o v} \quad \text{Equation 62}$$

The Nusselt number is empirically determined and is a function of the Reynolds and Prandtl numbers satisfying the following inequalities $1000 \leq Re_o \leq 4500$, $90 \leq Pr_o \leq 115$. These inequalities are confined for jet heights and orifice diameters in the range of $45 \leq z/d_o \leq 95$. For fully warm conditions *Easter et al* [4.25] describe the following Nusselt expression, i.e. $T_{oil} = 90^\circ\text{C}$,

$$Nu = 0.066 \left(\frac{z_{orifice}}{d_{orifice}} \right)^{-0.034} Re_o^{0.541} Pr^{0.4} \quad \text{Equation 63}$$

For conditions inclusive of warm-up and fully warm oil temperatures the following relation may be used again for the same Reynolds, Prandtl and jet height and orifice diameter ratios $1000 \leq Re_o \leq 4500$, $90 \leq Pr_o \leq 750$ and $45 \leq z/d_o \leq 95$ respectively,

$$Nu = 0.028 \left(\frac{z_{orifice}}{d_{orifice}} \right)^{-0.034} Re_o^{0.652} Pr^{0.4} \quad \text{Equation 64}$$

The heat transfer coefficient may then be determined by re-arranging the expression for the Nusselt number,

$$h_{pcj} = Nu \frac{k_{oil}}{d_{orifice}} \quad \text{Equation 65}$$

The formulae used in PROMETS defining the piston underside areas defined by *Law* [4.24] refer to a circular topography while the actual contact area for the oil jet is significantly less given the design of the pistons. The expressions based on work by *Law* [4.24] shown below have been halved to equate to more accurate areas,

$$A_{underside_crown} = 0.5 \frac{\pi}{4} (B - 2t_s)^2 \quad \text{Equation 66}$$

$$A_{underside_piston} = 0.5 \pi (B - 2t_s)(d_p - t_c) \quad \text{Equation 67}$$

Where t_c is the crown thickness, d_p is the depth of the piston, t_s is the thickness of the skirt.

4.9.2 Piston Cooling Jet Model Validation

The Nusselt number expression for conditions inclusive of warm-up and fully warm oil temperatures were found to give the most sensible modelled heat transfer coefficients. The agreement between the heat transfer coefficient found by *Easter et al* [4.24] for differing jet heights, and those modelled in PROMETS are shown on Figure 38 (A). Small oscillations are present for the modelled data due to the variation in brake load and thus heat transfer coefficient. Comparisons of modelled and experimental Reynolds number, at the jet orifice, and Nusselt number are shown in Figure 38 (B).

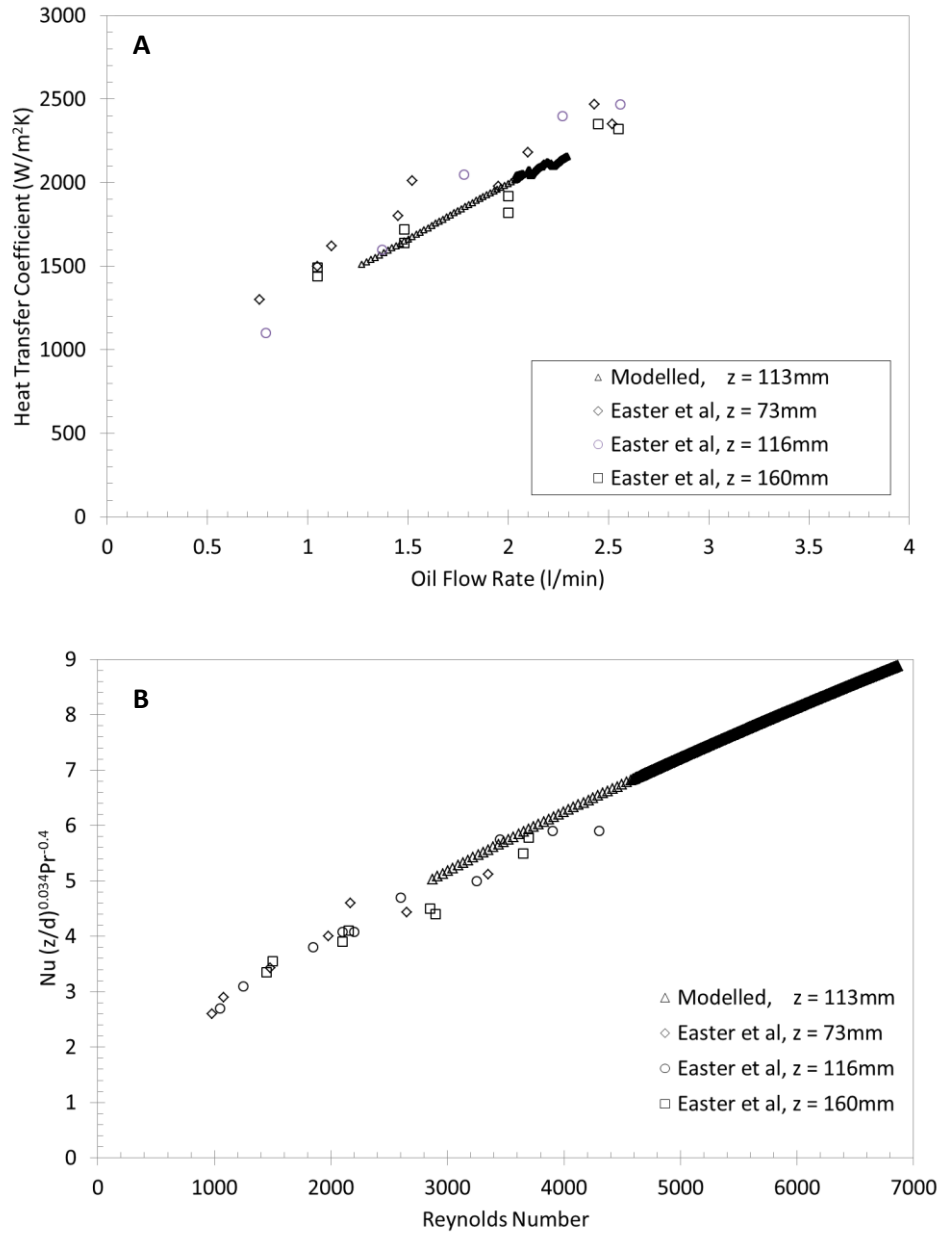


Figure 38: Comparison between model outputs and findings reported by *Easter et al* [4.24] (A) for piston cooling jet heat transfer coefficient and (B) relationship between Nusselt number expression and orifice Reynolds number.

4.10 Revised Fuelling and Intake Manifold Pressure Estimation

Historically PROMETS engine models specific to gasoline fuel have been tailored to non-turbocharged, naturally aspirated, intake systems. The only model tailored to a turbocharged gasoline engine relied on an empirically based formulation specific to the NEDC [4.28]. Model outputs were however non-generic. For this modelling instance, appropriately estimating the intake manifold pressure past the throttle was required such that fuel consumption benefits due to reduced pumping losses be robustly predicted. Given this requirement, this subsection defines a simple expression used to predict the intake manifold pressure; corrections based on empirical formulations for warm-up and fully-warm conditions; and validation of predicted pumping losses over four drive cycles are complemented with comparisons in second-by-second and cumulative fuel consumption.

4.10.1 Method for Estimating Turbocharged Intake Manifold Pressure

K. Zinner [4.29] developed an estimate for the boosted intake manifold pressure specific to diesel engines but applicable to any turbocharged engine. The derivation of the expression stems by initially referring to the cylinder volumetric efficiency of the engine, defined as the ratio of the volume of trapped air over the swept volume of the cylinder,

$$\eta_v = \frac{\frac{m_{tr}}{\rho_I}}{V_s} \quad \text{Equation 68}$$

The net indicated work is related to the volumetric efficiency through the following expression:

$$W_I = IMEP_g V_s \quad \text{Equation 69}$$

A relation between the gross indicated thermal efficiency, combustion efficiency and lower heating value of the combusted fuel is found through the following expression:

$$W_I = Q_{LHV} \eta_I \eta_c \quad \text{Equation 70}$$

Where the intensive form of the term for the lower heating value of fuel is:

$$Q_{LHV} = q_c m_f \quad \text{Equation 71}$$

Given two terms that equate to the net indicated work, Equation 69 and Equation 70, the lower heating value of gasoline may be expressed in terms of combustion efficiency, gross indicated thermal efficiency, net indicated mean effective pressure and engine swept volume. The mass flow-rate of air is assumed to account for EGR in this case and the net amount of fresh air needed may be calculated if calibration based EGR values are known. With this, utilising an intensive form of the lower heating value the volumetric efficiency may also be brought into the expression as shown:

$$Q_{LHV} = q_{LHV} \frac{m_a}{\lambda \cdot AFR} = \frac{q_{LHV} \eta_v V_s \rho_I}{\lambda \cdot AFR} \quad \text{Equation 72}$$

Equation 72 may then be equated with the definition of the lower heating value based on an indicated mean effective pressure and gross indicated thermal efficiency. Thus an expression for the gross indicated mean effective pressure in terms of volumetric efficiency, gross indicated thermal efficiency, combustion efficiency and intake air density for a given AFR results:

$$Q_{LHV} = \frac{IMEP_g V_s}{\eta_I \eta_c} = \frac{q_{LHV} \eta_v V_s \rho_I}{\lambda AFR}$$

$$\therefore IMEP_g = \frac{q_{LHV} \eta_v \eta_I \eta_c \rho_I}{\lambda AFR} \quad \text{Equation 73}$$

Substituting for the density form of the perfect gas equation in terms of intake manifold pressure, charge temperature and gas constant substituted to equate to the intake manifold pressure a simple relationship between the gross indicated mean effective pressure $IMEP_g$ and intake manifold pressure is thus shown,

$$IMEP_g = \frac{q_c \eta_v \eta_I \eta_c \frac{p_I}{RT_I}}{\lambda AFR}$$

$$p_I = \frac{IMEP_g \lambda AFR R T_I}{q_c \eta_v \eta_I \eta_c} \quad \text{Equation 74}$$

An iterative solution for the pumping mean effective pressure is required to appropriately estimate the intake manifold pressure. Direct calculations are badly conditioned to large errors requiring several iterations of the calculation such that the solution converges. It must be noted that the above expression does not segregate scavenging of air from the induced air charge. Thus the expression would have to be re-written subtracting the scavenged air in effect reducing intake pressure. The combustion efficiency and gross indicated thermal efficiency generally vary little once engine loads are marginally above idling conditions. An accurate estimate of cylinder volumetric efficiency is however required to calculate appropriate intake manifold pressures.

4.10.2 Cylinder Volumetric Efficiency Estimation

The ideal volumetric efficiency is dependent on compression ratio, exhaust and intake charge pressures (i.e. dependent on engine brake load) [4.30] and engine speed.

$$\eta_{vol,ideal} = \frac{1 + \gamma(r_c - 1) - \left(\frac{p_{ex}}{p_m}\right)}{\gamma(r_c - 1)} \quad \text{Equation 75}$$

However, standing alone, this expression is not typified for an engine and thus specific corrective functions must be added. The correction functions are based on engine speed, $fn_a(N)$, and intake manifold pressure, $fn_b(p_m)$, such that the product,

$$\eta_{vol} = \eta_{vol,ideal} f n_a(N) f n_b(p_m) \quad \text{Equation 76}$$

may be calibrated to account for waste-gate position, compressor and turbine characteristics, valve timing (i.e IVO and EVO), AFR and fuel vaporisation effects. The functions $f n_a(N)$ and $f n_b(p_m)$ have been defined for fully warm engine thermal state.

$$f n_a(N) f n_b(p_m) = \frac{\eta_{vol}[N,p_m]}{\eta_{vol,ideal}} \quad \text{Equation 77}$$

$\eta_{vol}[N,p_m]$ are volumetric efficiency values calculated based on conditions in the intake manifold. Corrections for the effect the intake port metal temperature, strongly bound by coolant temperature, and intake air charge temperature on the intake charge density follows from *Taylor* [4.31].

$$\frac{\eta_{vol,fw}}{\eta_{vol}} = \frac{T_c+1111}{T_{c,fw}+1111} \quad \text{Equation 78}$$

$$\frac{\eta_{vol}}{\eta_{vol,ideal}} = \sqrt{\frac{T_m}{T_{m,ideal}}} \quad \text{Equation 79}$$

Where the final form of the volumetric efficiency, accounting for engine speed and intake manifold based corrections dependent on engine calibration along with intake manifold and coolant temperature corrections results in the following expression:

$$\eta_{vol} = \eta_{vol,ideal} f n_a(N) f n_b(p_m) \sqrt{\frac{T_m}{T_{m,ideal}}} \frac{T_c+1111}{T_{c,fw}+1111} \quad \text{Equation 80}$$

Shown in Figure 39 (A) is the speed based correction function and Figure 39 (B) the intake manifold based correction function acquired from a collection of data sourcing from BP for the 1.0litre three cylinder engine from NEDC, FTP-75, US06 and HWFET drive cycles (i.e. for conditions up to 3500rpm and 2.15barA).

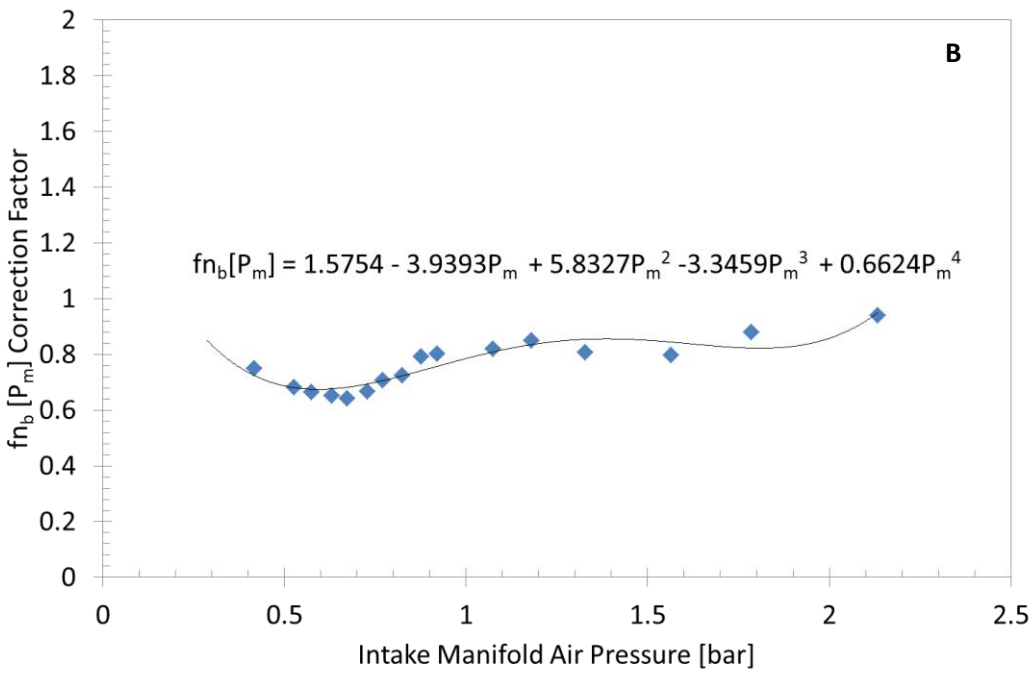
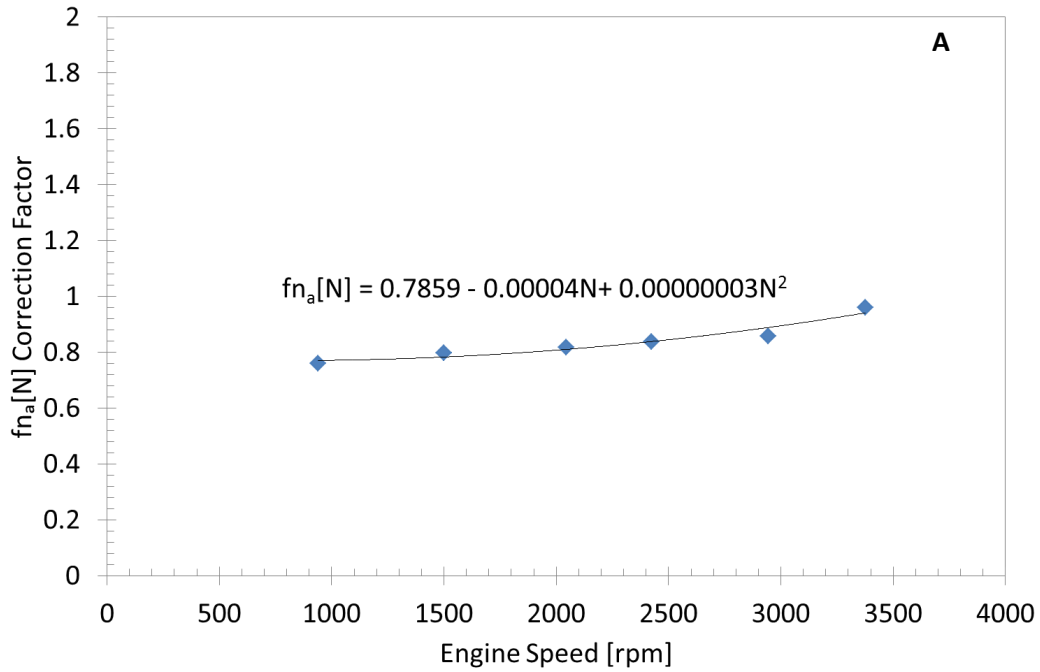


Figure 39: Volumetric efficiency corrective functions based on (A) engine speed $fn_a[N]$ and (B) intake manifold air pressure $fn_b[N]$. Characteristic of curve on plot (B) is specific to calibration of the waste-gate on the turbocharger.

4.10.3 Iteration for Intake Manifold Pressure and Fuel Consumption Prediction

A residual based iterative calculation, inserted into PROMETS in a c code script, predicts the fuel mass flow-rate, intake manifold pressure and pumping losses. The intake manifold pressure and volumetric efficiency are calculated using the methods described above. The exhaust gas pressure is referred to from a look-up table based on throttle position and waste-gate position (i.e. a function of brake torque and engine speed). Variations in exhaust pressure are generally significantly smaller compared to variations in intake pressure; in the range of 0.5 barA compared to 2barA. Thus the largest source of error in estimating pumping losses stems from the intake manifold pressure calculation. Implementing the iterative solution summarised in Figure 40, an estimate of the cylinder volumetric efficiency was made. The complete calculation process is shown in Appendix B, in a c-script format.

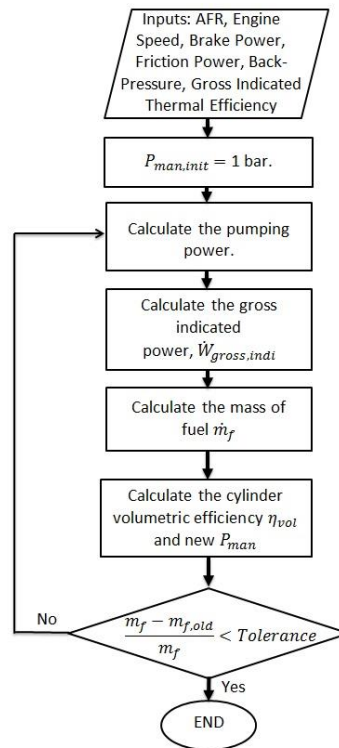


Figure 40: Residual convergence based iterative solution for the estimation of the intake manifold pressure and fuel consumption.

4.10.3.1 Validation of Predicted Intake Manifold Pressure and Fuel Consumption

Figure 41 (A) and (B) show the agreement between the measured and modelled volumetric efficiency over a warm-up process on the NEDC. Model predictions for the intake manifold pressure show good agreement with measured pressures as shown on Figure 42 (A). Although the exhaust manifold pressure is assigned through a look-up table, pumping work losses also agree very well with experimental data as shown for the NEDC, FTP-75, HWFET and US06 on Figure 42 (B). Second-by-second comparisons of

the intake manifold pressure and pumping mean effective pressure are shown in Appendix C on Figures 91 and 92 for the NEDC, FTP-75, HWFET and US06. 70% of PMEP data points lie within a $\pm 10\%$ error margin with 80% of the points lying in the $\pm 15\%$ error margin. In turn with the friction model calibrated to the TCE, robustness in the pumping losses the model proves to estimate fuel consumption over modal and transient drive cycles within -5% and -10% respectively. The model is validated in this respect by comparing instantaneous and cumulative fuel consumption over the NEDC and FTP-75 as shown on Figure 43 (A) and (B) respectively.

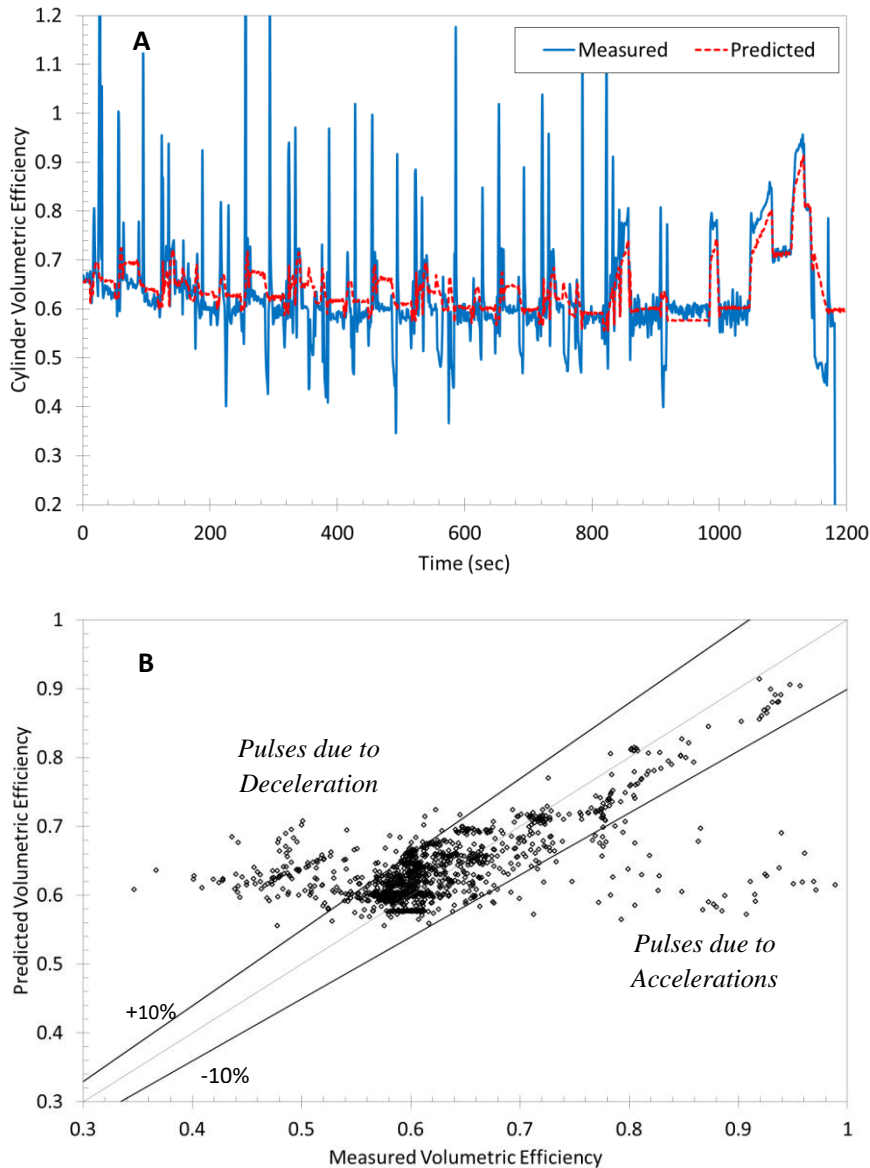


Figure 41: Comparison between modelled and measured (BP based on lambda sensor) cylinder volumetric efficiency over the NEDC on a (A) second-by-second basis and (B) measured versus modelled axes with $\pm 10\%$ bands. Measured mass flow-rate is calculated based on a lambda sensor reading and multiplied by the fuel flow-meter values on a second-by-second basis.

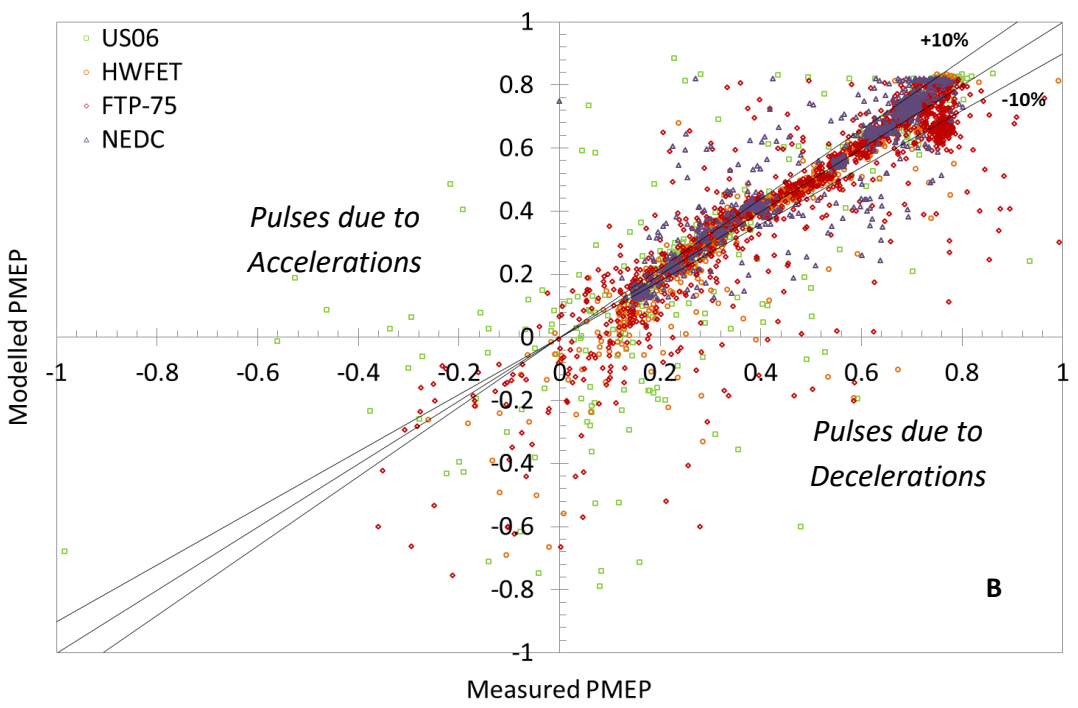
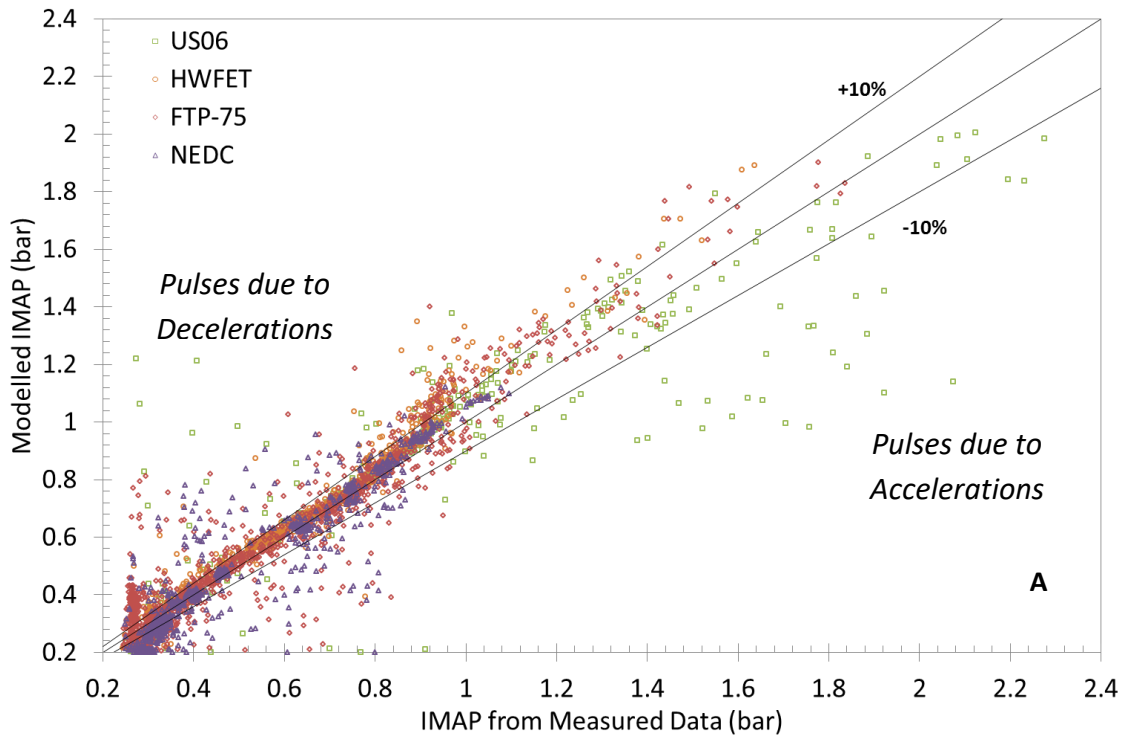


Figure 42: Modelled and measured (A) intake manifold pressures and (B) pumping mean effective pressures for the NEDC, FTP-75, HWFET and US06.

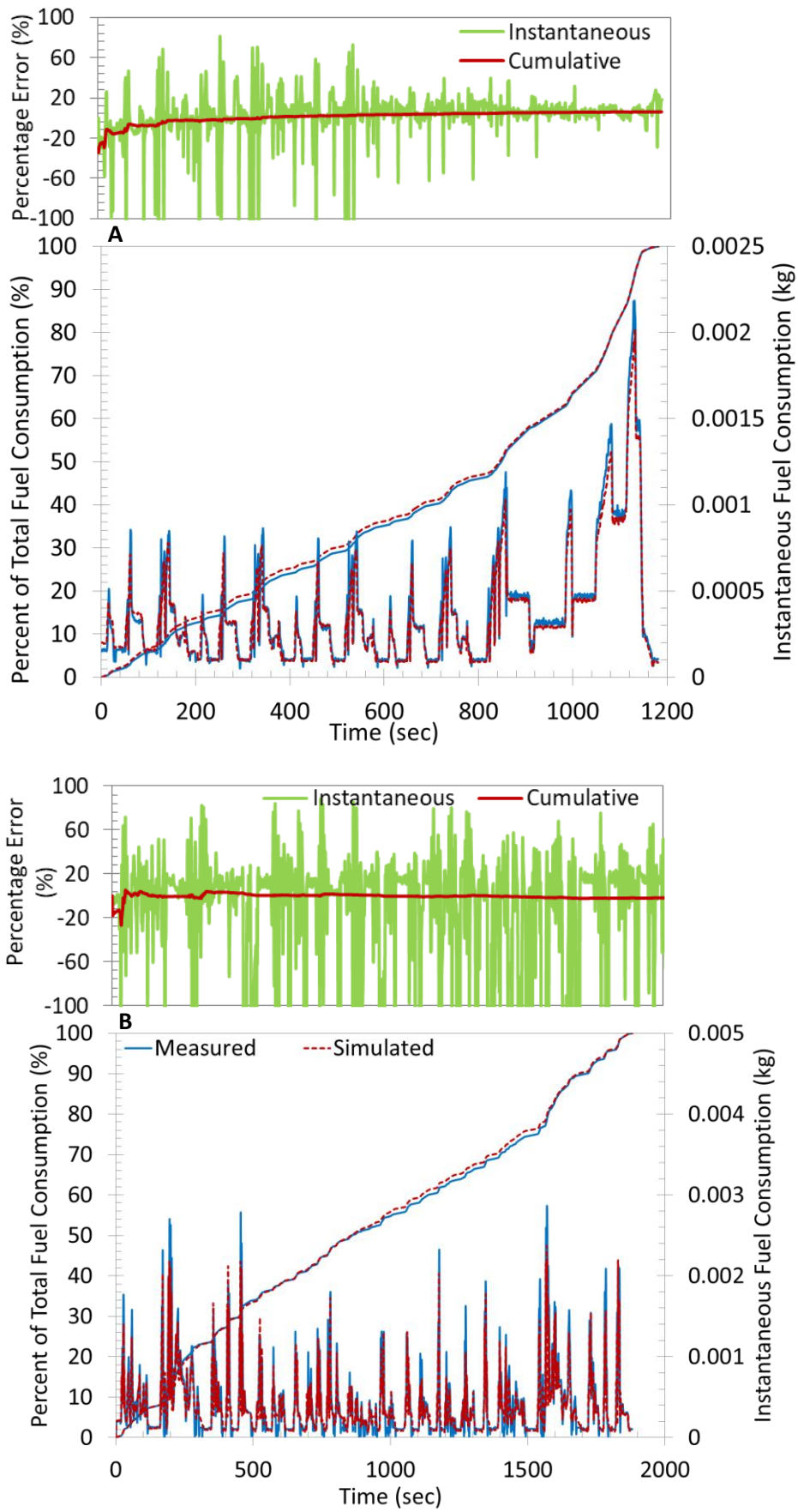


Figure 43: Simulated and experimental fuel consumption for the (A) NEDC and (B) FTP-75.

4.11 Estimating the Work Done on the Gas in a Deactivated Cylinder

4.11.1 Incentive for Estimating Motoring Work Penalty

The form of cylinder deactivation considered here shuts off gas exchange by leaving intake and exhaust valves closed, effectively sealing the cylinder, and disables fuel injection electronically. The trapped gas in the cylinder is compressed and expanded every engine revolution. The compression and expansion processes adjust within a small number of cycles to establish repeating closed pressure-volume figures. The cylinders are not perfectly sealed due to piston blow-by and leakage passed valves. Gas transfer occurs out of the cylinder when cylinder pressure is high and into the cylinder when pressure is low. The work required to motor the deactivated cylinder represents a performance penalty which needs to be accounted for in weighing the benefits and disadvantages of deactivation through PROMETS. Although *Leone and Pozar* [4.32] reported that the work penalty is small, representing a penalty of around 0.02 bar IMEP, this was left to be confirmed.

4.11.2 Procedure for Measuring Reduction in Bottom Dead Centre Pressure

Prior to estimating the work loss associated in motoring a cylinder the procedure to accurately measure this using a proto-type engine was established.

Different methods exist for measuring the in-cylinder pressure in an internal combustion engine. Three types of transducers exist: a differential pressure transducer, absolute pressure transducer and gauge pressure transducer [4.33]. Differential transducers were installed on the TCE to measure in-cylinder pressures. Typically a reference BDC pressure, serving as a nominal value, is assigned during the intake stroke. The reference in this case is the intake manifold air pressure. Any difference in measured pressure is cumulatively added or subtracted with reference to this pressure. The BDC value is refreshed every second cycle and this process is known as ‘pegging’. In order to observe if significant mass loss took place through blow-by, the pressure transducers were unpegged. Thus the transducer value was left to float such that the BDC pressure would initially increase, specifically after combustion while trapping an exhaust charge, and then reduce with time. An example of the initial degradation in the in-cylinder pressure, while trapping an exhaust charge, is shown on Figure 44.

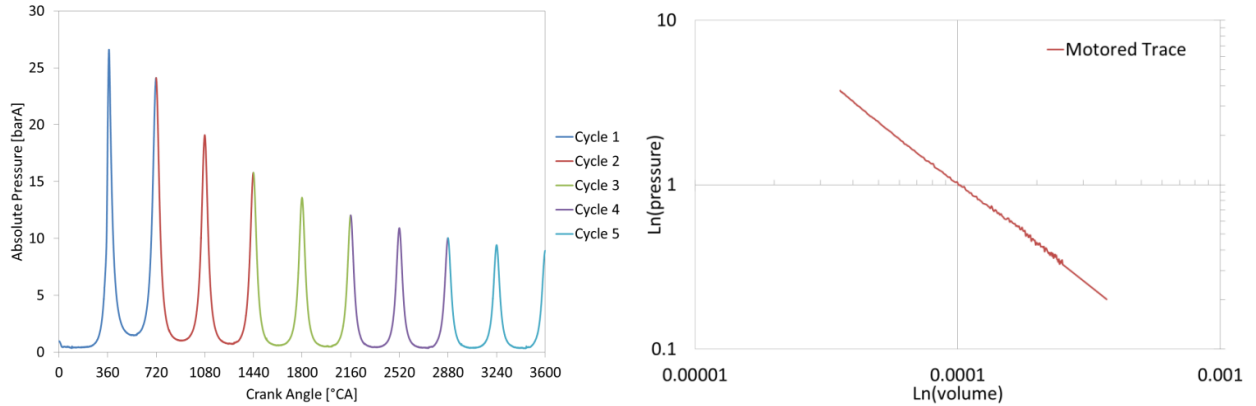


Figure 44 (left) and 44.1 (right): (Left) Reduction of BDC pressure measurement during deactivation when *unpegging* the pressure transducers to intake manifold air pressure values. (Right) Measured stabilised trace for an expansive process in a motored cylinder ($N = 1500\text{rpm}$, $T_b = 20\text{Nm}$, cycle no. 607).

For differential transducers the pressure may drift due to changes in temperature. The effect of drift over an extended number of cycles is difficult to understand as this is specific to the transducer. However, the reduction in BDC pressure for an unpegged trace may be verified against the reduction in TDC pressure for a stabilised pegged trace. The shift or decline in the BDC pressure for the motored cylinder is equated to the reduction in TDC pressure for the pegged trace and is generally applicable past 220 cycles when the trace stabilises. Note that this is specific to trapping an exhaust gas charge where the settling time is longer compared to trapping a fresh air charge. In effect, this method showed that BDC pressures reached sub-atmospheric levels thus creating a partial vacuum close to 0.1 barA. An example of a stabilised motored pressure trace during an expansive stroke is shown on Figure 44.1. The effect of heat and mass loss is past the time frame given for predicting effects of cylinder deactivation on engine performance. Therefore, for this thesis the subject is not regarded in great detail since the net mass remaining after stabilisation was required to calculate the work loss. This process is shown in the following subsection. Instead this is discussed in an experimental paper due for publication in the IMechE Part D: Journal of Automotive Engineering sometime in 2018.

4.11.3 Work Done on the Gas in the Deactivated Cylinder

Neglecting the losses associated with mass transfer into and out of the cylinder after the early transient conditions have settled, the dissipated work per revolution is the difference between work done on the trapped gas during the compression and expansion strokes. Because this difference is small, a direct calculation is badly conditioned to small errors in the values of the polytropic indices. More robustly, the total work dissipated can be equated to the heat transferred from the gas. The direction and magnitude of heat transfer are the same for both the compression and expansion strokes, and over the two

strokes is approximately twice the heat transfer during the compression stroke. Treating the cylinder as a closed-system the work done on the gas during the compression process [4.34]:

$$W = -m \int_1^2 p dv = \frac{-m(p_2 v_2 - p_1 v_1)}{(1-n)} \quad \text{Equation 81}$$

Substituting this value into the equation defining the First Law of Thermodynamics, with heat transfer *from* the gas taken to be positive:

$$W = Q + \Delta U$$

and expanding the internal energy term in its extensive form:

$$Q = -\frac{m(p_2 v_2 - p_1 v_1)}{1-n} - m c_v (T_2 - T_1) \quad \text{Equation 82}$$

Substituting for the specific heat capacity at a constant volume:

$$Q = mR(T_2 - T_1) \left(\frac{\gamma - n}{(n-1)(\gamma-1)} \right)$$

If the temperature change over the expansion is the same as during the compression, then over the compression and expansion strokes of one engine revolution:

$$\oint W = -\oint Q_{rev,n} = -2mR\Delta T \left(\frac{\gamma - n}{(\gamma-1)(n-1)} \right) \quad \text{Equation 83}$$

Where m is the trapped mass at BDC, γ the adiabatic index, n the polytropic index, R the gas constant for air and ΔT the estimated difference between the top dead centre and bottom dead centre temperatures. An estimate of the trapped mass according to the pressure values shown in Figure 45, is calculated assuming an ideal gas and no losses of mass within the revolution:

$$m_{trapped} = \frac{p_{BDC} v_{BDC}}{R T_{BDC}}$$

Where p_{BDC} is the pressure, T_{BDC} is the temperature (approximated to 400K) and the v_{BDC} cylinder volume at the BDC (the cylinder swept volume is of 333cc). Quantification of the net work loss when motoring a cylinder is set in Figure 46, for varying polytropic indices from an adiabatic reversible process, i.e. $n = 1.4$, tending towards an isothermal process, i.e. $n = 1$. Indices between 1.34 and 1.36 applied to Equation 83 result in a net work loss of roughly 2.2 to 3.2 Joules/rev which is consistent with findings in *Leone et al* [4.32]. Net-work losses calculated by integrating the area between measured expansion and compression strokes also resulted in a parasitic loss of ~ 0.02 bar IMEP (i.e. 2 Joules/rev). Experimental log-log traces for pressure and volume show that the polytropic index is between 1.34 and 1.36, agreeing with the experimentally calculated values. Care must be taken when extrapolating gradients from log-log traces that are prone to noise. The inferred polytropic index is very sensitive to oscillations in the trace

resulting from noise. It was noticed that the experimental trace is devoid of noise near top dead centre conditions typically between 0 and 25°CA aTDC. Therefore the index was typically extrapolated close to TDC. Due to the time-averaged approach used in the model, the penalty associated when enabling deactivation was taken to occur instantaneously.

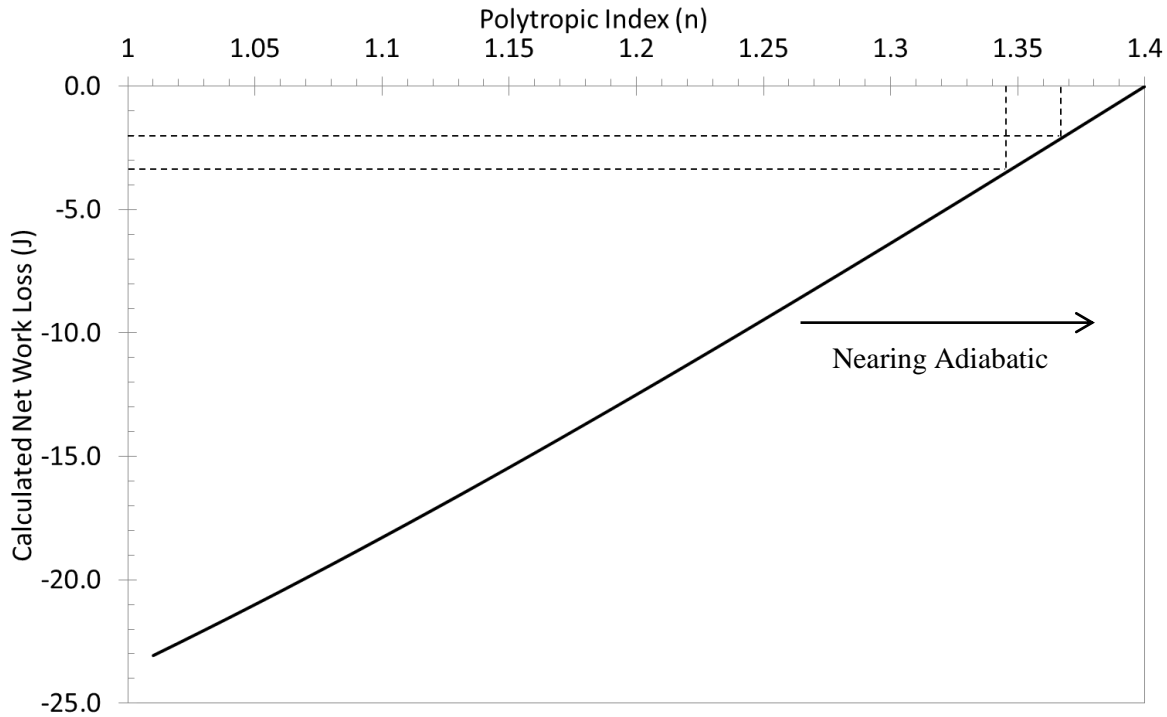


Figure 45: Calculated net-work loss when motoring a piston for $T_{BDC} = 400K$ and $p_{BDC} = 0.23barA$ used for mass calculations for a 367cc cylinder capacity (incl. $V_{clearance}$).

4.11.4 Estimated Mass Loss When Trapping an Exhaust Charge

The percentage of the initially total induced mass lost through blow-by or due to leakage past imperfect sealing of the valves against the valve seats from the onset of deactivation to the cycle prior to re-activation is of interest. Suction of oil from the crankcase, which is kept near atmospheric conditions, to the combustion chamber, which is in a partial vacuum, may result in the oxidation of oil resulting in high soot and/or smoke upon reactivation. This affects the calculated work loss and combustion quality when reactivating a cylinder. Although the effects on combustion quality are not in the scope of this study quantifying the percentage of mass lost is simply calculated by observation of the BDC pressure prior to deactivation and late into the motoring process. It is important that the measured motored BDC pressure value stabilises in order to minimise errors in the calculation of the mass lost so that factors such as the cylinder wall temperature do not significantly affect the pressure. For an engine speed of 1500rpm and

brake torque of 20Nm, a 47% mass loss is observed when an initial fill condition of 0.40barA, p_{BDC} , degrades to a stabilised 0.23barA, p_{BDC} . A mass loss of up to 70% is experienced when the stabilised motored trace reduces to a BDC pressure of 0.12barA [4.34].

4.11.5 Literary Suggestions for Reducing Prolonged Partial Vacuum and Oil Suction

Acknowledging mass loss within the deactivated cylinders it has been identified that the minimum desired BDC pressure should be around 0.2barA [4.35]. These findings were published and set in the public domain during the convention when the publication based on model findings [4.34] reported in this thesis were presented. The adverse effects of allowing the in-cylinder pressure to drop down between 0 – 0.2 barA could result in suction of oil fouling the injector tip and spark plug, increased PN, CO and THC emissions [4.35]. Counter-acting the near-vacuum condition may be achieved by ventilating air by opening the intake or exhaust valves at regular intervals. This is assuming that the engine at hand is fitted with a fully variable valvetrain. It is proposed that the exhaust valves open every 10 cycles such that the hot gases maintain the cylinder wall temperature elevated although at the cost of increasing the motored loss [4.35]. Alternatively the ring pack could be designed such that ring and groove clearances are reduced, cylinder bore distortion is ameliorated, or by promoting downwards flow of oil to the crankcase by redesigning the piston land or limiting oil supply to the oil ring through drain-holes [4.36]. In essence, the simplest alternative would be to disable piston cooling jets although oil accumulation effects for the specific engine would have to be investigated.

4.12 Discussion and Conclusions

Revisions made to the multi-cylinder model of PROMETS have been described in the aim of characterising the TCE. The design of the TCE differs from previously modelled engines due to the integration of the exhaust manifold in the engine head and the addition of an advanced cooling system.

A generic representation of the IEM was required to 1) represent the mass of the engine head and 2) model heat lost from the exhaust ports to the coolant. CAD models were referred to input appropriate exhaust port lengths and represent the surface area of coolant in contact with the exhaust ports. To validate the representations, thus the accuracy of the modifications, comparisons of the head mass were made such that an appropriate thermal inertia was encapsulated. Furthermore, heat rejection to coolant was evaluated by comparison with experimental measurements over the NEDC.

As a result of the increase in the exhaust port diameter the previous Nusselt-Reynolds expression for straight port runners derived by *Shayler and Chick* [4.9] was found to under-estimate the heat losses based on comparison with experimental data. As such the constants for the C_1C_2 expression were assigned new values. The Reynolds index was augmented to 0.723, instead of 0.7, and the constants were

iteratively adjusted to $C_1 = 1.3$ and $C_2 = 2$. Although, the changes mimic well the heat transfer in the TCE from the gas to coolant in the cylinder and exhaust port, the generic applicability of these changes to other engines with an IEM has not been validated. However this does not affect the robustness of results originating from PROMETS for the TCE.

The cooling system for the TCE comprises of a split circuit. In this set-up coolant passing through the exhaust side of the head is segregated from coolant in the block and intake side of the head. During warm-up the heat transfer coefficient in the block drastically reduces as the coolant remains quiescent. However, roughly 12% of the total coolant volume is held in block and therefore the thermal inertia of the coolant is significantly less providing quicker warm-up compared to a conventional system with forced convection. Several expressions for heat transfer in the form of natural convection in a vertical rectangular enclosure exist. However the Prandtl and Raleigh inequalities for which they are suitable lay outside the bounds observed experimentally. Thus an expression was derived in a Nusselt-Reynolds power law form. The expression was found to be adequate for the lumped element thermal capacity model and validated by comparison with experimental data.

Importance lay in accurately modelling heat transfer throughout the engine in order to utilise the model for the purpose of predicting the changes in heat transfer and component temperatures when deactivating a cylinder. Given this ambition, component temperatures were predicted within a 5% tolerance compared to experimental data. This was exemplified against temperature measurements taken across the length of two cylinders. The changes in heat transfer and component temperatures associated with cylinder deactivation are quantified and discussed more thoroughly in *Chapter 5*.

Aside from the thermal model a robust manner of predicting engine performance parameters specifically fuel consumption and pumping losses for a turbocharged engine was required. This was in-light of previous models used for predicting pumping losses and fuel consumption for naturally aspirated gasoline engines. A simple algebraic expression derived by Zinner [4.29] was used to iteratively calculate the required intake pressure past the throttle for a turbocharged engine. A more extensive approach describing the interaction between the compressor and throttle would be physically representative of the engine. However this would entail describing the effect that cylinder deactivation has on pulsations in the air ducts along with pressure fluctuations from bounce-back at the intake ports. This remains outside the scope of this study and would also require CFD analysis of the phenomenon in the air ducts. For the purpose of determining the fuel consumption benefit due to the reduction in pumping work associated with cylinder deactivation the simple approach used is sufficient. For engine operation with firing on all cylinders comparisons between modelled and experimental pumping losses and fuel consumption were

shown for the warm-up processes over the NEDC and FTP-75 and fully-warm operation the HWFET and US06 drive cycles.

Given the need to robustly characterise pumping losses and fuel consumption it was of importance that the work loss associated with motoring piston be quantified and represented in the model. Based on data emanating from a proto-type engine capable of shutting off intake and exhaust valves and cutting-off fuel injection, an analytical expression based on the first law of thermodynamics was used to express the work loss. The expression relies on input experimental data input of maximum and minimum in-cylinder pressure while assuming a BDC charge temperature. Furthermore, the polytropic index is based on stabilised in-cylinder pressure traces found to be between 1.34 and 1.36. This results in a work penalty between 0.02 to 0.03bar IMEPg. This work loss is negligible. However through the development of this expression and for informative purposes a large proportion of the initially induced mass was found to be lost through blow-by. When trapping an exhaust gas charge this was found to be in the range of 47 to 70% depending on the final BDC stabilised pressure.

As such given a robust and simple method of predicting engine performance for turbocharged gasoline engine the coupling of the thermal and performance models were used to predict engine performance due to cylinder deactivation as described in *Chapter 5* and *6*.

Sensitivity analyses were not carried out throughout this study as the purpose was mainly to characterise the engine accurately to use as a predictive tool. An extensive analysis of model sensitivity has been previously carried out by *Morgan* [4.37] and *Janowski* [4.38]. In these studies sensitivity to changes in the heat transfer correlations (i.e. the C1C2 expressions), friction model, changes in engine mass and changes in the input parameters for engine performance estimation have already been thoroughly assessed.

Chapter 5 Modelled Changes in Heat Transfer due to Cylinder Deactivation

5.1 Introduction

The application of PROMETS to simulate thermal responses to cylinder deactivation of the three cylinder engine is described in this chapter. Firstly the changes made to the heat transfer model to simulate cylinder deactivation are described. Consequently, simulation results such as: response times for temperatures to reach equilibrium conditions before/after deactivation; changes in component temperatures and heat fluxes; and temperature differences between adjoining components are described specific to constant operating conditions. The effects on warm-up rates are investigated for constant operating conditions and also over the NEDC. Possible thermal constraints which arise due to cylinder deactivation are also investigated. This is followed by suggested methods for minimising adverse thermal effects of cylinder deactivation through thermal management strategies. With very little information available in the public domain about the effects cylinder deactivation has on engine thermal behaviour this section provides new and informative knowledge on the subject.

5.2 Heat Transfer Model Revision to Account for Cylinder Deactivation

The form of cylinder deactivation considered in this study entails shutting of the intake and exhaust valves and cutting-off fuel injection while retaining a reciprocating piston. In this subsection the phenomenon due to cylinder deactivation occurring in the combustion chamber, engine intake side, engine exhaust side and at the friction level are described. In this modelling instance when deactivation ensues cylinder number one is prone to disablement while cylinders number two and three remain firing at all times. Thermal effects of varying the deactivated cylinder are discussed in further detail towards the end of this chapter. The effect of these revisions is exemplified with reference to a heat flow diagram showing the changes in heat transfer for the first cylinder before and after deactivation. For the deactivation period, heat flow diagrams for cylinder one are contrasted with the heat flow across cylinder two. The heat flow diagrams are shown on Figure 48 (A), (B) and (C) for a constant operating condition of $N = 2000\text{rpm}$ and $T_b = 60\text{Nm}$ at a fully-warm engine state.

5.2.1 Combustion Chamber Heat Transfer

Specific to a vehicle whose sole prime mover is an internal combustion engine, increasing the fuel injected in the firing cylinders is the only means of compensating for the absence of useful work delivered from the deactivated cylinder. Simply put for the firing cylinders the increase in heat transfer is proportional to the increase in mass of fuel injected. In a three cylinder engine when deactivating a single cylinder fuel injection in the firing cylinders increases by roughly 50% (i.e. factor of 1.5) more fuel injection. When deactivating two cylinders roughly 200% more fuel is injected in the single firing

cylinder (i.e. factor of 3). The reason for stating that a ‘rough’ increase in fuel injected takes place is due to the reduction in fuel consumed arising from the fuel consumption benefit that arises with deactivation. In effect the increase will always be less than the values stated above. The cycle-averaged in-cylinder Reynolds number, described in *Chapter 4 Section 4.7.1*, dictates the heat transfer from the combustion chamber to the coolant in the firing cylinder. Deactivation is accounted for by reducing the number of working cylinders, $n_{c,deac}$, as shown:

$$Re_g = \frac{4 \dot{m}_f \left(1 + \frac{AFR}{(1-EGR)}\right)}{(n_c - n_{c,deac}) \pi \mu_g B} \quad \text{Equation 84}$$

For the deactivated cylinder heat transfer to the cylinder walls drastically reduces and little information on the in-cylinder Reynolds number exists in literature. Therefore as substitute the *net* heat transferred to cylinder walls is equated to the heat produced by the polytropic process shown in *Chapter 4 Section 4.11.2*. The flux across the elements, i.e. representing the topography of the cylinder wall comprising the engine stroke, are segregated with respect to the proportion of time the trapped charge is exposed to the cylinder wall. This is based on an algorithm described by *Christian* [5]. Changes in heat flux in the combustion chamber experienced across the piston crown are the same as described for the cylinder walls for both deactivated and firing cylinders. The flux is however proportional to the total cycle-averaged flux in the combustion chamber, as described by the Q_{c1c2} expression, and the exposed surface area of the piston.

The modelled effect of these revisions before and after deactivation are shown on Figure 48. (A) shows heat fluxes for cylinder one prior to deactivation; (B) for cylinder one after deactivation; and (C) for cylinder two after deactivation. Modelled heat rejection from the combustion gas to coolant, for cylinder two, increases by 20%, equivalent to 289W, from 1166W to 1455W. Heat flux to the piston crown for cylinder two increases by 33% from 305W to 415W. For cylinder one on the other hand heat fluxes from the gas to piston reduces significantly.

5.2.2 Exhaust Side Heat Transfer

5.2.2.1 Exhaust Port

When deactivation occurs, closure of the exhaust valves prevents the flow of hot combustion gases through the exhaust ports. The heat transfer process changes from forced convection to natural convection and it is assumed that heat transfer in the exhaust port of the deactivated cylinder makes a small contribution to heat flow in the head. This can be neglected. In PROMETS, the heat exchange in the port is switched by, t_{deac} , from 0 to 1, representing the absence of flux as shown in the expression below.

$$\dot{Q}_{pt,total} = \dot{Q}_{pt} (1 - t_{deac}) + \dot{Q}_{valve} \quad \text{Equation 85}$$

Where \dot{Q}_{pt} is the heat transfer from the exhaust gas to the coolant and \dot{Q}_{valve} the heat transfer from the valve seat to the exhaust port. The only form of heat transfer to the exhaust port for the deactivated cylinders stems from the valve through the valve seat. This is described in the following subsection. For the firing cylinders, the increase in mass flow-rate through the exhaust ports and thus heat flux is reflected by an increase in Reynolds number.

The effect of nullifying heat rejection in the exhaust port for cylinder during deactivation is shown on Figure 48 (B). Modelled heat rejection rates for the firing cylinder at an operating condition of $N = 2000\text{rpm}$ and $T_b = 60\text{Nm}$ increases by 36% or 519W, from 1444W to 1963W. The latter value is depicted in Figure 48 (C) as a solid line connection between the exhaust port and engine head. The majority of heat is lost to coolant as the IEM is completely enveloped by coolant passages.

5.2.2.2 Exhaust Valve

In the deactivated cylinder, heat transfer from the exhaust valve head, \dot{Q}_{valve} , to the lower segment of the exhaust port is still present. As the trapped charge is compressed, an increase in pressure and thus temperature results in heating the exhaust valve face. Although this is generally very small on a cycle-averaged basis, ~ 2 watts per revolution, this is still modelled and applied to the term $\dot{Q}_{in-cylinder}''$ shown in the following expression,

$$\dot{Q}_{valve} = A_{valveface} \dot{Q}_{in-cylinder}'' \quad \text{Equation 86}$$

For the firing cylinders heat transfer to exhaust valves increases proportionally with the magnitude of fuel injected. This is modelled by multiplying the area of the exhaust valve head and lower stem with the revised combustion flux described through Equation 20.

Figure 47 shows the heat conduction path through the exhaust valve of a firing cylinder to the cylinder head and exhaust port. The lower stem of the exhaust valve remains significantly hotter compared to the other sections of the exhaust valve due to the absence of direct contact with the heat sinks.

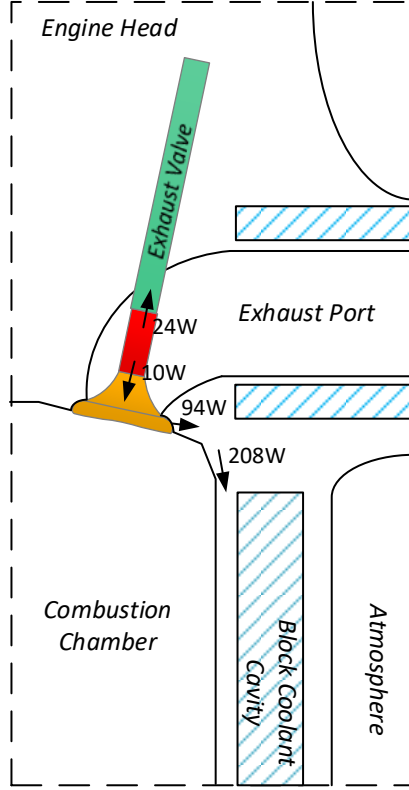


Figure 46: Illustration of the heat transfer paths from the exhaust valve to the cylinder head and block at $T_b = 60\text{Nm}$, $N = 2000\text{rpm}$.

5.2.3 Intake Side Heat Transfer

5.2.3.1 Intake Ports

The intake ports experience smaller changes in heat transfer coefficient relative to the exhaust ports due to the absence of hot gases. Dominated by the coolant temperature in contact with the intake port metal, increments in heat transfer coefficient are strongly dependent on the increase in the mass of air traversing the ports as described by the Reynolds number [5.1],

$$Re_{intake} = \frac{4 \dot{m}_f AFR}{n_c (1-EGR) \pi \mu_{air} d_{intake,port}} \quad \text{Equation 87}$$

Where the viscosity of the air, μ_{air} , is taken to have the same dependence on temperature as the viscosity defined for the in-cylinder gas, μ_g , i.e. Equation 55. With this the heat transfer coefficient in the intake port is expressed as follows,

$$h_{intake,port} = 0.0675 k_g \frac{Re_{intake}^{0.713}}{d_{intake,port}} \quad \text{Equation 88}$$

5.2.3.2 Intake Valves

For the intake valves belonging to the deactivated cylinder, although motionless, cooling through forced convection still occurs at the top of the valve head, lower stem and upper stem. This is due to the constant filling and emptying process taking place in the intake manifold and ports. The lower head section of the intake valve, i.e. facing the combustion chamber, is not prone to convective forces originating from the intake manifold but is subject to repeated in-cylinder compression and expansion processes. The net heat transfer to the intake valve head due to this irreversibility was modelled as a constant cycle-averaged $\sim 2\text{W}$ per revolution. The heat transfer expressions used for the intake valve stem and head for the deactivated and firing cylinders are those described by *Chick [5.1]* and are shown below.

Reynolds Number and Heat Transfer Coefficient Expression for the Intake Valve Head [5.1]

$$Re_{\text{intake-valve head}} = \frac{4 \dot{m}_f (1+AFR) n_{\text{intake, valve}} \pi d_{\text{intake-valve head}}}{n_{\text{cyl}} \mu_{\text{air}} (1-EGR) (d_{\text{intake, port}}^2 - d_{\text{intake-valve stem}}^2)} \quad \text{Equation 89}$$

$$h_{\text{intake-valve head}} = 5.73 k_g \frac{Re_{\text{intake-valve head}}^{0.408}}{d_{\text{intake-valve head}}} \quad \text{Equation 90}$$

Reynolds Number and Heat Transfer Coefficient Expression for the Intake Valve Lower Stem

$$Re_{\text{intake valve, stem}} = \frac{4 \dot{m}_f (1+AFR) n_{\text{intake, valve}} \pi d_{\text{intake-valve stem}}}{n_{\text{cyl}} \mu_{\text{air}} (1-EGR) d_{\text{intake, port}}^2} \quad \text{Equation 91}$$

$$h_{\text{intake-valve stem}} = a k_g \frac{Re_{\text{intk}}^x}{d_{\text{intake-valve stem}}}, \quad \begin{matrix} a = \begin{cases} a=0.612 & Re_{\text{intk}} < 4000 \\ a=0.173 & Re_{\text{intk}} \geq 4000 \\ a=0.0242 & Re_{\text{intk}} \geq 40000 \end{cases} \\ x = \begin{cases} x=0.466 & Re_{\text{intk}} < 4000 \\ x=0.618 & Re_{\text{intk}} \geq 4000 \\ x=0.802 & Re_{\text{intk}} \geq 40000 \end{cases} \end{matrix} \quad \text{Equation 92}$$

The Reynolds number for the intake valve head and stem are thus not modified. The expression for the intake valve stem is valid for Reynolds numbers up to 40,000 although simulation results do not exceed Reynolds numbers of 5000, i.e. for a brake load of 160Nm and engine speed of 5500rpm. For comparative purposes the engine brake torque is rated at 170Nm.

5.2.4 Heat Losses due to Friction with a Deactivated Cylinder

In this sub-section changes in heat transfer due friction at the level of the engine and specific to deactivated cylinder are described. Concordantly, the necessary modelled changes to physically represent these descriptions at both levels are described.

5.2.4.1 Piston Ring Friction

The continuing reciprocation of the piston dissipates work through rubbing friction. For this cycle-averaged model the thermal resistance between the piston rings and cylinder liner is constant.

$$R_{th,rings} = \frac{1}{n_{rings} \frac{\pi B k_{ring} t_{ring}}{d_{ring}}} \quad \text{Equation 93}$$

Where n is the number of rings, k the thermal conductivity of the ring, t the ring width and d the ring thickness. Based on an analysis by *Zammit* [5.2] the constant ring resistance bears a value of $R_{th,rings} = 0.1153\text{K/W}$; assuming an air filled gap between the ring and the groove in the piston. The presence of oil between the rings would have reduced the thermal resistance although this would only be the case for the lower segment of the piston stroke when in-cylinder pressures reach sub-atmospheric levels. Although *Zammit* [5.2] reports that for diesel engines the piston ring resistance is a function of engine speed; i.e. initially larger at around $\sim 0.4\text{ K/W}$ at 1000rpm reducing with speed down to $\sim 0.10\text{ K/W}$ at 3000rpm. In effect, heat is still transferred from the cylinder wall to the coolant over 91% of the piston stroke as the block coolant gallery does not extend to the BDC. The coolant temperature however is chief in maintaining a nominal cylinder wall temperature as frictional heat losses are small relative to the enthalpy carried by the coolant.

An illustration of the constant modelled resistance is shown by the dotted lines representative of friction between the piston and the liner, on Figure 48 (A), (B) and (C). Where for firing and deactivated cases no change in the value of friction is observed; i.e. a constant 210W heat dissipated to the liner and 40W rejected to the oil.

5.2.4.2 Camshaft Main Bearing Friction

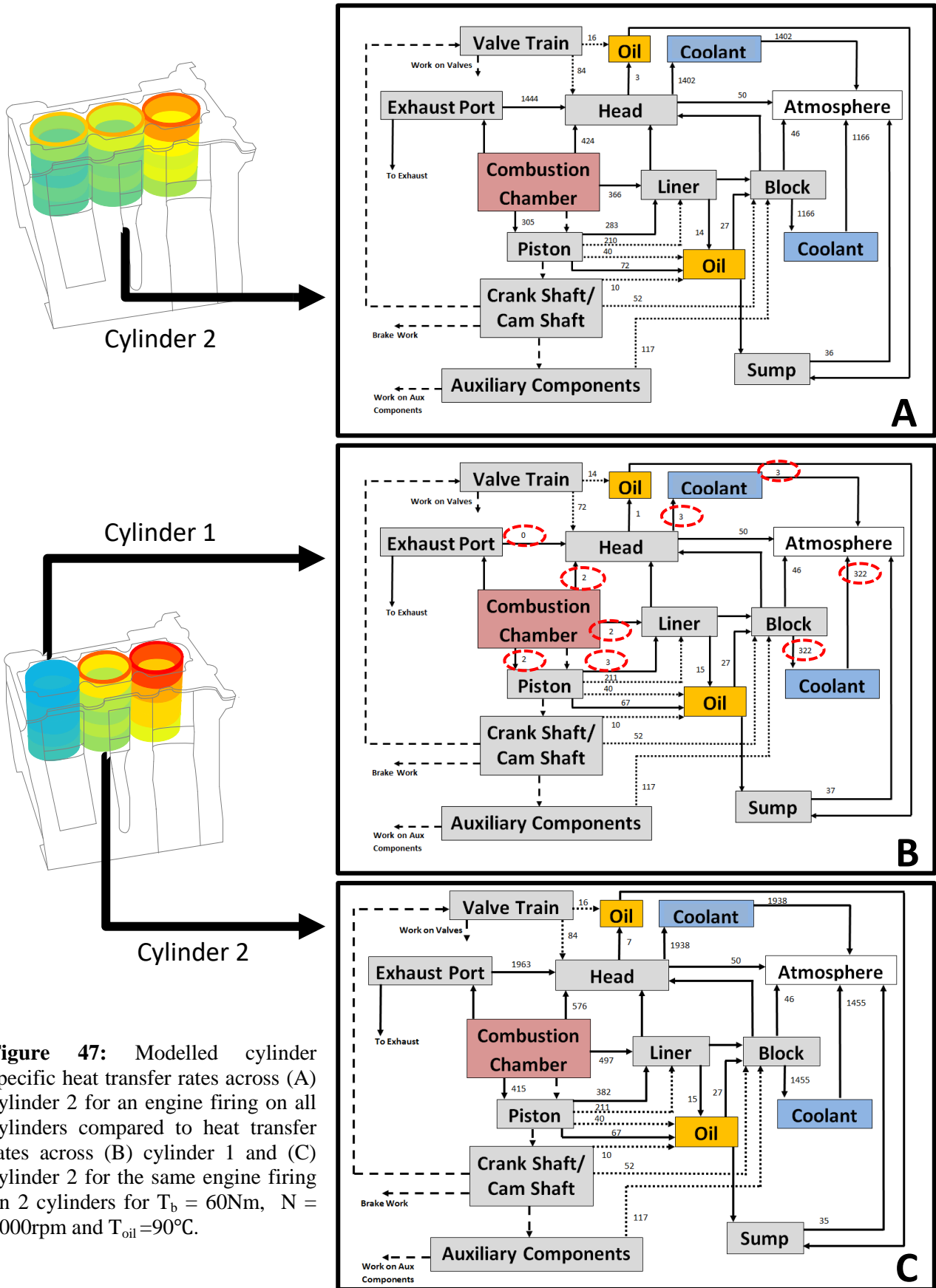
An increase in the thrust force due to deactivation experienced by the big end bearings for the firing cylinders increases bearing frictional losses [5.3]. This is attributed to augmented ‘squeezing’ of the oil film in effect reducing the thickness and increasing the temperature of the oil surrounding the journal bearing. Frictional losses, on a crank angle basis, possibly rise due to increased boundary/mixed lubrication regimes. For the deactivated cylinder the opposite process takes place. The film thickness increases significantly as the thrust force is smaller [5.4], even when compared to an engine idling condition. In turn, the film temperature reduces. However, the reduction is almost negligible thus not significantly affecting shearing losses. Tribo-dynamic simulations conducted by *Mohammadpour* [5.5] have shown that the net effect cylinder deactivation has on the change in frictional dissipation

experienced in the bearings are marginal. Thus in this modelling instance of PROMETS it was assumed that the global engine bearing frictional losses remain unchanged.

In effect, as shown on Figure 48 (A), (B) and (C), heat transfer on a per cylinder basis from the crankshaft assembly to the oil remains constant at a constant 10W regardless of whether the engine undergoes deactivation.

5.2.4.3 Valvetrain Friction

Valvetrain frictional losses in the deactivated cylinder reduce due to the arrested lifting motion of the intake and exhaust valves. The contact between the cam-lobe and the flat follower element are still present thus the fourth term describing the valvetrain friction is left unchanged. Mixed (i.e. rubbing of the asperities and hydrodynamic lubrication) and oscillating hydrodynamic lubrication regimes, describe the frictional losses at the valve lifter bore and guide assembly as shown describing the valvetrain friction. Friction at the lifter bore reduces for a roller finger follower as the retentive force of the spring holding the valve in a closed position does not resist any downward motion of the bore, thus the lifter is left motionless. This is accounted for in the sixth term describing the valvetrain friction by reducing the number of working valves, n_v , by a third. A modelled 4.34% reduction in the valvetrain friction is computed for the partial absence of this mixed lubrication regime. Additionally, the oscillating hydrodynamic friction between the valve stem and the valve guide zeros as the valves are inert thus the fifth term describing the valvetrain friction also reduces by a third resulting in a 0.26% reduction in modelled valvetrain friction. In effect the reduced valvetrain frictional losses amalgamate to a 0.87% reduction in engine rubbing friction.



This is represented in the heat transfer flow diagrams by comparing Figure 48 (A) and (B). Reduced valvetrain heat transfer to the oil and head metal structure, are illustrated on Figure 48 (B). Heat loss from the valvetrain friction when cylinder 1 is deactivated reduces from 16W to 14W to the oil and from 84W to 72W to the head metal structure. The combined 14W reduction in heat rejection is specific to cylinder 1, thus the total heat rejection due to rubbing friction from the valvetrain assembly reduces from 301W to 287W. Although changes in frictional losses are present at the valvetrain level these are minimal.

5.3 Changes in Heat Transfer to Engine Coolant

Set in Figure 49 (A) and (B) and Figure 50 (A) and (B) are the modelled changes in heat transfer from the gas to coolant with cylinder deactivation from the centre firing cylinder, cylinder two, and the entire engine. For these figures the maximum engine brake load when deactivating has been limited to 90Nm. For engine brake loads above 110Nm (i.e. 55Nm) the model does not converge due to excessive heating of the coolant and oil resulting in temperatures outside the bounds of model look-up tables (i.e. $T_{oil} > T_{oil,max} = 160^{\circ}\text{C}$). The overheating of oil is illustrative of the real engine where cooling of the cylinder wall is generally affected by enriching the air charge. Largely a 13 to 32% increase in the heat rejected from the remaining firing cylinders takes place when deactivating, shown on Figure 49 (B). Three data points lie significantly above this range corresponding to loads above 60Nm at 1000rpm. These result from a severe drop in the gross indicated thermal efficiency inputted into the model (refer to Appendix D for experimentally referred values). Excessive retardation in spark angle is required to avoid the onset of knock due to higher cylinder wall temperatures. As way of example, the discrepancy in heat rejection values at 1000rpm for the 70Nm, 80Nm and 90Nm load cases (i.e. a 37%, 39% and 45% increase in heat rejected shown on Figure 49 (B)) are associated with modelled gross indicated thermal efficiency values of 36, 33 and 29% respectively. To contrast this, at an engine speed of 2000rpm at 90Nm the gross indicated thermal efficiency reduces to only 37.3%.

The overall heat rejected to coolant from the engine reduces compared to when firing on all three cylinders. This is depicted in Figure 50 (A) and (B) with reference to changes in the absolute values of heat transfer and percentage respectively. Apart from the three load points, which demonstrate excessive heat loss to the coolant at 1000rpm, the reduction in heat rejected to coolant increases with engine brake load and reduces with engine speed. Reduced heat rejection resides within a 20.5% to 3% interval for engine speeds between 1000 and 4000rpm and brake loads between 20 and 90Nm.

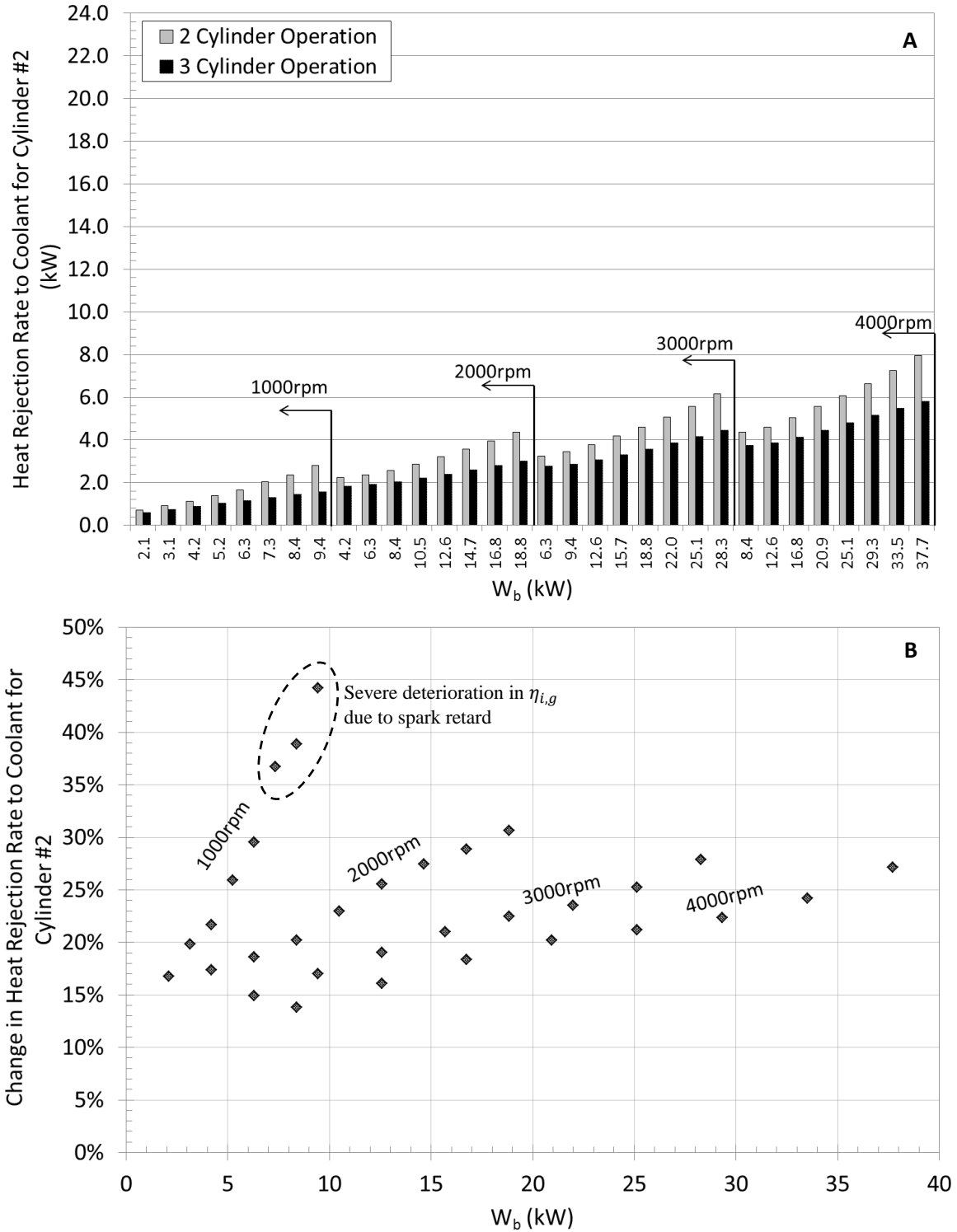


Figure 48: (A) Modelled heat rejection rates to coolant combined from the head and block sections and (B) the equivalent percentage change specific to cylinder number 2 when firing on two of three cylinders.

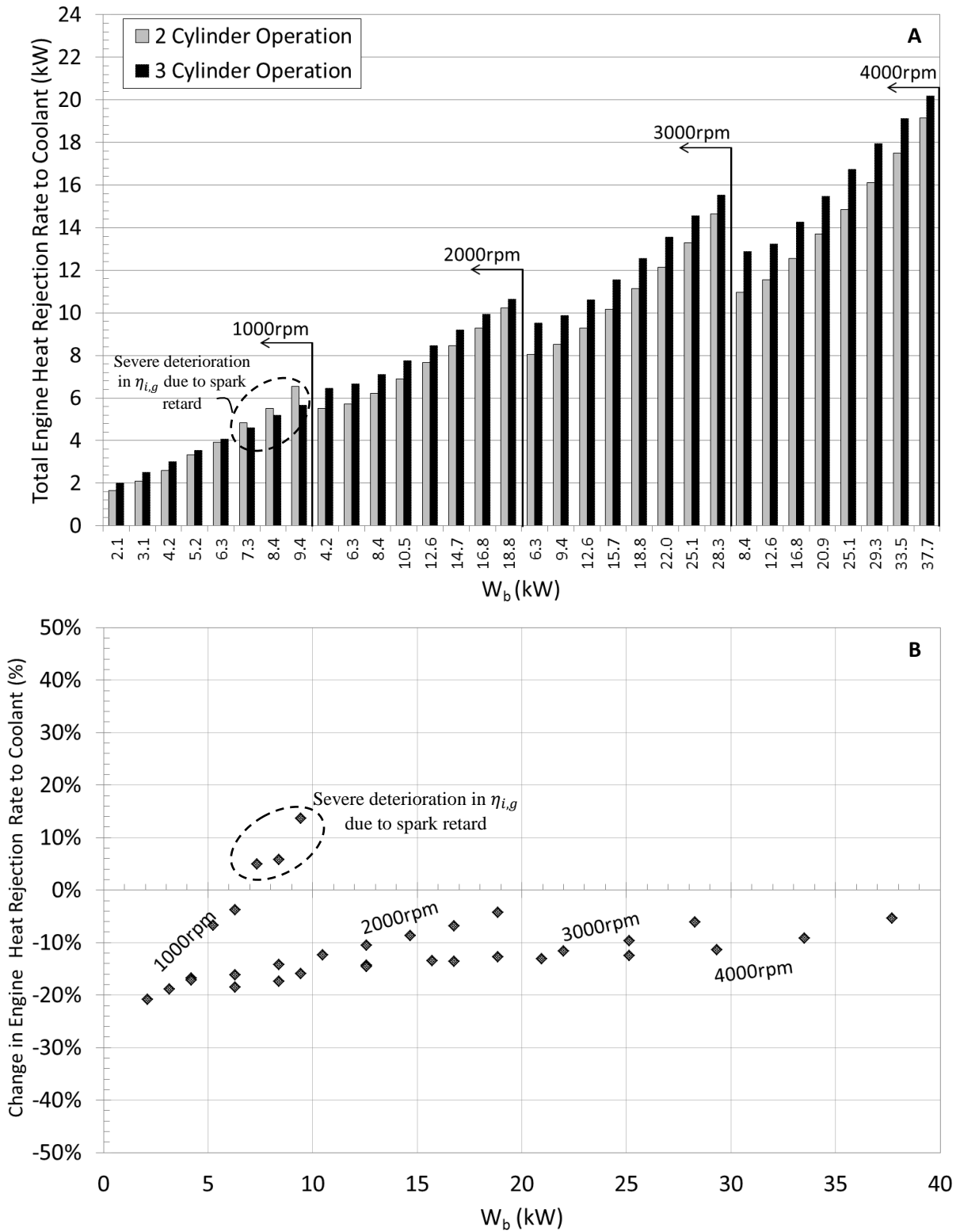


Figure 49: (A) Modelled total engine heat rejection rates to coolant combined from the head and block sections and (B) the equivalent percentage change specific to cylinder number 2 when firing on two of three cylinders.

5.4 Changes in Component Temperatures

5.4.1 Cylinder Walls

As a result of changes in heat transfer metal components settle to new equilibrium temperatures. An illustration of the modelled time dependent temperature response for the upper and mid sections of the cylinder wall for the firing and deactivated cylinders are shown in Figure 51. An illustration of the temperature distribution for all three cylinder liners for a constant operating condition of $T_b = 50\text{Nm}$ and $N = 3500\text{rpm}$ is shown on Figure 52.

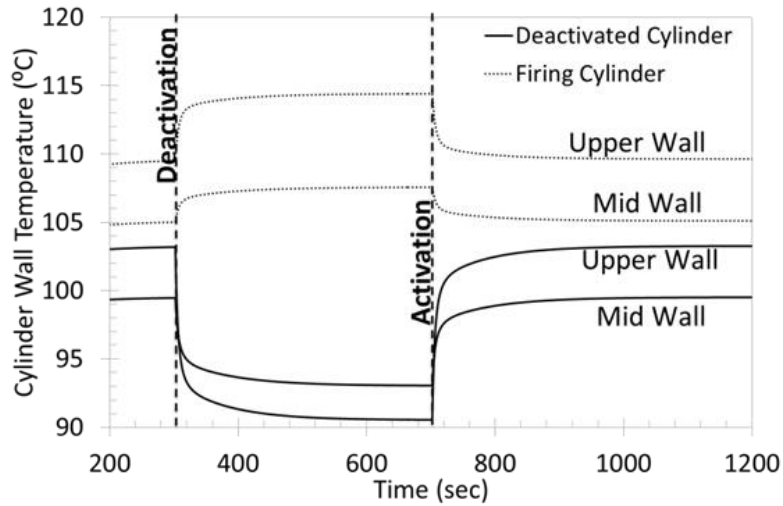


Figure 50: Example of modelled cylinder wall temperature change and response time; $T_b = 50\text{Nm}$, $N = 3500\text{rpm}$.

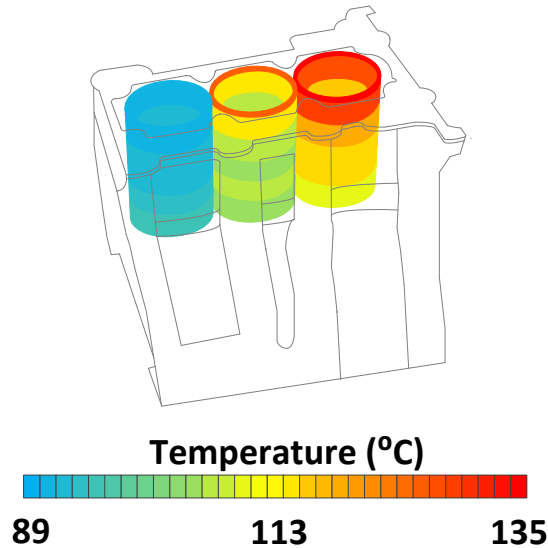


Figure 51: Modelled stabilised cylinder wall temperatures after deactivation; $N=2000\text{rpm}$ and $T_b= 60\text{Nm}$.

As seen on Figure 52 the deactivated cylinder cools to a near uniform temperature. The temperature to which the liner settles is dictated by the local coolant temperature. Cylinder number 3 operates at the highest temperature as the coolant initially enters the block cavity with lower temperature compared to the engine coolant outlet temperature. As shown in Figure 53 the largest temperature rise is observed at the top of the liner for the firing cylinder although the temperature change remains very small $\Delta T < 7^\circ\text{C}$. Dependent on engine load the top of the liner for the deactivated cylinder endures the largest temperature change $\Delta T < 20^\circ\text{C}$ as it falls to the coolant temperature.

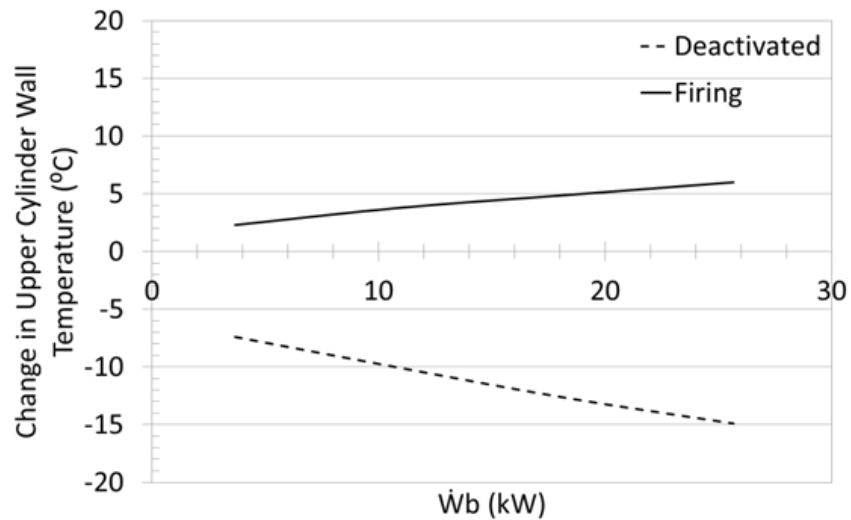


Figure 52: Modelled Cylinder #1 and #2 wall temperature changes for varying brake loads at an engine speed of 3500rpm.

5.4.2 Temperature Response Times

The response time, τ , is primarily a function of the wall thicknesses as well as the heat transfer coefficient of local heat sinks directly or indirectly in contact with the engine structural component. The response time is defined as the time taken for the component temperature to reach 63.2% {i.e. percentage of time defined for an increasing system to reach $1 - \frac{1}{e} \sim 63.2\%$ } of its equilibrium state after deactivation/reactivation. On Figure 54 modelled cylinder wall response times are plotted for varying engine speeds against brake power. The coolant pump is mechanically driven through the FEAD via the crankshaft with a gear ratio of 2:1. The increase in response time at 1000rpm compared to the 3500rpm engine speed case is primarily due to the very small temperature increase experienced across the cylinder wall. Thus as engine load increases the response time reduces. This is further promoted by the relatively low heat transfer coefficient present in the block at 1000rpm, i.e. $1950 \text{ W/m}^2\text{K}$, as shown on Figure 55. Response times for all engine components are in the range of 10 to 25 seconds.

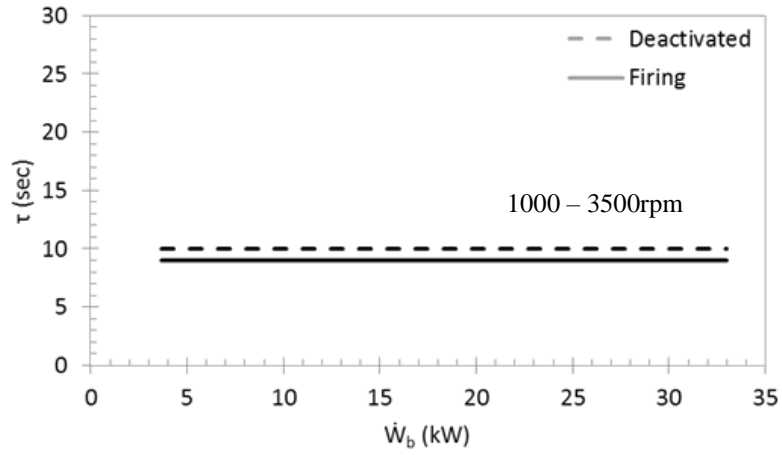


Figure 53: Cylinder wall response time for two engine speeds $N = 1000\text{rpm}$ and 3500rpm .

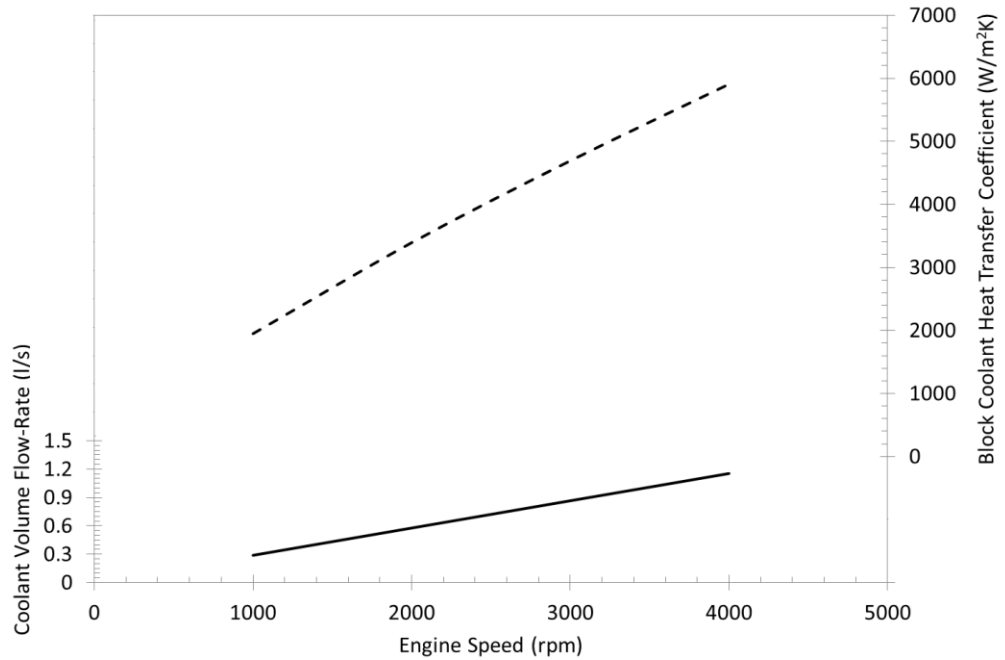


Figure 54: Modelled coolant volume flow-rates for a fully-warm engine thermal state ($T_{cool} = 90^\circ\text{C}$, $T_{oil} = 90^\circ\text{C}$) with respect to engine speed and corresponding block coolant heat transfer coefficients ($\text{W/m}^2\text{K}$).

5.4.3 Intake and Exhaust Valves

The largest changes in cycle averaged temperature takes place in the valve stem. An illustration of the intake and exhaust valve temperatures before and after the deactivation in all cylinders is shown on Figure 56.

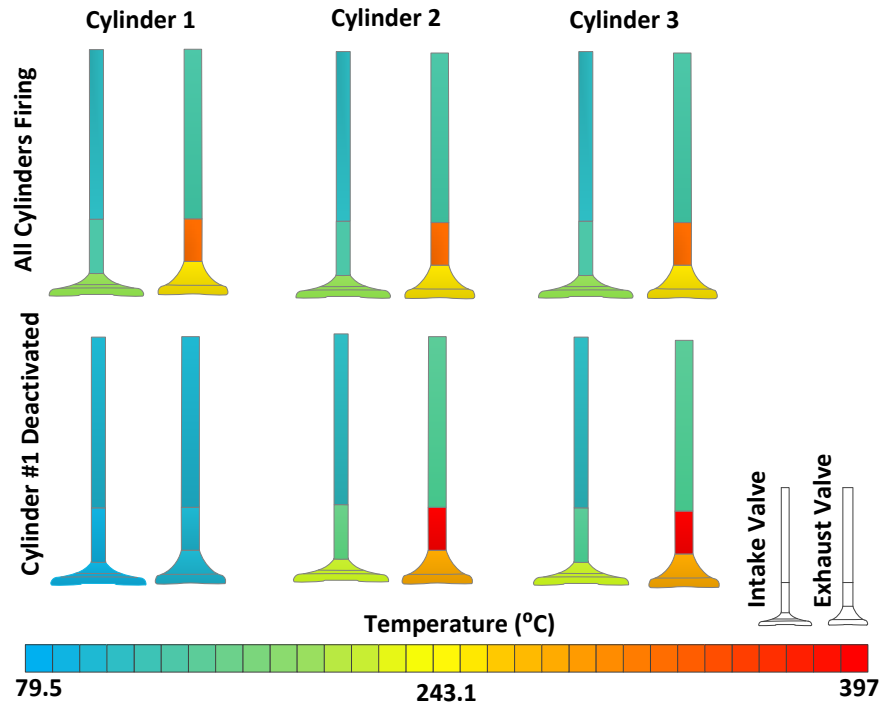


Figure 55: Modelled stabilised valve metal temperatures before and after deactivation; $N = 2000\text{rpm}$, $T_b = 60\text{Nm}$, $T_{\text{cool}} = 90^\circ\text{C}$.

The lower stems of the exhaust valves for the deactivated cylinder undergo the largest modelled temperature changes in contrast with all other engine components. The change in temperature of the exhaust valve lower stem with respect to engine brake load for an engine speed of 3500rpm is shown on Figure 57. The temperature increase of the exhaust valve lower stem for the firing cylinders is significantly smaller. With similar response times as described above, the new equilibrium temperatures for the deactivated intake and exhaust valves is approximately that of the coolant temperature. The largest reduction observed for an engine speed of 3500rpm and brake load of 70Nm is of 370°C. The largest temperature rise for the firing cylinder exhaust valve lower stem is in the range of 120°C. Exhaust valve head temperature changes lag behind lower stem temperatures generally by 40 °C. Intake valve temperature changes are significantly less with the largest change at the valve head being around ~50°C.

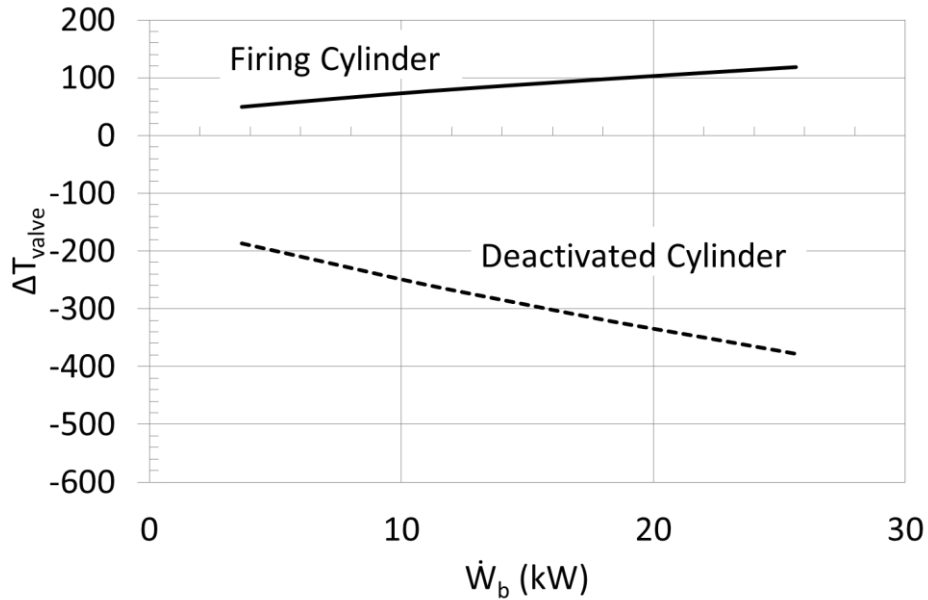


Figure 56: Modelled change in temperature for the exhaust valve lower stem component for the deactivated and firing cylinders at $N = 3500\text{rpm}$.

5.4.4 Piston Temperatures With and Without Cooling Jets

Figure 58 illustrates the effect cooling the piston underside with oil jets has on the temperature of the firing cylinder, number two, with and without cylinder deactivation. This is specific to a modelled nozzle aspect ratio of $z/d_o \sim 80.7$. An engine operating condition of $N = 3500\text{rpm}$, $T_b = 60\text{Nm}$ was chosen since the modelled fuel consumption benefit due to deactivation at this operating point nears zero, i.e. $\sim 1\%$; representing a near upper limit for the application of cylinder deactivation. Case (A) illustrates the nominal piston temperature for cylinder two when all cylinders are operating. The piston temperature for the deactivated cylinder (B) is contrasted by the significantly elevated temperature of the piston in the second cylinder regardless of whether the cooling jets are flowing, as is illustrated in cases (C) and (D). The temperature of the piston for the deactivated cylinder, cylinder one, stabilises to a temperature above that of the coolant, $T_{\text{piston}} = 101^\circ\text{C}$ compared to $T_{\text{coolant}} = 90^\circ\text{C}$. This difference is attributed to the combined effect of heat losses due to rubbing friction being directed towards the piston assembly as well as the small amount of heat lost to the piston from the trapped charge.

Compared to the nominal piston operating temperature (A), deactivating a cylinder, increases the crown temperature by 14% as depicted in case (D). In contrast switching on the jets, when deactivating a cylinder, reduces the cycle-averaged piston metal temperature by 12%. Operating at a significantly higher temperature with no cooling jets drives a significant proportion of the heat from the piston crown to the

pin. Heat dissipation within the inner-shell of the piston changes by a factor of four with jets on, as reported by *Nassif* [5.6]. In effect, although the time-averaged piston temperature is within the safe operating range, i.e. below 250 - 280°C [5.2], the expansion of the piston pin may restrict the rotational degree of freedom between the connecting rod and the piston. Furthermore, at temperatures above ~275°C the yield strength of aluminium alloys reduces by 50% several affecting the durability of the piston.

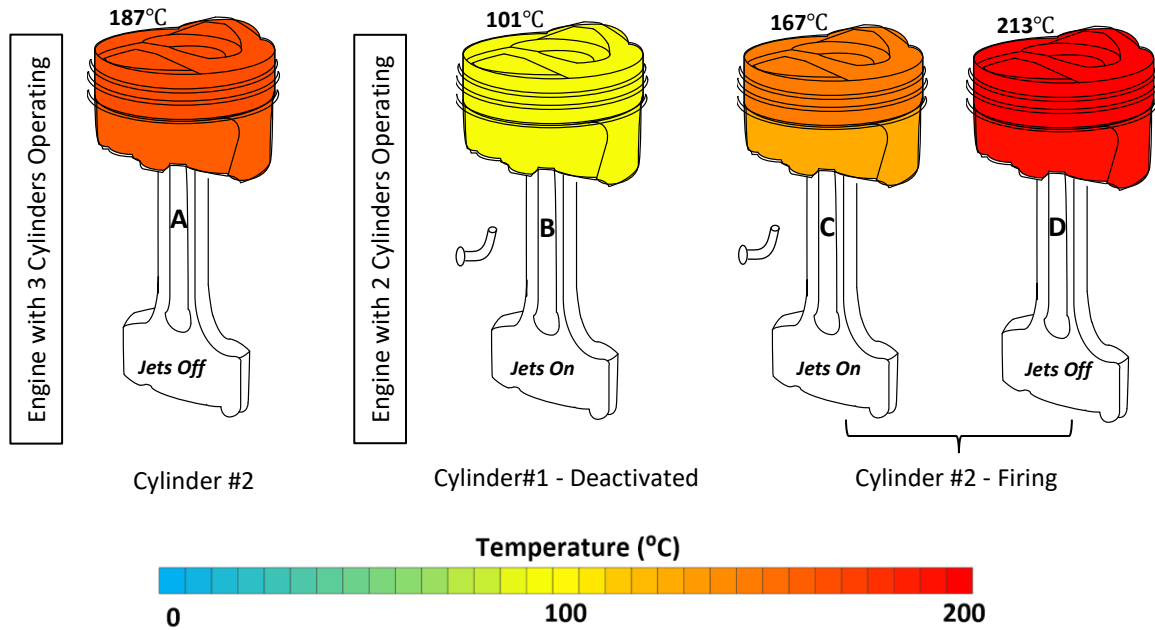


Figure 57: Sketch of piston illustrating change in piston crown and skirt temperature at $N = 3500\text{rpm}$ and $T_b = 60\text{Nm}$ with and without oil flowing through the piston cooling orifice.

5.5 Temperature Differences between Adjoining Metal Components

The largest temperature differences occur between adjoining components for cylinder one and two. These are shown in Figure 59 (A) for the cylinder wall, (B) lower block and (C) between the intake and exhaust ports. Cylinder number one is located closest to the coolant inlet aperture in the block and head. As illustrated on Figure 59 predicted temperature differences have been limited to the range where modelled fuel economy benefits due to deactivation are present, i.e. ~70Nm. As shown on Figure 59 (A), the top sections of the cylinder liners of the deactivated and firing cylinders experience the largest temperature difference. These are areas where the heat fluxes from the firing cylinder are highest. For the top of the cylinder liner temperature differences are primarily a function of engine load, i.e. 0.2 °C/Nm.

Engine speed increments of 1000rpm raise the difference by 2 to 3°C at 10Nm and up to 4 to 6°C at 70Nm as denoted by the different line types (e.g. dotted/dashed).

Moving down the length of the liner, differences are significantly lower driven due to a controlled coolant temperature and lower heat flux rejection. As shown in Figure 59 (B) temperature differences in the upper crankcase wall are generally 2 to 4°C higher compared to the bearing support plates and lower crankcase structure. The differences are generally less than 10°C. The engine speed dependence is less pronounced in these areas as heat fluxes are generally two orders of magnitude lower compared to the top of the cylinder liner.

Temperature differences between the firing cylinder and deactivated cylinder exhaust ports, as seen on Figure 59 (C), are the highest. The non-linear dependence with engine speed is a result of the plateauing of exhaust gas temperature at part loads. Initially the exhaust gas temperature is between 200 and 300°C, increasing to 600°C at part loads. Nearer to the intake valves temperature differences across the intake ports are smaller. A reduction in temperature difference is observed with increasing engine speed, inverse of the speed dependence observed on other components. This is associated with increased heat fluxes warming the exhaust side of the engine and cylinder resulting in heat traversing into the cooler intake side of the head.

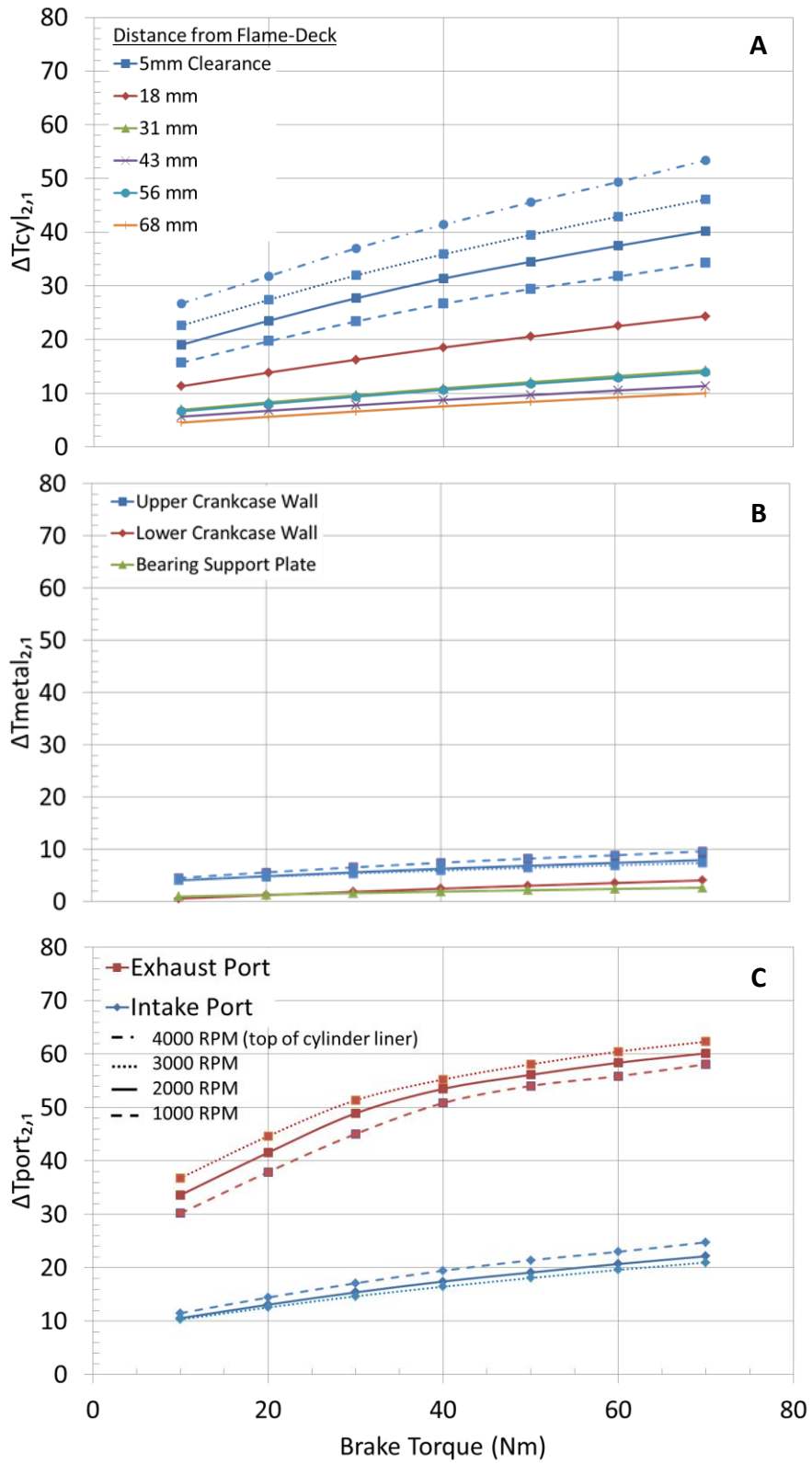


Figure 58: Modelled temperature difference for [A] the cylinder liner, [B] lower block and [C] exhaust/intake ports between the deactivated and firing cylinder as a function of brake torque.

5.5.1 Effect of Varying Compression Ratio and Spark Timing on Temperature Differences

Temperature differences between adjoining components are dependent on the cylinder geometric compression ratio. Increasing compression ratio reduces the temperature difference between the firing cylinder and deactivated cylinder. As example, given a constant amount of fuel injected into a firing cylinder with a fixed surface area, A_1 , the total surface area will reach an average metal temperature, T_1 . As the surface area of the combustion chamber is increased, such that $A_2 > A_1$, and the same magnitude of heat energy is exposed to the combustion chamber. Due to the increase in surface area the overall metal temperature will reduce such that $T_2 < T_1$. This is due to their being more surface area through which heat can be transferred thus resulting in greater heat losses. An illustration of this effect is shown on Figure 60 (A).

Temperature differences between components are also dependent on the gross indicated thermal efficiency. In practice, spark timing is kept close to the *maximum spark advance for best torque delivery* (MBTD) to promote more complete burn of fuel to ensure that the flame front fully develops close to TDC. At this point the maximum potential amount of work is extracted from the heat energy resulting from combustion. Retarding or advancing spark timing relative to MBTD, reduces the amount of useful work generated due to combustion in turn, increasing heat losses to the cylinder walls. A way of expressing this has been formulated by *Chick* [5.1],

$$\eta_{i,g} = 0.86 \left(1 - \frac{1}{r_c^{0.3}} \right) - 0.0002 \theta_{MBTD}^2 \quad \text{Equation 94}$$

Where θ_{MBTD} , is the spark timing relative to MBTD and the squared term indicates that advancing or retarding the spark angle relative to MBTD results in a deterioration of the gross indicated thermal efficiency. In practice, for an engine with a deactivated cylinder, as the cylinder load increases the spark angle is retarded to reduce the propensity for knock. The effect of varying the spark angle relative to MBTD has on the temperature difference between adjoining deactivated and firing cylinders is illustrated on Figure 60 (B).

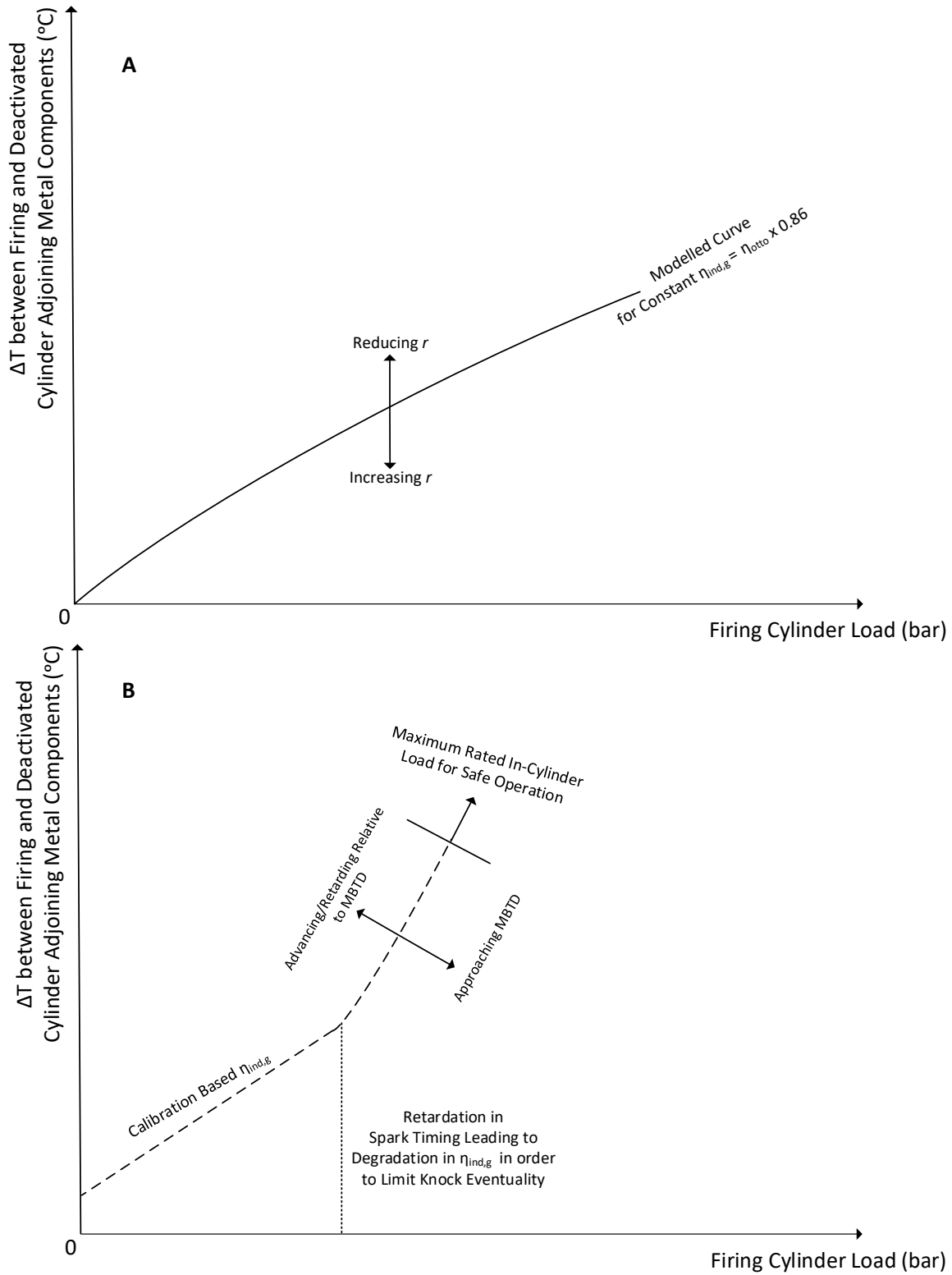


Figure 59: The non-quantitative effect of [A] varying the engine compression ratio and [B] the effect of reduced gross indicated thermal efficiency due to spark retard on the temperature difference between the deactivated and firing when employing cylinder deactivation.

5.6 Reducing Adverse Thermal Effects on the TCE

For the small three cylinder engine considered in this study, specific to the advanced coolant circuit described in *Chapter 4 subsection 4.8.1*, the choice of cylinder to deactivate in order to reduce temperature changes and differences have been considered by varying the pair of firing cylinders. An illustration of the effect for a fully warm coolant and oil temperature is shown in Figure 61. Deactivating the cylinder closest to the block coolant aperture (B), maximises the temperature of the firing cylinders 2 and 3 as the coolant stream progressively warms up as it travels up the block. The first cylinder is thus kept coolest and the temperature differences shown above are thus the largest. Similarly, when deactivating cylinder 2 (C) the temperature differences between cylinders 1 and 2 are relatively minimised however an unnecessary temperature gradient between the deactivated cylinder and the two firing cylinders arises. NVH implications when deactivating cylinder number two would restrict the availability of firing solely on the two outboard cylinders. Due to the firing order being 2-3-1, deactivating either of the outboard cylinders and the centre cylinder is of preference. If the centre cylinder were to be deactivated this would create significant bending moments at the centre of the crank-shaft considering that an imbalanced crankshaft is required for an odd number of cylinders. Deactivating cylinder 3 (D), the warmest cylinder, takes advantage of the warmer coolant downstream of the block inlet aperture minimising the temperature drop after deactivation while moderating the temperature rise of the firing cylinders. Thus cylinder 3 was the optimum cylinder to deactivate. In effect, the modelled temperature difference between the firing and deactivated cylinders reduce by 5°C and 10°C at the cylinder liner and exhaust ports, respectively, independent of load. This is equivalent to the rise in temperature observed when increasing the engine speed by 1000rpm as shown on Figure 59 (A).

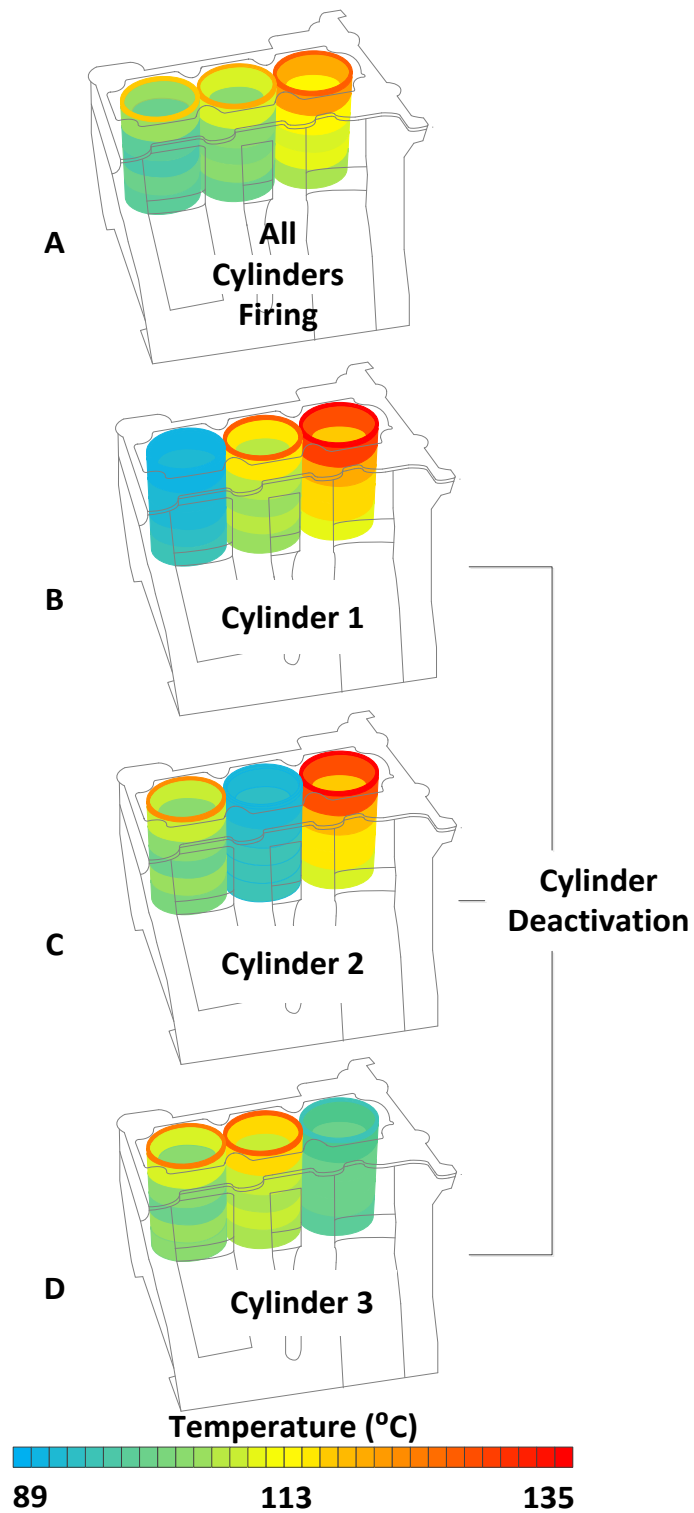


Figure 60: Modelled change in cylinder wall temperatures for cases after deactivating [B] cylinder 1, [C] cylinder 2 and [D] cylinder 3 contrasted with [A] engine operating on all cylinders ($T_b = 60\text{Nm}$, $N = 2000\text{rpm}$ and $T_{\text{cool}} = 90^\circ\text{C}$).

5.7 Exhaust Gas Temperature Changes when Deactivating

In addition to the fuel consumption benefit, faster catalyst ‘light-off’ times are had with cylinder deactivation [5.7]. The reduction in gas-side heat transfer to coolant exhausts higher temperature gases out of the firing cylinders. The geometry of the integrated exhaust manifold is not identical for each cylinder. The exhaust port surface area of the outboard cylinders is 21.9% greater than the surface area of the inboard cylinder. Effectively, this suggested that deactivating the centre cylinder exposes a total exhaust port surface area of 0.246m^2 while deactivating either out-board cylinder exposes an area of 0.219m^2 . This is equivalent to an 11% reduction in total exhaust port surface area. Utilising an energy balance approach in determining the exhaust gas temperature, PROMETS was utilised to compare gas temperatures at the outlet of the IEM.

The predicted change in exhaust gas temperature with varied brake work is shown in Figure 62. For a 10Nm engine brake load the modelled exhaust gas temperature when running on two cylinders is significantly lower compared to the three cylinder case. For loads above 10Nm, deactivation of the centre cylinder generally increases the exhaust gas temperature by 20 to 100 degrees. Denoted by the triangular markers, exposing a smaller surface area, i.e. deactivating one of the outboard cylinders increases the exhaust gas temperature by $\sim 25\text{ }^\circ\text{C}$ compared to when deactivating the centre cylinder. Table 7 summarises the modelled benefits of deactivating the outboard cylinder (i.e. furthest from coolant inlet aperture) compared to deactivating the cylinder closest to the FEAD, cylinder one, and the inboard cylinder, cylinder two. In principle deactivating cylinder three, furthest downstream of the coolant aperture is suggested in terms of minimising the temperature different between cylinders and retaining an elevated exhaust gas temperature. Modelled effects on warm-up times show little difference in deactivating cylinder one, two or three. Temperature changes in a gasoline engine are lower compared to that of diesel engines as the exhaust gas temperature is already significantly higher under normal operation. As engine operation moves away from low power operation, i.e. 10kW, the increase in exhaust gas temperature with respect to brake power plateaus. In effect, the increase in exhaust gas temperature for a diesel engine with cylinder deactivation is significantly better as the rise had during low and part load operation is significantly higher than that of petrol engines.

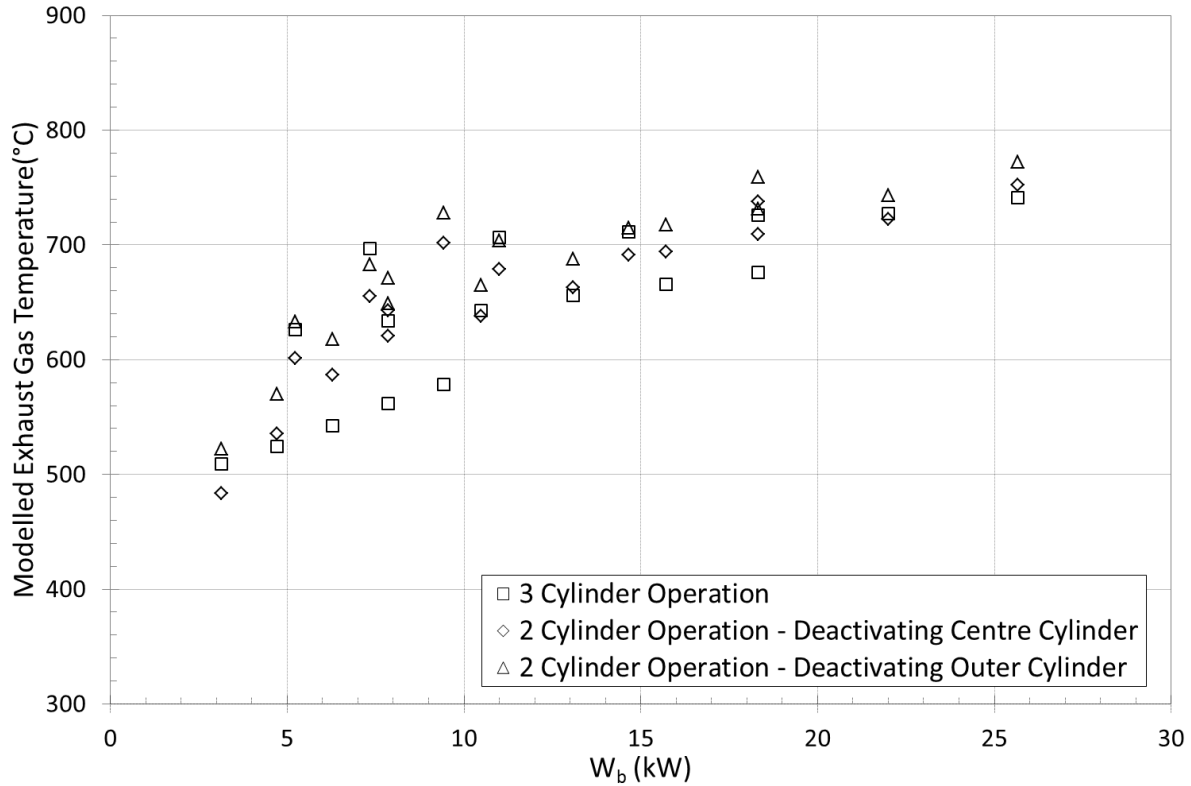


Figure 61: Modelled exhaust gas temperatures when operating on three cylinders compared to two cylinders when deactivating the out-board cylinder compared to the centre cylinder, $N = 1500 - 3500\text{rpm}$, $T_b = 20 - 70\text{Nm}$.

Attribute	<i>Deactivating Cylinder 1 (outboard)</i>	<i>Deactivating Cylinder 2 (centre)</i>	<i>Deactivating Cylinder 3 (outboard)</i>
Increase Pre-Turbine Exhaust Gas Temperature (K)	+	-	+
Increased Heat Release to Coolant Via Exhaust Ports (W/m^2)	-	+	-
Reduce Temperature Difference Between Adjoining Components (K)	-	-	+
Increase Wall Temperature of Deactivated Cylinder (K)	-	-	+

Key + Contribution
 - Counter-effective

Table 7: Comparison of the effect of deactivating said cylinders on the temperature and heat transfer.

5.8 Limiting the Adverse Delay in Warm-Up Time When Deactivating

Reduced coolant and oil warm-up rates associated with cylinder deactivation were investigated by varying the onset time for deactivation over the NEDC, as shown in Table 8. The NEDC was chosen over warm-ups performed under constant operating conditions due to the majority of the drive cycle performed over a warm-up. The reduction in fuel consumption during this warm-up process is attributed to an increase in the gross indicated thermal efficiency and pumping benefits. Deactivation was disabled when the deterioration of the gross indicated thermal efficiency resulted in a fuel consumption penalty. For reference purposes the zero percent is indicative of the reactivation point as shown on the BSFC map on Figure 63. Also, to retain some semblance to reality, deactivation was limited to 1250rpm to imitate a limit due to NVH. The NVH limit was based on vibrational characteristics of the chassis of the VW Polo powered by a 1.4l TSi engine capable of deactivation. Furthermore a minimum deactivation period of 2 seconds was modelled. This was based on observations that the ECU monitors that all the criteria for cylinder deactivation are met over a two second interval prior to enabling deactivation [5.11].

Generally, enabling cylinder deactivation over a longer time interval of the drive cycle prolongs the time for coolant to warm-up however the oil warm-up rate remains largely unaffected. If cylinder deactivation is present over the majority of a warm-up procedure the delay in warm-up time may be significantly be reduced if deactivation is onset past a coolant temperature of 40°C. This agrees well with data analysed by *McGhee et al* [5.11] where deactivation on the 1.4l four cylinder engine was enabled past a coolant temperature of 40°C and oil temperature of 10°C. Furthermore, modelling the effects of enabling piston cooling jets during the warm-up process proved not to enhance the warm-up rate of the coolant or oil.

Coolant Temperature at which deactivation enabled (°C)		20	30	40	50	60	70	90
<u>Source of m_f benefit</u> <i>Pumping losses and gross indicated thermal efficiency</i> <u>Time Constraint</u> <i>3 second minimum deactivation window</i> <u>Deactivation Operating Window</u> <i>Refer to BSFC map on Figure 63</i>	Time for coolant to reach 90°C	938	927	921	914	902	893	882
	Oil temperature when coolant reaches 90°C	84	83	82	80	80	78	76
	Fuel consumption reduction over NEDC (%)	3.31	3.21	3.05	2.79	2.39	2.00	0.41
	Percentage of Drive Cycle Time Deactivated (%)	40%	39%	37%	34%	30%	25%	16%

Table 8: Modelled delays in coolant and oil warm-up times over the NEDC and associated fuel consumption deterioration with the delays.

5.9 Discussion

In this chapter the effects cylinder deactivation has on engine thermal behaviour have been examined, with particular focus on quantifying cycle-averaged changes in component temperatures and reducing associated adverse thermal effects.

Based on good agreement between measured and predicted temperature distributions in the liner coolant and oil temperatures for the engine running on all three cylinders the model proved to be robust over various operating conditions. To model the effect of cylinder deactivation in the deactivated cylinder heat transfer from the gas-side was assumed to be small in the exhaust ports. This approach results in numerically increasing the mass of fuel injected into the firing cylinders such that the Reynolds number increases. In turn, the temperatures of the components comprising the deactivated cylinder reduce to local coolant temperatures. Consequential to this components of the deactivated cylinder endure the largest temperature changes in the engine. Temperature changes increase with engine brake load and engine speed.

Thermal models are time and cost-effective solutions in providing information on component temperatures which are difficult to access or restricted due to motion. The installation of thermocouples or infra-red sensors [5.9] to monitor the temperature of components such as exhaust valves or pistons [5.10] is a delicate, expensive and time consuming process. With this the model predicts that the lower exhaust valve stem undergoes the largest temperature change in the engine in the range of $< 400^{\circ}\text{C}$. The near vacuum pressures measured above the motored piston, see *Chapter 4 section 4.11.2*, would however discourage the use of non-individually controlled jets. The continued suction effect due to the vacuum would augment accumulation of oil on the top landing of the piston. However, this development is applicable if independent control of the piston cooling jet solenoids were made possible or piston design were improved to drain accumulation of oil [5.1].

Time constants for components to settle to new equilibrium temperatures when deactivating or reactivating are predicted in the range of 10 to 25 seconds. Dependence on coolant flow-rate and the magnitude of the temperature change are explanatory for the range of the time constants, although this might not be apparent when physically observing changes in an engine.

Changes in engine friction when considering cylinder deactivation are difficult to analytically resolve due to the complexity of the phenomenon. For instance, to understand the changes in the camshaft main bearing friction, associated with cylinder deactivation, crank-angle resolved tools are required to compute the effect of the transient change in bearing load and thus film thickness. This remains outside the scope of the time-averaged approach used in this modelling instance. For simplification, the viscosity correction

is based on a global engine oil temperature. This proves to be adequate for the purpose of modelling engine thermal behaviour which is primarily dependent on changes in the magnitude of heat transfer on a cylinder specific basis. Nonetheless, tribo-dynamic analysis carried out by *Mohammadpour* [5.5] show that the net effect cylinder deactivation has on friction dissipation experienced in the bearings are negligible. Thus this validates the approach used in this instance.

Friction at the piston level is however more complicated. The effect of the partial vacuum formed as the piston approaches BDC on piston ring conformity against the cylinder walls remains uncertain. Although studies by *Ma* [5.11] have shown that cumulatively the magnitude of oil sucked onto the top piston landing over extended deactivation periods can be larger than that for firing piston, this has been shown on a pressure trace where the minimum in-cylinder pressure for the deactivated cylinder reaches 0.65barA. Experimental findings for the TCE shown in *Chapter 4*, agreeing with experimental findings by *Gottschalk* [5.12] have shown that the minimum in-cylinder pressure can reduce to values below 0.20barA. As such the effect on oil consumption, oil contamination and contamination effects on friction levels remains unanswered. However this would require detailed experimental analysis coupled with analytical modelling of the piston friction. A simplification was taken in this modelling instance assuming that air is present between the piston ring and cylinder wall although the presence of oil and air between the piston ring and liner is left to be ascertained in future studies. A simple approach was instead taken where piston friction in the deactivated cylinder was modelled to be the same as the piston friction in the firing cylinders. Friction in the deactivated cylinder is modelled to slightly reduce, i.e. <1%, compared to when firing on all. This however has a negligible effect on fuel consumption.

Choosing the optimum cylinder to deactivate is dependent on the manufacturers' choice of valvetrain technology (i.e. packaging) along with dynamic considerations such as balancing of the crankshaft. For 'V' or 'W' type engines where entire banks of cylinders are deactivated *Adcock* [5.13] reported that altering deactivation between cylinder banks reduces the adverse thermal effects of deactivation. Contrarily employing dynamic skip-fire mitigates thermal changes due to deactivation thus rendering the dilemma obsolete [4.14]. However, at the time of this investigation the availability and commercial applicability dynamic skip-fire has not been exemplified. Nonetheless, for cylinder deactivation keeping the deactivated cylinders warm is preferential such that upon reactivation factors such as combustion quality, emissions and soot formation remain unaffected. In the case of the TCE the ideal cylinder to deactivate was shown to be that furthest downstream of the coolant inlet aperture. Furthermore temperature differences between components in firing and deactivated cylinders are also minimised by doing so. The reduction in temperature difference was found to be equivalent to the temperature increase a component endures at a given brake load when augmenting the engine speed by 1000rpm.

The warm-up rate of the coolant is delayed due to the reduced surface area reducing the transfer of heat from hot gases. Through modelling an optimisation study was carried out on the NEDC altering the onset time for deactivation based on coolant temperature. It was found that the delay in coolant warm-up is minimised when on-setting cylinder deactivation between temperatures of 40 and 50°C while still retaining a significant fuel consumption benefit over the drive cycle. This study has been conducted in light of ensuring that cabin heating is provided to the passengers without significant delays for comfort purposes. Experimental studies on cylinder deactivation applied to the two in-board cylinders of a 1.4l four cylinder engine used to power the VW Polo GT have shown deactivation is onset when the oil temperature is above 10°C and when coolant temperatures are above 42°C [5.8]. Further investigations on predicted fuel consumption improvements associated with cylinder deactivation are described in *Chapter 6*.

The main conclusions concerning operating the TCE safely thermally with cylinder deactivation can be summarised as follows:

- Heat resulting from rubbing friction in the liner of the deactivated cylinder is weakly affected by cylinder deactivation as this is strongly dependent on coolant temperature.
- In order to limit the prolonged effect on warm-up rate due to cylinder deactivation, the onset of deactivation should be between a coolant temperature of 40 to 50°C and an oil temperature of 20°C.
- Temperature changes in the lower exhaust valve stem due to cylinder deactivation remain within safe engine operating temperatures. The temperature change when deactivating one cylinder up to 33% WOT is analogous to a rapid acceleration event wherein the engine operates at 66% WOT followed by a rapid deceleration event and engine switch off.
- The largest modelled temperature difference between adjacent cylinders is in the inter-bore region being around ~60°C. Based on nominal temperature differences reported by *Rajput* [5.15] in the inter-bore region of 100°C for an engine firing on all cylinders, a 60°C remains within safe engine operating bounds.

Chapter 6 Cylinder Deactivation Effects on Engine Performance

6.1 Introduction

In this chapter fuel consumption improvements due to cylinder deactivation have been investigated for the TCE. This work was undertaken using the characterised multi-cylinder version of PROMETS described in *Chapter 4*. As a large proportion of the fuel consumption benefit stems from reduced pumping losses it was imperative that model predicted values compare well with experimental data over modal and transient drive cycles. Second-by-second comparisons over the NEDC, FTP-75, HWFET and US06 as mentioned in, *Chapter 4 subsection 4.10.3*, are shown in Appendix C. Modelled fuel consumption of the TCE, operating on all three cylinders, over cold starting NEDC and FTP-75 drive cycles were intrinsically well estimated.

With this, in the first part of this chapter differences between modelled and physical pumping work estimates are described. Modelled pumping improvements coupled with empirical expressions describing the changes in the gross indicated thermal efficiency, are then used to predict the potential cylinder deactivation has on reducing fuel consumption. Empirical functions were described through experimental work carried out at the University of Nottingham. Predicted magnitudes of fuel saved for cylinder deactivation with respect to engine brake load and engine speed are quantified. The potential for cylinder deactivation to reduce fuel consumption on different drive cycles was then investigated through simulation and expressed in percentages. The effect NVH has on the potential fuel consumption benefit over these drive cycles was simulated by setting arbitrary engine speed envelopes for operation of cylinder deactivation. With this the potential of using the technology over idling periods is also assessed.

Adding to the modelling work, real world driving data is used to visually depict engine speed and brake torque residence times over different routes. The influence of driving style on the proportion of total fuel consumed over the different routes is also addressed through this work. This expands on work carried out in collaboration with Dr. Michael McGhee [6] on a 1.4l four cylinder TSi gasoline engine used to power the VW Polo GT [6.1]. The impact cylinder deactivation has on fuel consumption benefits over real world driving routes was then assessed through PROMETS for the 1.4l engine and the TCE. Factors influencing the employment of cylinder deactivation such as traffic and gear selection are also briefly investigated for real world driving routes.

6.2 Modelling Performance Changes with Cylinder Deactivation

6.2.1 Pumping Losses and Gross Indicated Thermal Efficiency Calculations

Holistically, the improvement in fuel consumption is described through changes in pumping work and gross indicated thermal efficiency as shown in the expression below:

$$m_f = \frac{P_b + P_p + P_f + P_a}{\eta_{i,g} \eta_c} \quad \text{Equation 95}$$

Where P_b is the brake power, P_p the pumping power, P_f the friction power, P_a the ancillary power and P_m the power required to motor the deactivated piston in the deactivated cylinder. Modelled pumping losses are calculated by subtracting a look-up table based exhaust manifold pressure value, p_{ex} , with an iteratively solved intake manifold pressure value, p_i . The expression for the pumping loss is shown below.

$$P_p = (p_{EX} - p_i) V_s \frac{N}{120} \quad \text{Equation 96}$$

The expression is strongly dependent on the reduction in swept volume, V_s . For the TCE the volume reduces by 33%. Upon deactivation the cylinder volumetric efficiency increases. For a given engine speed, the volumetric efficiency correction factor based on the intake manifold translates horizontally up the x-axis. The effect of varying exhaust pulse frequency and valve timing are not accounted for through this expression. This remains outside the scope of this investigation as engine calibration entails a study in itself.

Any improvement or deterioration in the gross indicated thermal efficiency also affects the solution for the intake manifold pressure. This is representative of the spark retard relative to MBTD. Shown in Appendix D Figure 92 are the empirical expressions for the changes in gross indicated thermal efficiency with respect to engine brake load for various engine speeds. The experimentally observed change in gross indicated thermal efficiency is added or subtracted by a theoretical constant efficiency value that is based on the expression defined in Equation 97. For the TCE the theoretical gross indicated thermal efficiency at MBTD is 42.9%. Combustion efficiency, η_c , has been empirically expressed showing a dependence on equivalence ratio [6.2],

$$\eta_c = \begin{cases} 0.98 & \phi \geq 1 \\ 2.662 - 2.26\phi + 0.577\phi^2 & \phi < 1 \end{cases} \quad \text{Equation 97}$$

The equivalence ratio has been held at a constant value of 1 for the study of cylinder deactivation with no discrepancy for the engine firing on all cylinders. Combustion efficiency for this modelling instance is thus at a constant 98%. Effects of varying the intake charge temperature past the compressor have not been modelled such that the effectiveness of the inter-cooler was not assessed. For this investigation the intake charge temperature is held at a constant 20°C.

6.2.2 Discrepancy between Modelled and ‘Real’ Pumping Losses

Pumping losses in PROMETS are calculated as isobaric processes. In reality, when the intake valves open, during the suction phase, heat transferred from the cylinder wall to the fresh air charge increases the charge pressure. In effect, as the piston travels downwards, towards BDC, the reduction in the density of the trapped charge results in a reduction in the intake stroke pumping work. This reduces the resultant opposed force due to the crankcase pressure. Likewise, the process of internal scavenged flow or internal EGR, emanating from the exhaust side, marginally increases the in-cylinder temperature and thus pressure.

Inversely, when expelling the by-products of combustion, the in-cylinder pressure resists the upward travel of the piston ($p_{cyl} > p_{crank}$). The pressure in the exhaust manifold experiences large dynamic oscillations typically during part/high load conditions. Calibration settings aim at minimising the resistive force of the high pressured exhaust gases by advancing the exhaust valve opening times prior to the exhaust stroke. Although pressure fluctuations are present due to early exhaust valve opening, absolute changes in pressure are small.

6.3 Fuel Consumption Improvement on the TCE

6.3.1 Percentage Improvements at Constant Operation

Figure 63 shows modelled BSFC percentage improvements for the TCE under fully-warm conditions. Between 0 and 20Nm, the percentage improvement in fuel consumption remains largely constant regardless of engine speed, residing in the 25% to 10% reduction range, respectively. In practice for low loads poor mixture of the fuel and air charge may result in large coefficients of variation in in-cylinder pressures producing unstable readings of the fuel consumption improvement. For modelling purposes a constant fuel consumption improvement is taken. Between engine brake loads of 20 to 80Nm the percentage improvement in fuel consumption increases with increasing engine speed. This is realistically attributed to a smaller retard of the spark angle as engine speed increases. For loads between 40 and 80Nm, the improvement, if present, is balanced by the penalty imposed by the deterioration in gross indicated thermal efficiency and the persisting benefit due to reduced pumping losses.

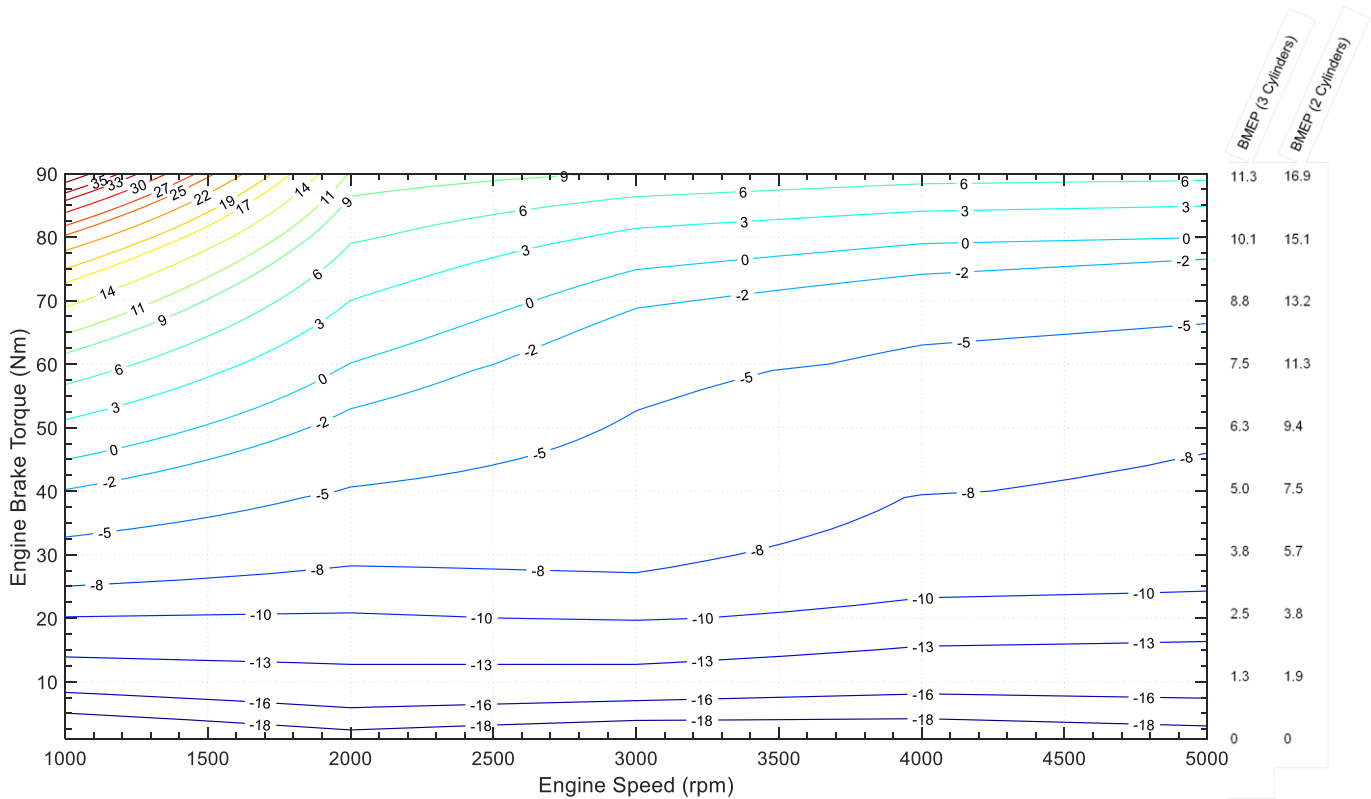


Figure 62: Modelled brake specific fuel consumption percentage improvements with deactivation of one cylinder on a 1.0l three cylinder engine (engine rated brake torque of 170Nm at 1500rpm).

The majority of the fuel consumption benefit is had at light engine loads, reducing as engine load increases. This is primarily due to the reduced importance pumping work has as engine load increases combined with the deterioration in gross indicated thermal efficiency. The break-down of the benefit stemming from changes in pumping and gross indicated thermal efficiency are shown in percentage terms in Appendix D Figure 93. Modelled pumping work changes with cylinder deactivation are also shown in kilowatts Appendix D Figure 94. Given this, for very low engine loads pumping work accounts for roughly 45 to 33% of total fuel consumption further reducing at part loads to values between 5 and 0.5%. Therefore any reduction in pumping work marginally affects the fuel consumption benefit as engine load increases. Given this the reduction in pumping work associated with deactivation accounts for 55 to 100% of the total fuel consumption benefit with respect to increasing brake load. As the importance of pumping work reduces the deterioration in the fuel consumption improvement at part load is chiefly due to the fall in the gross indicated thermal efficiency. Given this, the fuel consumption penalty due to the motoring of a piston is dependent on engine brake load but generally varies between 0.05 to 0.01% increase in fuel consumption at low and part loads respectively.

6.3.2 Magnitude of Improvement

At light loads although the percentage benefit is similar for differing engine speeds, the reduction in the magnitude of fuel injected into the firing cylinders is not the same. Figure 64 generally shows that the reduction in mass of fuel injected, for a given engine brake load, increases with engine speed. As engine speed increases the magnitude in fuel consumption reduction becomes significant compared to lower engine speed counterparts. The magnitude in fuel reduced for 1000rpm increments increases by a two fold equivalent or 100%. As example, for an engine brake load of 10Nm at 1000rpm five times more fuel is consumed and saved running when operating at 4000rpm.

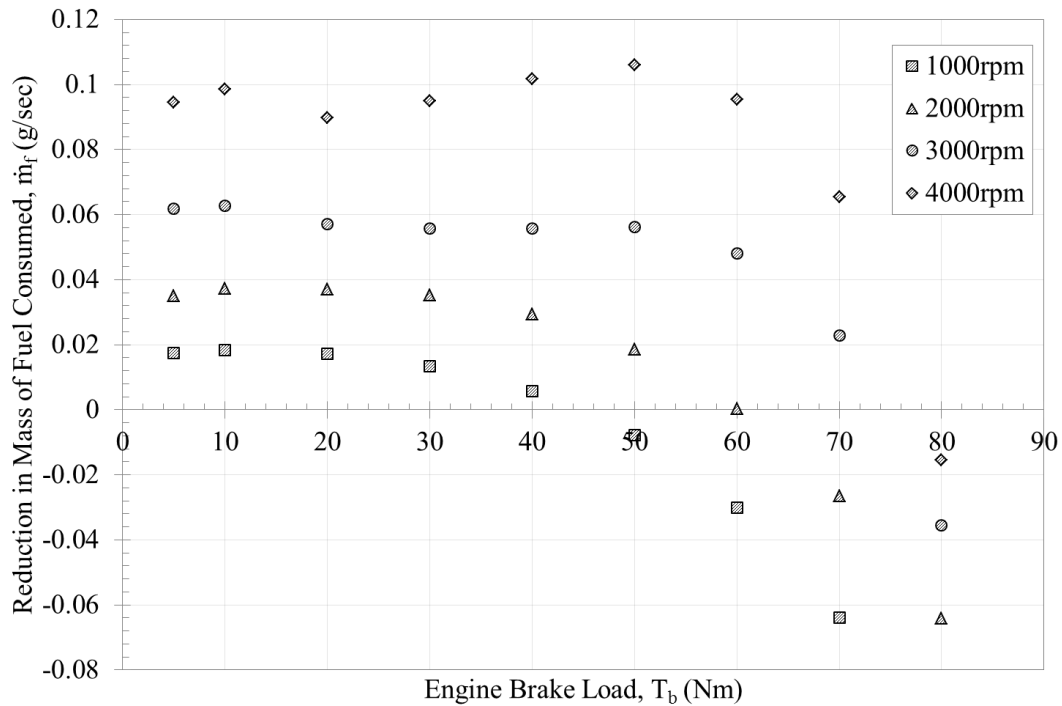


Figure 63: Modelled reduction in mass of fuel injected with deactivation of one cylinder on a 1.0l three cylinder engine.

6.4 Fuel Consumption Improvements on Drive Cycles

6.4.1 Drive Cycle Brake Torque and Engine Speed Inputs

Drive cycles are simulated through PROMETS by inserting second-by-second engine brake torque and engine speed traces. These two inputs can be acquired, 1) by performing a drive cycle on a chassis dynamometer wherein an operator or robot follows a designated vehicle speed trace or 2) by simulating resistive forces overcome by a vehicle. Data emanating from both these sources has been used to simulate

the effects cylinder deactivation has on fuel consumption over the NEDC, FTP-75, WLTC and ARTEMIS. For the NEDC and FTP-75, brake torque and engine speed traces were supplied by British Petroleum™. These traces were acquired through chassis dynamometer tests specific to an undisclosed commercially produced vehicle. Contrarily, WLTC and ARTEMIS inputs for PROMETS were acquired through a vehicle simulation tool named ‘Advanced Vehicle Simulator’ ADVISOR [6.3]. The principles and configuration of the simulation tool are briefly discussed in the following subsection.

6.4.1.1 Vehicle Simulator – Brake Torque and Engine Speed Outputs

It was important that specific vehicle attributes be retained for the simulation of drive cycles such that brake torque and engine speed traces accurately represent the target vehicle used on chassis dynamometer tests. Engine brake torque and engine speed were calculated by inputting vehicle speed traces for the WLTC and ARTEMIS [6.4] [6.5]. The required engine brake power is characterised by resistive forces impeding forward motion of vehicle and is expressed as the sum of the rolling resistance P_R , drag resistance P_D , momentum of the vehicle P_m , and resistance due to inclination P_g ,

$$P_{motive} = P_R + P_D + P_m + P_g \quad \text{Equation 98}$$

The mechanical efficiency of a powertrain reduces the *actual* brake torque outputted from the engine to the wheels. The TCE is fitted in traverse to the direction of motion of the vehicle therefore the mechanical efficiency of the powertrain was taken as $\eta \approx 0.95$ [6.6].

$$P_{motive} = P_i \eta \quad \text{Equation 99}$$

Vehicle rolling resistance describes the force required to overcome friction between the tyre and road surface. This is expressed as a product of the static mass of the vehicle, road surface resistance coefficient and velocity, as shown [6.7],

$$P_R = T_{RR} \omega = T_{RR} \frac{v}{r_o} = -F_z f_R r_o \frac{v}{r_o} = -F_z f_R v \quad \text{Equation 100}$$

Where T_{RR} is the torque generated due to the road resistance which is a function of the tyre radius, r_o ; force exerted on each tyre, F_z , due to the apparent mass, m' , of the vehicle; and the road surface resistance coefficient, f_R . The C-segment Ford vehicle represented here has a mass of 1,454kg inclusive of an 80kg passenger. Also, consideration of the effect of reciprocating and rotating components, i.e. crankshaft, camshaft and others, has to be accounted for while calculating the overall vehicle mass. These components create an effective inertial mass. Therefore an apparent mass m' is used as a substitute for the actual vehicle mass, m [6.6].

$$m' = 1.03 \cdot m \quad \text{Equation 101}$$

The resistance coefficient for typical passenger vehicles operating on tarmac is in the range of $0.01 < f_R < 0.02$. An intermediary value of 0.015 was used [6.8].

The drag force experienced by the vehicle is dependent on the vehicle's drag coefficient, frontal area, air density, velocity of travel and head wind, as shown,

$$P_D = \frac{1}{2} \langle \rho C_D A (v + v_o)^2 \rangle v \quad \text{Equation 102}$$

The density of air was calculated assuming a constant air temperature of 20°C while head wind effects were nullified. The C-segment vehicle has a drag coefficient of $C_D = 0.3$ and frontal surface area of $A = 2.22\text{m}^2$.

The momentum of the vehicle must also be accounted such that excess power required in accelerating the vehicle from a constant velocity or standstill position is accounted for. Contrarily while the vehicle is decelerating the momentum of the vehicle reduces the required brake torque to overcome rolling and drag resistances. This is shown through the following expression,

$$P_m = m' \frac{d^2x}{dt^2} v \quad \text{Equation 103}$$

Lastly, the increased or reduced resistive force due to road surface inclination or declination is accounted for in the following expression,

$$P_g = m' g \sin\theta v \quad \text{Equation 104}$$

Road gradients are not present on legislative drive cycles therefore this last term was nullified.

In ADVISOR engine speed is determined as a function of the tyre radius, r_{tyre} ; gear ratio, n_i ; and vehicle speed. Gear ratio is appropriated based on a vehicle speed band for a given number of gears. The expression for engine speed, $N_{i,Durashift-6HP}$, is shown below,

$$N_{i,Durashift-6HP} = \frac{v_i 16.7 n_i}{2\pi r_{tyre}} \quad \text{Equation 105}$$

Gear ratios for a 6-speed manual gearbox have been modelled with the shifting point occurring at a 40% of the maximum indicated speed for a given gear.

$$n_i = \begin{cases} 3.73, & v_{1,max} = 50kph \\ 2.05, & v_{2,max} = 90kph \\ 1.36, & v_{3,max} = 136kph \\ 1.03, & v_{4,max} = 179kph \\ 0.82, & v_{5,max} = 225kph \\ 0.69, & v_{6,max} = 267kph \end{cases}$$

6.4.2 Engine Speed Based Operating Envelopes

Table 9 shows modelled fuel consumption benefits for the TCE when employing cylinder deactivation over the NEDC, FTP-75, WLTC and ARTEMIS, for fully warm starting conditions ($T_{oil} = 90^{\circ}\text{C}$). The effect of limiting cylinder deactivation within different engine speed operating envelopes has been studied. The switchover from two to three cylinder operation, and vice-versa, is based on 0% fuel consumption line shown on the BSFC map. The reduction in the fuel consumption improvement when omitting deactivation periods less than two seconds long has also been studied. For lightly loaded cycles such as the NEDC and FTP-75 the largest fuel consumption benefits are to be had between the 1000 and 2000rpm engine speed range. As the upper limit on engine speed is increased from 2000 to 4000rpm, i.e. a 2000rpm increment, the benefit nearly doubles. On the other hand, for the WLTC and ARTEMIS due to more dynamic loading and reduced time spent in the lower brake torque regions the overall fuel consumption benefit reduces drastically regardless of the engine speed operating envelope. For the WLTC and ARTEMIS 53% and 51% of the total cycle duration is spent between 0 to 30Nm range respectively. This contrasted by 77% of the total time for the NEDC and 75% for the FTP-75, while 6% of the NEDC and FTP-75 is spent in the 60 to 90Nm range c.f. 17% for the WLTC and 18% for the ARTEMIS.

A large proportion of time is spent idling in the four drive cycles; 22.6%, 12.9%, 13.4% and 7.32% for the NEDC, FTP-75, WLTC and ARTEMIS respectively [6.5] [6.8] [6.10]. For engine speeds below 1000rpm the percentage improvement in fuel consumption is significant, denoted by the fourth column of Table 9. The lower engine speed limit has been set to 500rpm, given that the idling speed for the TCE is limited to 850rpm. Commonly the lower engine speed limit for engines capable of cylinder deactivation is cited at around 1250rpm [6.1] [6.9]. This is attributed to poor vehicle NVH characteristics at lower speeds when applying cylinder deactivation, as mentioned in *Chapter 2 subsection 2.3.9*.

<i>Drive Cycle/ Engine Speed</i>	1000 – 2000rpm	1000 – 3000rpm	1000 – 4000rpm	500 – 4000rpm	(500 – 4000rpm) 2 second limit
NEDC	2.72%	4.50%	4.50%	5.69%	5.65%
FTP-75	2.86%	5.35%	5.43%	6.59%	6.31%
WLTC	0.55%	1.37%	1.58%	2.23%	2.00%
ARTEMIS	0.22%	0.56%	0.74%	1.16%	0.76%

Table 9: Fuel consumption benefits for various engine speed envelopes when deactivating one cylinder on the 1.0litre three-cylinder engine over various drive cycles for $T_{oil} = 90^{\circ}\text{C}$.

Reducing the lower engine speed limit from 1000 to 500rpm; while maintaining the upper engine speed limit of 4000rpm, increases the potential fuel consumption benefit had by 1.19%, 1.16%, 0.65% and 0.52% over the NEDC, FTP-75, WLTC and ARTEMIS, respectively. This is equivalent to a 26.4%, 21.4%, 41.1% and 70.3% increase of the total fuel consumption benefit over the NEDC, FTP-75, WLTC and ARTEMIS, respectively. As the absolute reduction in mass of fuel consumed is largest for the lowest loads it is clear that cylinder deactivation should be implemented at lower engine speeds through the development of stiffer chassis [6.1]. This is if start/stop is not used during idling periods.

Simulation of deactivation periods shorter than two seconds were quantified in order to replicate the effect ECU processing-time may have on reducing fuel consumption improvements. This is shown on column five of Table 9. The reduction in fuel consumption benefit is small for the NEDC, i.e. 0.02%, characterised by its modality. For the FTP-75, WLTC and ARTEMIS the reduction increases by a magnitude 0.28%, 0.23% and 0.4% respectively. A 1.47% increase in fuel consumption improvement is had when starting from a fully warm state compared to a cold started cycle, shown in Table 9. The reduction under cold starting conditions is attributed to higher frictional losses.

6.5 Real World Driving

Drive cycles are referred to as a standard for comparing engine performance for legislative purposes. Real world driving data on the other hand is specific to a person's quotidian commute and this is varied. The characteristics of a commute are largely defined by the infrastructural development of the localities through which a driver travels. For example, as population density increases road signalling and traffic become more common to ensure safe environment for pedestrians [6.11]. Therefore during 'rush hour' the probability of traffic may increase resulting in a large proportion of time spent accelerating and decelerating. Contrarily commutes for inhabitants of rural areas are characterised by segments which encompass urban, motorway and rural passages. Traffic may be scarcer in these demographics and vehicle operation more modal in nature. Given these differences, it was of interest to model cylinder deactivation using real world brake torque and engine speed profiles to quantify fuel consumption improvements.

6.5.1 Description of Routes

Real world data on three quotidian commutes, shown in Figure 65, were obtained by driving a VW Polo GT powered by a 1.4l turbocharged TSi engine capable of deactivating two cylinders. An Influx Rebel CT data logger plugged into the OBD-II port relayed variables from the ECU to an SD storage chip providing second-by-second information on GPS position, fuel consumption, coolant and oil temperatures, AFR, brake torque and engine speed. The first route was known as the *City Route*: an urban route 12.8km

long comprised primarily of passages through the city centre and extra-urban segment of Nottingham. The second route as *Commute A*: a 35.2km long route comprised of a rural, urban, motorway and again brief urban passage. The third route as *Commute B*: a route 20.8km comprised of a short urban passage primarily defined by extra-urban and rural passages [6]. A collection of 12 repetitions for each route (i.e. a total 36 drives) were taken to supply data on the variables mentioned above and in the following subsections. Two drivers of differing age and background split the driving. These drives were performed at varied times during the day (i.e. with varying traffic conditions).

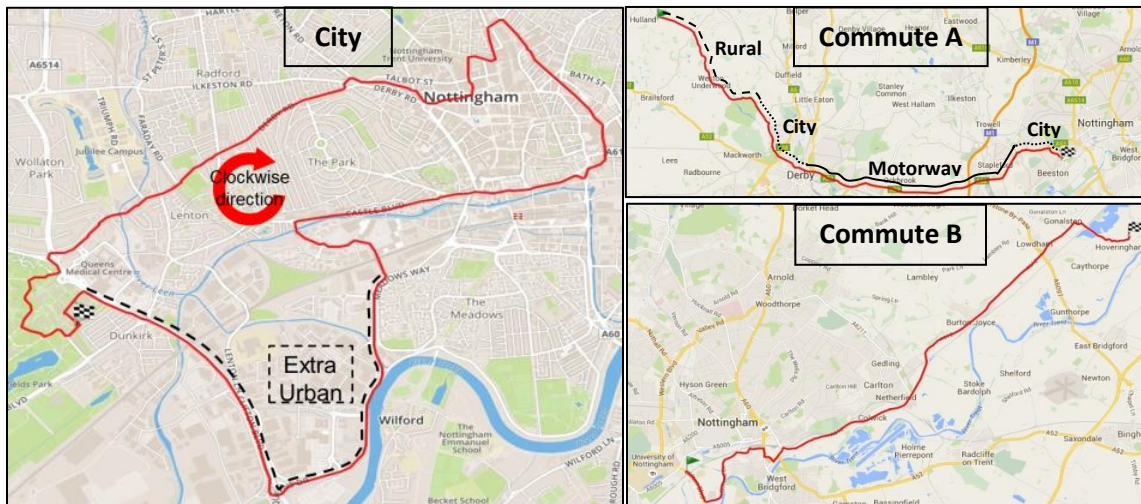


Figure 64. Real world driving routes [6].

Brake torque and engine speed data emanating from the ECU for the three routes were used as inputs for PROMETS for the TCE. Since the 1.4l engine has a higher power rating compared to the TCE, any excess load was capped to the rated brake torque value of 170Nm. Engine speed remains the same inferring that the same type gearbox is utilised.

6.5.2 Operating Condition Residence Times and Related Engine Fuel Consumption

To visually characterise the operational bias in each route, engine operating residence times are drawn on bubble graphs with respect to engine speed and brake load, as shown on Figure 66 (A-F). The graphs have a resolution of 20 by 25. Shown on Figure 66 G, are the residence times for the NEDC. The rated engine speed-torque curve for the 1.4l is denoted by a thick black line while the operating envelope for cylinder deactivation is denoted by a dashed line. Two driving styles are described; one is characterised as ‘economic’ aimed at reducing fuel consumption by minimising accelerations and the other as ‘urgent’ wherein the aim was to reduce time-spent commuting in a law-abiding manner. The ‘urgent’ driving style, shown on Figure 66 (B, D and F) is visually discernible by a larger proportion of time spent in the higher

brake torque and engine speed regions. The NEDC falls under an ‘economic’ driving style wherein the largest torque event achieved is equivalent to 52% of the rated torque while only touching upon specific engine operating points repeatedly. Figure 67 (A-G) shows the proportion of fuel consumed for a given operating point on Figure 66 (A-G). Generally all figures demonstrate that for a fixed engine speed the proportion of fuel consumed for a 10Nm increase in brake torque is of roughly 0.2grams, under fully warm conditions. A simple backhand calculation indicates that the fuel consumed over 10 seconds spent at a 25Nm brake load is equivalent to 1 second spent at a brake load of 250Nm. Therefore although little time is spent on aggregate in the higher brake load segments the percentage of the total fuel consumed in these regions is significant. What is largely inferred from the collection of graphs is that although a significant proportion of the real world routes are spent in the deactivation envelope more than 75% of fuel consumed is allocated to points outside this envelope. This is heavily influenced by long idling periods and short acceleration periods which draw large amounts of fuel relative to low and part load conditions. The following three paragraphs exemplify this by describing the percentage of the total time and total fuel consumed for brake torque bands demonstrating that cylinder deactivation is useful in reducing fuel consumption over moderate and modal type driving styles.

Referring to Figure 66 (A) and (B), pertinent to the *City Route*, operating points remain largely confined below 3000rpm. For the ‘economic’ driving style 74.1% of the total time is spent between the 0 to 50Nm interval of which 19.9% of the time spent is held idling/stopped. This is similar to the 22% observed on the NEDC shown on Figure 66 (G). The proportion of time spent in this region reduces to 70.3% under an *urgent* driving style. For the ‘economic’ driving style the time spent between 50 to 100Nm, 100 to 150Nm and 150 to 250Nm is equivalent to 22.5%, 2.74% and 0.64% of the total time (i.e. total of 25.9%) respectively. While for the ‘urgent’ driving style the spread biases towards the upper end

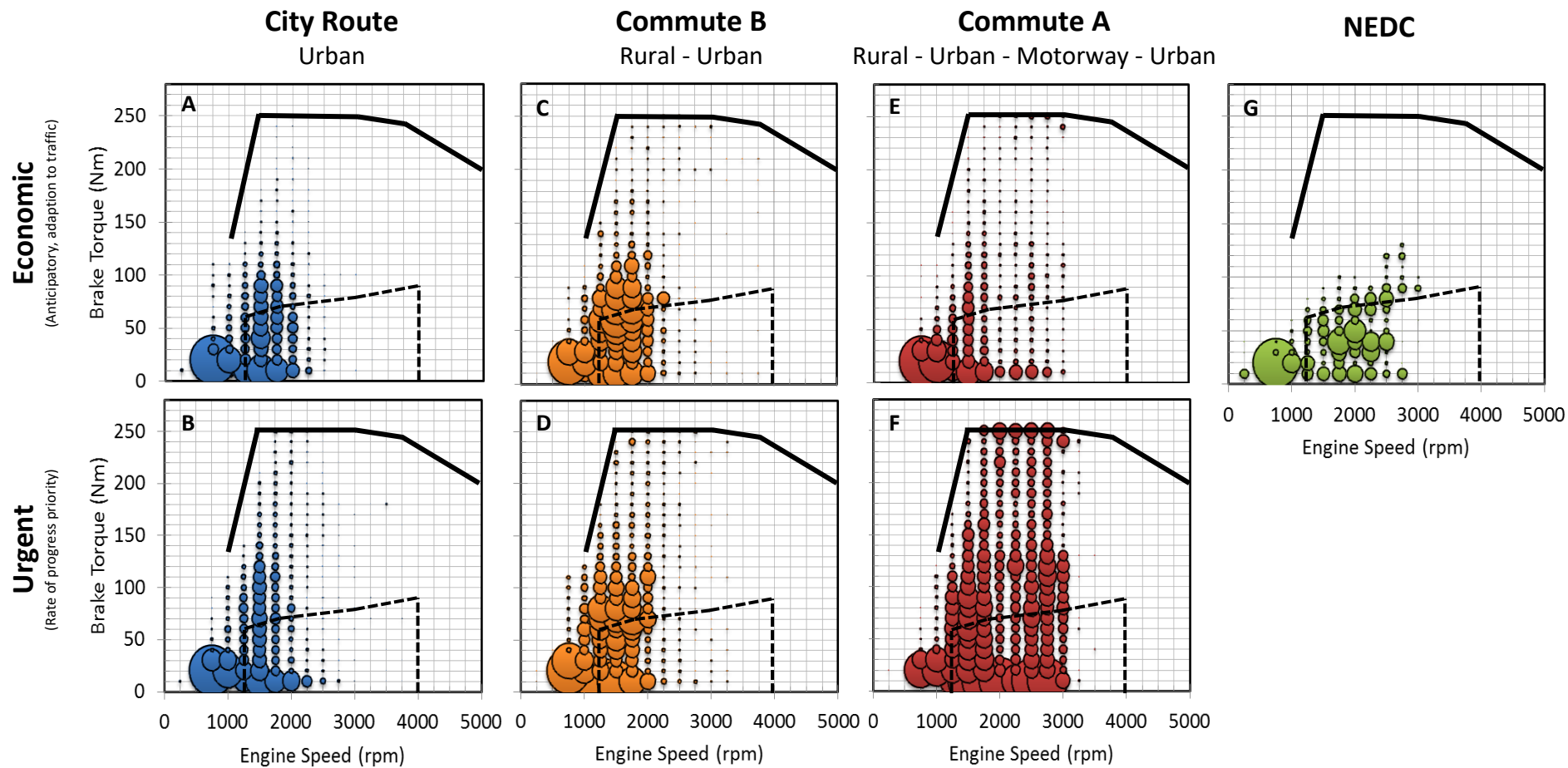


Figure 65: Brake torque and engine speed residence times for a given route/drive cycle.

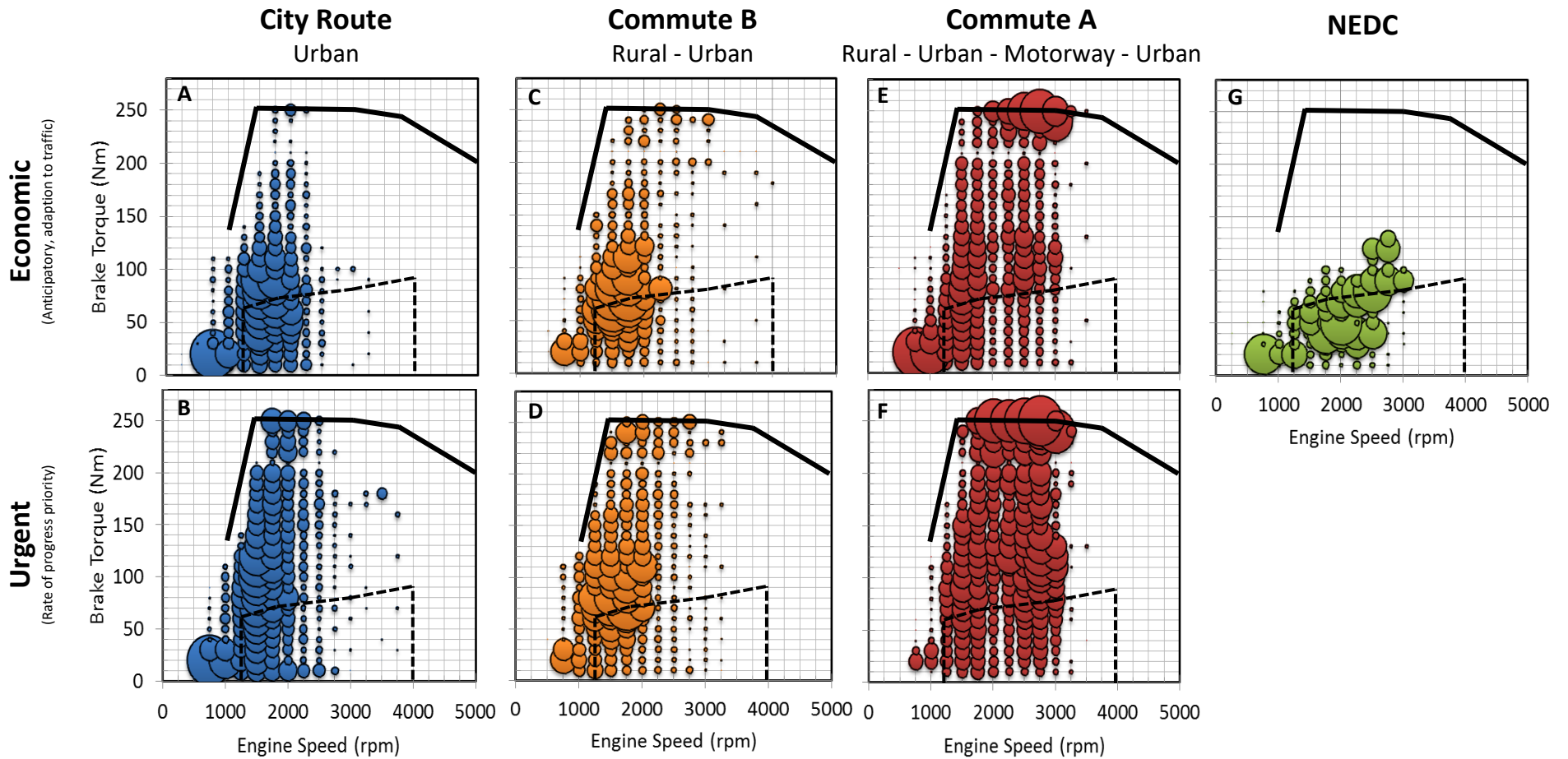


Figure 66: Magnitude of fuel spent on a given engine speed and brake torque operating condition (i.e. described in Figure 61 – torque and engine speed residence times).

at 18.1%, 7.88% and 3.64% (i.e. a total of 29.7%) respectively. Less time is spent in the upper brake torque region regardless of the driving nature due to the intermittency of traffic and traffic signalling resulting in standstill periods. With reference to Figure 67 (A) and (B) although a small change in the time spent in the 0 to 50Nm interval is observed, i.e. ~3.9%, the proportion of total fuel consumed changes dramatically from 39.1% for an 'economic' driving style to 29.1% for an 'urgent' driving style. In turn comparing the percentage of fraction of fuel spent for the 'economic' and 'urgent' driving styles for the remaining brake torque intervals the percentages at first reduce from 46.3% to 29.3% (between 50 to 100Nm) increasing from 10.2% to 21.9% (between 100 to 150Nm) and 4.39% to 19.6% (between 150 to 250Nm) respectively. The two following paragraphs render a similar style analysis of the fuel consumed specific for varying brake torque intervals for *Commute A* and *B* in the aim of informing the reader of the variability imposed on residence times and fuel consumption for varying driving styles.

Referring to Figure 66 (C) and (D) specific to *Commute B*, again operating points remain largely confined below 3000rpm although a larger spread of operating points is visible across the upper half of the engine rated torque region. For the 'economic' and 'urgent' driving styles the proportion of time spent between the 0 and 50Nm interval is similar at 55% of and 55.8% respectively. However less time is spent idling for the 'urgent' style at 2.12% compared to 8.73% for the 'economic' style. For the 'economic' driving style the time spent between 50 to 100Nm, 100 to 150Nm and 150 to 250Nm is equivalent to 38%, 4.49% and 1.7% of the total time (i.e. total of 45%) respectively. While for the 'urgent' driving style the spread this shifts to 33%, 7.56% and 3.6% (i.e. a total of 44.2%) respectively. Comparatively, a larger proportion of time is spent in the 100 to 250Nm interval for the 'urgent' style, i.e. 11.2% compared to 6.2%, resulting from harsher acceleration periods sustained over the entirety of the journey. Shown on Figure 67 (C) and (D) driving characteristics are similar to that of the *City Route*, although a small change in the time spent in the 0 to 50Nm interval is observed, i.e. ~0.8%, the proportion of total fuel consumed reduces by 6.94% for the 'urgent' case compared to the 'economic' case, from 26.9% to 19.9% respectively. In turn comparing the percentage of fraction of fuel spent for the 'economic' and 'urgent' driving styles for the remaining brake torque intervals; the percentage at first reduces from 53.5% to 44.5% (between 50 to 100Nm), increasing from 11.9% to 18.8% (between 100 to 150Nm) and 8.76% to 17.2% (between 150 to 250Nm) respectively.

Figure 66 (E) and (F) show that engine speed points for *Commute A* span across 1000 to 3000rpm although a larger spread of operating points is visible across the upper half of the engine rated torque region compared to the *City Route* and *Commute B*. For the 'economic' and 'urgent' driving styles the proportion of time spent between the 0 and 50Nm interval differs greatly residing in these regions for 76% and 54% of the total time respectively. Traffic conditions increase the number of stops per kilometre

significantly affecting the driving style as denoted in Figure 68. Points A and B are representative of an ‘urgent’ driving style while point C subjugates the driving style to an ‘economic’ one. The proportion of time spent idling is significantly affected by the number of stops encountered along the journey reducing from 18.9% for the ‘economic’ style to 2.79% for the ‘urgent’ style driving. For the ‘economic’ driving style the time spent between 50 to 100Nm, 100 to 150Nm and 150 to 250Nm is equivalent to 14.2%, 5.27% and 4.41% (i.e. total of 23.87%) respectively. While for the ‘urgent’ driving style the spread similarly biases towards the upper end at 20.9%, 13.26% and 11.8% (i.e. a total of 45.9%) respectively. Comparatively, a larger proportion of time is spent in the 100 to 250Nm interval for the ‘urgent’ style, i.e. 11.8% compared to 4.41%, resulting from harsher acceleration periods sustained over the entirety of the journey. With reference to Figure 67 (E) and (F) although a large proportion time is spent between 0 and 50Nm, i.e. 76% (economic) and 54% (urgent), the percentage of the total fuel consumed in this region is small accounting for 29.3% and 12.6% for the ‘economic’ and ‘urgent’ styles respectively. In turn comparing the percentage of fuel spent for the ‘economic’ and ‘urgent’ driving styles for the remaining brake torque intervals the percentage at first reduces from 24.9% to 22.8% (between 50 to 100Nm) increasing from 17.6% to 26.3% (between 100 to 150Nm) and 31.6% to 42.4% (between 150 to 250Nm) respectively.

6.5.3 Representation of the 1.4l Engine

Given the availability of information emanating from the ECU of the 1.4l engine [6], a model of the engine was built in PROMETS. This was undertaken to compare fuel consumption improvements when employing cylinder deactivation on the 1.4l against modelled improvements on the TCE on the three real world routes described above. Key dimensions used to model the 1.4l engine are shown in Appendix E Table 14. Coolant and engine oil volumes were increased proportionally to the volumes in the TCE. Block and radiator thermostat opening temperatures were kept the same as for the TCE agreeing with information found in literature [6.1].

A 6% overestimate in fuel consumption is outputted from the 1.4l engine when simulating the NEDC from a 20°C starting temperature. Given the lack of information available to the author this difference was considered acceptable. Differences are attributed to engine design specifics not readily available to the author such as coolant passage surface areas in the block and head and differences in engine calibration during warm-up. In modelling cylinder deactivation on the 1.4l engine emphasis was given in imitating the degradation in fuel consumption benefit with respect to brake torque. This was produced by matching modelled fuel consumption benefits on constant operating conditions against experimental data shown by *Middendorf et al* [6.1]. Thermally cylinder deactivation on the four cylinder engine is onset for coolant temperatures greater than 40°C and for oil temperatures above 10°C [6.1].

6.5.4 Fuel Consumption Improvements for a 4 Cylinder and 3 Cylinder Engine

Table 10 shows quantified modelled and measured fuel consumption benefits with cylinder deactivation for the 1.4l engine over the three real-world routes and the NEDC. Modelled fuel consumption benefits through cylinder deactivation for the TCE are also quantified. Good agreement exists between modelled and experimental fuel consumption improvements for all four drive cycles shown. Referring to modelled percentage improvements for both engines, the largest benefit is observed over the NEDC.

Rated Power (Psi)	Engine Size (l)	Attribute	Cold Start, $T_{oil} = 20^{\circ}\text{C}$			
			NEDC	City Route	Commute B	Commute A
140	1.4l 4 Cylinder (Deactivation of two cylinders)	$m_{f,total}$	0.469kg	0.593kg	0.696kg	1.68kg
		<i>Modelled Benefit due to Deactivation</i>	7.49%	3.22%	4.85%	1.53%
		<i>OBD Measured Benefit due to Deactivation</i>	~ 6%	~ 3%	~ 6%	~ 0%
120	1.0l 3 Cylinder (Deactivation of one cylinder)	$m_{f,total}$	0.406kg	0.521kg	0.616kg	1.13kg
		<i>Modelled Benefit due to Deactivation</i>	3.05%	1.16%	2.01%	1.72%

Table 10: Modelled fuel consumption percentage improvements over the NEDC and real world driving routes for a 1.4l four cylinder capable of deactivating 2 cylinders and 1.0l three cylinder engine capable of deactivating one cylinder.

The city route provides low fuel consumption benefits due to increased traffic density resulting in a larger percentage of the cycle time spent stopped [6]. *Commute B* shows fuel percentage improvements that are higher due to the calmer driving style adopted. An attempt to maximise deactivation while ensuring that the journey time did not remain compromised reflects the improvement. An aggressive driving style was adopted on *Commute A* with no regard given to the availability of cylinder deactivation on the vehicle. Therefore the magnitude of fuel used per kilometre is equivalent to that observed on the city route where staccato like driving style results in high fuel consumption considering the distance travelled. The estimated fuel consumed over 100 kilometres for the *City Route*, *Commute B* and *Commute A* are 4.6l/100km, 3.3l/100km and 4.8l/100km respectively.

Largely the three cylinder engine yields a smaller fuel consumption benefit through cylinder deactivation. This is due to a smaller potential to reduce pumping losses considering the downsized nature

of the engine, i.e. residing in the sub 1.0litre category. In other words, the relative change in the throttle position for the three cylinder engine for a given brake torque increment is larger compared to the change in the four cylinder engine. Thus cylinder deactivation provides larger benefits for heavily-throttled engine.

6.5.5 Factors Influencing Employment of Cylinder Deactivation

Driving style along with the journey type, whether limited in consistency in operating conditions due to traffic signalling or traffic conditions; as visualised and explained in *subsection 6.5.2* of this chapter, are factors which limit the benefit to be had from cylinder deactivation. Shown on Figure 68 is the effect of traffic volume on the number of stops per kilometre covered on *Commute A*. *Commute B* and the NEDC exemplify that a smoother driving style allows for larger benefits to be had when driving in a manner which is less volatile to acceleration and deceleration periods, as shown by the fuel consumption benefits listed in Table 11.

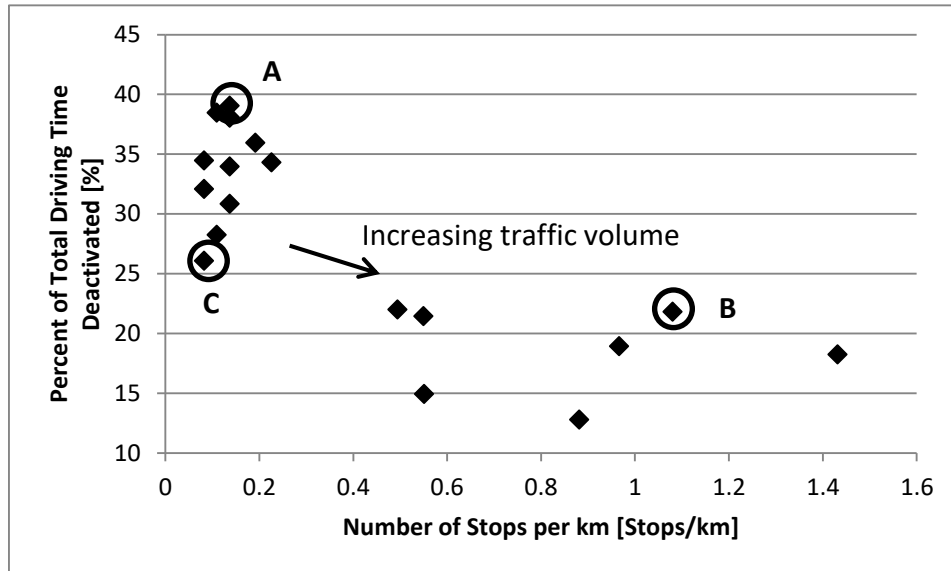


Figure 67: Dependency of time-spent deactivated on the traffic volume for Commute A.

Applying smart automatic gear selection control for constant speed cruising in city driving can yield large benefits assuring that traffic flow remains regular. This is demonstrated by the fuel economy benefit observed on Figure 69, when switching from 5th to 4th gear when cruising at 40kmph where switching from four to two cylinder operation yields a 16% reduction in mass of fuel. Contrarily switching to 3rd

gear imposes a penalty. As shown on Table 11 smart gear selection may be used to evade NVH limited operation on two cylinders [6].

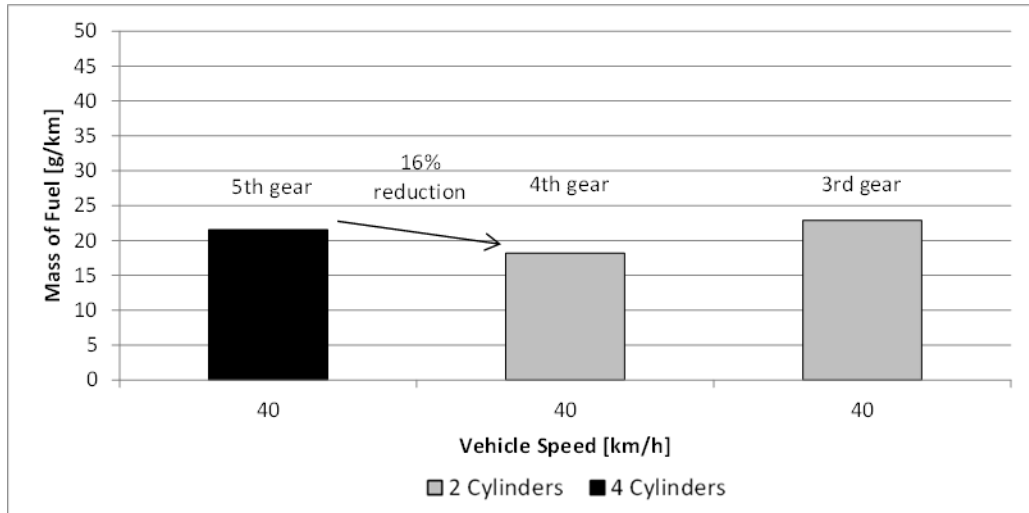


Figure 68: Fuel consumption benefit when downshifting from 5th to 4th gear enabling the use of two cylinder operation at a vehicle speed of 40kmph.

Gear Number	Vehicle Speed (km/h)	Engine Speed (rpm)	Vehicle Speed (km/h)	Engine Speed (rpm)	Vehicle Speed (km/h)	Engine Speed (rpm)
3		1510		2235		2959
4	32	1110	48	1656	64	2203
5		913		1357		1802
6		757		1121		1484

Table 11: Effect of gear number selection on engine speed in remaining outside the NVH constrained band [6].

6.6 Discussion and Conclusions

The effects of cylinder deactivation on the performance of a 1.0l three cylinder engine have not been previously reported in literature. This chapter has shown quantitative information on the benefits had when deactivating one cylinder through PROMETS used in conjunction with experimental data.

PROMETS is not calibrated to account for engine knock when deactivating a cylinder and therefore the higher IMEPs of the firing cylinders are not limited in the engine. The deterioration in the gross indicated thermal efficiency due to engine knock was therefore accounted for by inserting percentage changes emanating from a proto-type engine. In turn coupled with the predicted benefits due to the reduction in pumping, fuel consumption predictions show that the benefit due to the improvement in gross indicated thermal efficiency account for a maximum 45% of the benefit at the lightest engine loads. As engine load increases the deterioration in fuel economy, relative to operation on all cylinders, is solely due to the degradation in the gross indicated thermal efficiency.

Leone and Pozar [6.12] showed through the coupling of experimental and simulation work fuel consumption benefits to be had through cylinder deactivation are limited by six factors: hysteresis; warm-up delay; NVH constraints; no deactivation in the 1st or 2nd gear due to NVH constraints; no deactivation at idling and higher engine speed limits. By hysteresis the implication is that engine calibration decisions to switch into a deactivated cylinder mode should lag behind actual engine operation such that deactivation is not consistently enabled and disabled. Simulations on a 6.8l gasoline truck engine showed that over the EPA city and highway drive cycle benefits reduced by 8.5% from 14.5 to 6%.

Similarly, simulation of constraints on the operating window for cylinder deactivation on the TCE reduces the potential fuel consumption benefit had over the NEDC. Fuel consumption benefits are significant over the NEDC when no constraints are imposed and the cycle is commenced from a fully-warm engine state. Benefits are predicted at 5.69%. Imposing an arbitrary lower bound NVH constraint of 1000rpm however reduces the potential benefit had by 1.19% down to a total fuel consumption improvement of 4.50%. Furthermore, imposing a 2 second delay to represent the hysteresis had by the ECU to enable deactivation a small reduction of 0.06% is imposed. If the engine is started from an ambient temperature of 20°C the benefit further reduces by 1.19%, to a total of 3.31%. Deactivation also imposes an unwanted delay in warm-up time which can be minimised by delaying the onset of deactivation, as shown in *Chapter 5 subsection 5.8*, to a temperature between 40 and 50°C. This marginally affects the benefit reducing it by 0.28%, to a total of 3.03%. Warm-ups can potentially be mitigated by installing latent heat storage devices as suggested by [6.13]. Finally, arbitrarily limiting deactivation to an upper speed limit of 2000rpm shows that the benefit is reduced by a further 0.33%, to a total of 2.70%. An illustration of the effect of these constraints have on the potential fuel consumption improvement is

shown on Figure 70. In essence, based on the non-extensive work looking at arbitrary NVH limits, NVH and warm-ups are the main factors restricting the potential for cylinder deactivation to reduce fuel consumption.

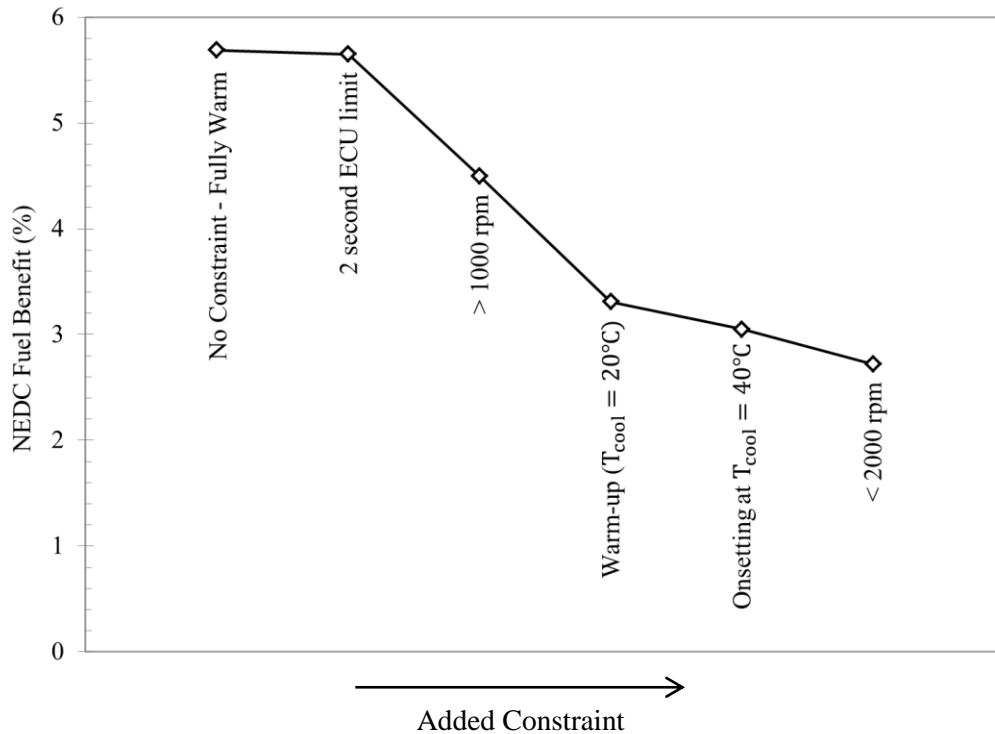


Figure 69: Modelled fuel economy sensitivity due to arbitrary modelled NVH limit and warm-up over the NEDC for the TCE.

Apart from the sensitivity in fuel consumption imposed by NVH factors and engine warm-up, driving style; the nature of the operating conditions encountered on a journey or drive cycle; and reducing engine size for a given vehicle mass reduce the potential fuel consumption benefit had from cylinder deactivation. Firstly, due to deactivation improving fuel consumption at light and part engine loads drive cycles characterised by their light loads show the greatest potential for fuel consumption reduction. As such, for non-constrained operation of cylinder deactivation on the TCE over the NEDC and FTP-75 benefits of 5.69% and 6.59% were modelled. More dynamically loaded cycles such as the WLTC and ARTEMIS show that the benefit reduces significantly down to 2.23% and 1.16% respectively. Furthermore, the potential fuel consumption reduction had by employing deactivation below 1000rpm on these cycles is also less significant due to distribution of fuel consumption biased towards the upper end of engine operation. As example, the benefits reduce from 2.23% down to 1.58% on the WLTC and 1.16% down to 0.74% on the ARTEMIS. Bearing this in mind, real world driving characterised by harsh acceleration and

deceleration periods along with frequent stoppage time minimises the potential fuel consumption improvement to be had.

The main conclusions concerning fuel economy improvements had from cylinder deactivation are as follows:

- The deterioration in gross indicated thermal efficiency is the main influence on the maximum operating point for cylinder deactivation.
- The largest magnitude improvement in fuel consumption with cylinder deactivation is had at low engine brake load conditions for any given engine speed. The magnitude in fuel consumption improvement for the 1.0l TCE increases by 80% for an engine speed increase of 1000rpm.
- Fuel consumption benefits with cylinder deactivation, for the 1.0l TCE, are highest on drive cycles which reside in part in the low and part load engine operation envelopes such as the NEDC or FTP-75.
- As the duration of the drive cycle increases and becomes more dynamic in nature (i.e. characterised by larger residence times in high load operating points) fuel consumption improvements due to cylinder deactivation reduce.
- Benefits due to cylinder deactivation are also severely diminished due to poor vehicle NVH characteristics for engine speeds below 1000rpm. Benefits could be improved by allowing for deactivation for engine speed below 1000rpm.
- For a vehicle fitted with an engine of larger swept volume cylinder deactivation improves fuel consumption benefits as pumping losses at low operation increase.
- Fuel consumption benefits due to cylinder deactivation can be improved if driving style is more anticipatory combined with optimised gear selection and reduced number of stops in a journey.

Chapter 7 Closed Loop Control System for Transient Drive Cycle Testing on ECTBs

7.1 Introduction

Although testing of modal drive cycles has been previously established on ECTBs the repeatability of engine response is poor for transient drive cycles. This translates to poor repeatability of measurements of fuel economy. The incentive to improve engine control over transient drive cycles on ECTBs led to the development of a control system. Aside from the main focus of this thesis pertaining to the modelled effects of cylinder deactivation on the TCE; the process involved in developing such a system is described in this chapter.

The evaluation of engine performance under drive cycle conditions is an important part of powertrain development. ECTBs are widely used in industry and research facilities due to their low inertia properties as well as low operation and maintenance costs. Having an exposed engine facilitates the process of replacing components, if not the engine itself, for the purpose of evaluating fuel consumption. Such upcoming technologies are optimised or electrically driven pumps, modified coolant circuits, variable cylinder deactivation, injection systems pressurised above 300bar and thermoelectric generators [7]. Better suited for running modal tests such as the NEDC, ECTBs perform poorly on high transient events. This is due to the dynamometer's inability to accurately and rapidly decelerate the engine to a designated engine brake torque and speed target with consistent accuracy. In this chapter the development of a closed loop control system is described consisting of a PID controller, feedforward (i.e. map based input) and integrator wind-up processors tuned and extensively tested to run transient drive cycles such as the WLTC on eddy-current test beds for gasoline engines of different sizes.

7.2 Initial PI Control Configuration and Step-Response Characteristics

Prior to the development of the transient closed loop system, four sets of input data were required to run a drive cycle on the eddy current test beds present at the University of Nottingham: dynamometer operating mode (i.e. speed or torque control mode), engine speed, engine brake torque, and engine throttle percentage. The Texcel V4 Froude Hoffman dynamometer controller switches between engine speed and torque control mode maintaining either attribute but neither at the same time. Either attribute is controlled by inducing an electromagnetic flux across a stator to a cooper rotor translating to a resistive torque. Apart from the switching of the control mode the requirement of engine brake torque, engine speed and throttle position over a given drive cycle, demands a precise second-by-second record of the these parameters. As example, to achieve a target brake torque output for a given throttle input while remaining in speed control mode first requires that the engine accelerate to the designated speed target and thereafter once the dynamometer applies a flux maintaining the target engine speed the engine produces a torque

output with any excess pedal position. The need to have a throttle position as an input parameter requires that a vehicle be tested on a rolling road assuring that the exact throttle position be recorded over the entirety of the test. This imposes a dependency on the facilities available or network present to provide this information. Given this if the input throttle position is not sufficient such that the throttle target is not achieved the input must then be iteratively modified until such target is achieved. This is a time-consuming process which would require modification for every drive cycle performed as well as remain dependent on the engine temperature. Also another weakness when depending on the controller speed mode is that the lag time from the point of assigning a target value on the dynamometer to attaining the target value for engine speed is greater than the lag time required to achieve a target engine brake torque. This is due to the dependency in the rate of change of the throttle position value. The engine speed was chosen as the parameter to be independently controlled and used as a source of error for assigning a closed-loop control system modulating throttle position as this was the most unstable engine output.

The first advantage of implementing a feedback control system is that the number of inputs reduces to two compared to four, these are engine brake torque and engine speed. These inputs are still preferably extracted from a vehicle dynamometer test while if not present vehicle chassis simulation tools may be used as a replacement. Figure 71 shows the block diagram schematic for the initial control system implemented solely applying a proportional gain and integral gain coefficients.

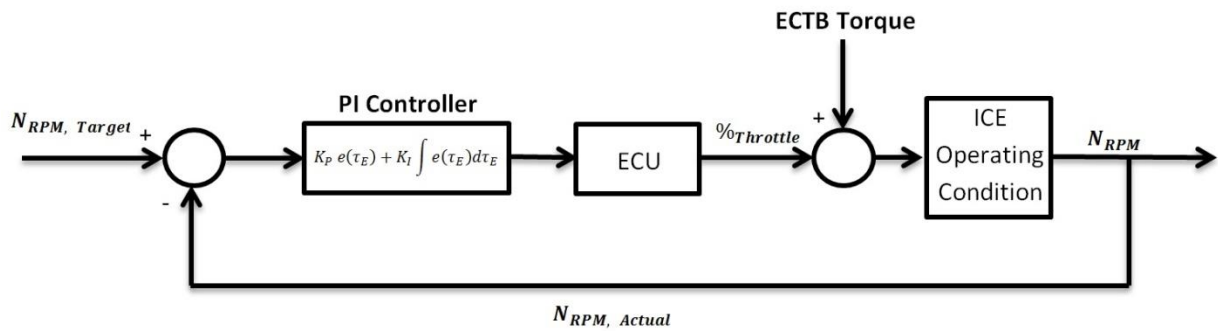


Figure 70: Closed loop proportional gain and integral block diagram for engine speed control.

If PI constants are too large, the system will respond by overshooting the target value and oscillate, requiring more time to stabilise. If constants are too small the system will undershoot, not attaining the target value, requiring more time to reach the target value or never reaching it. During transient tests large increments and decrements in torque and speed occur rapidly and successively. Hence while the controller assigns integral and gain values to meet the target value, it is desired to keep the error margin to a minimum. A method of preventing large accumulation in error is by increasing the rate at which the CPU performs error calculations, i.e. calculation frequency. For the monitoring of engine speed it was

found that due to inertial effects of rotating components within the engine a 10Hz refreshment rate is suitable. With this, the aim was to attain the target engine speed in the shortest amount of observable time within an engine speed error margin of 10%.

The starting point was to iteratively test sets of PI constants that would give good engine response. Tests were performed on a four cylinder gasoline engine commercially used to power a Jaguar XF and Ford Focus ST vehicle; engine details are shown below in Table 12.

Engine Type	In-line, 4-cylinder
Displaced Volume	1999cc
Stroke/Bore	87.5mm/83.1mm
Compression Ratio	10:1
Rated Torque/ Power	340Nm@1700rpm, 177kW@5500rpm
Fuel Injection Type	Direct Injection
Induction system	Turbocharged, Intercooled
Valvetrain Type	Twin-independent Variable Timing
Camshaft Type	Double Overhead Camshaft
Turbocharger Type	Waste-gated, Fixed Geometry

Table 12: Details of engine used for testing of transient drive cycle implementation on ECTBs

Figure 72 below, illustrates four of the 18 responses recorded for varying PI constant sets, where the torque was maintained at 10Nm and a target step profile (1000-1500-1000rpm) for the speed was defined.

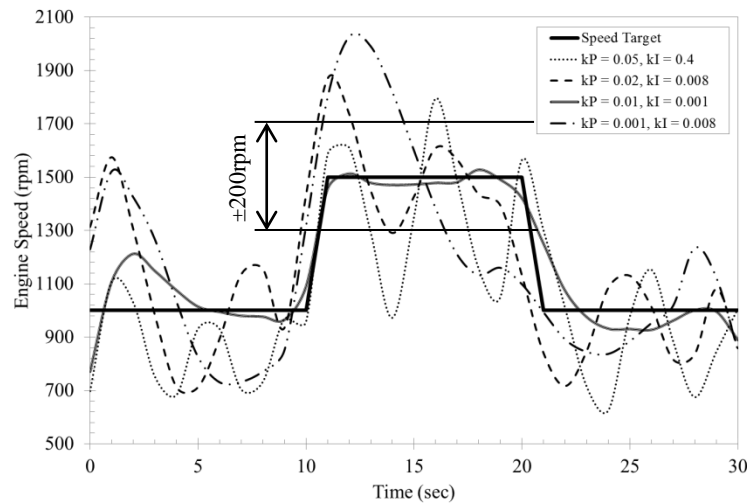


Figure 71: Step target speed profile with constant load of 10 Nm for evaluation of suitable PI constants.

For values of $K_p \geq 0.01$ and $K_I \geq 0.001$ the engine speed overshoot and undershoot by more than 200 rpm for the step changes shown above. The system did not stabilise in less than two seconds and therefore constants above these values were unsuitable for transient cycles. For values of $K_p \leq 0.01$ the system behaved in an unstable manner where overshooting occurred for step increases and the system did not

have sufficient time to stabilise. Effectively, the K_P and K_I values displaying the most accurate control of engine speed were 0.01 and 0.001 respectively. With these constants the ICE stabilised at the desired engine speed within 2 seconds and small undershoots and overshoots occurred remaining within less than the intended error margin of 10%.

Tests performed using the same proportional and integral gain coefficients over successive step changes in engine speed (1000 – 200rpm) and brake torque (i.e. 0 – 200Nm) showed a similar quality in response. However, the accuracy in engine speed response reduced when torque increments greater than 50Nm occurred over the period of 1 second.

7.3 The Effect of Ramping on Engine Speed Stability

From testing system response to step changes in engine speed and brake torque the next phase encompassed testing the PI control system over transient operating profiles over extended periods of time. An approximate ARTEMIS cycle was formulated by calculating a theoretical gross indicated torque profile (a poor substitute for a brake torque profile) based on bagged CO₂ emissions while using a second-by-second measured engine speed profile. This was deemed suitable for testing as long as the operating conditions remained within the engine speed-torque curve. Data for this test emanated from chassis roller dynamometer tests for a Jaguar XF powered by a 4 cylinder direct injection turbocharged engine coupled with an automatic 8 speed gear-box (ZF-8HP). The average of four engine speeds along with a 1Hz gross indicated torque averaged over 1 second intervals were used as engine speed targets. Although using a calculated gross indicated torque value would overestimate the actual brake torque this information was used as a stepping stone and indicator of system behaviour/response when under transient loading profiles. Figure 73 shows the engine speed response over a 200 second segment of the ARTEMIS cycle when undergoing transients with regard to both engine speed and brake torque.

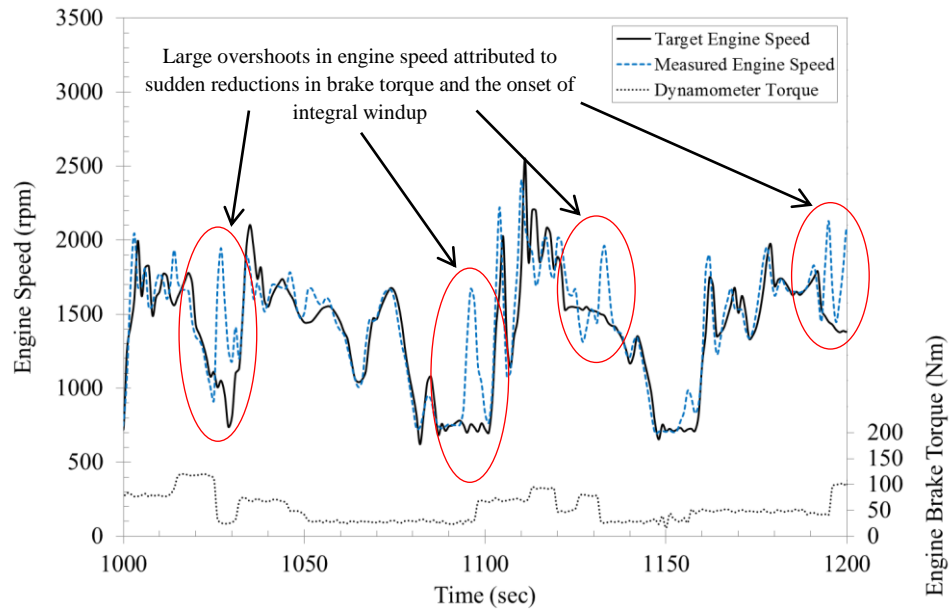


Figure 72: Instability in PI engine speed response over transients with step changes in the brake torque profile over a segment of the ARTEMIS drive cycle.

Although the difference between the target engine speed and measured engine speed remains small, overshoots are present during points where the measured brake torque plateaus significant due to onset of integral windup. Speed errors in the segments encircled in red are in the range of 20 to 130% remaining outside the target error band of 10%. In effect as time progresses the integral wind-up begins to severely affect system performance resulting in large overshoots and undershoots as shown in Figure 74.

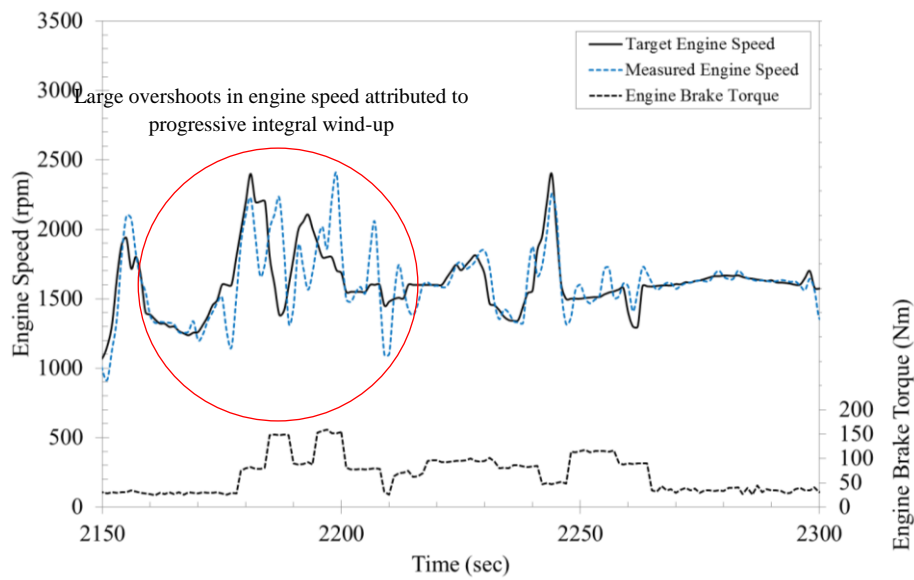


Figure 73: Instability in PI engine speed response attributed to the extended effect of integral wind-up.

To limit the effect of integral wind-up an iterative testing process was undertaken where ramping of the brake torque profile proved to absolve the engine speed instability. The ramping and thus modification of the brake torque profile was computed through a MATLAB script. Figure 75 shows the engine speed response for an un-ramped and ramped brake torque trace for an identical target speed trace. Ramping proves to be an effective technique in reducing wind-up and maintaining controller stability. However when referring to a drive cycle it remains important to withhold vehicle specific attributes through the brake torque trace as these are representative of the rolling resistance, drag force, inertia of the vehicle and if present road inclination. This in turn would revert to the initial time-consuming procedure of having to iteratively modify the brake torque profile for every drive cycle implemented using this system. Therefore the incentive to optimise the control system was undertaken in the aim that system response (i.e. engine speed) remains within a 10% error margin regardless of the severity of the brake torque and engine speed transients while also ascertaining that the system be transferrable to engines of different sizes.

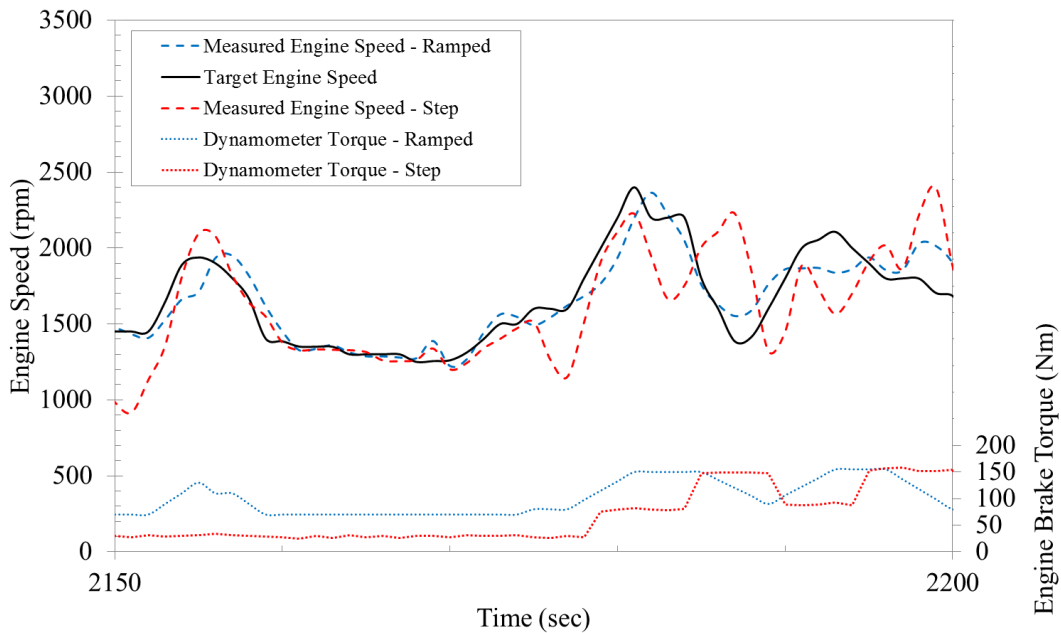


Figure 74: Effect of reducing integrator windup by ramping the brake torque profile on engine speed response (blue-line) compared to a non-ramped solution (red-line)

7.4 Feed-forward Loop and PID Synergy

The first initiative was to modify the control system so that whenever large torque increments or decrements took place during the cycle, the engine speed response would not severely under- or overshoot the target speed. Several pre-defined parameters were modified to understand whether a completely new strategy would have to be implemented in the system designed in the previous section. Such

modifications were increasing the rate of the engine speed error from 10Hz to 20Hz. For the latter larger oscillations in engine speed were observed on-setting instability within the first few seconds of running a drive cycle. Another parameter which was tuned was the time interval between each cell for the input brake torque and engine speed profiles. This data had initially been set to read at intervals of 1 second however this was increased to 0.1 second intervals. An increase in stability was observed however due to the extra computational steps, the system response (i.e. engine speed) lagged by one or two seconds when the cycle came close to 600 seconds. This led to large overshoots and undershoots later on in the cycle making the system unstable.

A feed-forward loop (FFL), capable of delivering a baseline pedal percentage based on the current speed and torque data being read was added to the system. The function of this FFL was to ensure that the engine always meets a minimum threshold pedal percentage. The minimum pedal position changes with respect to the operating condition - minimising the magnitude change in throttle position outputted through the closed loop control system. Two effects were desired in the process of introducing this FFL – 1. The quasi-steady engine speed segments would remain flat without the presence of oscillations (i.e. indicative of a stable system); 2. No significant under- and over-shoots during torque increments or decrements would be noticeable.

The process in defining the pedal position requires mapping the throttle position for constant speeds and varying torques (i.e. to allow for interpolation) on an eddy-current dynamometer. The process is easy and robust to perform requiring a maximum of three hours to test and implement. This may be achieved using the inbuilt dynamometer speed or torque control modes while manually changing pedal position to desired torque and speed operating points. An example of a pedal position map for the Jaguar XF 2.0 litre GTDi engine is shown in the Table 13.

		<u>Engine Speed (rpm)</u>						
		750	875	1000	1125	1250	1375	1500
<u>Engine Brake Torque</u> (Nm)	4.9	1.6	1.6	1.6	1.94	2.57	3.21	3.85
	50	7.95	8.84	9.73	10.62	11.50	12.39	13.28
	100	16.23	17.17	18.11	19.04	19.98	20.92	21.86
	150	24.73	25.51	26.30	27.09	27.88	28.66	29.45
	200	30.15	31.11	32.07	33.03	33.99	34.96	35.92
	250	39.13	40.33	41.53	42.73	43.93	45.13	46.33
	300	55.8	56.45	57.10	57.75	58.40	59.05	59.70
	350	36.48	40.56	44.63	48.71	52.78	56.86	60.93

Table 13: Example of a throttle position map as a function of engine speed and brake load.

A limiting torque and speed increment parameter was introduced into the first FFL system in order to ensure the optimum balance between the interaction of the PID and FFL systems. During idling and steady operating conditions this therefore ensured no FFL influence on the systems' stability by assigning full control to the PID system. This is shown in Figure 76. This was done by inputting the following limiting criteria:

$$N_{n+1} - N_n > N_{increment, threshold}$$

$$T_{n+1} - T_n > T_{increment, threshold}$$

If the increments are within the confined thresholds the feedforward will retain its previously outputted value. This is to ensure a minimum pedal percentage is satisfied so that system response is rapid and any adjustments in the actual speed requires minimal effort from the PID system.

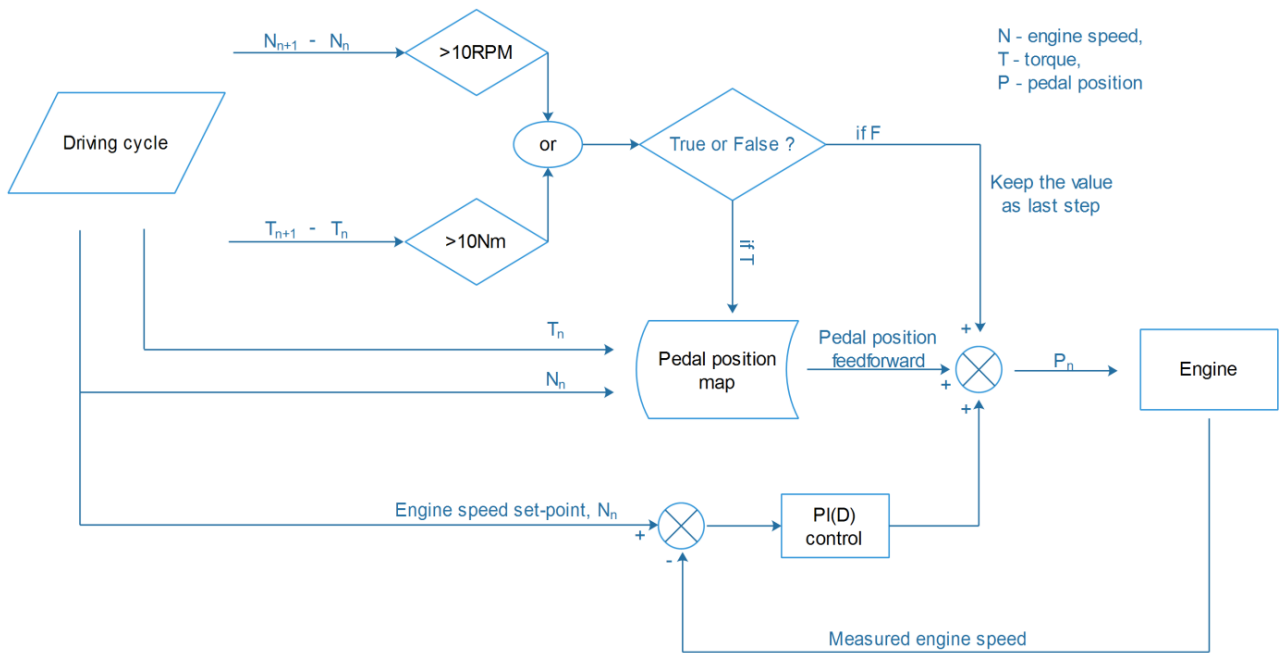


Figure 75: PI control schematic with the addition of FFL.

The role of the FFL and PI system on the pedal position output to the ECU is shown in Figure 77 (A) and (B). This time tests were conducted inputting brake torque and engine speed target traces for the WLTC computed through ADVISOR. Due to the dominance of the FFL on the throttle position output kP and kI constants were modified to reduce the bias of the PI controller such that instability would not ensue due to excess throttle output. The new constants were set to kP = 0.009, kI = 0.00052.

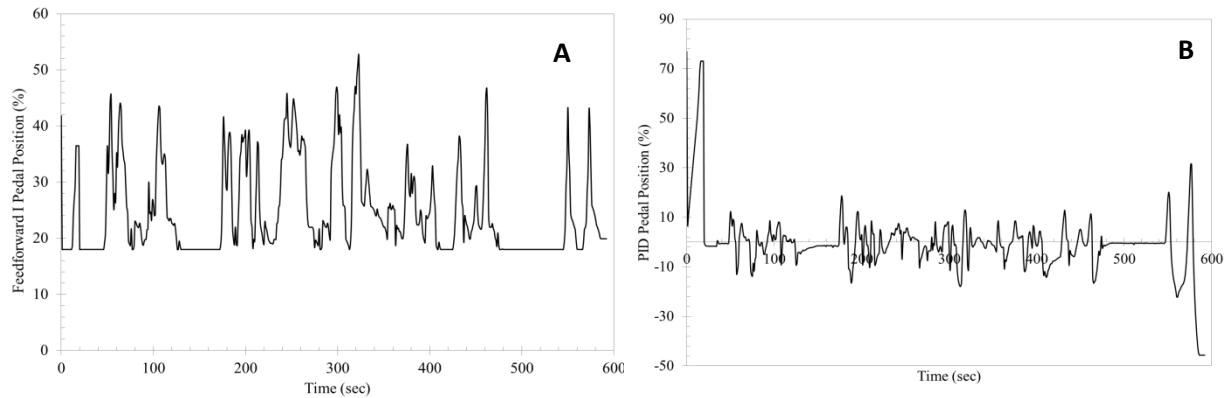


Figure 76: Pedal position output from (A) the FFL and (B) pedal position output from the PI control system over a 600 second trial run of the WLTC.

The application of a baseline pedal position (i.e. FFL) significantly stabilises system response during transient events, as shown in Figure 78. However, the addition of a baseline pedal position combined with the effect of integral windup after long idling periods followed by large engine speed increments increased the magnitude of the engine speed error. This is shown in Figure 79.

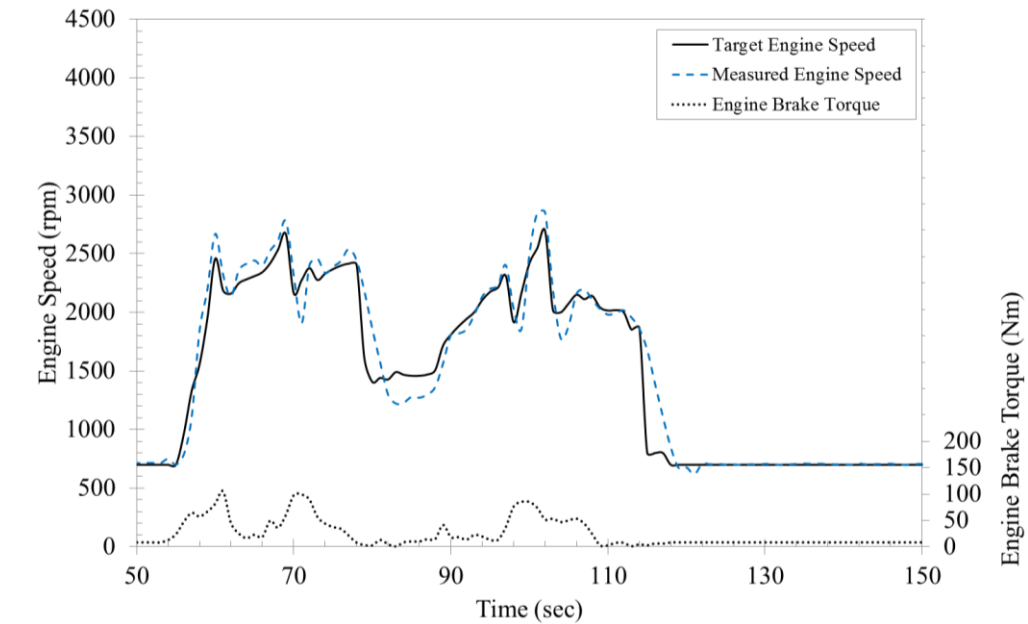


Figure 77: Improved engine speed response after implementing an integral windup with error margins of $\pm 10\%$.

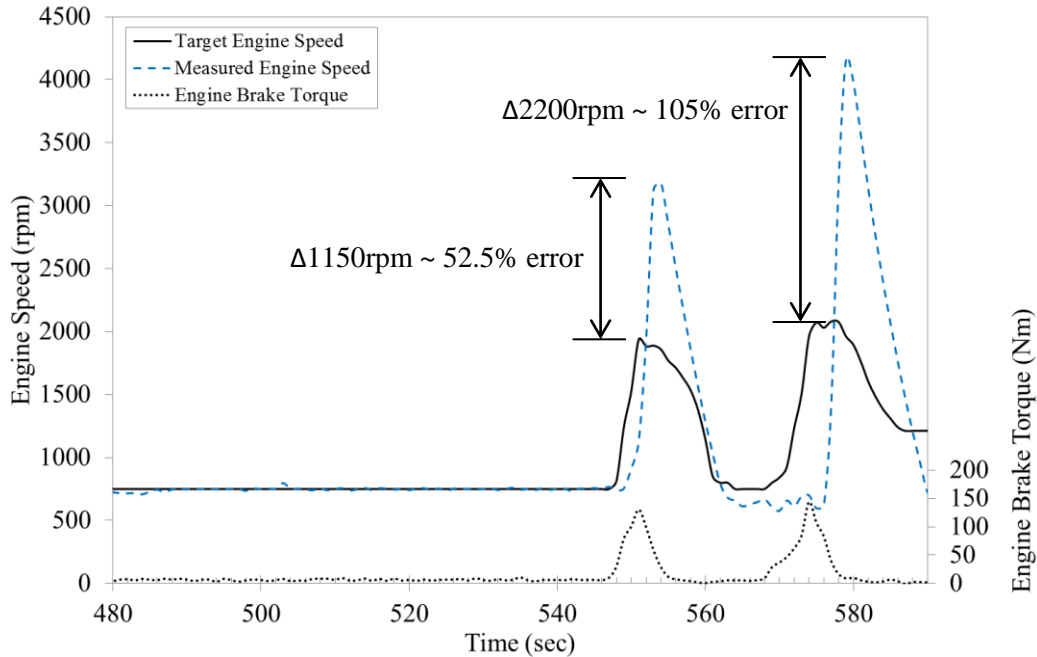


Figure 78: Extreme overshoots in engine speed due to integral windup coupled with the FFL system throttle position output after extended idling periods.

7.5 Addition of an Integrator Wind-Up Nullifier

In order to reduce the eventuality of large cumulation of integral action, specifically during idling periods, an inequality based statement recognises when the output FFL throttle position is that required for idling conditions. Thus in this case an output pedal position of 1.6% is equivalent to the idling pedal position. When outputting this value the engine speed based error calculation channeled to the integrator action is nullified and thus the integral action at the beginning of the idling periods remains constant to the value previously outputted. This retains the added benefit of implementing a FFL to ensure that a baseline pedal position is met while eliminating large errors encountered only during idling periods. A block diagram of the control system capable of running transient drive cycles incorporating a FFL, PID and integrator wind-up nullifier is shown in Figure 80. The corresponding schematic with the conditional statements is shown in Figure 81. The block diagrams created on National Instruments LabVIEW for the FFL, PID and integrator wind-up nullifier are shown in Appendix F Figures 97 and 98.

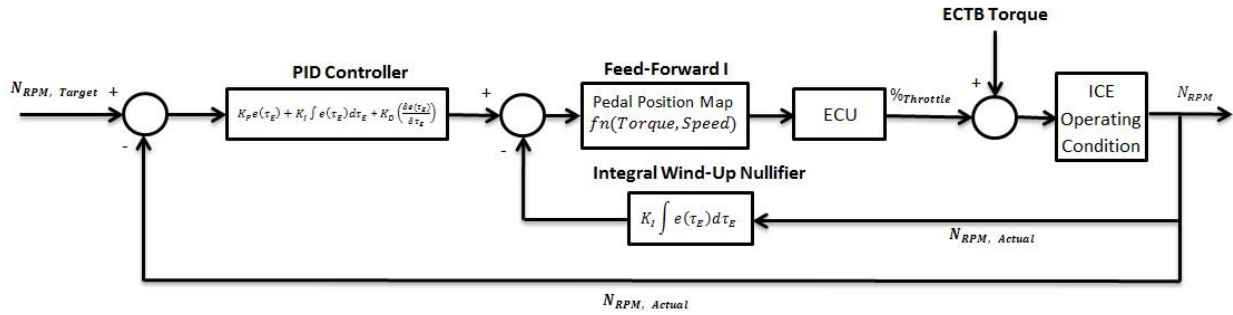


Figure 79: Block diagram for a closed loop proportional, integral and derivative gain system with an integral wind-up.

The addition of a derivative action to a control system provides ‘smoother’ response compared to solely using a proportional and integral gain system. The coefficients for the proportional, integral and derivative actions for the running of transient drive cycles on ECTBs are 0.008, 0.0004 and 0.06 respectively. These constants are intended for a system that runs symbiotically with a FFL providing a baseline pedal position. The effect of solely applying the FFL on the same target engine speed trace is shown on Figure 82 (A) while Figure 82 (B) shows the effect of solely applying the PID system.

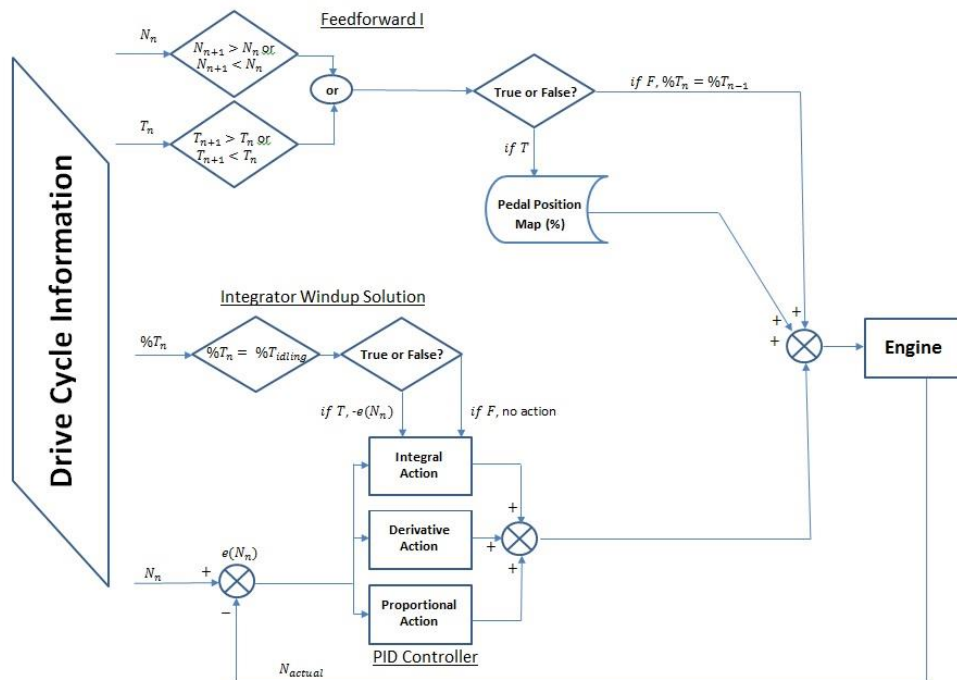


Figure 80: Schematic of the devised pedal control system for transient drive cycle testing incorporating a PID, Feedforward and integral wind-up processors.

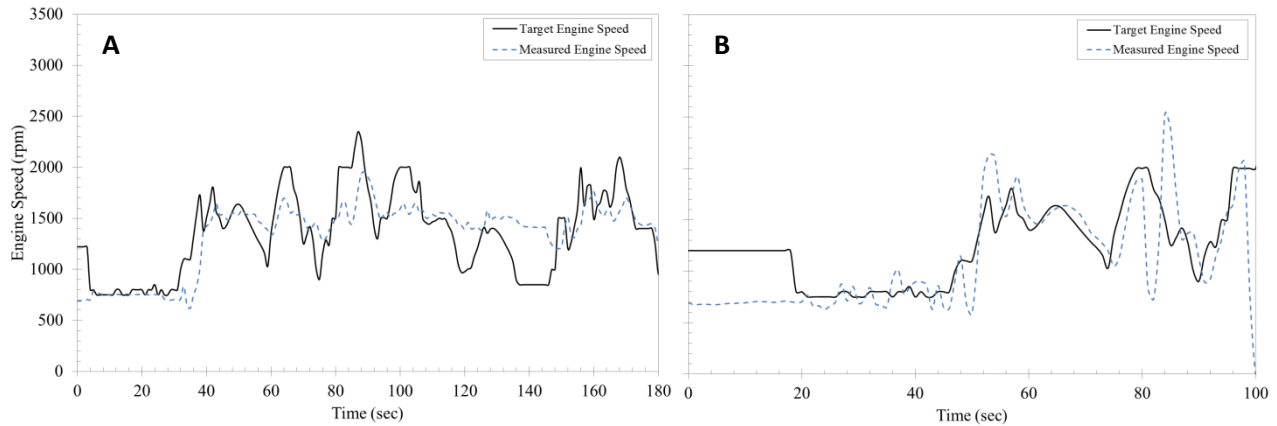


Figure 81: Engine speed response solely with (A) the feedforward loop system outputting pedal percentage to ECU and (B) the PID control system.

7.6 Transferability to All Engine Builds, Repeatability of Results and Robustness of System Performance

The robustness and applicability of the combined PID, FFL and integral wind-up nullifier control system were tested on the four cylinder 2.0litre gasoline direct injection turbocharged engine as described above. Figure 83 and 84 (A) and (B) show the fidelity of system control by comparing the engine speed and brake torque between repeats and compared to the target profiles inputted into the system over warm-up processes. The repeatability of the warm-up process by reference to the coolant and oil temperature is shown on Figure 85 (A) and (B). The repeatability for controlled starting oil temperatures is excellent demonstrating the robustness of the control system as a result of the same magnitude of fuel being consumed. Figure 88 (A) shows the cumulative fuel consumption measurements using a Coriolis Emerson Micro Motion High Pressure fuel flow-meter for four repetitions of the WLTC. The error band on a per gram basis is within $\pm 4g$ equivalent to a $\pm 0.36\%$ difference.

Application of the control system was further tested on a smaller engine, namely a prototype 1.0l three-cylinder engine whose specifications may not be disclosed. This was ensued in order to understand whether control system properties such as the PID coefficients required alteration when transferring the National Instruments LabVIEW block diagrams to different engine sizes. Figure 86 and 87 (A) and (B) demonstrate that measured engine speed and engine brake torque, thus brake energy, show an excellent level of agreement between five repetitions and compared to target values for hot and fully warm operating conditions. Figure 88 (B) shows that a robust level of confidence for instantaneous fuel consumption resulting in an error margin of $\pm 3g$ equivalent to a $\pm 0.67\%$ for the cumulative fuel consumption over five repeats of the NEDC. A $2g$ increase in fuel consumption was captured for an

NEDC test starting at 67°C instead of 88°C demonstrative of the ability to capture fuel consumption dependence on engine temperature.

The excellence and accuracy of implementing the control system on two different drive cycles is exemplified with second by second comparisons of engine speed responses for the 1.0l three cylinder and 2.0l four cylinder engines in Figure 89 and 90.

The transferal process is achievable in less than four hours of consistent work. PID coefficients do not require modification when transferring the control system to different engine sizes. This can be an arduous task and thus removing this process for control implementation purposes is a significant achievement. The only parameters requiring modification is the mapping of the pedal position with respect to engine speed and engine brake load. This must be done for any new engine fitted with an ECU whose throttle position has not been mapped before. If an ECU is transferred to a different engine then the mapping process is not required given that the monitored ECU throttle position result in the same delivery of engine brake work. Therefore for engines with cylinder deactivation it is important that the displayed throttle position with a deactivated cylinder or when firing on all cylinders result in the same brake work delivery although the physical throttle position (i.e. butterfly valve angle) changes. Albeit, if the same ECU is transferred to a different engine it is advised that the mapping process still be undertaken to ensure that an appropriate FFL baseline throttle position be outputted.

The transfer process to different engines installed on ECTBs may be summarised in four steps:

- 1) Transfer the National Instruments LabVIEW sub virtual interactive window for the FFL and PID controller (inclusive of the integrator wind-up nullifier) to the virtual interactive window containing the throttle emulator.
- 2) Map the throttle position for a matrix of engine speed and brake torque values, preferably within 250rpm intervals up to WOT.
- 3) Apply the mapped throttle position and appropriate x and y axes to indicators 1,2 and 3 shown in Appendix F Figure 97 and 98 and ensure that the kP, kI and kD constants are 0.008, 0.0004 and 0.06 respectively.
- 4) Run a drive cycle to test system response. (**Note:** it is necessary that the drive cycle commence with none zero load segments and elevated engine speed (i.e. not idling) such that the integral and derivative actions adapt to the engine behaviour within the first five seconds of the drive cycle.)

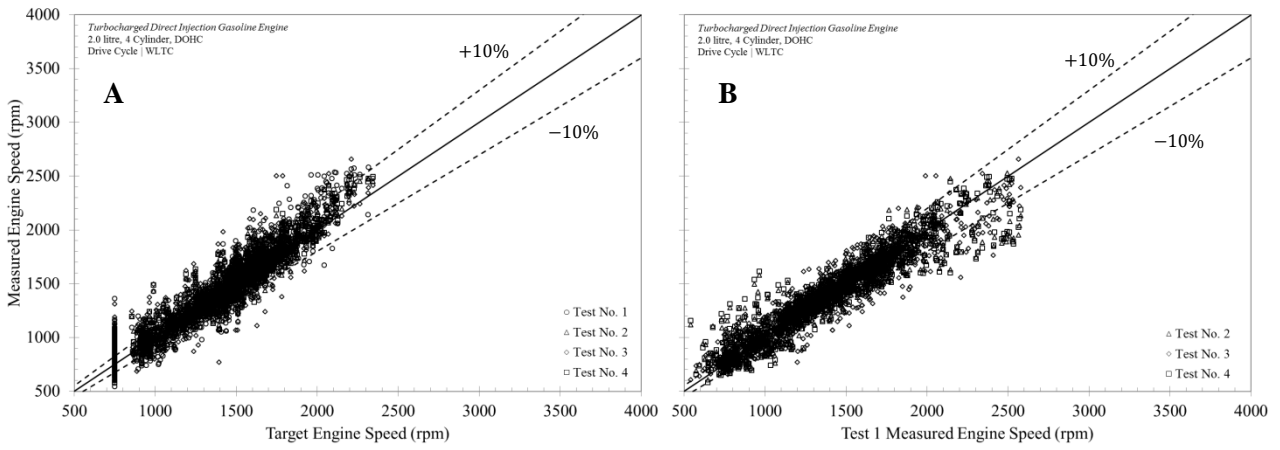


Figure 82: Comparison (A) between target and measured engine speed and (B) repeatability of measured engine speed for four repetitions of the WLTC on a 2.0litre four cylinder engine.

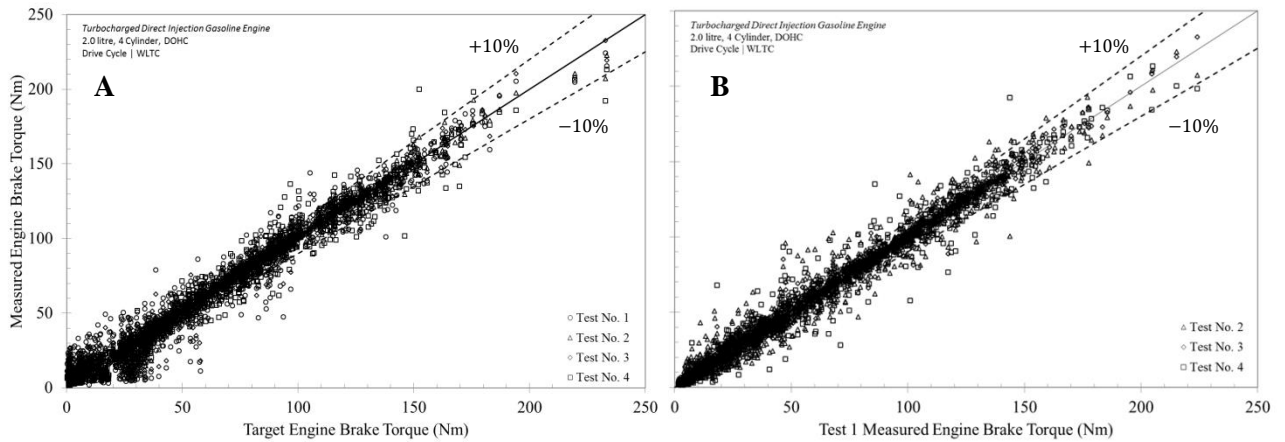


Figure 83: Comparison (A) between target and measured engine brake torque and (B) repeatability of measured engine brake torque for four repetitions of the WLTC on a 2.0litre four cylinder engine.

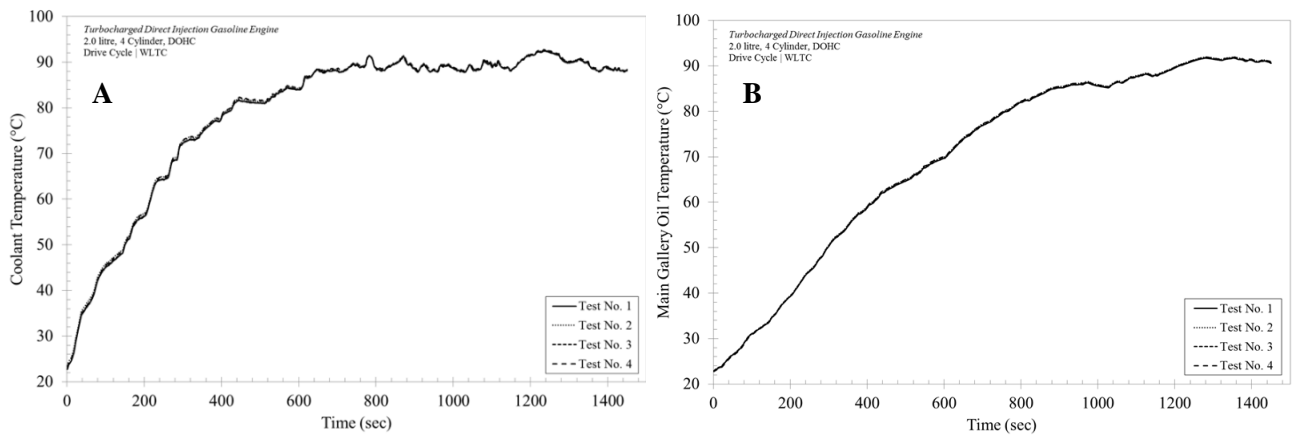


Figure 84: Comparison of (A) coolant temperature and (B) oil temperature in the main gallery over a warm-up procedure on the WLTC for four repeated tests on a 2.0litre four cylinder engine.

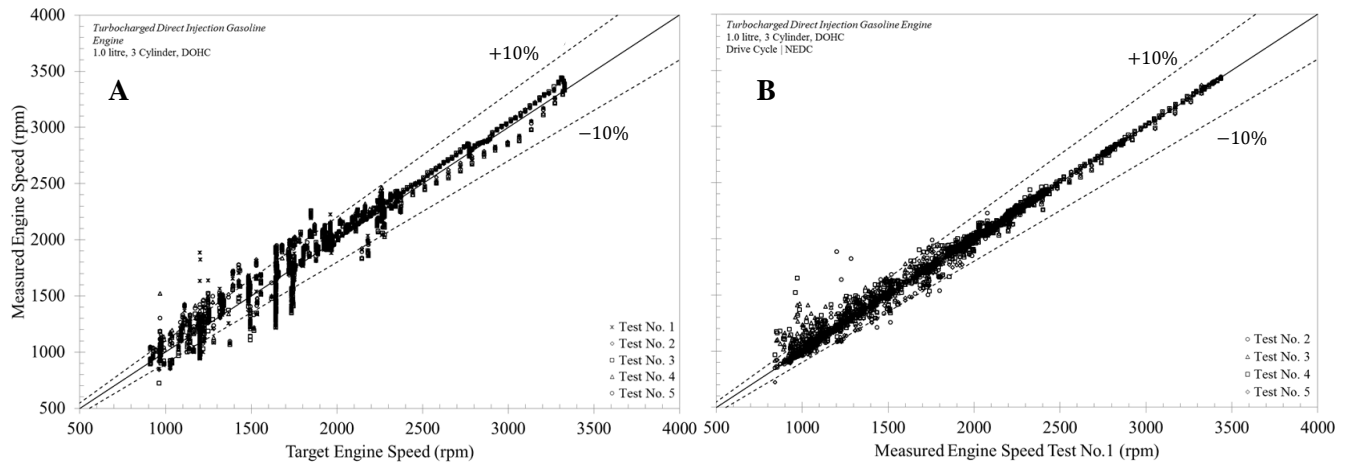


Figure 85: Comparison (A) between target and measured engine speed and (B) repeatability of measured engine speed for five repetitions of the NEDC on a 1.0litre three cylinder engine.

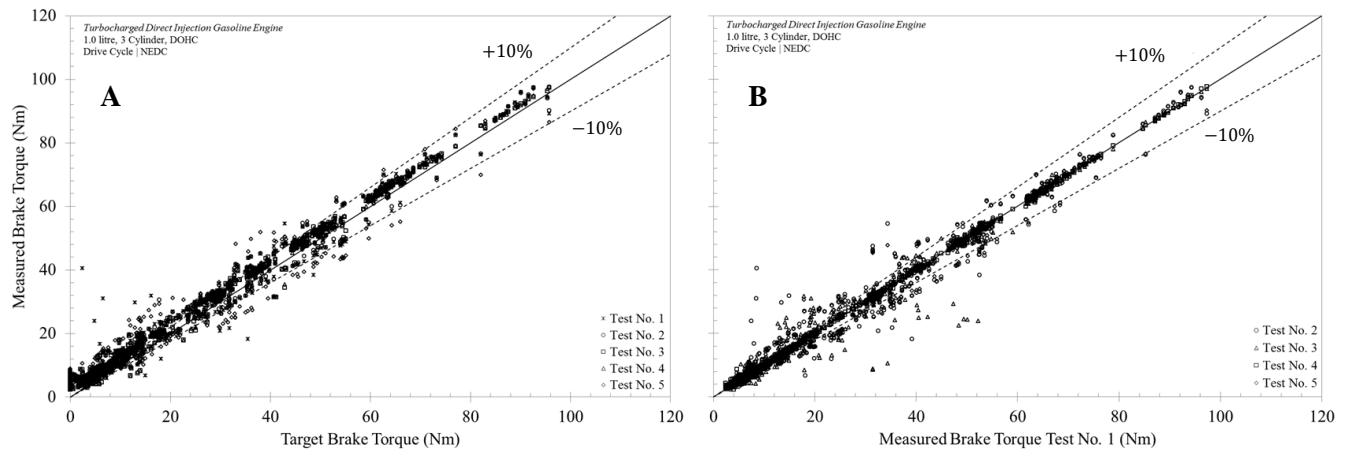


Figure 86: Comparison (A) between target and measured engine brake torque and (B) repeatability of measured engine brake torque for five repetitions of the NEDC on a 1.0litre three cylinder engine.

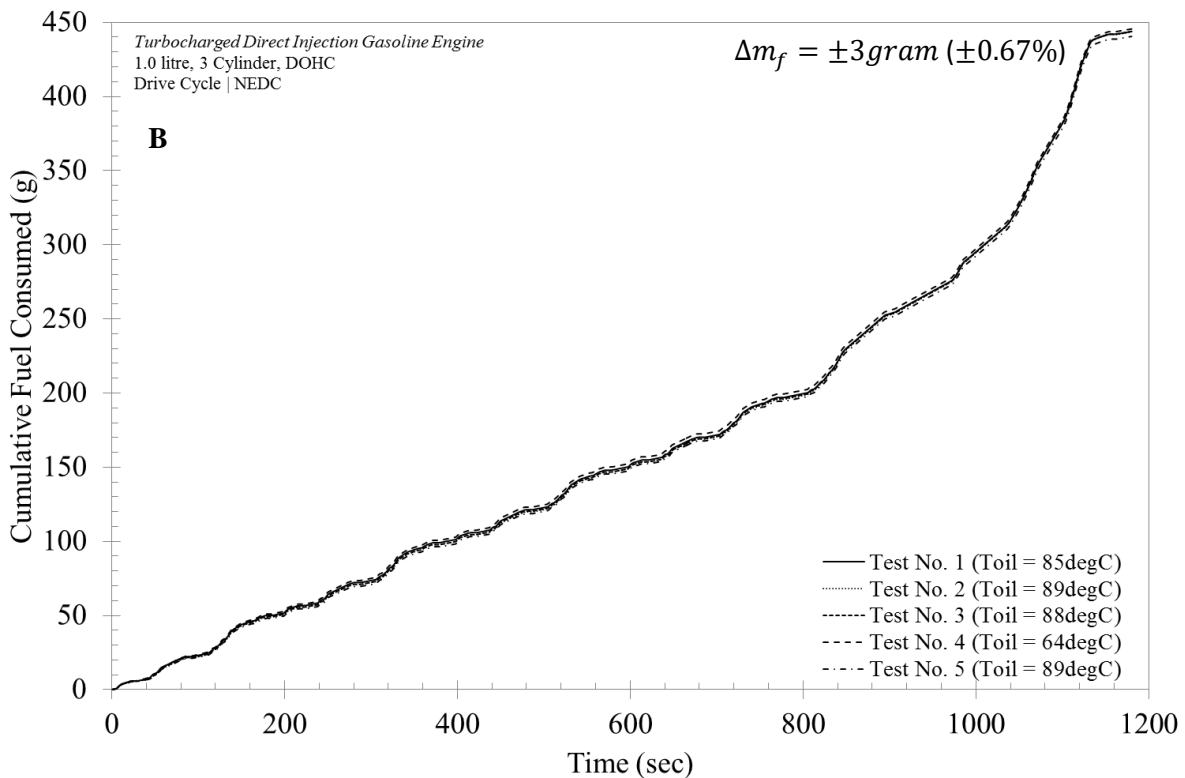
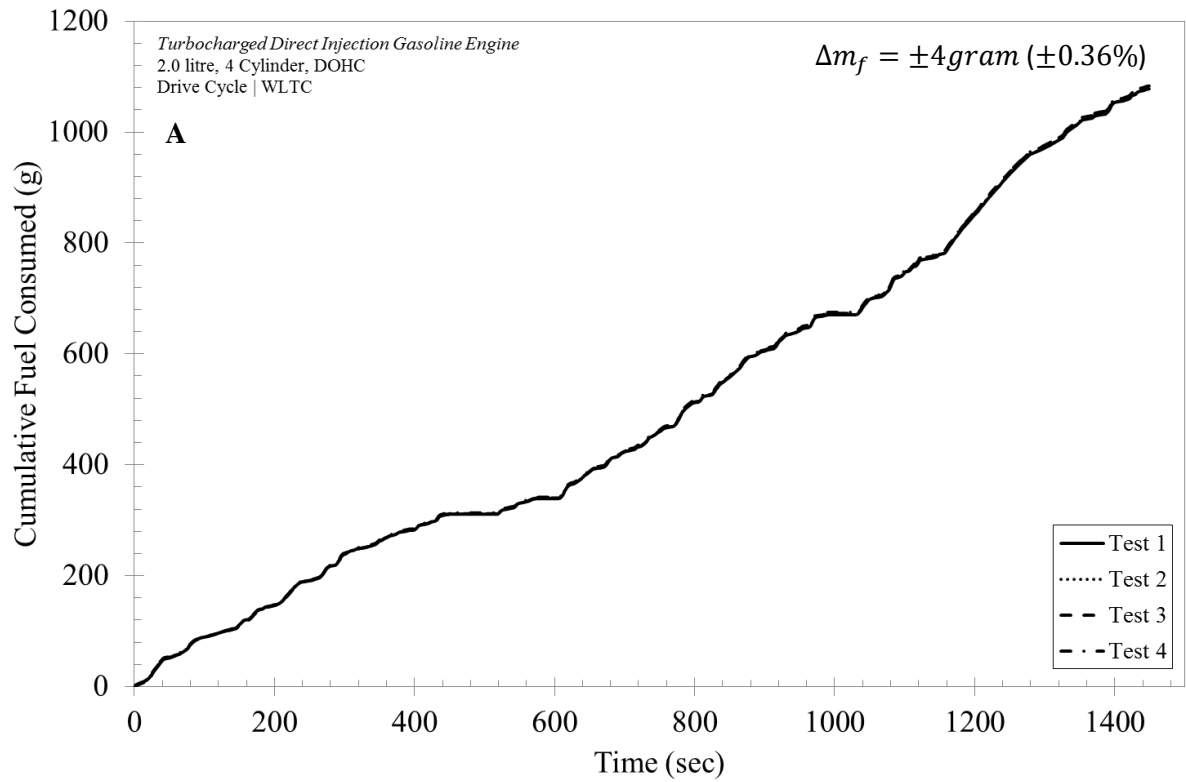


Figure 87: Cumulative fuel consumed over four tests (A) for a cold started ($T_{oil} = 23^{\circ}\text{C}$) WLTC test on 2.0l four cylinder engine and five tests for (B) hot and fully-warm started NEDC test on 1.0l three cylinder engine.

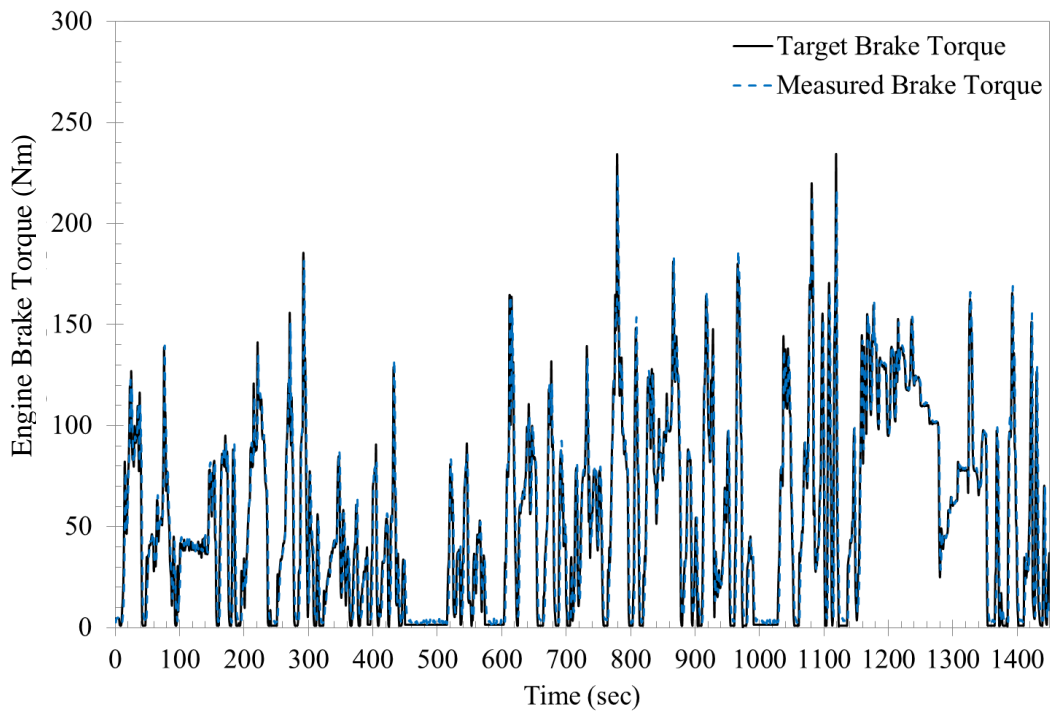
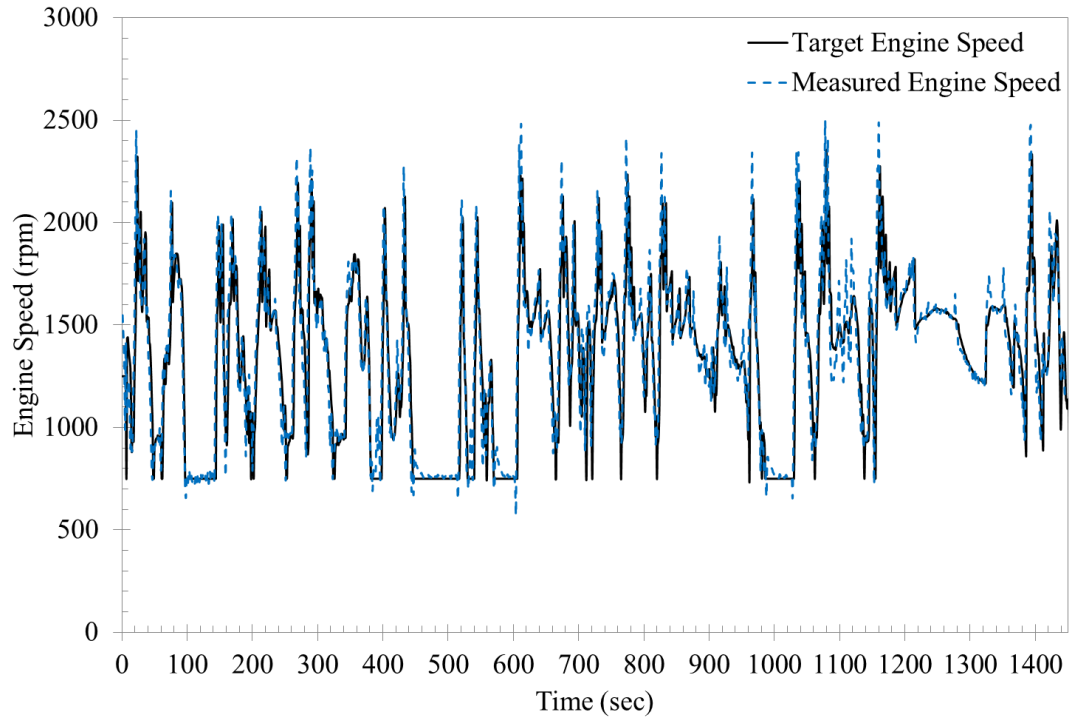


Figure 88: Second-by-second comparison of the measured and target (A) engine speed and (B) engine brake torque over the WLTC for the four cylinder 2.0l gasoline turbocharged engine.

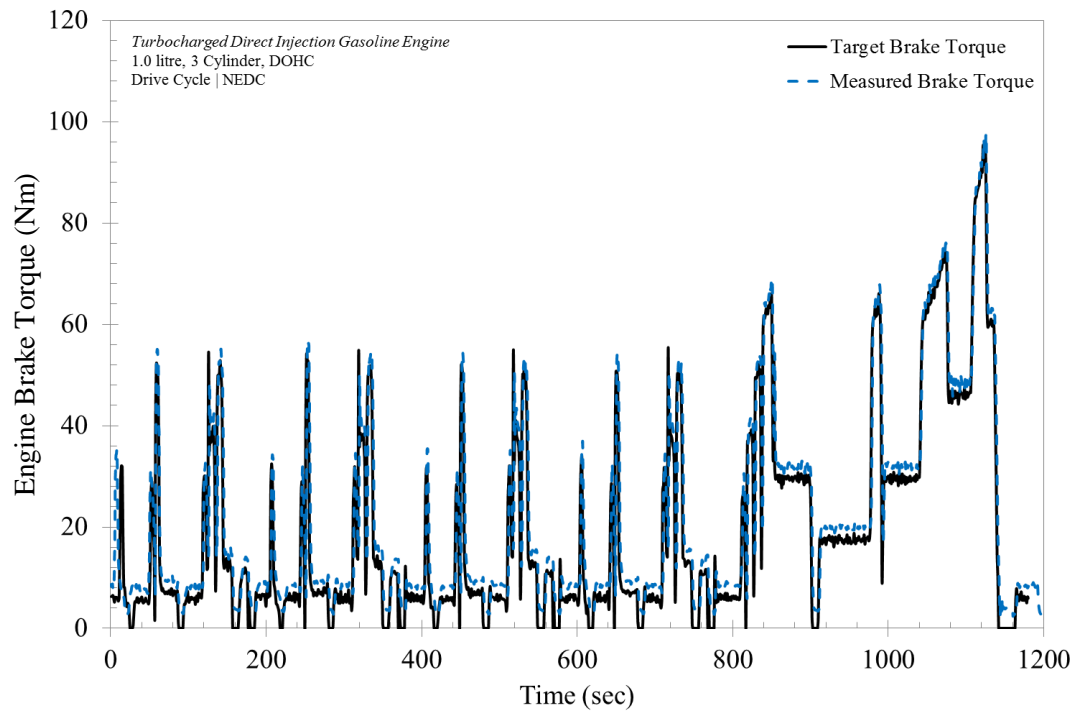
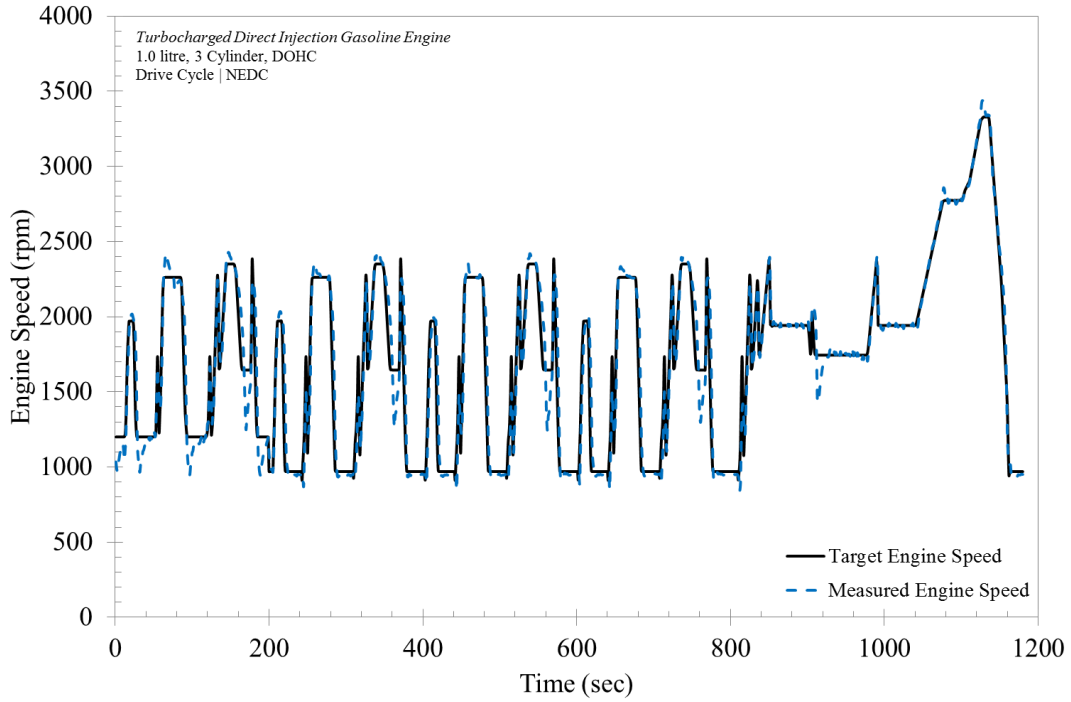


Figure 89: Second-by-second comparison of the measured and target (A) engine speed and (B) engine brake torque over the NEDC for the three cylinder 1.0l gasoline turbocharged engine.

7.7 Conclusions

In this chapter a control system developed to control engine power output over transient drive cycles on an ECTB has been described. The control system consists of a PID controller, feed-forward throttle position look-up table and integrator wind-up working in synergy outputting engine throttle position commands based on calculated engine speed errors. The purpose of the development of this control system arises from the relatively cheaper equipment used to test engines in laboratory conditions. The system is to be used for the purpose of evaluating fuel consumption improvements on drive cycles in the aim of asserting improvements had by modifying engine components.

The main conclusions to be drawn from the development of this system are:

- The control system is applicable to the virtual environment available on LABVIEW™ National Instruments 2012 or newer versions.
- The development of the control system was made such that it is transferable and generic to engines of different sizes while requiring minimal work from the operator.
- The performance and successful application of the control system has been validated on two engines of differing size and this has proven to be successful for the purpose of satisfying the initiative of devising a method for carrying out transient drive cycles on ECTBs. Although a successful step, further tests on a variety of engine sizes and differing drive cycles are required as more engines are made available on ECTBs at the University of Nottingham to provide feedback on potential improvements of system response.
- Engine speed and engine brake torque, preferably sought from vehicle chassis tests, are the only inputs required to successfully run the engine over a drive cycle such as the WLTC. The transfer process is made simple, achieved in four steps.
- The repeatability and accuracy of the system has been validated for cold started WLTC tests run on a 2.0l gasoline engine and hot started NEDC tests run on a 1.0l gasoline engine. Repeatability has been shown to be excellent through the use of an Emerson MicroMotion Coriolis fuel flow-meter with the spread in recorded fuel consumption remaining within a $\pm 4g$ error band.

Chapter 8 Discussion, Future Work and Conclusions

8.1 Discussion

A version of PROMETS has been used to characterise the TCE, in the aim of predicting and quantifying the effects of cylinder deactivation on engine thermal behaviour and performance. Based on model predictions knowledge of the changes in engine heat transfer and effect on component temperatures have been outlined. Predictions indicate that while cylinder deactivation is not limited by engine thermal behaviour potential benefits remain sensitive to engine temperature and operating characteristics.

For a three cylinder engine if one cylinder is deactivated the brake torque output of the two firing cylinders increases by 50%. In turn, the total engine metal surface area exposed to combustion and exhaust gases reduces by approximately one third. The reduction in surface area reduces heat transfer to coolant between 2 and 22% depending on engine brake load. As a result of retaining heat within the combustion chamber the in-cylinder charge and exhaust gas have higher enthalpy. In effect, model predictions indicated that the exhaust gas temperature increases in the range of 20 to 100°C, increasing with engine brake load. Studies made on an experimental diesel engine [8] have shown that increased exhaust gas temperatures due to cylinder deactivation result in the catalyst reaching optimum operating temperatures faster. Thus this is beneficial for the purpose of entraining oxidation of unwanted emissions.

As a result of reducing heat losses coolant warm-up rates reduce. Although heat transfer to coolant is affected, heat losses to oil are minimally affected. Slowing coolant warm-up rates reduces the available heat input to the passenger compartment and slows the gradual reduction in higher rubbing friction. Rubbing friction changes negligibly due to an average 1% reduction in overall engine friction associated with deactivation. An optimisation study was carried out in the model varying the onset temperature of deactivation over the NEDC in the aim of reducing the delay in warm-up rate without severely affecting the benefit due to deactivation. It was found that cylinder deactivation minimally affects warm-up rates when onset from a coolant temperature between 40 and 50°C.

Heat transfer changes due to cylinder deactivation result in engine structural temperature changes. All components comprising the deactivated cylinder stabilise to a temperature close to that of the coolant temperature. On the other hand, the temperatures of the components in the firing cylinders augment dependent on engine power. To build confidence in model results predicted temperature data was correlated against cylinder wall thermocouple data from a three cylinder engine firing on all cylinders. In *Chapter 4 subsection 4.7.2* it was shown that predicted data correlated very well with experimental data. The model was capable of predicting metal temperatures sensitive to local coolant temperatures specific

to cylinder location within a maximum error band of $\pm 5^{\circ}\text{C}$. With knowledge of some component temperatures it was inferred that heat transfer to the rest of the engine structure was well represented and thus temperatures were also well predicted. Based on this the model was used as a tool to predict and inform on temperature changes throughout the engine structure when enabling cylinder deactivation. For a fully warm engine state the time required for all engine components to reach an equilibrium temperature were predicted to reside in a 10 to 25 second interval. The largest temperature change was predicted in components which are small in volume and frequently exposed to hot gases. As such the lower stem of the exhaust valve, for the deactivated cylinder, is the component that undergoes the largest change in temperature; i.e. in the magnitude of $< 400^{\circ}\text{C}$. This being said it was predicted that the piston cooling jets significantly reduced piston operating temperatures at the upper end of the deactivation window at high engine speeds. When operating on all cylinders piston cooling jets were enabled at engine speeds above 3000rpm. Consequently when deactivating a cylinder, the pistons cooling jets are disabled to reduce the risk of oil accumulation on the top landing of the piston as suggested by [8.1]. The disablement of cooling jets could have negative effects on piston assembly durability. This would however require further analysis with FEA tools. Temperature changes in the rest of the engine were predicted to be relatively small. In the upper cylinder wall temperature, where the cylinder fluxes are large, differences are in the range of ~ 2 to 15°C . Although significant temperature changes occur in the exhaust valve lower stem these were asserted to remain within safe operating limits of the engine. As a means of comparison, when operating at the rated engine load and reducing back down to an idling condition the temperature difference endured by the exhaust valve is similar to when deactivation occurs.

Significant temperature differences arise in components between the firing and deactivated cylinders. The largest temperature differences occur at the top of the cylinder liner and exhaust ports in the region of $< 70^{\circ}\text{C}$. This is largely due to the consistent exposure these components have to combustion and exhaust gases. It is beneficial to minimise these temperature differences while reducing the temperature of the operating cylinders and keeping the deactivated cylinder warm is beneficial [8.2]. For the firing cylinders it is useful to keep the metal temperature cool to reduce the probability of knock or auto-ignition due to local hot spots. For the deactivated cylinder, on the other hand, *Serrano et al* [8.3] has found that when reactivation ensues combustion quality improves if the cylinder walls are kept warm. Through modelling it was found that deactivating the cylinder furthest downstream of the coolant aperture reduces the temperature difference between cylinders by 5°C while increasing the temperature of the deactivated cylinder by the same amount. This is equivalent to the temperature change experienced by the cylinder wall, at a fixed load, for a 1000rpm increase in engine speed.

The thermal investigations presented here have been limited to 0D cycle averaged analysis of component temperature changes along with macroscopic effects on engine performance. The effect of continued deactivation and reactivation events on component integrity and lifetime remains outside the scope of lumped capacity analysis and time-frame of this study. The stress-strain behaviour of components undergoing large temperature changes can be analysed through FEA tools such as ABAQUS. For instance the effect cylinder deactivation has on the integrity of the cylinder bore shape and thus piston slap, oil consumption and blow-by have not been ascertained [8.4]. The results presented in *Chapter 5* can however be used to direct future computational work involving cylinder deactivation to specific components such as the lower stem of the exhaust valve and cylinder bore.

Cylinder deactivation for the TCE does not severely worsen distortions or temperature differences between and across the height of the cylinders. Observations by *Rajput* [8.5] on gasoline engines show that temperature differences between adjacent cylinder bores for an engine firing on all cylinders nominally raise up to 100°C at the top of the cylinder liner. For the TCE temperatures between cylinders and across the height of the cylinder wall remain within rated engine operating load; residing in the <70°C region. Distortions are therefore not greater during deactivation compared to when the engine operates at rated power. Furthermore, based on the work of *Nishino et al* [8.6] inter-bore cooling slits reduce the thermal load between adjacent cylinders. For the TCE, medium sized inter-bore cooling slits are present such that cylinders remain thermally isolated from one another remaining near the coolant temperature. For larger engines where several cylinders are deactivated it is preferable to reduce the number of cylinders prone to temperature differences by spatially grouping the deactivated cylinders. This in turn reduces the possibility of increasing the order of distortion. The feasibility of selecting the cylinders to deactivate is however dependent on packaging constraints. As example, on the 1.4l four cylinder gasoline engine the two in-board cylinders are deactivated due to the sliding cam-shaft mechanism not being packaged to deactivate outboard cylinders [8.7]. For larger engines of V-type configuration, as mentioned in *Chapter 5* section 5.9, whole banks are deactivated to mitigate the occurrence of temperature differences between cylinders.

The retention of heat in the firing cylinders augments the amount of energy resulting from combustion used in a propulsive fashion pushing the piston downwards at low loads. Due to the improvement in channelling heat energy to provide engine brake torque the magnitude of fuel required reduces thus translating to an improvement in the gross indicated thermal efficiency. Experimental data stemming from a proto-type engine describing the changes in the efficiency were inputted into the model for various engine speeds under the form of empirical based functions. Difficulty lay in physically

describing the phenomenon however for the purpose of robustly predicting fuel consumption benefits this approach was deemed suitable.

The benefits due to cylinder deactivation stem from an improved gross indicated thermal efficiency and reduced pumping losses. The largest benefits, for a given engine speed, are had at the lightest engine loads, reducing as load increases due to a deterioration in gross indicated thermal efficiency. The maximum benefit had is of 25% and the maximum magnitude reduction in fuel consumption is at the highest applicable engine speed for the lowest engine brake load.

Applying cylinder deactivation over a warm-up period reduces the potential fuel consumption reduction. Compared to a fully warm engine state as the amount of fuel spent overcoming friction losses during a warm-up reduces the amount of fuel saved relative to the total fuel consumed. Thus as engine temperatures reach optimal conditions the percentage fuel economy is maximised. With this, the fuel consumption benefit had over a drive cycle is highly dependent on the cycle characteristics (e.g. duration, operating conditions and vehicle mass). As engine operating regions tend towards higher brake loads the potential availability of deactivating a cylinder reduces while the importance of the warm-up is less accentuated. In effect, benefits are highest on drive cycles which reside mostly in the lower brake torque region such as the NEDC and FTP-75. As the operation nears full rated power the proportion of fuel reduced due to reduced pumping losses and increased thermal efficiency is small relative to the large proportions of fuel spent at high operating conditions. Therefore over drive cycles such as the WLTC and ARTEMIS fuel consumption improvements are small. To quantify these differences; on a fully warm NEDC and WLTC run the predicted benefit due to deactivation is 4.50% and 1.58% respectively. Vehicle mass also affects the proportion of time spent deactivating a cylinder. As the mass increases the engine is required to deliver larger brake loads to overcome inertial and rolling resistances therefore minimising the time spent in a deactivated engine state. However, this may be alleviated by fitting a larger size engine with more cylinders and the ability to deactivate cylinders based on driver requested engine torque although the baseline fuel consumption is higher. This is generally due to larger engines being heavily throttled at low and part loads therefore relatively reducing fuel consumption with cylinder deactivation.

Currently, innovative solutions are picking up in the automotive industry with technologies that are giving way to full independent control of intake and exhaust valves. In 2014, Freevalve AB [8.8] patented a design which replaces conventional camshaft driven valves with electronically controlled pneumatically actuated valves. This solution will allow gasoline engines to operate without a throttle and therefore the intake manifold pressure remains near atmospheric. This renders the throttle plate obsolete in a gasoline engine. In turn pumping losses are extensively minimised with a range of modifications made to the engine build, combustion and after-treatment systems. Modelled estimates for the TCE indicate that by

solely removing pumping losses from fuelling calculations over the NEDC for warm-up and fully warm conditions an estimated 13.1% and 13.7% improvement in fuel consumption may be had. However, this benefit is to be weighed against the penalty in installing the equipment necessary to supply pressurised air to the valves. With this technology engines will be able to deactivate cylinders without the need to build valve or cam-shifting technologies. The development of such technology is still in the concept stage [8.9] and its on-road usage is in the phase development stages by merger with the Chinese automobile manufacturer Qoros. However this does not mitigate the limitations in applying cylinder deactivation associated with NVH and driving style.

Fuel economy improvements shown in *Chapter 6 subsection 6.5.5* indicate that real world journeys with frequent stoppage time and harsh driving style, i.e. a larger spread in engine brake torque operating points, minimise the amount of time spent with cylinder deactivation. Modelled fuel consumption reduction figures for a city route and a route characterised by an aggressive driving style minimise benefits keeping them around 1.16% and 1.72% respectively. The potential for the technology in reducing fuel consumption may be improved by operating the vehicle in a modal type manner and smart gear selection refraining operation from entering NVH limited engine speed bands. Furthermore with the advent of autonomous driving traffic systems and driving style will change. As described in the conclusion of *Chapter 6*, the factors limiting the potential benefit to be had from cylinder deactivation will therefore need to be addressed in ECU development phase. This is also pertinent even if engines serve as range extenders for hybrid vehicles.

8.2 Future Work

The motoring loss described and analytically defined in *Chapter 4* served as means of quantifying the performance penalty when deactivating a cylinder. This offers a manner of calculating the fuel consumption deterioration for stabilised in-cylinder pressure traces in terms of the gross indicated mean effective pressure when deactivating cylinders. There are a considerable number of topics pertaining to the motoring of a piston that remain unanswered requiring detailed analysis. Describing the mass loss process, when trapping fresh air and exhaust gas charges, by detailing the flow of air through the piston ring pack can provide engine designers with methods of reducing the occurrence of in-cylinder mass. Although means of alleviating the occurrence of very low in-cylinder pressures have been suggested through ventilating strategies by *Gottschalk et al* [8.10] the physical phenomenon is not thoroughly described. With this there is uncertainty on the effect the vacuum created at BDC has on oil lifetime, consumption and engine friction. If excessive amounts of oil were to be sucked into the combustion chamber there would be need to determine the effect this has on oil contamination and thus engine friction over engine lifetime. If oil were to be sucked into the combustion chamber understanding the

effect this has on the spark plug, injector, valves, the exhaust after treatment system, emissions and soot would be necessary.

There is increased interest in the application of cylinder deactivation for throttled gasoline engines in the form of dynamic skip fire and displacement on demand (DoD). The current revisions made to thermal and performance models of PROMETS are specific to cylinder deactivation cutting off fuel injection and shutting off the intake and exhaust valves. The basis of the model revisions are made suitable and transferrable to future models characterised for different size engines. This will allow the model to accurately represent the impact thermal behaviour has on warm-ups and thus fuel consumption. This is applicable to engines fitted with technologies that allow for DoD under cylinder deactivation. In terms of engine performance, the impact that DoD has on fuel consumption has not been compared with cylinder deactivation and dynamic skip fire. For dynamic skip fire, formulating a time-averaged description of the thermal behaviour of the engine would be required. This thesis presents a simple manner of determining the pumping losses for a turbocharged engine and robustly estimates pumping loss reductions with and without cylinder deactivation. However, the occurrence of dynamic skip fire would enable cylinder deactivation further up the engine rated load spectrum therefore a more detailed model of turbocharger behaviour and throttle plate response would be required to accurately model performance behaviour. The occurrence of pressure fluctuations across the throttle plate when closing valves would also have to be investigated.

In the author's opinion, several upcoming innovations in the automotive world will affect the way traffic and thus driving style propagates in the next 50 years. The advent of autonomous driving will give rise to smarter traffic systems. This will potentially render obsolete traffic signalling systems while allowing for optimisation of traffic flow in real time such that engine efficiency may be kept at a maximum [8.11]. Thus vehicles fitted with larger displacement engines coupled with technologies such as that presented by FreeValve [8.12] allowing for displacement on demand (DoD) [8.13] are suggested methods for maximising the benefits to be reaped from cylinder deactivation. This process has already begun and will become more common with time. As example, Tesla remotely patched vehicle control units, in 2015, with semi-autonomous functionality [8.14]. Google on the other hand plans to render autonomous vehicles publicly available by 2020 [8.15]. As legislation consents the advent of autonomous vehicles; first demonstrated in 2012 by the state of Nevada - being the first state in the United States to pass a law allowing for autonomous cars to be used on road [8.16], the driver's influence on fuel economy will reduce excess use of fuel by rendering driving more modal in nature thus allowing for smarter gear selection. Most recently, on April 14 2017 the state of California issued autonomous vehicle testing permits to 33 companies [8.17].

The vacuum created when deactivating a cylinder poses unknown experimental problems to performance in direct injection spark ignition turbocharged gasoline engine. Low speed pre-ignition (LSPI) can cause heavy knock at low engine speeds which can result in broken spark plugs and cracked pistons [8.18]. Several theories exist as to why LSPI exists. The first is that droplets of oil get trapped between the piston and the cylinder wall. As the oil is trapped and fuel is injected prior to the power stroke oil and fuel mix causing auto-ignition. Although more theories for LSPI exist and can be further read upon in literature, cylinder deactivation is pertinent to the suction of oil. As example partial or near vacuum combustion chamber pressures, during deactivation, could enable the excessive sucking of oil and thus promote LSPI during reactivation events. Ways to mitigate this are required especially with the downsized and highly boosted nature of the TCE and other engines. This however requires experimental validation and would be a study worthy of being undertaken for deactivation events at low speeds. Studying the travel of oil around the piston during deactivation and the effect that low engine speeds has on this are mechanisms that will have to be defined and well understood. Likewise, the effect that deactivation has on oil entrapment and the eventuality of super knock remains to be observed [8.19] giving room for future work.

8.3 Conclusions

The main conclusions drawn from the investigations in this thesis are:

Motoring a Cylinder

- Combusting a fresh air charge and trapping the exhaust charge in a motored cylinder results in mass loss of 47% if the minimum in-cylinder pressure reduces from 0.40 to 0.23 barA. A mass loss of up to 70% is experienced if the same minimum in-cylinder pressure drops down to 0.12 barA.
- Cylinder deactivation imposes a small penalty on engine performance in the range of 0.02 to 0.03 bar IMEP equivalent to 2.2 to 3.2 Joules/rev. This agrees with findings reported by *Leone and Pozar* [8.20]. The polytropic index of a stabilised in-cylinder air charge for the expansion and compression strokes is in the range of 1.34 and 1.36, indicating a near adiabatic process.
- The work loss when motoring a cylinder may be expressed in the following manner using experimental based values defining the polytropic index of the trace, n , mass of the charge, m , while assuming a BDC temperature equal to the cylinder wall metal temperature.

$$\oint W = - \oint Q_{rev,n} = -2mR\Delta T \left(\frac{\gamma - n}{(\gamma - 1)(n - 1)} \right)$$

Time-Averaged Effects of Cylinder Deactivation on Engine Heat Transfer

- Although heat rejection to coolant from the firing cylinders increases, total engine heat transfer to coolant reduces for a given engine load. Predictions for the TCE indicate that heat rejection for the firing cylinders increases by between 14 and 30%, increasing with in-cylinder load. Predictions for engine heat rejection show a reduction between 22 and 2%, reducing as engine load increases.
- Engine operation with cylinder deactivation is not limited by excessive temperatures due to in-cylinder loads peaking at 50% of the rated load.
- Temperature differences between adjacent components can be minimised by deactivating the cylinder furthest downstream of the coolant inlet aperture. In this manner, the deactivated cylinder remains warmed by higher enthalpy coolant in contact with the firing cylinders. In turn, temperature differences between adjacent cylinders are also reduced.

Effects of Cylinder Deactivation on Engine Performance

- Fuel consumption benefits due to cylinder deactivation reduce during warm-up. This is due to a higher proportion of fuel used in overcoming friction losses. As example, a warm-up from a 20°C starting temperature over the NEDC reduces fuel improvement by 1.45%, from 4.50% to 3.05%.
- The benefit due to cylinder deactivation reduces as drive cycle torque residence times are more evenly distributed (i.e. covering engine rated load) and drive cycle duration increases. As example, fuel consumption improvements over the NEDC and FTP-75 are 4.50% and 5.43%, respectively, while for the WLTC and ARTEMIS benefits are around 1.58% and 0.74% respectively.
- The fuel consumption reduction due to cylinder deactivation for a throttled gasoline engines increases with engine swept volume. This is due to a larger proportion of engine operation spent under naturally aspirated conditions. Modelled fuel consumption improvements for a 1.0l three cylinder engine (deactivating one cylinder) and 1.4l four cylinder engine (deactivating two cylinders) indicate that over the NEDC roughly three times more fuel is reduced.

Transient Drive Cycle Testing on ECTBs

- A closed loop control system consisting of a PID, feed-forward look-up table and integrator wind-up solution have been devised to accurately test engines on transient drive cycles for fuel consumption benchmarking on ECTBs.
- The system is transferrable to engines of all sizes by following four steps requiring a total of 6 hours for set-up and testing of system functionality.
- The accuracy of the system has been validated with fuel measurements for the NEDC and WLTC taken on an Emerson MicroMotion Coriolis flow-meter showing repeatability within an error band of $\pm 4g$.

References

Chapter 1

- [1] Penistone, Amanda. *2015 UK Greenhouse Gas Emissions, Final Figures*. Statistical Release, London: Department for Business, Energy and Industrial Strategy, 2017.
- [1.1] Department for Transport. *Vehicle Licensing Statistics: Annual 2016*. Statistical Release, National Statistics, 2017.
- [1.2] Stabinsky, M, et al. "Active Fuel Management (TM) Technology: Hardware Development on a 2007 GM 3.9l V6 OHV SI Engine." *SAE Technical Paper 2007-01-1292*, doi: 10.4271/2007-01-1292, 2007.
- [1.3] Middendorf, Hermann, Jorg Theobald, Leonhard Lang, and Kai Hartel. "The 1.4l TSI Gasoline Engine with Cylinder Deactivation." *MTZ (MTZ) Volume 73 (03 2012)*: 4 - 8.
- [1.4] Leahu, C I, and S Tarulescu. "The Influence of Thermal Regime on Gasoline Direct Injection Engine Performance and Emissions." *7th International Conference on Advanced Concepts in Mechanical Engineering*. IOP Conf. Series: Materials Science and Engineering, 2016.
- [1.5] Oreskes, Naomi, and Erik M Conway. *Merchants of Doubt*. New York: Bloomsbury Press, 2010.
- [1.6] Lynch, Patrick. *NASA / A Year in the Life of Earth's CO2*. 17 November 2014. <https://www.nasa.gov/press/goddard/2014/november/nasa-computer-model-provides-a-new-portrait-of-carbon-dioxide/> (accessed December 23, 2014).
- [1.7] European Commission. "Environment: Transport Emissions." *Air Pollutants from Road Transport* .29 June 2007. <http://eur-lex.europa.eu/LexUriServ/LexUriServ.do?uri=OJ:L:2007:171:0001:0016:EN:PDF> (accessed April 21, 2017).
- [1.8] Boretti, Alberto, and Joseph Scalco. "Piston and Valve Deactivation for Improved Part Load Performances of Internal Combustion Engines." *SAE 2011 World Congress & Exhibition*. SAE International, 2011.
- [1.9] Ilhlemann, Arndt, and Norbert Nitz. "Cylinder Deactivation: A Technology with a Future or A Niche Application?" *10th Schaeffler Symposium*. Schaeffler, 2014. 172 - 184.
- [1.10] Knowling, Michael. *Cylinder Deactivation Reborn - Part I*. 10 August 2005. <http://www.autospeed.com.au/cms/article.html?&title=Cylinder-Deactivation-Reborn-Part-2&A=2623> (accessed February 2, 2005).
- [1.11] Falkowski, A, M McElwee, and M Bonne. "Design and Development of the DaimlerChrysler 5.7l HEMI Engine Multi-Displacement Cylinder Deactivation System." *SAE Technical Paper 2004-01-2106*, doi: 10.4271/2004-01-2106, 2004.
- [1.12] EPA. "A Study of Potential Effectiveness of Carbon Dioxide Reducing Vehicle Technologies." *EPA420-R-08-004a* (EPA), June 2008.

- [1.13] Senapati, Uday, Ian McDevitt, and Aaron Hankinson. "Vehicle Refinement Challenges for a Large Displacement Engine with Cylinder Deactivation Capability." *SAE International 2011-01-1678*, doi: 10.4271/2011-01-1678, 2011.
- [1.14] Eichler, F, J Gindele, M Hart, T Ramsteiner, G Thater, and T Tschamon. "Der Neue AMG 5.5l Saugmotor mit Zylinderabschaltung." *20th Aachen Colloquium Automobile & Engine Technology Conference, Day 2*. 2011. 981 - 1004.
- [1.15] Adcock, Ian. *Bentley Develops W12 Cylinder Deactivation*. 13 March 2015. <http://articles.sae.org/13975/> (accessed February 2, 2017).
- [1.16] Volkswagen Group. *W12 Engine*. 2 March 2010. http://wikicars.org/index.php?title=W12_engine&action=history (accessed February 20, 2017).
- [1.17] Wirth, Martin. *Ford's EcoBoost Technology: A Central Element of a Sustainable CO2 and Fuel Economy Strategy with Affordable Products*. PowerPoint Presentation, Brussels: ACEA Automotive Summit, 2010.
- [1.18] Union Of Concerned Scientists. *What is ZEV?* 31 October 2016. <http://www.ucsusa.org/clean-vehicles/california-and-western-states/what-is-zev#.WPuTjalkouU> (accessed April 22, 2017).
- [1.19] Debord, Matthew. *Ford Just Made a \$4.5billion Investment to Completely Transform its Business*. 4 January 2017. <https://www.businessinsider.com.au/ford-45-billion-investment-autonomous-vehicles-2017-1> (accessed April 22, 2017).
- [1.20] Cipollone, R, D D Battista, and A Gualtieri. "Head and Block Splot Cooling in ICE." *The International Federation of Automatic Control (IFAC)*, 2012.
- [1.21] Nielsen, Christian F.B. *ENERGINET*. 7 September 2016. <http://www.energinet.dk/EN/KLIMA-OG-MILJOE/Miljoerapportering/Elproduktion-i-Danmark/Sider/Elproduktion-i-Danmark.aspx> (accessed April 21, 2017).
- [1.22] Tessum, C W, J D Hill, and J D Marshall. "Life Cycle Air Quality Impacts of Conventional and Alternative Light Duty Transport in the United States." *PNAS 1406853111*, 2014.
- [1.23] Rubin, Z J, S A Munns, and J J Moskwa. "The Development of Vehicular Powertrain System Modelling Methodologies: Philosophy and Implementation." *SAE Technical Paper No: 971089*, 1997.
- [1.24] Karlsson, J, and J Fredriksson. "Cylinder-by-Cylinder Engine Models vs. Mean Value Engine Models for Use in Powertrain Control Application." *SAE Technical Paper No: 1999-01-090X*, 1999.
- [1.25] Louca, L S, J L Stein, G M Hulbert, and J Sprague. "Proper Model Generation: An Energy-Based Methodology." *3rd International Conference on Bond Graph Modelling and Simulation*, January 1997.
- [1.26] Dow, Peter Ivan. *The Development and Integration of Systems Models to Simulate Engine and Vehicle Performance*. PhD Thesis, University of Nottingham, 2001.
- [1.27] Ochiai, Naoya, Jun Ishimoto, Akira Arioka, Nobuhiko Yamaguchi, Yuzuru Sasaki, and Nobuyuki Furukawa. "Integrated Computation Study for Total Atomisation Process of Primary Breakup to Spray Droplet Formation in Injector Nozzle." *SAE Technical Paper 2016-01-2202*,

doi: 10.4271/2016-01-2202, 2016.

Chapter 2

- [2] Halderman, J D. "Automotive Engines: Theory and Servicing, Chapter 13: Cooling System Operation and Diagnosis." *Automotive Engines Theory*. n.d. <https://worldtracker.org/media/library/College%20Books/Automotive%20Engines%20Theory%20and%20Servicing/Chapter13.pdf> (accessed 10 04, 2014).
- [2.1] Cipollone, R, D D Battista, and A Gualtieri. "Head and Block Splot Cooling in ICE." *The International Federation of Automatic Control (IFAC)*, 2012.
- [2.2] Hoag, Kevin L. *Vehicular Engine Design*. Lavanttal: Springer-Verlag and Society of Automotive Engineers International, 2006.
- [2.3] Heywood, J B. *Internal Combustion Engine Fundamentals*. McGraw-Hill, 1998.
- [2.4] Friedfeldt, R, T Zenner, R Ernst, and A Fraser. "Three Cylinder Gasoline Engine with Direct Injection." *ATZ 02/2012* Volume 12 (2012).
- [2.5] The Engineer. "Integrated Exhaust" *Lotus Engineering*. May 3 2007. <https://www.theengineer.co.uk/issues/may-2007-online/integrated-exhaust/> (accessed February 5 2018).
- [2.6] Kuhlback, K., Mehring, J., Borrmann, D. and Friedfeldt, R. "Cylinder Head with Integrated Exhaust Manifold for Downsizing Concepts." *MTZ* Volume 70 (04 2009): 12 – 17, <https://link.springer.com/content/pdf/10.1007/BF03226940.pdf> (accessed February 5 2018).
- [2.7] Nishino, T, S Hiromichi, and N Murakami. *Study of Engine Cooling Technologies for Knock Suppression in Spark Ignition Engines*. Technical Review , Mitsubishi Motors, 2004.
- [2.8] Leone, T, and M Pozar. "Fuel Economy Benefit of Cylinder Deactivation." *SAE Technical Paper 2001-01-3591*, doi: 10.4271/2001-01-3591, 2001.
- [2.9] Doller, Steffen, Frank Sören, Sascha Sengpiehl, and Torsten Semper. "Activable Displacement SI Engine from IAV for CO2 Reduction." *MTZ* Volume 74 (12 2013): 20 - 24.
- [2.10] Ma, Zheng. "Oil Transport Analysis of a Cylinder Deactivation Engine." *SAE Technical Paper 2010-01-1098*, doi: 10.4271/2010-01-1098, 2010.
- [2.11] Zammit, J.P., McGhee, M.J., and Shayler, P.J. "The Effects of Early Inlet Valve Closing and Cylinder Disablement on Fuel Economy and Emissions of a Direct Injection Diesel Engine." *Elsevier: Energy Volume 79 Pages 100 – 110*, <https://doi.org/10.1016/j.energy.2014.10.065> , 2015.
- [2.12] Ilhlemann, Arndt, and Norbert Nitz. "Cyliner Deactivation: A Technology with a Future or A Niche Application?" *10th Schaeffler Symposium*. Schaeffler, 2014. 172 - 184.
- [2.13] Souflas, Ioannis, Byron Mason, Mark Cary, and Peter Schaal. "Mode Transition Optimisation for Variable Displacement Engines." *SAE Technical Paper 2016-01-0619*, doi: 10.4271/2016-01-0619, 2016.

- [2.14] Hoffmann, Hermann, Adam Loch, Richard Widmann, Gerhard Kreusen, Daniel Meehsen, and Martin Rebbert. "Cylinder Deactivation for Valvetrains with Roller Finger Follower." *MTZ* Volume 70 (04 2009): 26-30.
- [2.15] Radulescu, Andrei, James McCarthy Jr, and Scott Brownell. "Development of a Switching Roller Finger Follower for Cylinder Deactivation in Gasoline Engine Applications." *SAE Technical Paper 2013-01-0589*, doi: 10.4271/2013-01-0589, 2013.
- [2.16] Fujiwara, M, K Kumagai, M Segawa, R Sato, and Yuichi Tamura. "Development of a 6-Cylinder Gasoline Engine with New Variable Cylinder Management Technology." *SAE Technical Paper 2008-01-0610*, doi: 10.4271/2008-01-0610, 2008.
- [2.17] Spath, Mark J., Hendriksma, Nick. J, and Fox, Michael. J. Valve Lifter Assembly for Selectively Deactivating a Cylinder. United States Patent 7263956 B2. 26 November 2002.
- [2.18] Stabinsky, M, et al. "Active Fuel Management (TM) Technology: Hardware Development on a 2007 GM 3.9l V6 OHV SI Engine." *SAE Technical Paper 2007-01-1292*, doi: 10.4271/2007-01-1292, 2007.
- [2.19] Middendorf, Hermann, Jorg Theobald, Leonhard Lang, and Kai Hartel. "The 1.4l TSI Gasoline Engine with Cylinder Deactivation." *MTZ (MTZ) Volume 73 (03 2012): 4 - 8.*
- [2.20] Kortwittenborg, Thomas, and Frank Walter. "Strategy to Control the Cylinder Deactivation." *MTZ* Volume 74 (02 2013): 19 - 21.
- [2.21] Moore, Wayne, Matthew Foster, Ming-Chia Lai, Xing-Bin Xie, Yi Zheng, and Atsushi Matsumoto. "Charge Motion Benefits of Valve Deactivation to Reduce Fuel Consumption and Emissions in a GDi, VVA Engine." *SAE International 2011-01-1221*, 2011.
- [2.22] Laing, P. "Development of an Alternator-Powered Electrically-Heated Catalyst System." *SAE Technical Paper 941042*, doi: 10.4271/941042, 1994.
- [2.23] Socha, L, Thompson D, and Weber P. "Optimisation of Extruded Electrically Heated Catalysts." *SAE Technical Paper 9404648* doi: 10.4271/940468, 1994.
- [2.24] Burch, S, T Potter, M Keyser, M Brady, and Kenton F Michaels. "Reducing Cold-Start Emissions by Catalytic Converter Thermal Management." *SAE Technical Paper 950409*, 1995.
- [2.25] Bharath, Anand Nageswaran, Yangdongfang Yang, Rolf D Reitz, and Christopher Rutland. "Comparison of Variable Valve Actuation, Cylinder Deactivation and Injection Strategies for Low-Load RCCI Operation of a Light Duty Engine." *SAE Technical Paper 2015-01-0843*, doi: 10.4271/2015-01-0843, 2015.
- [2.26] Bohac, S, and D Assanis. "Effect of Exhaust Valve Timing on Gasoline Engine Performance and Hydrocarbon Emissions." *SAE Technical Paper 2004-01-3058*, doi: 10.4271/2004-01-3058, 2004.
- [2.27] Parvate-Patil, G, H Hong, and B Gordon. "Analysis of Variable Valve Timing Events and Their Effects on Single Cylinder Diesel Engine." *SAE Technical Paper 2004-01-2965*, doi: 10.4271/2004-01-2965, 2004.
- [2.28] Roberts, L, et al. "Modelling the Impact of Early Exhaust Valve Opening on Exhaust Aftertreatment Thermal Management and Efficiency for Compression Ignition Engines."

International Journal of Engine Research, 2014.

- [2.29] Far, Kian Eisazadeh, and Matthew Younkins. "Fuel Economy Gains through Dynamic-Skip-Fire in Spark Ignition Engines." *SAE Technical Paper 2016-01-0672*, doi: 10.4271/2016-01-0672, 2016.
- [2.30] Kuruppu, Chavithra, and Apostolos Pesiridis. "Investigation of Cylinder Deactivation and Variable Valve Actuation on Gasoline Engine Performance." *SAE Technical Paper 2014-01-1170*, doi: 10.4271/2014-01-1170, 2014.
- [2.31] Said, Mohd Farid Muhamad, Azhar Bin Abdul Aziz, Zulkanain Abdul Latiff, Amin Mahmoudzadeh Andwari, and Shahril Nizam Mohamed Soid. "Investigation of Cylinder Deactivation (CDA) Strategies on Part Load Conditions." *SAE Technical Paper 2014-01-2549*, doi: 10.4271/2014-01-2549, 2014.
- [2.32] Flierl, Rudolf, Wilhelm Hannibal, Anton Schurr, and Jorg Neugartner. "Turbocharged Three-Cylinder Engine with Activation of a Cylinder." *MTZ Volume 75 (06 2014): 22 - 26*.
- [2.33] Flierl, Rudolf, and Frederic Lauer. "Mechanically Fully Variable Valvetrain and Cylinder Deactivation." *MTZ Volume 74 (04 2013): 50 - 57*.
- [2.34] Tian, Tian, and Adam Vokac. "An Experimental Study of Oil Transport on the Piston Third Land and the Effects of Piston and Ring Designs." *SAE Technical Paper 2004-01-1934*, doi: 10.4271/2004-01-1934, 2004.
- [2.35] Senapati, Uday, Ian McDevitt, and Aaron Hankinson. "Vehicle Refinement Challenges for a Large Displacement Engine with Cylinder Deactivation Capability." *SAE International 2011-01-1678*, doi: 10.4271/2011-01-1678, 2011.
- [2.36] Binder, Scott William, Matthias Fischer, Christoph Sasse, and Joerg Trampler. "New Launch Devices for Automatic Transmissions." *SAE Technical Paper 2013-01-0233*, doi: 10.4271/2013-01-0233, 2013.
- [2.37] Orlamuender, A, M Fischer, D Lorenz, and M Kuehner. "New Torsional Damping Systems for Highcharged 3 and 4 Cylinder Engines Power Split to Replace the Pendulum Type Absorber." *VDI*, 2011.
- [2.38] Boretti, Alberto, and Joseph Scalco. "Piston and Valve Deactivation for Improved Part Load Performances of Internal Combustion Engines." *SAE 2011 World Congress & Exhibition*. SAE International, 2011.
- [2.39] Doller, Steffen, Frank Sören, Sascha Sengpiehl, and Torsten Semper. "Actrvable Displacement SI Engine from IAV for CO2 Reduction." *MTZ Volume 74 (12 2013): 20 - 24*.
- [2.40] Chein, Li Chun, Matthew Younkins, and Mark Wilcutts. "Modelling and Simulation of Airflow Dynamics in A Dynamic Skip Fire Engine." *SAE Technical Paper 2015-01-1717*, doi: 10.4271/2015-01-1717, 2015.
- [2.41] Carlson, Urban, Anders Höglund, and Christian Von Koenigsegg. Internal Combustion Engine for a Vehicle Comprising at Least One Compressor Cylinder at Least on Compressor Cylinder connected to a Air Tank. United States Patent US8800510 B2. 12 August 2014.
- [2.42] Venkatesh, Deepak, and Arockia Selvakumar. "A Novel Design of Pneumatic Actuator for

- Camless Engines." *SAE Technical Paper 2016-01-0099*, 2016.
- [2.43] AB, Freevalve. *Freevalve*. 27 February 2016. <http://www.freevalve.com/> (accessed February 27, 2016).
- [2.44] Ghasemi, A. "CAE Simulations for Engine Block Bore Distortion." *Society of Automotive Engineers Technical Paper*, doi: 10.4271/2012-01-1320, 2012.
- [2.45] Jaaskelainen, Hannu. *Piston-Ring-Liner Design for Low Oil Consumption - 1. Bore Distortion*. 2009. https://www.dieselnets.com/tech/lube_cons_ring.php (accessed April 4, 2017).
- [2.46] Hill, S H. "Piston Ring Designs for Reduced Friction." *Society of Automotive Engineers*, 841222, doi: 10.4271.841222, 1984: 1 -20.
- [2.47] Scheider, E W. "Effect of Cylinder Bore Out-of-Roundness on Piston Ring Rotation and Engine Oil Consumption." *Society of Automotive Engineers*, 930796, doi: 10.4271/930796, 1993: 139 - 160.
- [2.48] Timoshenko, S. *Theory of Elastic Stability*. New York: McGraw Hill, 1936.
- [2.49] Prescott, J. *Applied Elasticity*. New York: Dover Publications, 1946.
- [2.50] Englisch, C. *KoblenRinge*. Vienna: Springer-Verlag, 1958.
- [2.51] Gintsburg, B Y. "Splitless-type Piston Rings." *Russian Engineering Journal* 48 no. 7 (1968): 37-40.
- [2.52] Bardzimashvili, Teimuraz, James F Kelly, and Elene Romelashvili. *Distortion Inside a Piston Bore*. Industrial Math Project, Ann Arbor: University of Michigan, 2004.
- [2.53] Tian, T. "Dynamic Behaviours of Piston Rings and Their Practical Impact. Part 1: Ring Flutter and Ring Collapse and Their Effects on Gas Flow and Oil Transport." *Proceedings of Institution of Mechanical Engineers Part J: Journal of Engineering Tribology* 216 (2002): 209 - 227.
- [2.54] Rajput, R K. *Internal Combustion Engines*. New Dehli: Laxmi Publications, 2005.
- [2.55] Loenne , K, and R Ziemba. "The Goetze Cylinder Distortion Measurement System and the Possibilities of Reducing Cylinder Distortions." *Society of Automotive Engineers Technical Paper*, 880142, doi: 10.4271/880142, 1988.
- [2.56] Rahnejat, Homer. *Tribology and Dynamics of Engine and Powertrain*. Oxford: Woodhead Publishing Limited, 2010.
- [2.57] Flores, G. "Graded Freeform Machining of Cylinder Bores using Form Honing." *Society of Automotive Engineers Technical Paper*, doi: 10.4271/2015-01-1725, 2015.

Chapter 3

- [3] Mason, Brian Richard. *Thermal Analysis of S.I. Engines with High Reinforced Plastic Content*. PhD Thesis, University of Nottingham, 1990.

- [3.1] Christian, S J. *A Spark Ignition Engine Model for Heat Flow and Friction Characteristics*. PhD Thesis, University of Nottingham, 1992.
- [3.2] Yuen, H C.R. *An Investigation of Thermal Conditions in Spark Ignition Engines*. PhD Thesis, University of Nottingham, 1995.
- [3.3] Chick, J P. *The Modelling of Engine Thermal Systems*. PhD Thesis, University of Nottingham, 1998.
- [3.4] Baylis, W S. *An Investigation of Heat Transfer and Friction in Turbocharged Diesel Engines*. PhD Thesis, University of Nottingham, 1999.
- [3.5] Patton, Kenneth J, Ronald G Nitschke, and John B Heywood. "Development and Evaluation of a Friction Model for Spark Ignition Engines." *SAE 890836*, 1989.
- [3.6] Leong, D K. *Investigations of Friction Losses in Automotive Internal Combustion Engines*. PhD Thesis, University of Nottingham, 2004.
- [3.7] Morgan, Tessa Joanne. *The Modelling of Internal Combustion Engine Thermal Systems and Behaviour*. PhD Thesis, University of Nottingham, 2003.
- [3.8] Chick, J P. *The Modelling of Engine Thermal Systems*. PhD Thesis, University of Nottingham, 1998.
- [3.9] Shayler, Paul J, K W Leong, and Michael Murphy. "Contributions to Engine Friction During Cold, Low Speed Running and the Dependence on Oil Viscosity." *SAE Technical Paper 2005-01-1654*, doi: 10.4271/2005-01-1654, 2005.
- [3.10] Addison, James. *The Benefits of Thermal Management to Reduce Friction Losses in Engines*. PhD Thesis, University of Nottingham, 2015.
- [3.11] Taylor, CF, and TY Toong. "Heat Transfer in Internal Combustion Engines." *ASME*, 1957: 57-HT-17.
- [3.12] Shayler, PJ, JP Chick, and T Ma. "Correlation of Engine Heat Transfer for Heat Rejection and Warm-Up Modelling." *SAE International*, 1997.
- [3.13] Dittus, F.W., and L.M.K Boetler. *Heat Transfer in Automobile Radiators of the Tubular Type*. Berkley: University of California (Berkley) Pub. Eng, 1930.
- [3.14] Forster, H.K., and N, Zuber. "Dynamics of Vapor Bubbles and Boiling Heat Transfer." *AIChE Journal* 1 (4) (1955): 531-535.
- [3.15] Chen, J C. "Correlation for Boiling Heat Transfer to Saturated Fluids in Convective Flow." *Industrial & Engineering Chemistry Process and Development* 5 (3) (July 1966): 322 - 329.
- [3.16] Finlay, I C, D Harris, D J Boam, and B I Parks. "Factors Influencing Combustion Wall Temperatures in a Liquid Cooled, Automotive, Spark-Ignition Engine." *Proceedings of the Institution of Mechanical Engineers, Part D: Transport Engineering 1984-1988* Volume 199 (1985): 207-214.

Chapter 4

- [4.1] Friedfeldt, R, T Zenner, R Ernst, and A Fraser. "Three Cylinder Gasoline Engine with Direct Injection." *ATZ 02/2012* Volume 12 (2012).
- [4.2] Gitano, Horizon. "Dynamometer Basics." *SkyShorz University Resources*. n.d. http://skyshorz.com/university/resources/dynamo_basics.pdf (accessed October 24, 2014).
- [4.3] Chick, J P. *The Modelling of Engine Thermal Systems*. PhD Thesis, University of Nottingham, 1998.
- [4.4] Hoegfeldt, I, A Druschitz, and D Fitzgerald. "Lightweight Crankshafts." *SAE Technical Paper 2006-01-001*, doi: 10.4271/2006-01-0016, 2006.
- [4.5] Lapp, Michael T, and Chris C Hall. "Mahle Develops Ultra-Lightweight Connecting Rod." *SAE Automotive Engineering*, August 31, 2011.
- [4.6] Patton, Kenneth J, Ronald G Nitschke, and John B Heywood. "Development and Evaluation of a Friction Model for Spark Ignition Engines." *SAE 890836*, 1989.
- [4.7] Shayler, Paul J, K W Leong, and Michael Murphy. "Contributions to Engine Friction During Cold, Low Speed Running and the Dependence on Oil Viscosity." *SAE Technical Paper 2005-01-1654*, doi: 10.4271/2005-01-1654, 2005.
- [4.8] Canciam, C A. "Effect of Temperature on Dynamic Viscosity of Lubricating Oils SAE 5W20, SAE 5W30 and SAE 5W40." *Revista de Universidade Vale do Rio Verde* Vol. 11 (2) (2013): p. 239-250.
- [4.9] Shayler, PJ, JP Chick, and T Ma. "Correlation of Engine Heat Transfer for Heat Rejection and Warm-Up Modelling." *SAE International*, 1997.
- [4.10] Dittus, F.W., and L.M.K Boetler. *Heat Transfer in Automobile Radiators of the Tubular Type*. Berkley: University of California (Berkley) Pub. Eng, 1930.
- [4.11] Hires, S.D., and G.L. Pochmara. "An Analytical Study of Exhaust Gas Heat Loss in A Piston Engine Exhaust Port." *SAE Technical Paper*, 1976.
- [4.12] Malchow, GL, SC Sorenson, and RO Buckius. "Heat Transfer in the Straight Section of an Exhaust Port of a Spark Ignition Engine." *SAE Paper 790309*, 1979.
- [4.13] Caton, JA, and JB Heywood. "An Experimental and Analytical Study of Heat Transfer in an Engine Exhaust Port." *International Journal of Heat Transfer* 24, 1981: 581.
- [4.14] Meisner, S, and SC Sorenson. "Computer Simulation of Intake and Exhaust Manifold Flow and Heat Transfer." *SAE Paper 860242*, 1986.
- [4.15] Heywood, J B. *Internal Combustion Engine Fundamentals*. McGraw-Hill, 1998.
- [4.16] Taylor, CF, and TY Toong. "Heat Transfer in Internal Combustion Engines." *ASME* , 1957: 57-HT-17.
- [4.17] Hoag, Kevin L. *Vehicular Engine Design*. Lavanttal: Springer-Verlag and Society of Automotive Engineers International, 2006.

- [4.18] Hayak, Jan. "Personal Communication." Ford Motor Company, 2014, n.d.
— . *Personal Communication*. Ford Motor Company, 2014.
- [4.19] Bejan, Adrian. *Convection Heat Transfer*. Somerset : John Wiley & Sons, 2013.
- [4.20] Cengel, Yunus A. *Heat Transfer - A Practical Approach Second Edition*. Higher Education, 2002.
- [4.21] Shayler, Paul. n.d.
- [4.22] Cerveny, Dr. Randy. *World Meteorological Organization's World Weather & Climate Extremes Archive*. n.d. <https://wmo.asu.edu/> (accessed 02 18, 2017).
- [4.23] Rathakrishnan, Ethirajan. *Elements of Heat Transfer*. CRC Press: Taylor & Francis Group, 2012.
- [4.24] Law, Theo. *The Effects of Lubrication System Modifications on Engine Friction and Thermal Behaviour*. University of Nottingham: PhD Thesis , 2007.
- [4.25] Easter, J, et al. "An Area-Average Correlation for Oil Jet Cooling of Automotive Pistons." *Journal of Heat Transfer (ASME)* Vol. 136, no. doi: 10.1115/1.4027835 (2014).
- [4.26] Mian, A. "Design and Analysis of Engine Lubrication Systems." *SAE Paper 970637*, 1997.
- [4.27] Lichtarowicz, A, R K Duggins, and E Markland. "Discharge Coefficients for Incompressible Non-Cavitating Flow Through Long Orifices." *Journal of Mechanical Engineering Science* Vol. 7 (2) (1965): pp. 210 - 219.
- [4.28] Addison, James. *The Benefits of Thermal Management to Reduce Friction Losses in Engines*. PhD Thesis, University of Nottingham, 2015.
- [4.29] Zinner, Karl A. *Supercharging of Internal Combustion Engines*. Berlin Heidelberg New York: Springer-Verlag, 1978.
- [4.30] Taylor, Charles Fayette. *The Internal Combustion Engine in Theory and Practice Volume 1: Thermodynamics, Fluid Flow, Performance*. Cambridge: MIT Press, 1985.
- [4.31] Taylor, Charles Fayette. *The Internal Combustion Engine in Theory and Practice Volume 1: Thermodynamics, Fluid Flow, Performance*. Cambridge: MIT Press, 1985.
- [4.32] Leone, T, and M Pozar. "Fuel Economy Benefit of Cylinder Deactivation." *SAE Technical Paper 2001-01-3591*, doi: 10.4271/2001-01-3591, 2001.
- [4.33] First Sensor. *Understanding the Difference between Absolute, Gauge and Differential Pressure* . 2017. <https://www.first-sensor.com/en/products/pressure-sensors/pressure-sensors-and-transmitters/pressure-types.html> (accessed 03 06, 2017).
- [4.34] Bech, Alexander, Paul Shayler, and Michael McGhee. "The Effects of Cylinder Deactivation on the Thermal Behaviour and Performance of a Three Cylinder Spark Ignition Engine." *SAE International Journal of Engines* , doi: 10.4271/2016-01-2160 Volume 9 Issue 2 (2016): 1999-2009.

- [4.35] Gottschalk, Wolfram, Rene Rink, and Matthias Schultablers. "Investigations on Ventilation Strategies for SI Cylinder Deactivation Based on a Variable Valve Train." *SAE Technical Paper 2016-01-2346*, doi: 10.4271/2016-01-2346, 2016.
- [4.36] Ma, Zheng. "Oil Transport Analysis of a Cylinder Deactivation Engine." *SAE Technical Paper 2010-01-1098*, doi: 10.4271/2010-01-1098, 2010.
- [4.37] Morgan, Tessa Joanne. *The Modelling of Internal Combustion Engine Thermal Systems and Behaviour*. PhD Thesis, University of Nottingham, 2003.
- [4.38] Janowski, Nils Peter Bernd. *Targeted Heating of Powertrain Components To Improve Vehicle Fuel Economy During Warm-Up*. PhD Thesis, University of Nottingham, 2011.

Chapter 5

- [5] Christian, S J. *A Spark Ignition Engine Model for Heat Flow and Friction Characteristics*. PhD Thesis, University of Nottingham, 1992.
- [5.1] Chick, J P. *The Modelling of Engine Thermal Systems*. PhD Thesis, University of Nottingham, 1998.
- [5.2] Zammit, Jean Paul. *Managing Engine Thermal State to Reduce Friction Losses During Warm-up*. PhD Thesis, Nottingham: University of Nottingham, 2013.
- [5.3] Stachowiak, G W, and A W Batchelor. *Engineering Tribology*. Amsterdam: Elsevier, 1993.
- [5.4] Leong, D K. *Investigations of Friction Losses in Automotive Internal Combustion Engines*. PhD Thesis, University of Nottingham, 2004.
- [5.5] Mohammadpour, M, R Rahmani, and H Rahnejat. "Effect of Cylinder Deactivation on the Tribo-Dynamics and Acoustic Emission of Overlay Big End Bearings." *Proceeding IMechE: Part K* Vol. 228 Issue 2 (2014): pp. 138-151.
- [5.6] Nasif, Ghassan. *CFD Simulation of Oil Jets with Application to Piston Cooling*. PhD Thesis University of Windsor, 2014.
- [5.7] Parvate-Patil, G, H Hong, and B Gordon. "Analysis of Variable Valve Timing Events and Their Effects on Single Cylinder Diesel Engine." *SAE Technical Paper 2004-01-2965*, doi: 10.4271/2004-01-2965, 2004.
- [5.8] McGhee, Michael, Alexander Bech, and Paul J Shayler. "Operation of Cylinder Deactivation of a 1.4l SI Engine Under Real World Driving Conditions." September 2016: Paper F2016-ESYA-012.
- [5.9] Ronald, Hanson K, et al. *Smart Sensors for Advanced Combustion Systems*. The Global Climate and Energy Project (GCEP) Technical Report 2005, Standford: Stanford University, 2005.
- [5.10] Law, Theo. *The Effects of Lubrication System Modifications on Engine Friction and Thermal Behaviour*. University of Nottingham: PhD Thesis , 2007.
- [5.11] Ma, Zheng. "Oil Transport Analysis of a Cylinder Deactivation Engine." *SAE Technical Paper 2010-01-1098*, doi: 10.4271/2010-01-1098, 2010.

- [5.12] Gottschalk, Wolfram, Rene Rink, and Matthias Schultablers. "Investigations on Ventilation Strategies for SI Cylinder Deactivation Based on a Variable Valve Train." *SAE Technical Paper 2016-01-2346*, doi: 10.4271/2016-01-2346, 2016.
- [5.13] Adcock, Ian. *Bentley Develops W12 Cylinder Deactivation*. 13 March 2015. <http://articles.sae.org/13975/> (accessed February 2, 2017).
- [5.14] Serrano, Joe, Geoff Routledge, Norman Lo, Mark Shost, Vijay Srinivasan, and Biswa Ghosh. "Methods of Evaluating and Mitigating NVH when Operating an Engine in Dynamic Skip Fire." *SAE International Journal of Engines V123*, doi: 10.4271/2014-01-1675, 2015.
- [5.15] Rajput, R K. *Internal Combustion Engines*. New Dehli: Laxmi Publications, 2005.

Chapter 6

- [6] McGhee, Michael, Alexander Bech, and Paul J Shayler. "Operation of Cylinder Deactivation of a 1.4l SI Engine Under Real World Driving Conditions." September 2016: Paper F2016-ESYA-012.
- [6.1] Middendorf, Hermann, Jorg Theobald, Leonhard Lang, and Kai Hartel. "The 1.4l TSI Gasoline Engine with Cylinder Deactivation." *MTZ (MTZ) Volume 73 (03 2012)*: 4 - 8.
- [6.2] Chick, J P. *The Modelling of Engine Thermal Systems*. PhD Thesis, University of Nottingham, 1998.
- [6.3] Energy, National Renewable Energy Laboratory for the United States Department of. *Advanced Vehicle Simulator*. 2009. <https://sourceforge.net/projects/adv-vehicle-sim/> (accessed July 22, 2015).
- [6.4] Barlow, T J, S Latham, S McCrae, and P G Boutler. *A Reference Book of Driving Cycles Use in the Measurement of Road Vehicle Emissions*. Published Project Report, TRL Limited, 2009.
- [6.5] —. *Worldwide Harmonized Light Vehicles Test Cycle (WLTC)*. March 2017. <https://www.dieselnet.com/standards/cycles/wltp.php> (accessed June 22, 2014).
- [6.6] Robert Bosch GmbH. *Automotive Handbook*. Vol. 7th Edition. John Wiley & Sons Ltd , 2007.
- [6.7] Milliken, W. *Race Car Vehicle Dynamics*. Warrendale: Society of Automotive Engineers Inc., 1995.
- [6.8] Clark, S. *A Handbook for the Rolling Resistance of Pneumatic Tyres*. Ann Arbor, United States of America: University of Michigan, 1979.
- [6.9] Adcock, Ian. *Bentley Develops W12 Cylinder Deactivation*. 13 March 2015. <http://articles.sae.org/13975/> (accessed February 2, 2017).
- [6.10] DieselNet. *ECE 15 + EUDC/NEDC*. March 2017. https://www.dieselnet.com/standards/cycles/ece_eudc.php (accessed October 22, 2014).
- [6.11] Queensland Government. *Traffic Signals Information*. 2017 April 2017. <https://www.tmr.qld.gov.au/Travel-and-transport/Road-and-traffic-info/Traffic-Signals->

Information (accessed May 5, 2017).

- [6.12] Leone, T, and M Pozar. "Fuel Economy Benefit of Cylinder Deactivation." *SAE Technical Paper 2001-01-3591*, doi: 10.4271/2001-01-3591, 2001.
- [6.13] Zammit, Jean Paul. *Managing Engine Thermal State to Reduce Friction Losses During Warm-up*. PhD Thesis, Nottingham: University of Nottingham, 2013.

Chapter 7

- [7] Tan, Gangfeng, Xuefeng Yang, Li Zhou, Kangping Ji, and Yang Mengying. "Heat Transfer Analysis for Exhaust Waste Heat Recovery System Based on Mg₂Si(1-x)Sn(x) Thermoelectric Materials." *SAE Technical Paper 2016-01-2161*, doi:10.4271/2016-01-2161, 2016.

Chapter 8

- [8] Parvate-Patil, G, H Hong, and B Gordon. "Analysis of Variable Valve Timing Events and Their Effects on Single Cylinder Diesel Engine." *SAE Technical Paper 2004-01-2965*, doi: 10.4271/2004-01-2965, 2004.
- [8.1] Ma, Zheng. "Oil Transport Analysis of a Cylinder Deactivation Engine." *SAE Technical Paper 2010-01-1098*, doi: 10.4271/2010-01-1098, 2010.
- [8.2] Adcock, Ian. *Bentley Develops W12 Cylinder Deactivation*. 13 March 2015. <http://articles.sae.org/13975/> (accessed February 2, 2017).
- [8.3] Serrano, Joe, Geoff Routledge, Norman Lo, Mark Shost, Vijay Srinivasan, and Biswa Ghosh. "Methods of Evaluating and Mitigating NVH when Operating an Engine in Dynamic Skip Fire." *SAE International Journal of Engines VI23*, doi: 10.4271/2014-01-1675, 2015.
- [8.4] Kagnici, Fatih, and Akalin, Ozgen. *The Effect of Cylinder Bore Distortion on Lube Oil Consumption and Blow-By*. *Journal of Tribology 136(1)*, Elsevier, doi: 10.1115/1.4025208, 2013.
- [8.5] Rajput, R K. *Internal Combustion Engines*. New Dehli: Laxmi Publications, 2005.
- [8.6] Nishino, T, S Hiromichi, and N Murakami. *Study of Engine Cooling Technologies for Knock Suppression in Spark Ignition Engines*. Technical Review , Mitsubishi Motors, 2004.
- [8.7] Middendorf, Hermann, Jorg Theobald, Leonhard Lang, and Kai Hartel. "The 1.4l TSI Gasoline Engine with Cylinder Deactivation." *MTZ (MTZ) Volume 73 (03 2012)*: 4 - 8.
- [8.8] Carlson, Urban, Anders Höglund, and Christian Von Koenigsegg. *Internal Combustion Engine for a Vehicle Comprising at Least One Compressor Cylinder at Least on Compressor Cylinder connected to Air Tank*. United States Patent US8800510 B2. August 12, 2014.
- [8.9] Vijayenthiran, Viknesh. *1.6-litre Camless Engine Delives 230HP in Qoros 3*. 21 November 2016. http://www.motorauthority.com/news/1107384_1-6-liter-camless-engine-delivers-230-hp-in-qoros-3#image=100581791 (accessed February 24, 2017).
- [8.10] Gottschalk, Wolfram, Rene Rink, and Matthias Schultablers. "Investigations on Ventilation Strategies for SI Cylinder Deactivation Based on a Variable Valve Train." *SAE Technical Paper*

2016-01-2346, doi: 10.4271/2016-01-2346, 2016.

- [8.11] Schwab, Klaus. *The Fourth Industrial Revolution*. Geneva: Penguin RandomHouse UK, 2017.
- [8.12] Carlson, Urban, Anders Höglund, and Christian Von Koenigsegg. Internal Combustion Engine for a Vehicle Comprising at Least One Compressor Cylinder at Least on Compressor Cylinder connected to a Air Tank. United States Patent US8800510 B2. 12 August 2014.
- [8.13] Taylor, Michael. "End of Downsizing?" *Engine Technology International*, March 2017: 43-48.
- [8.14] McHugh, Mollyt. *Tesla's Cars Now Drive Themselves, Kinda*. 14 October 2015. <http://www.wired.com/2015/10/tesla-self-driving-over-air-update-live> (accessed April 2, 2017).
- [8.15] Halleck, Thomas. *Google Inc. Says Self-Driving Car Will be Ready by 2020*. 14 January 2015. <http://www.ibtimes.com/google-inc-says-self-driving-car-will-be-ready-2020-1784150> (accessed April 2, 2017).
- [8.16] Knapp, Alex. *Nevada Passes Law Authorizing Driverless Cars*. 12 June 2011. <http://www.forbes.com/sites/alexknapp/2011/06/02/nevada-passes-law-authorizing-driverless-cars> (accessed April 2, 2017).
- [8.17] State of California. *State of California Department of Motor Vehicles Testing of Autonomous Vehicles*. 14 April 2017. <https://www.dmv.ca.gov/portal/dmv/detail/vr/autonomous/testing> (accessed May 15, 2017).
- [8.18] Chevron,Oronite. *Shedding Light on Low Speed Pre-Ignition (LSPI)*. February 2018. <https://www.oronite.com/products/lspi.asp> (accessed February 5, 2018).
- [8.19] Qi, Y., Xu, Y., Wang, Z., and Wang, J., "The Effect of Oil Intrusion on Super Knock in Gasoline Engine," SAE Technical Paper 2014-01-1224, 2014, <https://doi.org/10.4271/2014-01-1224>.
- [8.20] Leone, T, and M Pozar. "Fuel Economy Benefit of Cylinder Deactivation." *SAE Technical Paper 2001-01-3591*, doi: 10.4271/2001-01-3591, 2001.

Appendix

A) Method for Calculating Exhaust Port Elements

1) Lower section of the exhaust port

For $v_{exhaust,port1}$:

$$v_{lower} = d_{ex,port} \cdot b_{ex,port} \cdot t_{port,wall}$$

Where:

$$d_{ex,port} = 0.91 \cdot d_{exhaust,valve}$$

$$b_{ex,port} = d_{ex,port} \cdot n_{exhaust,valve}$$

$$n_{exhaust,valve} = 2$$

$$t_{port,wall} = t_{cyl,wall} \cdot 0.8$$

$$\text{wherein: } 0.006 > t_{port,wall} < 0.00449$$

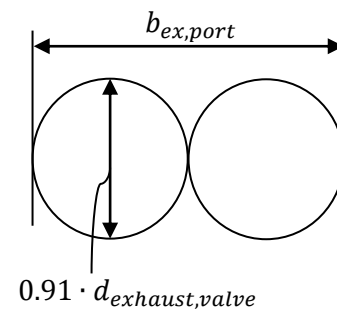
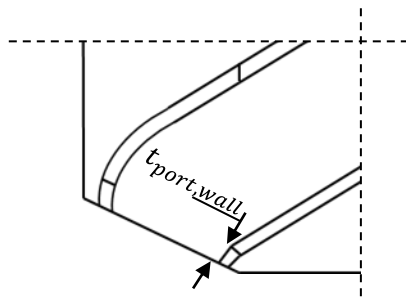
For $v_{exhaust,port2}$:

$$v_{lower2} = b'_{ex,port} \cdot d'_{ex,port} \cdot t_{port,wall}$$

Where:

$$b'_{ex,port} = b_{ex,port} \cdot (2 \cdot t_{port,wall})$$

$$d'_{ex,port} = d_{ex,port} \cdot (2 \cdot t_{port,wall})$$



2) Middle section of the exhaust port (defined as the area between an arc and the center of a circle)

For $v_{exhaust,port1}$:

$$v_{middle} = \frac{1}{2} \cdot \theta_4 \cdot d_{ex,port}^2 \cdot b_{ex,port}$$

Where:

$$d_{ex,port} = 0.91 \cdot d_{exhaust,valve}$$

$$b_{ex,port} = d_{ex,port} \cdot n_{exhaust,valve}$$

$$\theta_4 = \frac{\pi}{2} - \theta_3$$

$$\theta_3 = \tan^{-1} \left(\frac{g_{ex}}{hex} \right)$$

$$g_{ex} = FEX - e_{ex}$$

$$e_{ex} = t_{cyl,wall}$$

$$hex = l_{ex,port}^* - \frac{1}{2} d_{ex,port}$$

$$l_{ex,port}^* = \text{user defined value (0.14)}$$

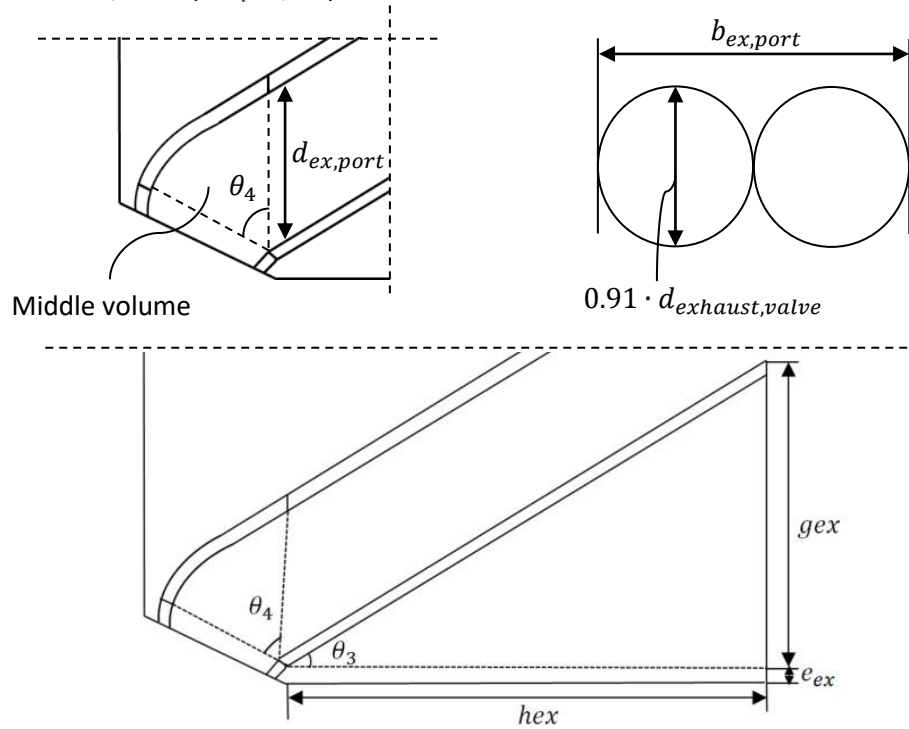
$$v_{middle2} = \frac{1}{2} \cdot \theta_4 \cdot (d'_{ex,port})^2 \cdot b'_{ex,port}$$

For $v_{exhaust,port2}$:

Where:

$$d'_{ex,port} = 0.91 \cdot d_{exhaust,valve} \cdot (2 \cdot t_{port,wall})$$

$$b'_{ex,port} = d_{ex,port} \cdot n_{exhaust,valve} \cdot (2 \cdot t_{port,wall})$$



3) Upper section of the exhaust port

For $v_{exhaust,port1}$:

$$v_{upper} = a_{upper} \cdot l'_{ex,port}$$

$$a_{upper} = \left[\frac{(d_{ex,port} - A2EX) \cdot (b_{ex,port} - B2EX)}{3} \right] + \left[(d_{ex,port} - A2EX) \cdot B2EX \cdot \frac{1}{2} \right] \\ + \left[(b_{ex,port} - B2EX) \cdot A2EX \cdot \frac{1}{2} \right] + [A2EX \cdot B2EX]$$

Where:

$$d_{ex,port} = 0.91 \cdot d_{exhaust,valve}$$

$$b_{ex,port} = d_{ex,port} \cdot n_{exhaust,valve}$$

For $v_{exhaust,port2}$:

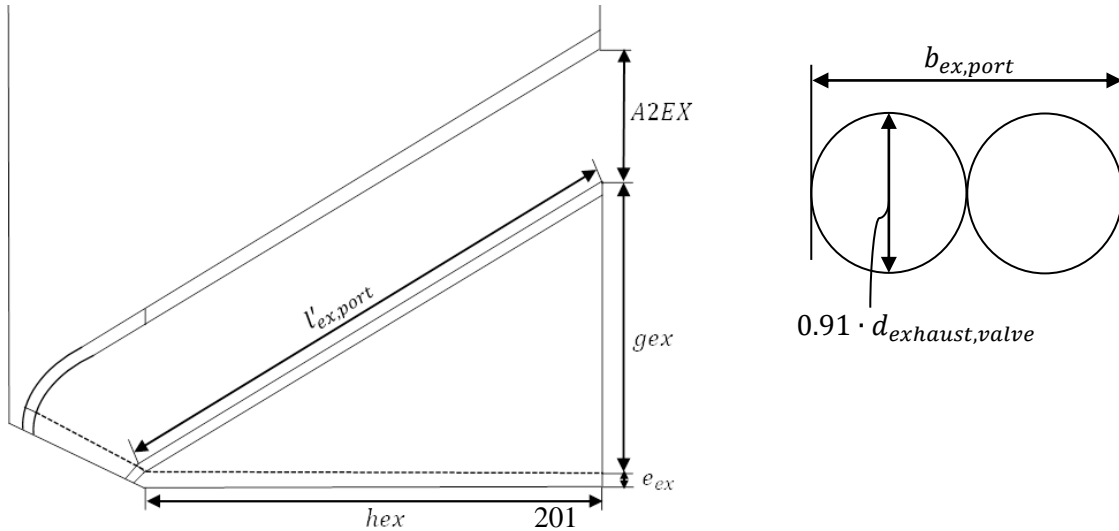
$$v_{upper2} = a_{upper2} \cdot l'_{ex,port}$$

$$a_{upper2} = \left[\frac{(d'_{ex,port} - A2EX) \cdot (b'_{ex,port} - B2EX)}{3} \right] + \left[(d'_{ex,port} - A2EX) \cdot B2EX \cdot \frac{1}{2} \right] \\ + \left[(b'_{ex,port} - B2EX) \cdot A2EX \cdot \frac{1}{2} \right] + [A2EX \cdot B2EX]$$

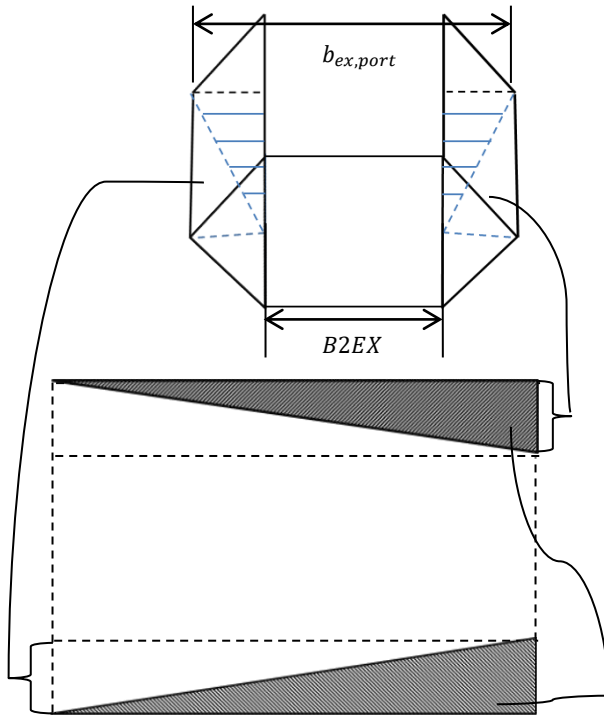
Where:

$$d'_{ex,port} = 0.91 \cdot d_{exhaust,valve} \cdot (2 \cdot t_{port,wall})$$

$$b'_{ex,port} = d_{ex,port} \cdot n_{exhaust,valve} \cdot (2 \cdot t_{port,wall})$$



Top-view



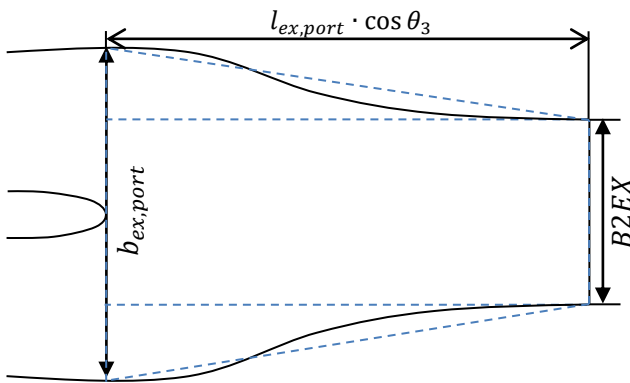
Expression for Outer Prisms

$$\frac{1}{2} \cdot A2EX \cdot (b_{ex,port} - B2EX) \cdot l'_{ex,port}$$

Expression for Pyramid

$$\left[\frac{(d_{ex,port} - A2EX) \cdot (b_{ex,port} - B2EX)}{3} \right] \cdot l'_{ex,port}$$

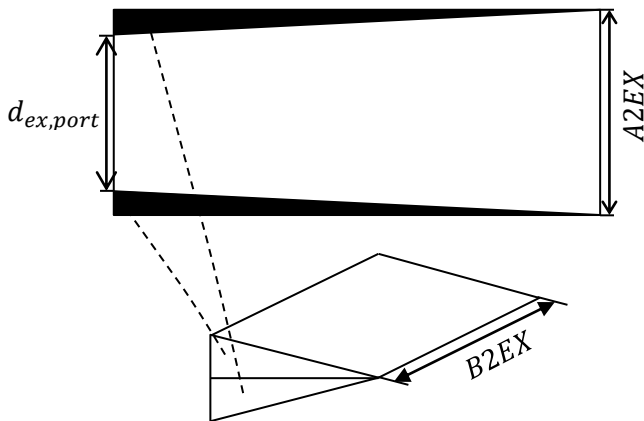
Top-view



Expression for Centre Rectangle

$$A2EX \cdot B2EX$$

Side-view



Expression for Volume of a Prism

$$\frac{1}{2} \cdot B2EX \cdot (d_{ex,port} - A2EX) \cdot l'_{ex,port}$$

B) Fuelling and Intake Manifold Pressure Iteration

Fuelling Iteration C-Script in Matlab S-Function

```
/*
 *
 *
 *
 *   Promets fuel prediction and intake manifold air pressure model
 */

#define S_FUNCTION_NAME Gasoline_turb_fuelling

#include "simstruc.h"
#include "math.h"
double turb_p_3_bar;
double P_man;
double V_swept;
double Eng_speed;
double gamma;
double Tamb;
double fric_alpha1;
double fric_alpha2;
double Pis_m_speed;
double C_R;
double P_brake;
double P_fric;
double eta_c;
double eta_indi;
double mf_old;
double mf;
double P_pump;
double P_fric_gas_loading;
double P_indi_gross;
double AFRst;
double eta_vol;
double eta_v;
double P_man_old;
double P_motored;
double P_ex;
double IMEP_desired;
double N_correction;
double P_correction;
double Torque;
double exp(P_man);
double T_coolant;
double T_coolant_fw;
double T_intake_metal;
double T_intake_metal_ideal;
double eta_vol_engine;

//double fuelling_load;
//int i;

/*
 * mdlInitializeSizes - initialize the sizes array
 */
static void mdlInitializeSizes(SimStruct *S)
{
    ssSetNumContStates( S, 0); /* number of continuous states */
    ssSetNumDiscStates( S, 1); /* number of discrete states */
    ssSetNumInputs( S, 17); /* number of inputs */
    ssSetNumOutputs( S, 10); /* number of outputs */
}
```

```

        ssSetDirectFeedThrough(S, 1); /* direct feedthrough flag */
        ssSetNumSampleTimes( S, 1); /* number of sample times */
        ssSetNumSFcnParams( S, 0); /* number of input arguments */
        ssSetNumRWork( S, 0); /* number of real work vector elements */
        ssSetNumIWork( S, 0); /* number of integer work vector elements*/
        ssSetNumPWork( S, 0); /* number of pointer work vector elements*/
    }

/*
 * mdlInitializeSampleTimes - initialize the sample times array
 */
static void mdlInitializeSampleTimes(SimStruct *S)
{
    ssSetSampleTime(S, 0, -1.0);
    ssSetOffsetTime(S, 0, 0.0);
}

/*
 * mdlInitializeConditions - initialize the states
 */
static void mdlInitializeConditions(double *x0, SimStruct *S)
{
}

/*
 * mdlOutputs - compute the outputs
 */

static void mdlOutputs(double *y, double *x, double *u, SimStruct *S, int tid)
// sets input variables to simulink variable name u[x]; where 'x' is the variable name
{

    V_swept=u[0]; // total swept volume [m^3]
    eta_c = u[1]; // combustion efficiency [%]
    eta_indi = u[2]; // indicated efficiency [%]
    P_fric = u[3]; // friction power [W]
    P_brake = u[4]; // brake power [W]
    Tamb = u[5]; // ambient temperature [K]
    Eng_speed = u[6]; // engine speed [rev/min]
    fric_alpha1 = u[7]; // friction factor 1
    fric_alpha2 = u[8]; // friction factor 2
    Pis_m_speed = u[9]; // piston mean velocity [m/s]
    C_R = u[10]; // compression ratio
    AFRst = u[11]; // air-to-fuel ratio
    mf = u[12]; // initial fuel flow
    P_motored = u[13]; //Power due to motoring
    turb_p_3_bar = u[14]; //turbocharged pre-turbine pressure
    T_coolant = u[15]; // coolant temperature above the intake port metal
    T_intake_metal = u[16]; //intake port metal temperature

    gamma = 1.4; // gas index number, ideal gas at 1.4
    P_ex = 1.01325; // exhaust manifold [bar]
    T_coolant_fw = 363;
    T_intake_metal_ideal = 363;
    Torque = P_brake/(Eng_speed*(2*3.1416)/60);
    P_man = 1;
    P_motored = (P_motored*Eng_speed*1E-3)/(120); //W

```

```

do{
mf_old = mf;
P_pump = ((turb_p_3_bar-P_man)*1E5)*V_swept*Eng_speed/120;
P_indi_gross = P_brake+P_fric+P_pump+P_motored; // Desired Indicated Power
mf = P_indi_gross/(44E6*eta_c*eta_indi); // Mass of Fuel Required
N_correction = (0.7859-4E-5*Eng_speed+3E-8*Eng_speed*Eng_speed); // speed correction
P_correction = (1.5754-3.9393*P_man+5.8327*P_man*P_man-
3.3459*P_man*P_man*P_man+0.6624*P_man*P_man*P_man*P_man); // pressure correction
eta_vol = (1+gamma*(C_R-1)-(turb_p_3_bar/P_man))/(gamma*(C_R-
1))*N_correction*P_correction; // engine volumetric efficiency
IMEP_desired = ((P_indi_gross*120)/(Eng_speed*V_swept))/100000; // Desired Indicated
Mean Effective Pressure
P_man = 0.5*(P_man_old+(((IMEP_desired)*287.1*Tamb*AFRst)/(eta_vol*44E6*eta_indi))); //
Required Manifold Air Pressure
P_man_old = P_man;

}while((fabs(mf-mf_old)/mf)>0.00001);

mf = mf; // kg/sec
P_indi_gross = P_indi_gross; // Indicated gross power
P_fric_gas_loading = ((fric_alpha+fric_alpha2*Pis_m_speed)*4.2*(1.01325-(1.01325-
P_man))*(0.088*C_R+0.182*pow(C_R,(1.33-(2.38E-2*Pis_m_speed)))))*V_swept*Eng_speed/120;
eta_vol = eta_vol*((T_coolant_fw)/(T_coolant))*pow((T_intake_metal/293),0.5); //
cylinder volumetric efficiency (/100)
IMEP_desired = IMEP_desired; // Gross Indicated Mean Effective Pressure (bar)
N_correction = N_correction; // Engine Speed Correction
eta_vol_engine = ((mf*AFRst*120)/(V_swept*(P_man*1E5/(287.1*293))*Eng_speed));

    y[0]=mf;//kg/sec
    y[1]= P_indi_gross;//Ws
    y[2]= P_pump;//W
    y[3]= P_man;//bar,3.25
    y[4]= P_fric_gas_loading;//W
    y[5]= eta_vol;//volumetric efficiency
    y[6]= IMEP_desired;
    y[7]= N_correction;
    y[8]= turb_p_3_bar; // Exhaust Pressure
    y[9]= eta_vol_engine; // engine volumetric efficiency

}
/*
 * mdlUpdate - perform action at major integration time step
 */

static void mdlUpdate(double *x, double *u, SimStruct *S, int tid)
{
}

/*
 * mdlDerivatives - compute the derivatives
 */
static void mdlDerivatives(double *dx, double *x, double *u, SimStruct *S, int tid)
{
}

/*
 * mdlTerminate - called when the simulation is terminated.

```

```
*/
static void mdlTerminate(SimStruct *S)
{
}

#ifdef MATLAB_MEX_FILE      /* Is this file being compiled as a MEX-file? */
#include "simulink.c"      /* MEX-file interface mechanism */
#else
#include "cg_sfun.h"      /* Code generation registration function */
#endif
```

C) Correlation between Modelled and Measured IMAP and PMEP

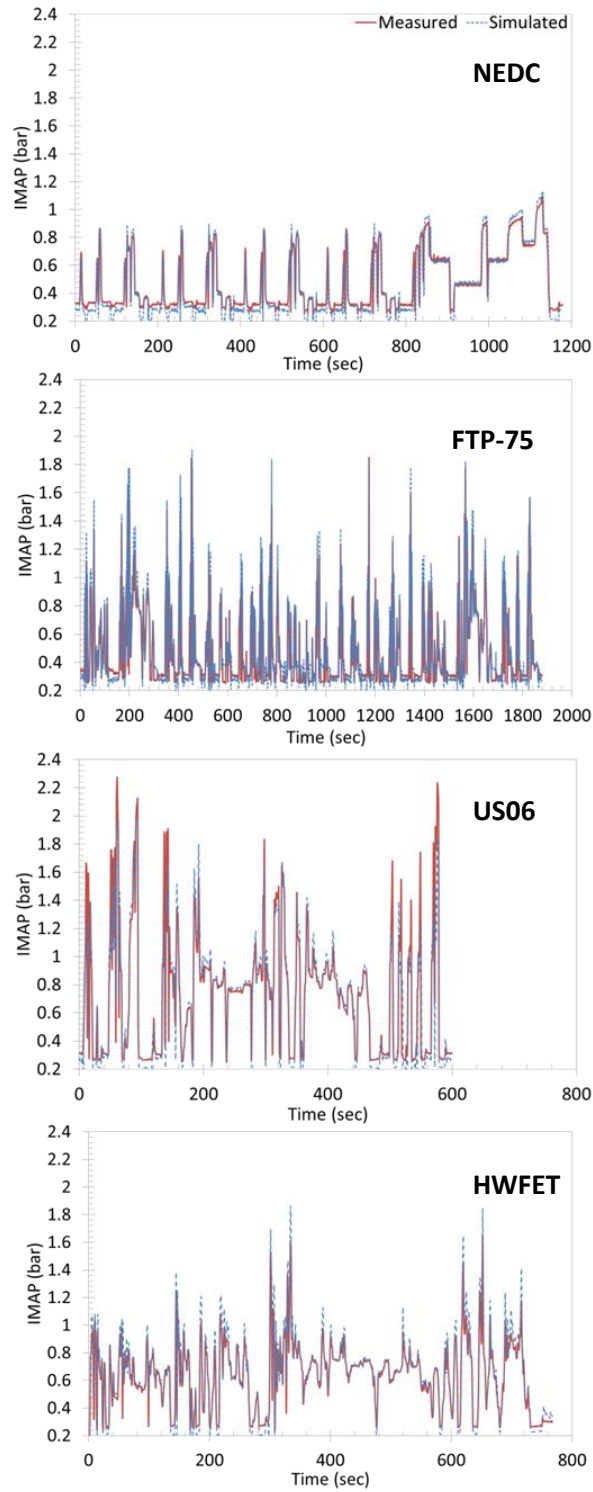


Figure 90: Modelled and measured intake manifold air pressure (bar) values for the NEDC, FTP-75, US06 and HWFET legislative drive cycles.

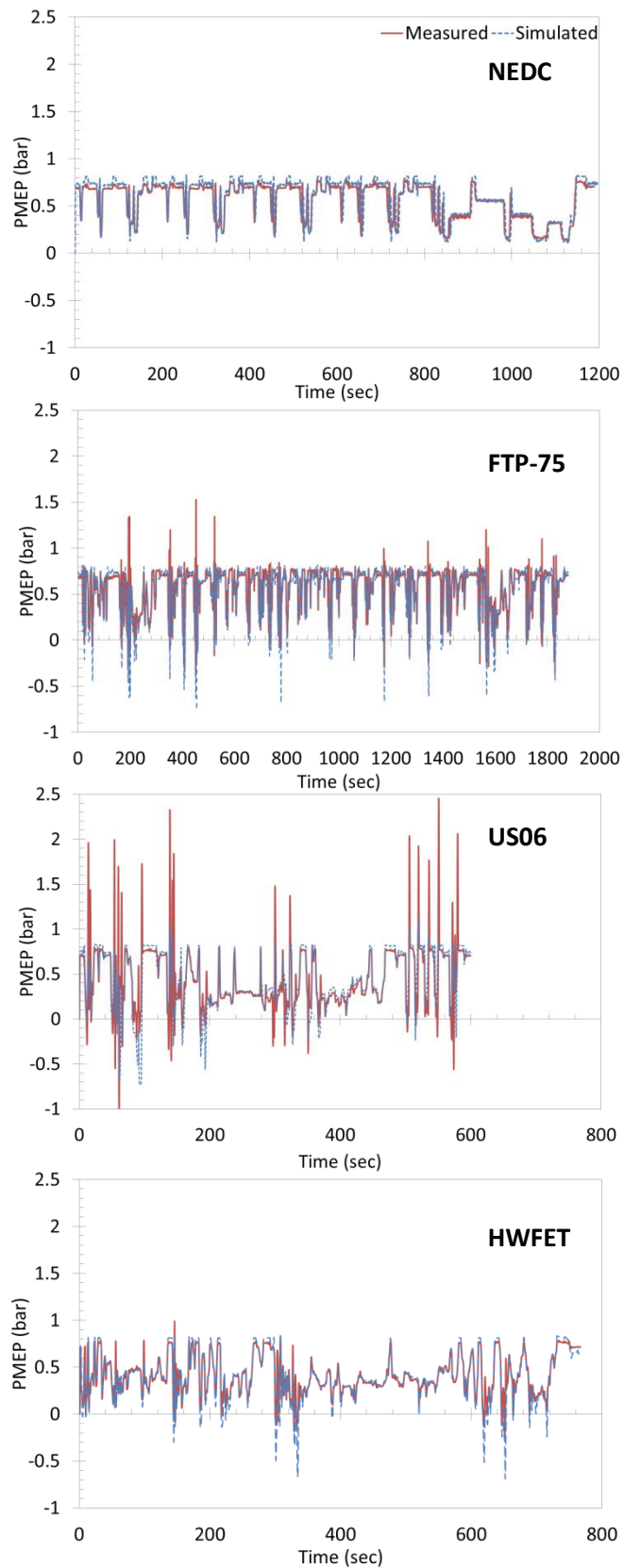


Figure 91: Modelled and measured pumping mean effective pressures (PMEP) for the NEDC, FTP-75, US06 and HWFET legislative drive cycles.

D) Experimental Changes in $\eta_{i,g}$ and Modelled Fuel Consumption Benefits

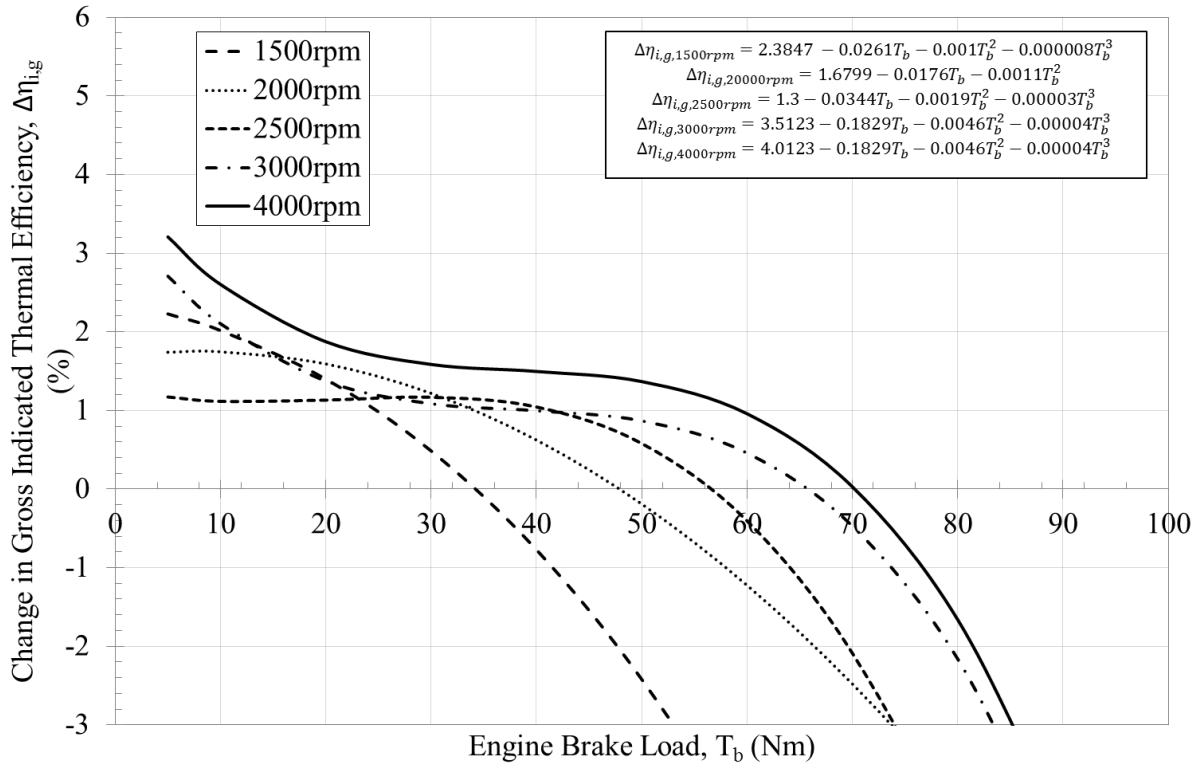


Figure 92: Measured load dependent deterioration in gross indicated thermal efficiency with deactivation of one cylinder on a three cylinder engine.

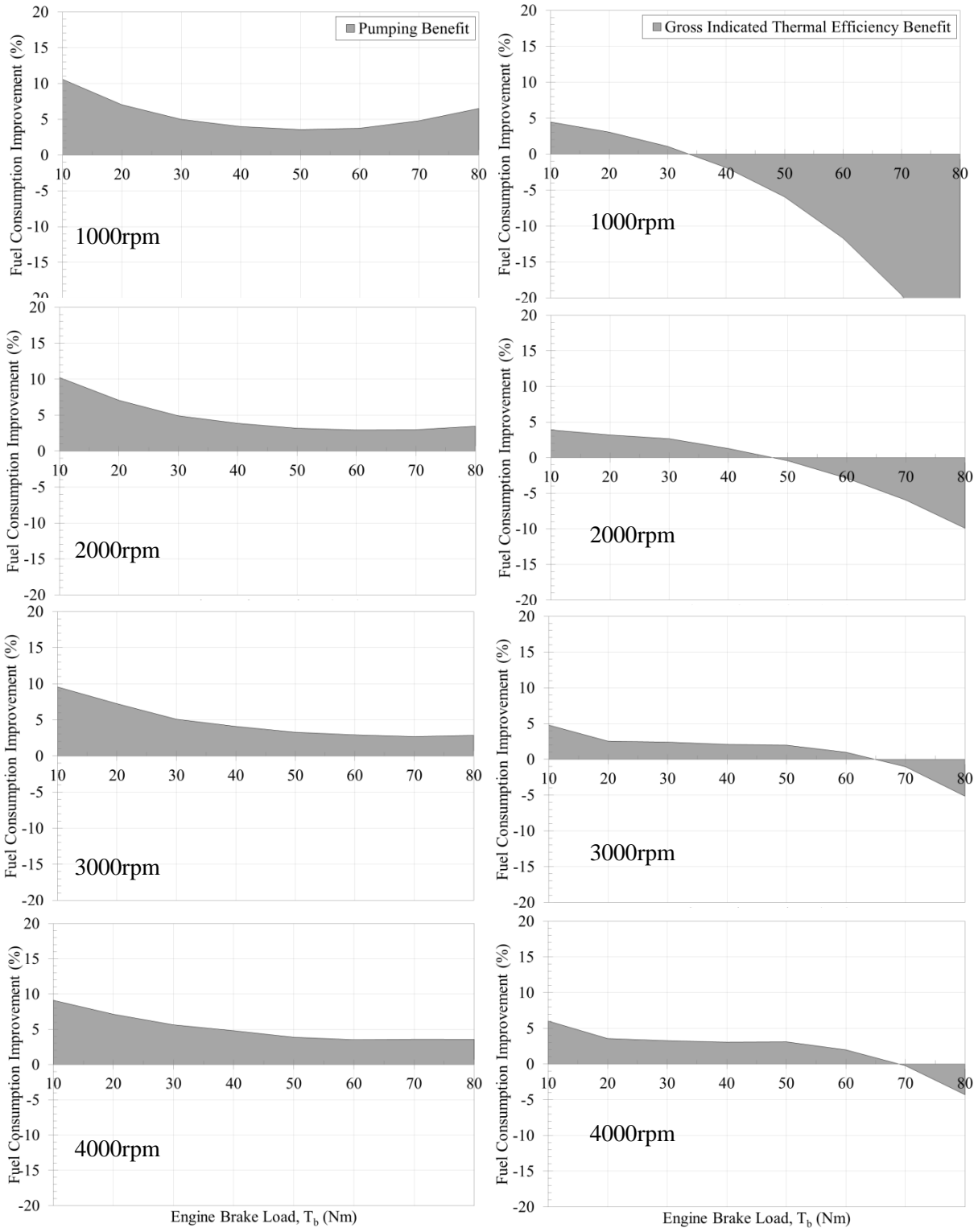


Figure 93: Attribution of percentage benefit in fuel consumption to reduced pumping work and gross indicated thermal efficiency for various engine speeds.

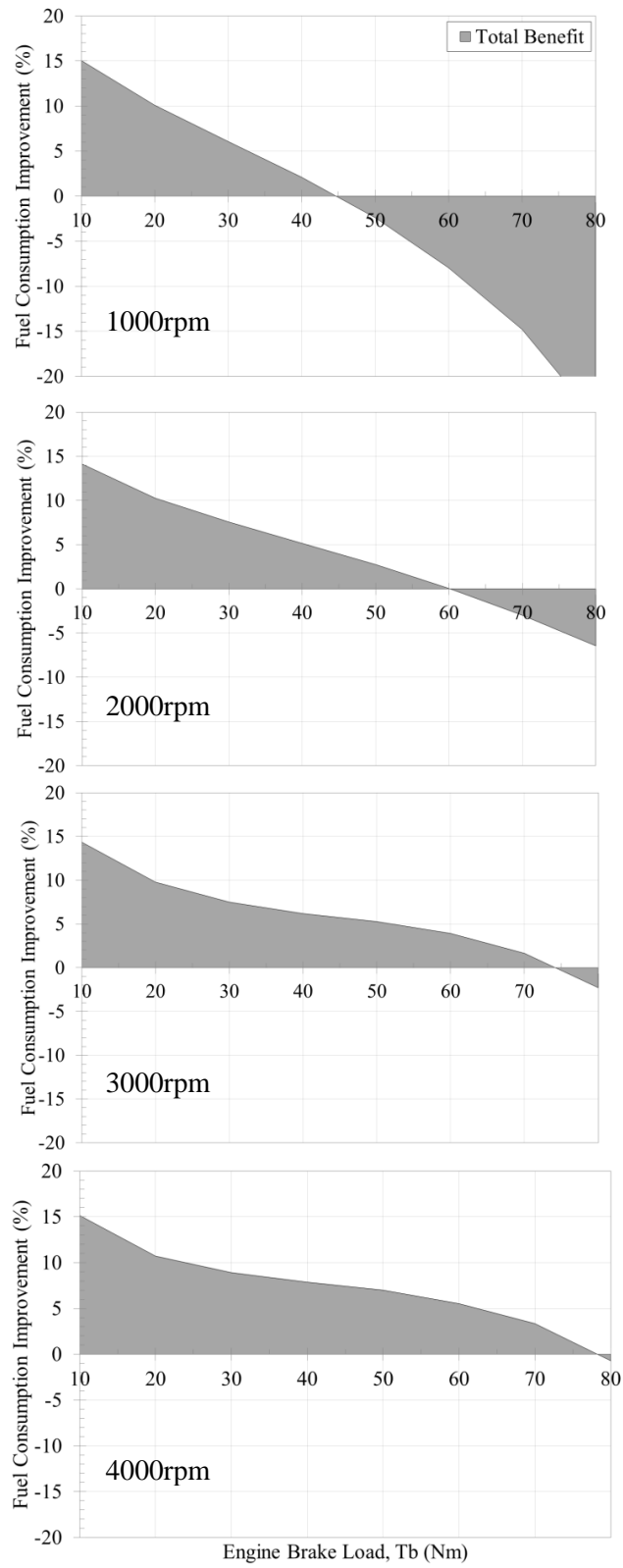


Figure 94: Net fuel consumption benefit when deactivating one of three cylinders for various engine speeds.

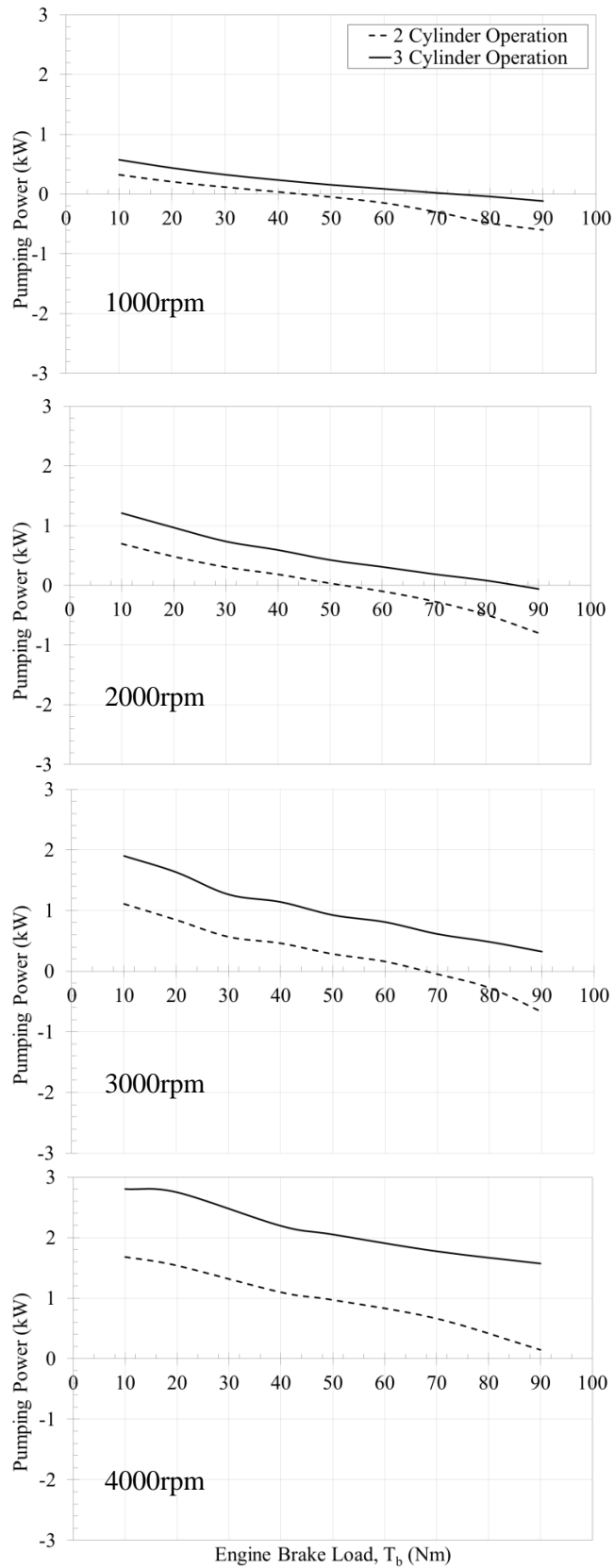


Figure 95: Modelled reduction in pumping work when deactivating one of three cylinders for various engine speeds.

E) Input Parameters for Modelling of the 4 cylinder 1.4litre TSI Engine

Variable Name	Dimension
Bore	74.5 mm
Stroke	80 mm
Cylinder Spacing	82 mm
Compression Ratio	10.5
Total Engine Mass	106 kg
Crankcase Material	Aluminium
Crankcase Mass	19 kg
Follower Configuration	Roller Tappet
Valve Angle	120°
Main Bearing Diameter	48mm
Crankshaft Mass	9.17 kg
Connecting Rod Mass (1 connecting rod)	0.370 kg
Piston Material	Aluminium
Camshaft Bearing Size (plain bearing)	24 mm
Cylinder Liner Material	Grey Cast Iron
Head Material	Aluminium
Camshaft Configuration	DOHC

Table 14: Model inputs for the 1.4l TSI Engine capable of cylinder deactivation [1.3].

F) LabVIEW Block Diagrams for the Transient Drive Cycle Control System

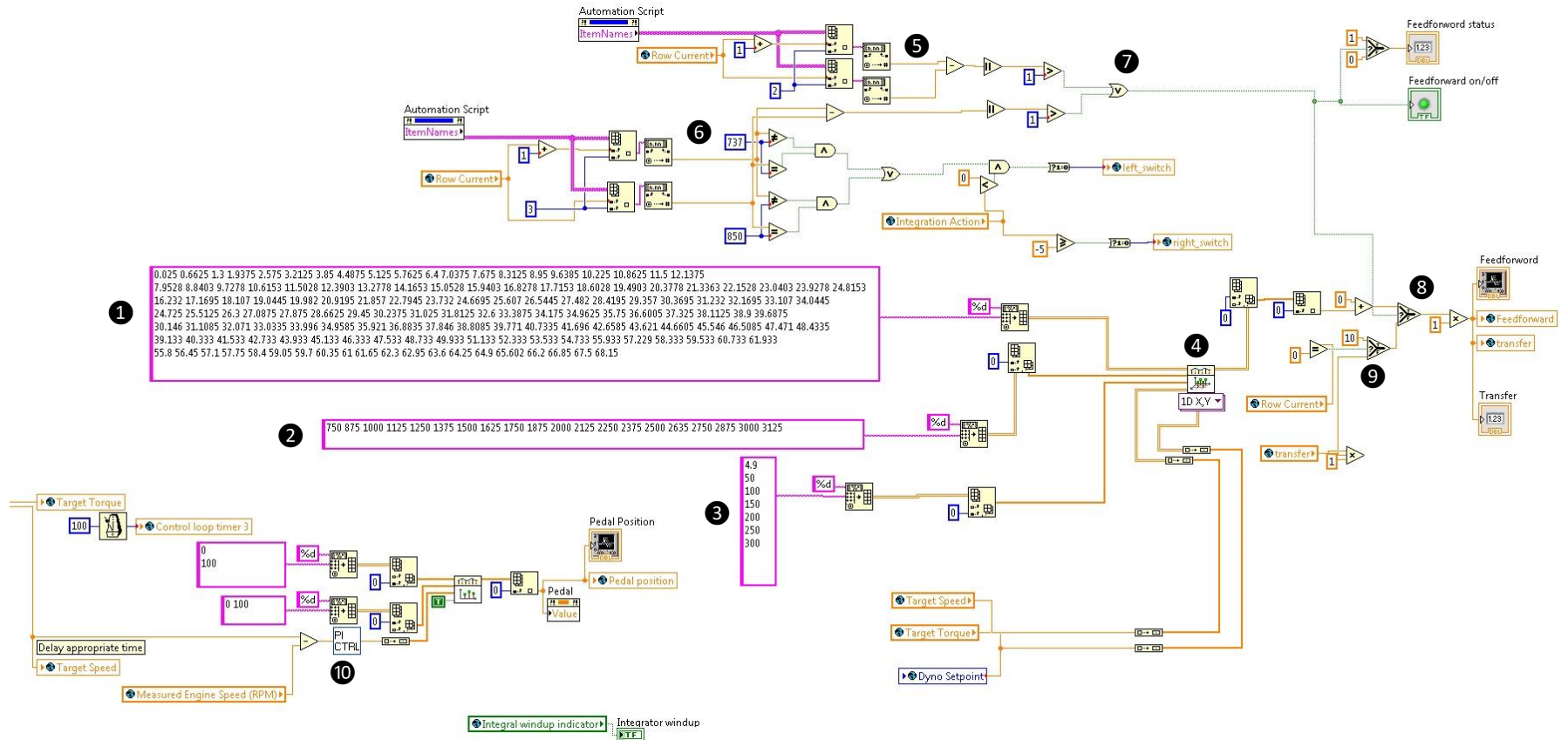


Figure 96: National Instruments LabVIEW™ upper level block diagram of the PID and FFL controller.

- ① Throttle Position Map
- ② Map X-Axis (Engine Brake Torque)
- ③ Map Y-Axis (Engine Speed)
- ④ Bilinear Throttle Position Interpolator Based on Map
- ⑤ Brake Torque Change Identifier (for Feedforward I)
- ⑥ Identifier Engine Speed Change (for Feedforward I)
- ⑦ Feedforward Asserter
- ⑧ Feedforward Throttle Output
- ⑨ Initial Feedforward Throttle Output (10% Output)
- ⑩ PID Control System

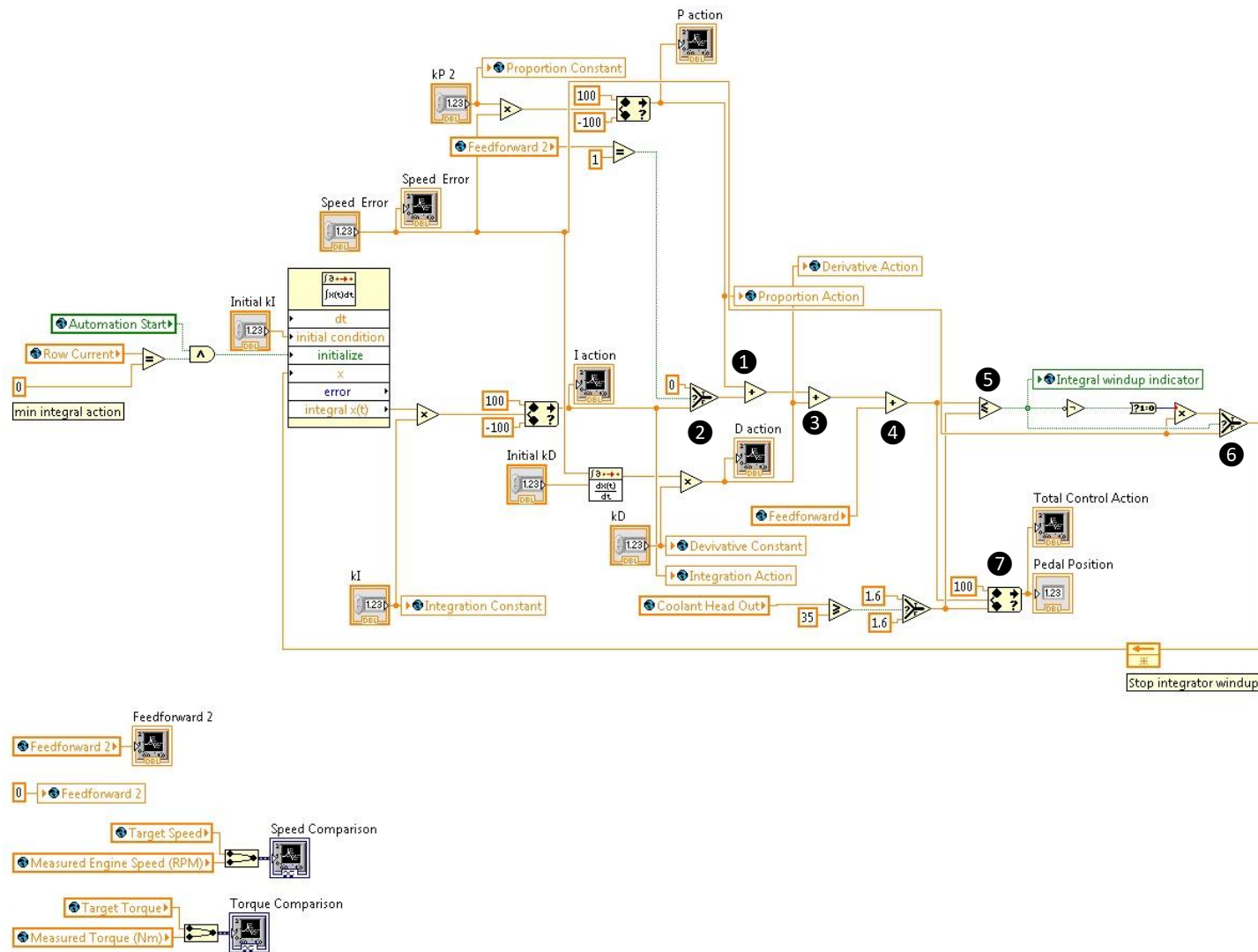


Figure 97: National Instruments LabVIEW™ PID controller and integrator wind-up nullifier block diagram.

- ① Proportional Action ② Integral Action ③ Derivative Action ④ Feed-forward I (Baseline Pedal) ⑤ Integrator Windup Control ⑥ Speed Error Nullifier ⑦ Output Pedal Position